



Universiteit  
Leiden  
The Netherlands

## Hydrogen dissociation on metal surfaces: A semi-empirical approach

Nour Ghassemi, E.

### Citation

Nour Ghassemi, E. (2019, September 19). *Hydrogen dissociation on metal surfaces: A semi-empirical approach*. Retrieved from <https://hdl.handle.net/1887/76855>

Version: Not Applicable (or Unknown)

License: [Licence agreement concerning inclusion of doctoral thesis in the Institutional Repository of the University of Leiden](#)

Downloaded from: <https://hdl.handle.net/1887/76855>

**Note:** To cite this publication please use the final published version (if applicable).

Cover Page



Universiteit Leiden



The following handle holds various files of this Leiden University dissertation:  
<http://hdl.handle.net/1887/76855>

**Author:** Nour Ghassemi, E.

**Title:** Hydrogen dissociation on metal surfaces: A semi-empirical approach

**Issue Date:** 2019-09-19

Hydrogen Dissociation  
on  
Metal Surfaces  
A Semi-empirical Approach

PROEFSCHRIFT

ter verkrijging van  
de graad van Doctor aan de Universiteit Leiden,  
op gezag van Rector Magnificus prof. mr. C.J.J.M. Stolker,  
volgens besluit van het College voor Promoties  
te verdedigen op donderdag 19 september 2019  
klokke 11:15 uur

door

Elham Nour Ghassemi  
geboren te Tabriz, Iran, 1980

Promotor: Prof. dr. G. J. Kroes  
Co-promotor: Dr. M. F. Somers

Promotiecommissie: Prof. dr. H. S. Overkleeft (voorzitter)  
Prof. dr. M. T. M. Koper (secretaris)

Overige commissieleden: Prof. dr. A. Groß (Universität Ulm, Duitsland)  
Prof. dr. G. C. Groenenboom (Radboud Universiteit  
Nijmegen)  
Dr. C. Díaz (Universidad Autónoma de Madrid,  
Spanje)  
Dr. I. M. N. Groot



**European Research Council**  
Established by the European Commission

### **European Research Council**

The work in this thesis was supported by the ERC  
Advanced grant 338580.

ISBN: 978-94-028-1638-9

The research reported in this thesis has been performed in the theoretical chemistry group of the Leiden Institute of Chemistry (Einsteinweg 55, 2333 CC, Leiden NL). This work has been supported financially by the Nederlandse Organisatie voor Wetenschappelijk Onderzoek (NWO) and by the European Research Council through an ERC-2013 advanced grant (Nr. 338580), and with computer time granted by NWO Exacte Wetenschappen, EW (NWO Physical Science Division).



Typeset with L<sup>A</sup>T<sub>E</sub>X.

Cover design and printed by: IPSKAMP.

Original image of the cover under license from Shutterstock.com.

Copyright © 2019 Elham Nour Ghassemi, The Netherlands.



To Radin,



# Contents

<b>Contents</b>	<b>vii</b>
<b>1 Introduction</b>	<b>1</b>
1.1 Reactions of molecules on surfaces . . . . .	3
1.2 Scattering of molecules from surfaces . . . . .	7
1.3 Aim of this thesis . . . . .	14
1.4 Main results . . . . .	15
1.5 Outlook . . . . .	18
<b>2 Theoretical Background</b>	<b>29</b>
2.1 Modelling the molecule surface interaction . . . . .	31
2.2 Density functional theory . . . . .	33
2.3 Density functional theory for periodic systems . . . . .	39
2.4 Construction of potential energy surfaces . . . . .	41
2.5 Molecular dynamics . . . . .	44
<b>3 Chemically Accurate Simulation of Dissociative Chemisorption of D<sub>2</sub> on Pt(111)</b>	<b>59</b>
3.1 Introduction . . . . .	61
3.2 Method . . . . .	63
3.3 Results and discussion . . . . .	68
3.4 Conclusions and outlook . . . . .	77
<b>4 Test of the Transferability of the Specific Reaction Parameter Functional for H<sub>2</sub> + Cu(111) to D<sub>2</sub> + Ag(111)</b>	<b>85</b>
4.1 Introduction . . . . .	87
4.2 Method . . . . .	92
4.3 Results and discussion . . . . .	102
	vii

4.4	Conclusions . . . . .	119
<b>5</b>	<b>Transferability of the Specific Reaction Parameter Density Functional for <math>H_2 + Pt(111)</math> to <math>H_2 + Pt(211)</math></b>	<b>131</b>
5.1	Introduction . . . . .	133
5.2	Theoretical methodology . . . . .	138
5.3	Results and discussion . . . . .	151
5.4	Conclusion . . . . .	169
<b>6</b>	<b>Assessment of Two Problems of Specific Reaction Parameter Density Functional Theory : Sticking and Diffraction of <math>H_2</math> on Pt(111)</b>	<b>179</b>
6.1	Introduction . . . . .	182
6.2	Experiments and beam parameters used to simulate the experiments . . . . .	185
6.3	Method . . . . .	194
6.4	Results and discussion . . . . .	200
6.5	Conclusions . . . . .	211
6.A	Appendix . . . . .	214
	<b>Summary</b>	<b>225</b>
	<b>Samenvatting</b>	<b>229</b>
	<b>Curriculum Vitae</b>	<b>235</b>
	<b>List of Publications</b>	<b>237</b>
	<b>Afterword</b>	<b>239</b>

CHAPTER 1

**Introduction**





## 1.1 Reactions of molecules on surfaces

Molecule surface interactions are very important, not only in many industrial applications [1], but also in our daily life. There are very simple examples of molecule-surface interactions in the world around us. For example, when an iron chain has turned to red, oxidation reactions have taken place: iron reacts with the oxygen in the air and get rusted in a humid environment. Many physicists and chemists study these kinds of phenomena to understand how gas or liquid molecules interact with solids.

The simplest aspect of a chemical reaction based on our elementary background of chemistry knowledge is that two molecules approach each other and climb the potential energy barrier, their bonds get pulled apart in the transition state and finally separate. New products are formed. However, complexity is added in chemical reactions when the reactant is a metal surface [2]. In the meantime, it is known that catalysts reduce the energy required for material productions. Catalysts create an alternative energy pathway to increase the speed and outcome of the reaction. It would be difficult to imagine our industrialized world without catalysts. For example, catalytic converters in vehicles convert pollutants in the exhaust to safer substances [3]. Catalytic production of ammonia (the so-called Haber-Bosch process [4]) enabled a dramatic increase of the agricultural production [5]. Heterogeneous catalysis, which has a crucial role in chemical technology, is a type of catalysis in which the molecules involved in the catalytic reaction are in a different phase (often in the gas phase) and the catalyst is often a solid metal surface. The understanding of catalysis has rapidly increased in the last decades [6]. However, there are many complexities. The catalyst itself may have a very complicated structure, and understanding catalysts under real working conditions often involving high temperature and pressure is not easy.

Surface science techniques have already enabled us to understand many catalytic reactions both from an experimental and theoretical perspective. One of the most well-known examples is the understanding of the reaction mechanism for ammonia synthesis, for which Gerhard Ertl has been awarded the Nobel Prize in chemistry [7]. The experimental works on this process, also known as the Haber-Bosch process, lead to the conclusion that the rate-

limiting step of this process is the dissociative chemisorption of nitrogen on the catalyst surface. For the Haber-Bosch process commonly iron or ruthenium based catalysts are used.

The modern instruments provide the facilities to clean and orient catalyst samples with very high accuracy. To avoid polluting atoms and molecules which might deposit on a surface, the samples are kept at very low pressure under ultrahigh vacuum conditions. Clean and well-defined flat surfaces reduce the complexity of the system to a great extent. Several spectroscopic, diffraction and microscopic methods are used to study catalysis. Supersonic molecular beams experiments are especially useful among the methods to study catalysts. The translational energy of the gas molecules can be controlled by changing the nozzle temperature, or by seeding with other gases. The angle of incidence is often controlled in the molecular beam experiments. These experiments allow measuring sticking probabilities of gas molecules to a surface as a function of all these observables (*i.e.*, incidence energy, angle, or in some cases initial rotational or vibrational state of the gas molecule).

A large amount of information on the gas surface interaction can thus be obtained from molecular beam experiments. It is also very beneficial to understand the underlying potential energy surface (PES) for the molecule-surface interaction. However, based on the experimental results only, understanding microscopic details of the interaction is very difficult. Theoretical modeling and molecular dynamics simulations are now able to reproduce molecular beam experiments, which is crucial to understanding the details of the molecule-surface interaction. Molecular dynamics simulations are often cheaper than the experiments. Molecular beam simulation in some cases is able to match experiments very accurately, however in other cases there is still plenty of room for improvement. From another point of view, molecular beam experiments can be of help with the development of theoretical models for the molecule-surface interactions [8]. In the absence of an accurate *ab initio* method for computing molecule-metal surface interactions, it seems that the best can be achieved by a combination of both experiments and theoretical modeling to understand and develop new catalysts [8].

Modeling a reaction on a surface is typically a two-step process. First, the interaction energy of the molecule on the surface is computed for various configurations and then used to construct a PES. In this step, the most important challenge is to obtain a reaction barrier within chemical accuracy. The next step is to calculate the dynamics, *i.e.*, to determine how

the molecule moves on the PES and exchanges energy until the products are formed. This two-step procedure amounts to modeling the reaction with the so-called Born-Oppenheimer (BO) approximation [9]. In molecule-metal surface interactions, the continuum of electronic states of a metal surface can be an extra energy exchange channel between molecule and surface. A small amount of energy can be transferred from molecular degrees of freedom (DOF) to the electrons lying just under the Fermi level. This generates an electron-hole pair. The accurate description of the effect of electron-hole pair excitation on molecule-surface reactions is an important challenge to achieving chemical accuracy for some molecule-surface reactions. Multiple electronic states and coupling between them may have to be taken into account.

When a molecule meets a surface, various events can occur. The most common events are shown in Figure 1.1. The process of adsorption of molecules or atoms is one of the key steps in molecule-surface reactions. A molecule can be adsorbed to a surface through several mechanisms: (a) dissociative chemisorption, in which a bond of an incoming molecule is broken and two new bonds are formed between the fragments and surface atoms, (b) abstraction, in which a bond of the incoming molecule is also broken but only one fragment is absorbed to the surface while the other fragment escapes to the gas phase, (c) molecular adsorption, in which a molecule gets adsorbed on the surface as a whole, either by chemisorption or physisorption, but the bond in the molecule is not broken. The combination of adsorbed fragments is also possible. Three other events are shown in the figure : (d) the Langmuir-Hinshelwood reaction, in which two fragments that are accommodated to the surface meet each other, form a new bond and the newly formed molecule desorbs (This mechanism can be regarded to be the reverse of dissociative chemisorption, and is also called associative desorption.), (e) Eley-Rideal reaction, in which a fragment coming from the gas phase collides with an adsorbed fragment, forms a new bond and the molecule that is formed in this way, desorbs, (f) hot atom reaction, in which a fragment coming from the gas phase collides with the surface and makes several bounces while it is not yet in thermal equilibrium with surface, collides with an other adsorbed fragment on the surface which is in thermal equilibrium with it, forming a new bond and the molecule formed desorbs. Dissociative chemisorption is an elementary step in many catalyzed reactions and often a rate-limiting step in the overall reaction [7]. This reaction is therefore of particular interest in the field of heterogeneous catalysis.

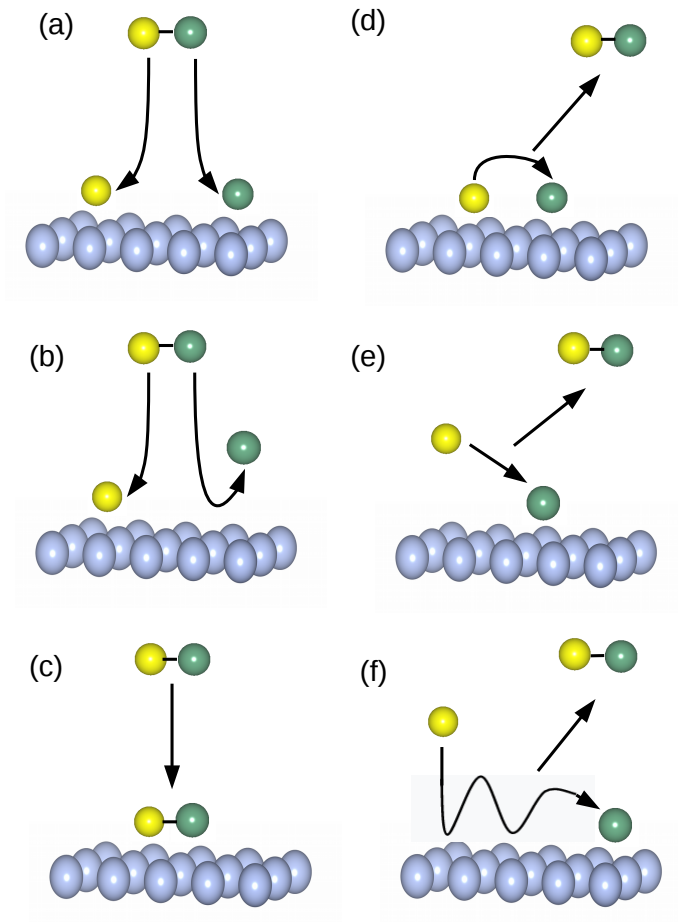


Figure 1.1: Different mechanisms for molecule-surface reactions: (a) dissociative chemisorption, (b) abstraction, (c) molecular adsorption, (d) Langmuir-Hinshelwood, (e) Eley-Rideal and (f) the hot-atom mechanism.

## 1.2 Scattering of molecules from surfaces

To study the chemical reaction occurring at a surface, it is conceptually important to understand the scattering and adsorption of a molecule on the surface. A relatively simple molecule like hydrogen scattering from or getting adsorbed on a surface can serve as an ideal model system to study. There are several reasons for this. First, a hydrogen molecule is a homonuclear diatomic molecule and the simplest molecule for which dissociative chemisorption occurs. Second, in spite of the fact that phonon and nonadiabatic effects play a role in dissociative and reactive scattering, both thermal surface atom displacements due to phonons and electron-hole pair excitations are expected to have a small effect on the dissociative chemisorption of hydrogen on metal surfaces [10]. The full discussion of these effects and a detailed overview of theoretical results on  $\text{H}_2$  dissociation on and scattering from a surface can be found in Refs. [10–13]. For a  $\text{H}_2$ -metal surface system we can then assume reaction to take place on a ground state PES, and on a static surface. Briefly, it has been argued that electron-hole pair excitation can be neglected for  $\text{H}_2$ -metal systems because, for  $\text{H}_2$  dissociation on Pt(111) and using a single PES it was possible to accurately describe both reaction and diffractive scattering [14]. Furthermore, electron-hole pair excitation effects were studied explicitly in  $\text{H}_2$  dissociation on Cu(111) [15, 16], Cu(110) [17] and Ru(0001) [18] in dynamical calculations using the molecular dynamics with electronic friction (MDEF) model. These studies have shown that non-adiabatic effects play a small role in these systems. Additionally, due to the large mismatch between the mass of  $\text{H}_2$  and the surface atoms, the energy transfer from the molecule to the metal surface should be small and unlikely to influence the scattering results [19–21]. If we neglect the surface atoms DOFs, we only consider the motion of the molecule in its six DOFs on the ground state PES.

### 1.2.1 The hydrogen molecule

Let us consider the hydrogen molecule in the gas phase and solve the Schrödinger equation. The solutions are labelled with three quantum numbers,  $\nu$ ,  $j$  and  $m_j$ . The first quantum number,  $\nu$  defines the vibrational motion of the molecule. The interaction energy between two atoms in the diatomic molecule is shown as a function of the vibrational coordinate, *i.e.*, the internuclear distance  $r$ .  $r = r_{eq}$  is the equilibrium bond length of the

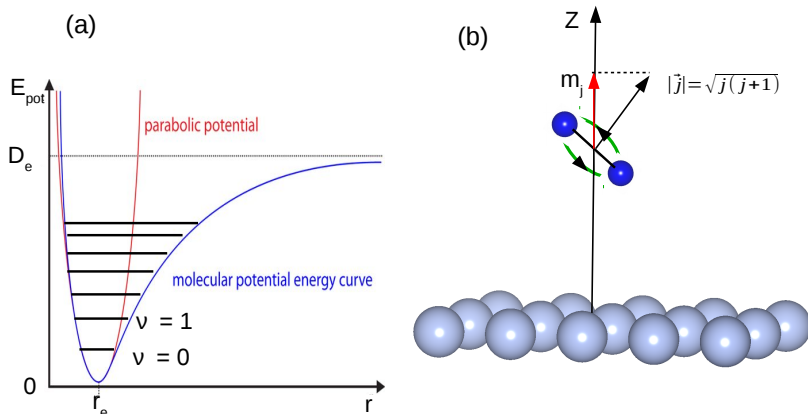


Figure 1.2: (a) Interaction energy curve as a function of molecular bond length for hydrogen molecule. The equilibrium bond length and the dissociative energy are shown as  $r_e$  and  $D_e$ , respectively. (b) Classical representation of the angular momentum vector  $\vec{j}$  of  $\text{H}_2$  together with its projection ( $m_j$ ) on the surface normal ( $Z$ ), and the definition of its angular momentum quantum number  $j$ .

molecule where the energy curve has its minimum. Near the equilibrium position in the potential energy curve, the molecule can be described fairly well by a quadratic equation (as a simple harmonic oscillator). The energy curve increases for both smaller and larger values of  $r$  than  $r_e$ . For large internuclear distances the interaction energy is close to the dissociation energy. The horizontal lines in Figure 1.2 (a) represent the allowed energy levels associated with the vibrational quantum number.  $\nu = 0$  has a particular vibrational energy called the zero-point energy (ZPE) ( $E_{\nu 0} = 1/2h\nu$ ). The rotational motion of the molecule is represented by the next two quantum numbers,  $j$ , and  $m_j$ . The angular momentum vector  $\vec{j}$  together with its projection  $m_j$  onto a space-fixed axis ( $Z$ ) are shown in Figure 1.2 (b).  $\vec{j}$

is oriented perpendicular to the plane of rotation and has a length equal to  $\sqrt{j(j+1)}$  in atomic units, where  $j$  is an integer number and called the rotational or angular momentum quantum number. The projection of  $\vec{j}$  on the surface normal,  $m_j$ , the rotational magnetic quantum number can take any integer value between  $-j$  and  $j$ . Therefore, for a given value of  $j$ , there are  $2(j+1)$  possible  $m_j$  states for a nuclear wave function, which are degenerate. In the rigid rotor approximation the rotational energy of the molecule is given by  $\frac{j(j+1)}{2\mu r_e^2}$  in which  $\mu$  is the reduced mass of the molecule, and is a function of only the quantum number  $j$ . In the gas phase, the hydrogen molecule, not only vibrates (associated with one DOF) and rotates (associated with two DOFs) but it also moves translationally in three directions. Therefore, translational motion of the molecule accounts for three of the six molecular DOFs. Molecular translational motion is not quantized. Hence, the molecule can have any amount of initial translational energy with an arbitrary incidence direction.

### Hydrogen interacting with a surface

When a hydrogen molecule situated in the gas phase has translational energy towards the metal surface, it will approach the surface and finally interact with the surface. The bond length of the approaching molecule may extend and if the molecule has enough translational or internal energy, it may overcome the barrier to dissociation. The PES of  $\text{H}_2$  interacting with a metal surface is not that of a molecule interacting with an ideal flat surface; the corrugation in  $X$  and  $Y$  can give rise to scattering in or out of the incidence collision plane (See Figure 1.3). During this physical process, the molecule can also transfer (gain) energy to (from) the surface. Based also on this energy transfer we can distinguish the following phenomena: (a) elastic scattering: if no energy is transferred between the molecule and the surface during the collision; (b) vibrationally inelastic scattering: the molecular vibrational energy increases or decreases during the collision, because energy is transferred towards (from) the molecular vibrational motion; (c) rotationally inelastic scattering: the molecular rotational energy increases or decreases during the collision; (d) diffraction or diffractive scattering: the parallel (to the surface) momentum of the molecule near a surface can only change by discrete quantities, due to the periodicity of the surface; as a result the angular distribution of the scattered molecule presents a discrete peaks distribution. The associated quantum numbers are  $n$  and  $m$  and

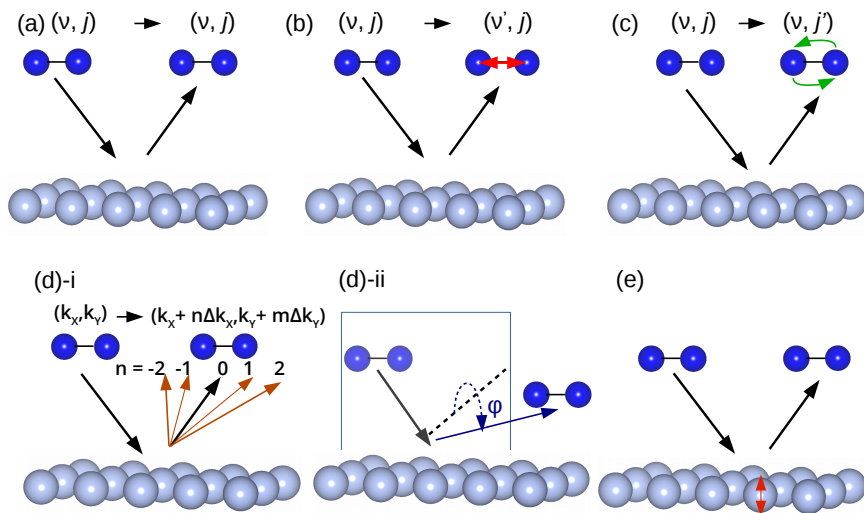


Figure 1.3: Graphical representation of some of the possible outcomes that can happen when a molecule approaches to a surface. (a) elastic scattering, (b) vibrationally inelastic scattering, (c) rotationally inelastic scattering, (d) diffractive scattering (i- in plane, ii- out-of-plane scattering) (e) phonon inelastic scattering.

the diffraction quantum  $\Delta k$  is a surface reciprocal lattice vector and is determined by the periodicity of the direct lattice. For a square surface the diffraction quanta are given by  $\Delta k_X = \frac{2\pi}{L_X}$  and  $\Delta k_Y = \frac{2\pi}{L_Y}$ , where  $L_X$  and  $L_Y$  are the length of surface unit cell, respectively. There is special case of diffraction called specular scattering or specular reflection when  $n = m = 0$ . In all these processes, the molecule may also excite surface DOFs, *i.e.*, phonons (surface vibrations) and electron-hole pairs (Figure 1.3 (e)).

The details of the dynamics give us information about the topography of the PES. To study the reaction mechanisms, the reaction barrier height, and the barrier position are very important to classify the dynamics of molecule-surface interactions. The existence or lack of a barrier to dissociation in the most favorable reaction pathway on the PES distinguishes the type of H<sub>2</sub>-



metal surface system. Such a system can show activated or non-activated dissociation.

H<sub>2</sub> dissociation is activated on noble metals, examples of activated systems include H<sub>2</sub> dissociation on Cu(111) [22], Cu(110) [22], Cu(100) [22], Ag(111) [23] and Au(111) [23]. These systems show late (close to the surface, long H–H distance), high barriers to dissociation for all possible configurations of the molecule relative to the surface. The reaction probability generally increases as a function of incidence energy monotonically up to saturation value.

Dissociation of H<sub>2</sub> is often non-activated on transition metal surfaces. The systems with non-activated dissociation show no barrier at least in some of the reaction pathways. The other reaction pathways show barriers that can be either early or late. In contrast to the case of direct activated dissociation, in which the reaction probability increases with increasing incidence energy, for lower incidence energies the reaction may also increase with decreasing incidence energy due to trapping of a molecule in a well in the potential. Trapping is only prevalent at low energies when physisorption is important. Examples of non-activated systems include H<sub>2</sub> dissociation on Pd(111) [24], Pd(100) [25], Ni(110) [25], and Ni(100) [25].

There are also systems in between strongly activated and non-activated systems that share properties of both these systems. Examples of these systems are H<sub>2</sub> dissociation on Ru(0001) [26, 27], Pt(111) [14, 28] and Ni(111) [25]. The PES shows only very low barriers to dissociation that often are far away from the surface, *i.e.*, early barriers. The reaction probability curve in these systems is similar to that in highly activated systems, in that reaction increases with increasing incidence energy.

The barrier to dissociation can also change in two different ways when the molecule moves across the surface. Different ways in which the barrier changes give rise to different corrugations of the PES are called energetic corrugation, in which the barrier changes its height, and geometric corrugation, in which the barrier changes its distance to the surface [29, 30]. PES corrugations couple molecular motion parallel and perpendicular to the surface. If there is a specific balance between energetic and geometric corrugation on the surface, it would be expected that dissociation depends only on the component of the incidence energy normal to the surface (normal energy scaling) [30, 31].

## Approximations

Unfortunately, it is usually impossible to solve the Schrödinger equation for systems of very high-dimensions. Evidently, some approximations should be made to render the problem tractable. Almost all discussions of chemical reaction dynamics begin with the BO approximation [9]. Under the following circumstances, the validity of the BO approximation holds : (1) the rearrangement of the electron cloud associated with a change of nuclear positions must be gradual; *i.e.*, non-adiabatic coupling must be small; (2) there must be a wide separation in energy between the electronic states of the system; and (3) to permit the electrons to adjust completely their motions, the velocities of the nuclei must be sufficiently small. It can be anticipated that the BO approximation breaks down in molecule-metal surface reactions, because the metal surface exhibits a continuum of electronic states, *i.e.*, there is no energetic gap between electronic states. When a molecule collides with a surface, it can excite electrons on the surface. Electron-hole pair excitation in the electronic levels in the metal can provide a mechanism for energy transfer with an adsorbate molecule, which may cast doubt on the concept of nuclear motion on a PES. Classical mechanical based models which are called friction models have been applied to describe energy transfer between molecular motion and electron-hole pair excitations at metal surfaces [32–34]. One of these methods is called molecular dynamics with electronic friction (MDEF) [34–36], which treats non-adiabatic dynamics at metal surfaces. For H<sub>2</sub> dissociation on Cu(111) [15, 16, 37], Cu(110) [17] and Ru(0001) [18] MDEF has been used to study non-adiabatic effects in dynamical calculations. The studies showed that for H<sub>2</sub> dissociation on metal surfaces, electron-hole pair excitations have a very small effect on reactive and non-reactive scattering, and the BO approximation should work rather well for the reaction of H<sub>2</sub> and D<sub>2</sub> on metal surfaces.

The next approximation is the ideal static surface approximation, in which the surface atoms are fixed and sit in their ideal lattice positions, and as a result, energy exchange between the molecule and the surface atoms and the effect of the increased corrugation of the surface due to surface atom motion are neglected. However, a broadening of the reaction probability curve with surface temperature is found in experiments on H<sub>2</sub> and D<sub>2</sub> desorbing from hot Cu(111) surfaces [38, 39]. *Ab initio* molecular dynamics (AIMD) calculations provide the opportunity to model the effect of surface temperature and surface atom motion on a gas-surface reaction, and have

recently been used to study the dissociation of  $\text{CH}_4$  on metal surfaces [40–42]. The study of static surface temperature effects on  $\text{H}_2$  dissociation on  $\text{Cu}(111)$  [43] and AIMD calculations on dissociation of  $\text{D}_2$  on  $\text{Cu}(111)$  [44] showed that the approximation of an ideal static surface works rather well for low surface temperatures, in particular for the simulation of molecular beam experiments for these systems ( $T_s = 120$  K).

For many-body systems like a molecule interacting with a metal surface, density functional theory (DFT) is the current method of choice for obtaining an approximate solution to the Schrödinger equation. The central object in DFT is the so-called exchange-correlation (XC) functional. Approximations have to be used to construct the XC functionals, and this affects the accuracy of the description of a molecule-surface reaction. The well-known generalized gradient approximation (GGA) [45, 46] level functionals are commonly used to describe molecule-surface reactions, and these are available in many quantum chemistry software packages. At a lower level than the GGA is the local density approximation (LDA) [47], which does not work well for molecule-surface reactions [48–50]; it yields too low barriers for activated processes compared to experimental data. Further descriptions of the approximation levels for the XC functionals are found in Section 2.2.1.

In order to accurately describe the molecule-surface interaction, a highly accurate PES is required. The PESs obtained from the latest electronic structure theory based on DFT with functionals incorporating a GGA or one step higher level of theory than GGA, *i.e.*, meta-GGA [10, 12, 51] exhibit errors for barrier heights. Furthermore, the long range interaction (van der Waals interaction), which could be important for molecule-metal systems, is not taken into account in common semi-local XC functionals at the GGA level. Recently, a novel implementation of the specific reaction parameter (SRP) approach to DFT, adopted to molecule-surface interactions, was proposed [52]. At present, this methodology is the only DFT approach that has been demonstrated to provide chemically accurate values of barrier heights for reactions of small molecules with metal surfaces. This approach has yielded accurate values of barrier heights for the dissociative chemisorption of  $\text{H}_2$  on  $\text{Cu}(111)$  [52],  $\text{Cu}(100)$  [53], and  $\text{Pt}(111)$  [54] and of  $\text{CHD}_3$  on  $\text{Ni}(111)$  [41],  $\text{Pt}(111)$ , and  $\text{Pt}(211)$  [42]. The SRP–DFT method is semi-empirical, and systematically improves the accuracy of the XC functional by fitting an adjustable parameter in the density functional, such that supersonic molecular beam experiments on the system of interest are reproduced. This method is at the heart of this thesis and it will be

discussed thoroughly in the following chapters.

### 1.3 Aim of this thesis

As discussed before, one of the main problems in the accurate description of a molecule interacting with a metal surface is the choice of the XC functional used to perform the DFT calculations. In this thesis, the main aim is to provide an improved description of  $\text{H}_2$  dissociative chemisorption on metal surfaces based on the semi-empirical SRP method in which the accuracy of XC functionals are systematically improved in a semi-empirical and system specific way, by comparing the experimental data with theoretical results. The goal is to construct a database of reaction barriers with chemical accuracy for  $\text{H}_2$  interacting with metal surfaces. The aims of the work reported in the following chapters are briefly summarized here.

- In Chapter 2 the modeling of molecule-surface interactions is described. The basis of the DFT method is described and the SRP method is also briefly explained. The interpolation method used for construction of the PES is given. Finally, the theory of the molecular dynamics methods used in this thesis is represented.
- In Chapter 3, the aim is to extend the development of SRP density functionals, and the database, with a result for a weakly activated dissociative chemisorption reaction of  $\text{H}_2$  with a transition metal surface. For this aim, a SRP-DF is developed, in which a SRP functional incorporates in the correlation part the revised version of the vdW-DF developed by Lee *et al.* [55] and called vdW-DF2, for the dissociation of dihydrogen on Pt(111). The study has been performed using semi-empirical density functional theory and the quasi-classical trajectory (QCT) method. The validity of the QCT method is investigated by showing that QCT calculations on reaction of  $\text{D}_2$  with Pt(111) closely reproduce quantum dynamics (QD) results for reaction of  $\text{D}_2$  in its rovibrational ground state. The goal is to achieve a chemically accurate description of  $\text{D}_2$  dissociation on Pt(111) with molecular beam simulations, while reproducing the experimental results at normal and off-normal incidence.

- In Chapter 4, the main focus is on the transferability of an SRP functional among chemically related systems. The SRP functional originally developed to describe chemisorption of dihydrogen on Cu(111) [56] (called SRP48 functional) is tested here on dissociation of the same molecule on Ag(111), with Cu and Ag belonging to the same group of the periodic table. We investigate whether the SRP density functional derived for  $\text{H}_2 + \text{Cu}(111)$  also gives chemically accurate results for  $\text{H}_2 + \text{Ag}(111)$ . For this purpose, we performed QCT calculations using the six-dimensional PES of  $\text{H}_2 + \text{Ag}(111)$  within the Born-Oppenheimer static surface (BOSS) approximation. The computed reaction probabilities are compared with both state-resolved associative desorption and molecular beam sticking experiments.
- In Chapter 5, the main goal is to address the question whether the SRP-DF functional derived for  $\text{H}_2 + \text{Pt}(111)$  is transferable to the  $\text{H}_2 + \text{Pt}(211)$  system. Most importantly, the work reported in Chapter 5 also investigates the transferability among systems in which  $\text{H}_2$  interacts with different faces of the same transition metal, which is relevant to heterogeneous catalysis.
- In Chapter 6, the focus is on two basic problems of the SRP-DFT methodology. The first problem is that sticking probabilities (to which SRP-DFs functionals are usually fitted) might show differences across experiments, of which the origins are not always clear. The second problem is that it has proven hard to use experiments on diffractive scattering of  $\text{H}_2$  from metals for validation purposes, as dynamics calculations using a SRP-DF may yield a rather poor description of the measured data, especially if the potential used contains a van der Waals well.

## 1.4 Main results

The main results of the work reported in the following chapters are discussed here.

### Chapter 3: Chemically Accurate Simulation of Dissociative Chemisorption of D<sub>2</sub> on Pt(111)

In Chapter 3, we obtained an SRP density functional for H<sub>2</sub> + Pt(111) by adjusting the  $\alpha$  parameter in the PBE $\alpha$ -vdW-DF2 functional until reaction probabilities computed with the QCT method reproduced sticking probabilities measured for normally incident D<sub>2</sub> with chemical accuracy. We found that using the vdW-DF2 functional improves the description of the molecule-surface interaction compared to the original vdW-DF. Comparison of QD calculations for the initial ( $\nu = 0, j = 0$ ) state of D<sub>2</sub> with the QCT results establishes the appropriateness of the use of the QCT method. Reproducing the experimental data by using the SRP-DF functional and QCT calculations for off-normal incidence for  $\theta_i = 30^\circ$  and  $45^\circ$ , for which computed reaction probabilities show no dependence on the plane of incidence, confirms the quality of the SRP functional. We report that the minimum barrier height obtained for the reaction is -8 meV, in agreement with the experimental observation of no, or only a small energetic threshold to reaction [28]. This value can be entered into a small [8], but growing [41] database with barriers of reactions of molecules with metal surfaces, for which chemical accuracy is claimed.

### Chapter 4: Test of the Transferability of the Specific Reaction Parameter Functional for H<sub>2</sub> + Cu(111) to D<sub>2</sub> + Ag(111)

In Chapter 4, we study the transferability of the SRP48 functional, which was initially derived to reproduce experiments for H<sub>2</sub> on Cu(111) with chemical accuracy [56]. In this chapter, we use the QCT method to compute molecular beam sticking probabilities and initial-state resolved reaction probabilities. To establish the appropriateness of the QCT method, we performed the QD calculations for several rovibrational states, and compared with the QCT results. It is found that the QCT reproduces the QD results very well. Results for vibrationally (in)elastic scattering, *i.e.*, probabilities  $P(\nu = 2, j = 0 \rightarrow \nu = \nu')$  as function of incidence energy, are also presented and discussed. It is found that the barrier heights in the SRP48 PES are higher than obtained with the PBE functional as reported by Jiang *et al.* [57]. We also computed molecular beam sticking probabilities and compared with the experimental results of Cottrell *et al.* [58]. The

energy differences between the computed data and the spline interpolated experimental curve were in the range 2 – 2.3 kcal/mol. Thus, no chemical accuracy was achieved in our theoretical results. Our results show that the SRP48 functional is not transferable to the  $\text{H}_2 + \text{Ag}(111)$  system, although Cu and Ag belong to the same group.

### **Chapter 5: Transferability of the Specific Reaction Parameter Density Functional for $\text{H}_2 + \text{Pt}(111)$ to $\text{H}_2 + \text{Pt}(211)$**

In Chapter 5, we study the transferability of the SRP–DF functional which was originally derived for the  $\text{H}_2 + \text{Pt}(111)$  system and is able to reproduce experiments on this system with chemical accuracy. We used the same functional to model the reaction of  $\text{H}_2$  on the stepped Pt(211) surface. We have performed molecular beam simulations with the QCT method using the BOSS model. The accuracy of the QCT method was assessed by comparison with QD results for reaction of the ro-vibrational ground state of  $\text{H}_2$ . The study shows that the theoretical results for sticking of  $\text{H}_2$  and  $\text{D}_2$  on Pt(211) are in quite good agreement with experiment, but uncertainties remain due to a lack of accuracy of the QCT simulations at low incidence energies, and possible inaccuracies in the reported experimental incidence energies at high energies. We also investigate the non-adiabatic effect of electron-hole pair excitation on the reactivity using the MDEF method, employing the local density friction approximation (LDFA). Only small effects of electron-hole pair excitation on sticking are found.

### **Chapter 6: Assessment of Two Problems of Specific Reaction Parameter Density Functional Theory : Sticking and Diffraction of $\text{H}_2$ on Pt(111)**

In Chapter 6, we study two problems faced by the SRP–DFT approach. To address the first problem of the SRP–DFT approach, we have simulated three sets of measurements of sticking probabilities available for  $\text{D}_2 + \text{Pt}(111)$ , using four different sets of molecular beam parameters. We compared these experiments on a one-to-one basis. We report that substantial differences exist between the three sticking probability curves measured for  $\text{D}_2 + \text{Pt}(111)$ . We discuss the origin of the discrepancies between different experimental data and report the mean absolute deviations between

the data of the experiments. We use four different sets of molecular beam parameters to simulate molecular beam sticking probabilities. Theoretical results for different sets of parameters are compared with available experimental data, and the agreement (disagreement) of theory with experiments is discussed and shown in this chapter. We also discuss the question of which set of beam parameters can best be used to simulate a particular set of molecular beam experiments. We obtained that all three sets of experiments can be described with chemical accuracy using molecular beam parameters describing seeded molecular beams that are broad in energy. Performing simulations with different sets of molecular beam parameters also provide insight into under which conditions the experiments should agree with one another.

To address the second problem of the SRP–DFT approach, we performed diffractive scattering calculations comparing with experiments, using the SRP–DF. The theoretical results are shown and compared with experimental results for off-normal incidence for two incidence directions. Our results show that there are both quantitative and qualitative discrepancies between theory and experiments. Our study suggests that the SRP–DF for  $\text{H}_2 + \text{Pt}(111)$  may not yet be accurate enough to describe the diffraction in this system. The van der Waals well plays a role in the description of scattering of  $\text{H}_2$  from  $\text{Pt}(111)$  surface and with the use of a PES exhibiting a van der Waals well, part of the scattering should be indirect. A similar study on  $\text{H}_2$  scattering from  $\text{Ru}(0001)$  [59] has shown that the agreement between experiment and theory with inclusion of a van der Waals well in the PES was improved by assuming a static surface disorder of metal surface. However, our results established that making this assumption will not improve the agreement between theory and experiment in the case of  $\text{H}_2$  scattering from  $\text{Pt}(111)$ .

## 1.5 Outlook

By combining the results of molecular beam experiments and QCT calculations, it has been shown that the SRP functional quantitatively (to within chemical accuracy) reproduces the initial dissociation probabilities for  $\text{H}_2$  on  $\text{Pt}(111)$ , and that it is transferable from the flat (111) surface to a stepped (211) surface of the same metal, as show in Chapter 3 and Chapter 5. Several questions still remain open in this thesis, which are



described and discussed in this section.

It is interesting to check the performance of the SRP–DF functional which was derived for the  $\text{H}_2 + \text{Pt}(111)$  system, for other molecule-metal surface systems in order to test the transferability of the functional among the transition metals in the same group of the periodic table that experimental results are available for  $\text{H}_2 + \text{Ni}(111)$  [60],  $\text{H}_2 + \text{Pd}(111)$  [24]. Experimental results are also available for  $\text{D}_2$  dissociative chemisorption on  $\text{Sn}/\text{Pt}(111)$  measured by Hodgson and co-workers [61] to investigate the effect of alloying in an unreactive metal, Sn, on the dynamics of  $\text{D}_2$  reacting on  $\text{Pt}(111)$ . It is very interesting to test whether the SRP–DF functional can also be successfully applied to  $\text{H}_2$  reacting on a Pt surface with a non-reactive metal alloyed into it. Furthermore, it would be worthwhile to investigate whether the SRP–DF functional developed for  $\text{H}_2 + \text{Pt}(111)$  will also allow a chemically accurate description of the experimentally investigated reaction of  $\text{H}_2$  on the stepped  $\text{Pt}(533)$  surface [62], and on a Pt surface poisoned by CO [63].

In order to construct a diverse database of reaction barriers with chemical accuracy for molecules interacting with the transition metal surfaces, it is interesting to develop better functionals for these systems, for example, to develop an SRP functional for the  $\text{H}_2 + \text{Cu}(111)$  system that is also able to describe the  $\text{H}_2 + \text{Ag}(111)$  system quantitatively. Our results for  $\text{H}_2$  reacting on  $\text{Ag}(111)$  based on the SRP–DF functional for  $\text{H}_2 + \text{Cu}(111)$  underestimate available experimental results, as shown in Chapter 4. Therefore, a chemically accurate description of the dissociative chemisorption of  $\text{D}_2$  on  $\text{Ag}(111)$  is not yet obtained with the SRP48 DFT functional. In this case, the SRP–DF was based on GGA XC functionals. Unfortunately, GGA functionals are not good at both describing the molecule-surface interaction accurately, *i.e.*, reaction barrier heights, and metal surfaces, *i.e.* lattice constants and surface energies [64]. There are several questions related to the performance of XC functionals for molecule-surface reactions that are used so far. The performance of higher level DFT calculations based on for example meta-GGA XC functional is not clear yet. Among the computationally efficient semi-local XC functionals, meta-GGA functionals are most accurate and give both a good description of molecule-surface interaction as well as the surface itself [65]. However, it is still unclear how adding a van der Waals correlation by combining vdW-DF or vdW-DF2 correlations with a meta-GGA exchange functional would affect the PES and dynamics of molecule-surface systems. Further studies are necessary to address the

question whether with a meta-GGA functional it would be possible to get a chemically accurate description of the dissociative chemisorption of  $\text{H}_2$  on Cu(111) while at the same time giving a better description for the lattice constant of Cu. Additionally, the other open question should be addressed whether with the meta-GGA functional derived for  $\text{H}_2 + \text{Cu}(111)$  it would be possible to describe accurately the dissociative chemisorption of  $\text{H}_2$  on and associative desorption from Ag(111).

The ability to accurately describe the molecule-surface interaction is dependent on an understanding of the source of error in the design, evaluation and analysis of the underlying model. In general, it is not yet fully understood how large the error of GGA functionals is for barrier heights of molecule-surface systems. Additionally, it is not fully clear how this inaccuracy leads to errors in dynamical observables, which are our only sources for comparison with experiments. Only for reaction probabilities it is obvious that a too high barrier height will usually result in too low reaction probabilities and *vice versa*. Previous studies have shown that the barrier heights, and also the way in which the barrier height varies with the impact site are highly dependent on the choice of XC functional [66]. However, barrier calculations alone will not give us more information about the reaction mechanism, dynamics calculations are also necessary [11]. According to the hole model [67], the reaction probability reflects the proportion of impact sites and molecular orientations for which the collision energy exceeds the barrier height at the impact sites and molecular orientations. There are reaction paths without or with only very low barriers as well as reaction paths with substantial barriers to dissociation, *i.e.*, the dissociation takes place over a distribution of barriers varying in height [68]. The curvature of the reaction path in the 2D PES, *i.e.* coupling of translational motion along the minimum energy path (MEP) to vibrational motion is also dependent on the choice of the XC functional [11]. It was shown that this coupling is larger for the SRP functional than GGA functional due to the presence of the van der Waals well [42]. A dynamical effect (called bobsled effect [69]) may remove energy from motion along the MEP and convert it to motion away from the MEP, and reduce the reactivity. Vibrational efficacies greater than 1.0, as shown in Chapter 4, can also be explained in this way that the molecule cannot follow the MEP and slides off it [52, 70].

There is a clear need for more complicated dynamical properties in order to investigate more detailed properties of the PES. Rotationally inelastic scattering or diffractive scattering are far more sensitive to subtle details of

DFT-based PESs [71]. However, the agreement for diffractive scattering of  $\text{H}_2$  from Pt(111) compared to diffraction probabilities extracted from the measured angular distributions by Nieto *et al.* [14] is clearly not as good as the agreement obtained for the reaction probabilities of the  $\text{H}_2 + \text{Pt}(111)$  system with the SRP–DF functional. There are qualitatively and quantitatively large differences, as shown in Chapter 6. The previous theoretical results by Nieto *et al.* [14], which were based on the use of a GGA functional, demonstrated better agreement with the experiments. The inclusion of van der Waals effects is crucial to properly describe diffraction of  $\text{H}_2$  from metal surfaces and the performance of DFT to describe diffraction spectra may rely on the accuracy of the van der Waals functionals used [72, 73].

Also we note that the SRP–DFT method is semi-empirical and the accuracy of the computed results is no better than the accuracy of the underlying experimental data. Therefore, the availability of highly accurate experimental data is essential and lack of accuracy in the experiments limits the possibility for improving semi-empirical method. As shown in Chapter 6, parameters that describe translational energy distributions of molecular beams play roles in accurately calculating the sticking probabilities. These parameters are extracted from experimental time-of-flight (TOF) measurements. It should be noted that errors may be made in the analysis of the TOF measurements. There is a need for measurements of sticking probabilities accompanied by accurate characterization of the molecular beams used.

Moreover, there is no direct way to compare DFT energies to the molecular beam experiments. Instead, intermediate dynamical simulations are necessary. This makes the fitting procedure indirect and can introduce uncertainties due to (the simplified description of) phonon and electron-hole pair excitations in the surface and the (lack of) quantum-classical correspondences. Thus, it is not yet fully clear how much dynamical models and methods contribute to errors and uncertainties. On the side of theory, development of the QD method incorporating the effects of phonons and electron-hole pair excitation would be useful to improve the accuracy in describing the reaction and describing the diffraction. Also, recent quantum Monte-Carlo (QMC) results for  $\text{H}_2 + \text{Cu}(111)$  suggest that in the future it may be possible to put the SRF–DFT approach on an *ab initio* basis by fitting the SRP–DFT to a few points computed with QMC.

## References

1. Somorjai, G. A. & Li, Y. Impact of Surface Chemistry. *Proceedings of the National Academy of Sciences* **108**, 917–924 (2011).
2. Hasselbrink, E. Capturing the Complexities of Molecule-Surface Interactions. *Science* **326**, 809–810 (2009).
3. Bagot, P. Fundamental Surface Science Studies of Automobile Exhaust Catalysis. *Materials Science and Technology* **20**, 679–694 (2004).
4. Smil, V. Detonator of the Population Explosion. *Nature* **400**, 415 (1999).
5. Erisman, J., Sutton, M., Galloway, J., Klimont, Z. & Winiwarter, W. How a Century of Ammonia Synthesis Changed the World. *Nature Geoscience* **1**, 636–639 (2008).
6. Macquarrie, D. I. Chorkendorff and J. W. Niemantsverdriet. Concepts of Modern Catalysis and Kinetics. Wiley-VCH, 2003, 469 pp; ISBN 3-527-30574-2 (hardcover). *Applied Organometallic Chemistry* **19**, 696–696 (2005).
7. Ertl, G. Studies on the Mechanism of Ammonia Synthesis: The P. H. Emmett Award Address. *Annalen der Physik* **21**, 201–223 (1980).
8. Kroes, G. J. Toward a Database of Chemically Accurate Barrier Heights for Reactions of Molecules with Metal Surfaces. *Journal of Physical Chemistry Letters* **6**, 4106–4114 (2015).
9. Born, M. & Oppenheimer, R. Zur Quantentheorie der Molekeln. *Annalen der Physik* **389**, 457–484 (1927).
10. Kroes, G. J. Six-Dimensional Quantum Dynamics of Dissociative Chemisorption of H<sub>2</sub> on Metal Surfaces. *Progress in Surface Science* **60**, 1–85 (1999).
11. Gross, A. Reactions at Surfaces Studied by *Ab Initio* Dynamics Calculations. *Surface Science Reports* **32**, 291–340 (1998).
12. Kroes, G. J. & Somers, M. F. Six-Dimensional Dynamics of Dissociative Chemisorption of H<sub>2</sub> on Metal Surfaces. *Journal of Theoretical and Computational Chemistry* **04**, 493–581 (2005).
13. Kroes, G. J. & Díaz, C. Quantum and Classical Dynamics of Reactive Scattering of H<sub>2</sub> from Metal Surfaces. *Chemical Society Reviews* **45**, 3658–3700 (2016).

14. Nieto, P. *et al.* Reactive and Nonreactive Scattering of H<sub>2</sub> from a Metal Surface Is Electronically Adiabatic. *Science* **312**, 86–89 (2006).
15. Luntz, A. C. & Persson, M. How Adiabatic Is Activated Adsorption/Associative Desorption? *Journal of Chemical Physics* **123**, 074704 (2005).
16. Muzas, A. S. *et al.* Vibrational Deexcitation and Rotational Excitation of H<sub>2</sub> and D<sub>2</sub> Scattered from Cu(111): Adiabatic Versus Non-adiabatic Dynamics. *Journal of Chemical Physics* **137**, 064707 (2012).
17. Juaristi, J. I., Alducin, M., Muiño, R. D., Busnengo, H. F. & Salin, A. Role of Electron-Hole Pair Excitations in the Dissociative Adsorption of Diatomic Molecules on Metal Surfaces. *Physical Review Letters* **100**, 116102 (2008).
18. Fücksel, G., Schimka, S. & Saalfrank, P. On the Role of Electronic Friction for Dissociative Adsorption and Scattering of Hydrogen Molecules at a Ru(0001) Surface. *Journal of Physical Chemistry A* **117**, 8761–8769 (2013).
19. Busnengo, H. F., Dong, W., Sautet, P. & Salin, A. Surface Temperature Dependence of Rotational Excitation of H<sub>2</sub> Scattered from Pd(111). *Physical Review Letters* **87**, 127601 (2001).
20. Busnengo, H. F., Di Césare, M. A., Dong, W. & Salin, A. Surface Temperature Effects in Dynamic Trapping Mediated Adsorption of Light Molecules on Metal Surfaces: H<sub>2</sub> on Pd(111) and Pd(110). *Physical Review B* **72**, 125411 (2005).
21. Gross, A. *Theoretical Surface Science* (Springer Berlin, 2003).
22. Michelsen, H. A. & Auerbach, D. J. A Critical Examination of Data on the Dissociative Adsorption and Associative Desorption of Hydrogen at Copper Surfaces. *Journal of Chemical Physics* **94**, 7502–7520 (1991).
23. Hammer, B. & Nørskov, J. Electronic Factors Determining the Reactivity of Metal Surfaces. *Surface Science* **343**, 211–220 (1995).
24. Beutl, M. *et al.* There Is a True Precursor for Hydrogen Adsorption After All: the System H<sub>2</sub>/Pd(111)+ Subsurface V. *Chemical Physics Letters* **342**, 473–478 (2001).
25. Rendulic, K., Anger, G. & Winkler, A. Wide Range Nozzle Beam Adsorption Data for the Systems H<sub>2</sub>/Nickel and H<sub>2</sub>/Pd(100). *Surface Science* **208**, 404–424 (1989).

26. Luppi, M., Olsen, R. A. & Baerends, E. J. Six-Dimensional Potential Energy Surface for H<sub>2</sub> at Ru(0001). *Physical Chemistry Chemical Physics* **8**, 688–696 (2006).
27. Groot, I. M. N., Ueta, H., van der Niet, M. J. T. C., Kleyn, A. W. & Juurlink, L. B. F. Supersonic Molecular Beam Studies of Dissociative Adsorption of H<sub>2</sub> on Ru(0001). *Journal of Chemical Physics* **127**, 244701 (2007).
28. Luntz, A. C., Brown, J. K. & Williams, M. D. Molecular Beam Studies of H<sub>2</sub> and D<sub>2</sub> Dissociative Chemisorption on Pt(111). *Journal of Chemical Physics* **93**, 5240–5246 (1990).
29. Gross, A. The Role of Lateral Surface Corrugation for the Quantum Dynamics of Dissociative Adsorption and Associative Desorption. *Journal of Chemical Physics* **102**, 5045–5058 (1995).
30. Darling, G. R. & Holloway, S. The Role of Parallel Momentum in the Dissociative Adsorption of H<sub>2</sub> at Highly Corrugated Surfaces. *Surface Science* **304**, L461–L467 (1994).
31. Darling, G. R. & Holloway, S. The Dissociation of Diatomic Molecules at Surfaces. *Reports on Progress in Physics* **58**, 1595 (1995).
32. d’Aglia, E. G., Kumar, P., Schaich, W. & Suhl, H. Brownian Motion Model of the Interactions Between Chemical Species and Metallic Electrons: Bootstrap Derivation and Parameter Evaluation. *Physical Review B* **11**, 2122–2143 (1975).
33. Brako, R. & News, D. The Electron-Hole Mechanism for Sticking of Adsorbates: A Soluble Model. *Solid State Communications* **33**, 713–715 (1980).
34. Head-Gordon, M. & Tully, J. C. Molecular Dynamics with Electronic Frictions. *Journal of Chemical Physics* **103**, 10137–10145 (1995).
35. Tully, J. C. Chemical Dynamics at Metal Surfaces. *Annual Review of Physical Chemistry* **51**, 153–178 (2000).
36. Wodtke, A. M., Tully, J. C. & Auerbach, D. J. Electronically Non-adiabatic Interactions of Molecules at Metal Surfaces: Can We Trust the Born-Oppenheimer Approximation for Surface Chemistry? *International Reviews in Physical Chemistry* **23**, 513–539 (2004).

37. Spiering, P. & Meyer, J. Testing Electronic Friction Models: Vibrational De-Excitation in Scattering of H<sub>2</sub> and D<sub>2</sub> from Cu(111). *Journal of Physical Chemistry Letters* **9**, 1803–1808 (2018).
38. Michelsen, H., Rettner, C. & Auerbach, D. On the Influence of Surface Temperature on Adsorption and Desorption in the D<sub>2</sub>/Cu(111) System. *Surface Science* **272**, 65–72 (1992).
39. Rettner, C. T., Michelsen, H. A. & Auerbach, D. J. Quantum-State-Specific Dynamics of the Dissociative Adsorption and Associative Desorption of H<sub>2</sub> at a Cu(111) Surface. *Journal of Chemical Physics* **102**, 4625–4641 (1995).
40. Nattino, F. *et al.* *Ab Initio* Molecular Dynamics Calculations versus Quantum-State-Resolved Experiments on CHD<sub>3</sub> + Pt(111): New Insights into a Prototypical Gas-Surface Reaction. *Journal of Physical Chemistry Letters* **5**, 1294–1299 (2014).
41. Nattino, F. *et al.* Chemically Accurate Simulation of a Polyatomic Molecule-Metal Surface Reaction. *Journal of Physical Chemistry Letters* **7**, 2402–2406 (2016).
42. Migliorini, D. *et al.* Surface Reaction Barriometry: Methane Dissociation on Flat and Stepped Transition-Metal Surfaces. *Journal of Physical Chemistry Letters* **8**, 4177–4182 (2017).
43. Wijzenbroek, M. & Somers, M. F. Static Surface Temperature Effects on the Dissociation of H<sub>2</sub> and D<sub>2</sub> on Cu(111). *Journal of Chemical Physics* **137**, 054703 (2012).
44. Nattino, F. *et al.* Dissociation and Recombination of D<sub>2</sub> on Cu(111): *Ab Initio* Molecular Dynamics Calculations and Improved Analysis of Desorption Experiments. *Journal of Chemical Physics* **141**, 124705 (2014).
45. Langreth, D. C. & Mehl, M. J. Beyond the Local-Density Approximation in Calculations of Ground-State Electronic Properties. *Physical Review B* **28**, 1809–1834 (1983).
46. Becke, A. D. Density-Functional Exchange-Energy Approximation with Correct Asymptotic Behavior. *Physical Review A* **38**, 3098–3100 (1988).
47. Kohn, W. & Sham, L. J. Self-Consistent Equations Including Exchange and Correlation Effects. *Physical Review* **140**, A1133–A1138 (1965).

48. Hammer, B., Jacobsen, K. W. & Nørskov, J. K. Role of Nonlocal Exchange Correlation in Activated Adsorption. *Physical Review Letters* **70**, 3971–3974 (1993).
49. Hammer, B., Scheffler, M., Jacobsen, K. W. & Nørskov, J. K. Multidimensional Potential Energy Surface for H<sub>2</sub> Dissociation over Cu(111). *Physical Review Letters* **73**, 1400–1403 (1994).
50. White, J. A., Bird, D. M., Payne, M. C. & Stich, I. Surface Corrugation in the Dissociative Adsorption of H<sub>2</sub> on Cu(100). *Physical Review Letters* **73**, 1404–1407 (1994).
51. Abufager, P. N., Crespos, C. & Busnengo, H. F. Modified Shepard Interpolation Method Applied to Trapping Mediated Adsorption Dynamics. *Physical Chemistry Chemical Physics* **9**, 2258–2265 (2007).
52. Díaz, C. *et al.* Chemically Accurate Simulation of a Prototypical Surface Reaction: H<sub>2</sub> Dissociation on Cu(111). *Science* **326**, 832–834 (2009).
53. Sementa, L. *et al.* Reactive Scattering of H<sub>2</sub> from Cu(100): Comparison of Dynamics Calculations Based on the Specific Reaction Parameter Approach to Density Functional Theory with Experiment. *Journal of Chemical Physics* **138** (2013).
54. Ghassemi, E. N., Wijzenbroek, M., Somers, M. F. & Kroes, G. J. Chemically Accurate Simulation of Dissociative Chemisorption of D<sub>2</sub> on Pt(111). *Chemical Physics Letters* **683**. Ahmed Zewail (1946–2016) Commemoration Issue of Chemical Physics Letters, 329–335 (2017).
55. Lee, K., Murray, É. D., Kong, L., Lundqvist, B. I. & Langreth, D. C. Higher-Accuracy van der Waals Density Functional. *Physical Review B* **82**, 081101 (2010).
56. Nattino, F., Díaz, C., Jackson, B. & Kroes, G. J. Effect of Surface Motion on the Rotational Quadrupole Alignment Parameter of D<sub>2</sub> Reacting on Cu(111). *Physical Review Letters* **108**, 236104 (2012).
57. Jiang, B. & Guo, H. Six-Dimensional Quantum Dynamics for Dissociative Chemisorption of H<sub>2</sub> and D<sub>2</sub> on Ag(111) on a Permutation Invariant Potential Energy Surface. *Physical Chemistry Chemical Physics* **16**, 24704–24715 (2014).
58. Cottrell, C., Carter, R. N., Nesbitt, A., Samson, P. & Hodgson, A. Vibrational State Dependence of D<sub>2</sub> Dissociation on Ag(111). *Journal of Chemical Physics* **106**, 4714–4722 (1997).



59. Kroes, G. J., Wijzenbroek, M. & Manson, J. R. Possible Effect of Static Surface Disorder on Diffractive Scattering of H<sub>2</sub> from Ru(0001): Comparison Between Theory and Experiment. *Journal of Chemical Physics* **147**, 244705 (2017).
60. Robota, H., Vielhaber, W., Lin, M., Segner, J. & Ertl, G. Dynamics of Interaction of H<sub>2</sub> and D<sub>2</sub> with Ni(110) and Ni(111) Surfaces. *Surface Science* **155**, 101–120 (1985).
61. Samson, P., Nesbitt, A., Koel, B. E. & Hodgson, A. Deuterium Dissociation on Ordered Sn/Pt(111) Surface Alloys. *Journal of Chemical Physics* **109**, 3255–3264 (1998).
62. Groot, I. M. N., Kleyn, A. W. & Juurlink, L. B. F. The Energy Dependence of the Ratio of Step and Terrace Reactivity for H<sub>2</sub> Dissociation on Stepped Platinum. *Angewandte Chemie International Edition* **50**, 5174–5177 (2011).
63. Hahn, C., Shan, J., Groot, I. M., Kleyn, A. W. & Juurlink, L. B. Selective Poisoning of Active Sites for D<sub>2</sub> Dissociation on Platinum. *Catalysis Today* **154**, 85–91 (2010).
64. Schimka, L. *et al.* Accurate Surface and Adsorption Energies from Many-Body Perturbation Theory. *Nature materials* **9**, 741–4 (2010).
65. Perdew, J. P., Ruzsinszky, A., Csonka, G. I., Constantin, L. A. & Sun, J. Workhorse Semilocal Density Functional for Condensed Matter Physics and Quantum Chemistry. *Physical Review Letters* **103**, 026403 (2009).
66. Wijzenbroek, M. & Kroes, G. J. The Effect of the Exchange-Correlation Functional on H<sub>2</sub> Dissociation on Ru(0001). *Journal of Chemical Physics* **140** (2014).
67. Karikorpi, M., Holloway, S., Henriksen, N. & Nørskov, J. Dynamics of Molecule-Surface Interactions. *Surface Science* **179**, L41–L48 (1987).
68. Olsen, R. A., Kroes, G. J. & Baerends, E. J. Atomic and Molecular Hydrogen Interacting with Pt(111). *Journal of Chemical Physics* **111**, 11155–11163 (1999).
69. Levine, R. D. in (Cambridge University Press: Cambridge, 2005).
70. Smith, R. R., Killelea, D. R., DelSesto, D. F. & Utz, A. L. Preference for Vibrational Over Translational Energy in a Gas-Surface Reaction. *Science* **304**, 992–995 (2004).

71. Díaz, C., Olsen, R. A., Busnengo, H. F. & Kroes, G. J. Dynamics on Six-Dimensional Potential Energy Surfaces for H<sub>2</sub>/Cu(111): Corrugation Reducing Procedure versus Modified Shepard Interpolation Method and PW91 versus RPBE. *Journal of Physical Chemistry C* **114**, 11192–11201 (2010).
72. Del Cueto, M. *et al.* Role of van der Waals Forces in the Diffraction of Noble Gases from Metal Surfaces. *Physical Review B* **93**, 060301 (2016).
73. Del Cueto, M. *et al.* Performance of van der Waals DFT Approaches for Helium Diffraction on Metal Surfaces. *Journal of Physics: Condensed Matter* **31**, 135901 (2019).

CHAPTER 2

# Theoretical Background



In this chapter we provide the background that is required for the following chapters. The diatomic molecule interacting with an ideal static surface model is discussed. A brief description of density functional theory (DFT) is presented followed by methods for construction of potential energy surfaces. Methods for dynamics calculations on H<sub>2</sub>-surface systems and for computing properties from the results of dynamics calculations are described.

## 2.1 Modelling the molecule surface interaction

The interaction between a molecule and a surface is fully described by the Schrödinger equation [1] as :

$$\hat{H}_{tot}\psi(\vec{r}, \vec{R}) = E_{tot}\psi(\vec{r}, \vec{R}), \quad (2.1)$$

in which  $E_{tot}$  is the total energy and  $\psi(\vec{r}, \vec{R})$  is the wave function, depending on all the electronic coordinates  $\vec{r}$  and the nuclear coordinates  $\vec{R}$ .  $\hat{H}_{tot}$  is the Hamiltonian that describes both the electronic and nuclear motions. The electronic Hamiltonian is composed of kinetic energy term of the electrons ( $\hat{T}_e$ ) and electrostatic potentials ( $V$ ),

$$\hat{H}_e = \hat{T}_e + V_{ee} + V_{nn} + V_{ne}, \quad (2.2)$$

so that the total Hamiltonian is given

$$\hat{H}_{tot} = \hat{T}_n + \hat{H}_e, \quad (2.3)$$

where  $\hat{T}_n$  is the kinetic energy of the nuclei (with mass  $M_j$ ) in atomic units, given by

$$\hat{T}_n = \sum_{j=1}^M \frac{-1}{2M_j} \nabla_{\vec{R}_j}^2. \quad (2.4)$$

Note that throughout this chapter we will use atomic units. The kinetic energy of the electrons is given by

$$\hat{T}_e = \sum_{i=1}^N -\frac{1}{2} \nabla_{\vec{r}_i}^2. \quad (2.5)$$

$V_{ee}$  is the electron-electron (repulsive) interaction potential

$$V_{ee} = \sum_{i=1}^N \sum_{k>i}^N \frac{1}{|\vec{r}_i - \vec{r}_k|}, \quad (2.6)$$

$V_{nn}$  is the nuclear-nuclear (repulsive) interaction potential with atomic numbers  $Z$

$$V_{nn} = \sum_{j=1}^M \sum_{k>j}^M \frac{Z_j Z_k}{|\vec{R}_j - \vec{R}_k|}, \quad (2.7)$$

and  $V_{ne}$  is the nuclear-electron (attractive) interaction potential

$$V_{ne} = \sum_{j=1}^M \sum_{i=1}^N \frac{-Z_j}{|\vec{r}_i - \vec{R}_j|}. \quad (2.8)$$

In the framework of the Born-Oppenheimer (BO) approximation [2], the ground state potential energy surface (PES) arises from solving the electronic Schrödinger equation for the problem by the partition of the problem into electronic and nuclear degrees of freedom (DOFs),

$$\hat{H}_e \psi_e(\vec{r}; \vec{R}) = (\hat{T}_e + V_{ee} + V_{nn} + V_{ne}) \psi_e(\vec{r}; \vec{R}) = E_e(\vec{R}) \psi_e(\vec{r}; \vec{R}), \quad (2.9)$$

and

$$\hat{H}_n \psi_n(\vec{R}) = [\hat{T}_n + E_e(\vec{R})] \psi_n(\vec{R}). \quad (2.10)$$

This approximation allows us to write the full wave function in a separable form :

$$\psi(\vec{r}, \vec{R}) = \psi_e(\vec{r}; \vec{R}) \psi_n(\vec{R}), \quad (2.11)$$

where  $\psi_e(\vec{r}; \vec{R})$  is the corresponding electronic wave function that parametrically depends on all nuclear coordinates  $\vec{R}$ , and  $\psi_n(\vec{R})$  is the nuclear wave function. In Equation 2.9,  $E_e$  is the electronic energy of the system (for the ground state, this is the lowest value) which depends on the nuclear positions. For this thesis we neglect the surface atom DOFs and the molecule interacts with the frozen ideal surface.  $E_e(\vec{R})$  will be referred to as the potential energy surface (PES) for the ground electronic state. The most efficient electronic structure method to solve the electronic Schrödinger equation for the molecule-surface interaction in an approximative but still accurate way is density functional theory (DFT). It will be the subject of the next section in this chapter.

## 2.2 Density functional theory

To obtain the potential energy for a particular configuration, which needs to be done for many configurations to map out a PES, an electronic structure method is needed. The problem in electronic structure calculations arises when the system is described by a high dimensional many-electron wave function. To solve this problem, a much simpler three dimensional quantity, *i.e.*, the electron density  $n(\vec{r})$  is used to replace the high-dimensional many-body wave function [3]. The electron density in a system with  $N$  electrons depends on only three DOFs and the computational cost of the method scales as  $N^3$  instead of  $N^m$  for the wave function based methods, with  $m \geq 4$ .

Hohenberg and Kohn [3] showed that for any system of interacting particles in an external potential  $V_{ext}(\vec{r})$ , the electron density is uniquely determined, in other words, the ground state wave function is a unique functional of the density  $n(\vec{r})$ . Furthermore, they showed that a universal functional for the energy  $E[n(\vec{r})]$  can be defined in term of the density. The exact ground state corresponds to the global minimum value of this functional. This makes it possible to use the variational principle to obtain the minimum energy and the ground state electronic density. All physical information about the system is given by  $\hat{H}_e$  and according to the theorem, there is a one-to-one correspondence between  $\hat{H}_e$  and the ground state electronic density. Therefore, from the Hohenberg and Kohn theorem, the energy is a functional of the electron density,

$$E_e[n(\vec{r})] = \hat{T}_e[n(\vec{r})] + V_{ee}[n(\vec{r})] + V_{ne}[n(\vec{r})] = F_{HK}[n(\vec{r})] + V_{ne}[n(\vec{r})]. \quad (2.12)$$

$F_{HK}$  is the Hohenberg and Kohn functional which is universal and independent of the system.  $V_{ne}[n(\vec{r})]$  is the system dependent term and is called the external potential. We note that in practice  $V_{nn}$  is also added to the electronic Hamiltonian, even though this just adds a constant to the value of the energy for a specific configuration of the nuclei.  $F_{HK}$  is unknown and approximation is needed to express it. It is very useful to separate  $F_{HK}$  in three different contributions as

$$F_{HK} = \hat{T}_e[n(\vec{r})] + E_H[n(\vec{r})] + G_{XC}[n(\vec{r})], \quad (2.13)$$

in which  $E_H[n(\vec{r})]$  is the Hartree interaction of the electrons, given by

$$E_H[n(\vec{r})] = \frac{1}{2} \int \frac{n(\vec{r})n(\vec{r}')}{|\vec{r} - \vec{r}'|} d\vec{r}d\vec{r}', \quad (2.14)$$

$G_{XC}[n(\vec{r})]$  is a functional that contains quantum mechanical many-body effects and it is unknown. Here, in the Hohenberg and Kohn theorem  $\hat{T}_e[n(\vec{r})]$  is the kinetic energy of the electrons.

Kohn and Sham [4] developed a practical way to avoid problems with calculating the kinetic energy from the electronic density. They proposed a fictitious system consisting of non-interacting electrons in an effective external potential (the Kohn-Sham potential  $V_{KS}$ ). The many-electron problem can be reformulated as a set of  $N$  single-electron equations referred to as the Kohn-Sham equations,

$$\left[ \frac{-\nabla^2}{2} + V_{KS}(\vec{r}) \right] \phi_i(\vec{r}) = \varepsilon_i \phi_i(\vec{r}). \quad (2.15)$$

$\phi_i$  is the single particle orbital or Kohn-Sham (KS) orbital obtained for an fictitious non-interacting system and yields the electron density of the original system

$$n(\vec{r}) = \sum_{i=1}^N |\phi_i(\vec{r})|^2. \quad (2.16)$$

The first term on Equation 2.15 yields the kinetic energy of the non-interacting electrons,  $\hat{T}_S$ . The total kinetic energy of the system  $\hat{T}_e$  can be separated in a non-interacting contribution  $\hat{T}_S$  and an unknown component  $\hat{T}_C$  that contains correlation through many-body effects. This component is also a functional of the electron density and together with  $G_{XC}$  forms the well-known exchange-correlation (XC) functional  $E_{XC} = G_{XC} + \hat{T}_C$ . This name comes from the fact that it contains the exchange interaction due to the Pauli exclusion principle and many-body electron-electron correlation. This unknown XC functional is approximated in particular calculations and its approximations will be discussed in the Section 2.2.1. The total energy functional 2.12 can be rewritten with respect to these definitions as

$$E_e[n(\vec{r})] = \underbrace{\hat{T}_s[n(\vec{r})] + E_H[n(\vec{r})] + V_{ne}[n(\vec{r})]}_{\text{known}} + \underbrace{E_{XC}[n(\vec{r})]}_{\text{unknown}}. \quad (2.17)$$

Minimizing this energy functional is done through the solution of the single particle Kohn-Sham equations (Equation 2.15). The Kohn-Sham potential in Equation 2.15 is given by

$$V_{KS}[n(\vec{r})] = V_{ext}[n(\vec{r})] + V_H[n(\vec{r})] + V_{XC}[n(\vec{r})]. \quad (2.18)$$



Here,  $V_{ext}$  is the external potential from the nuclei,

$$V_{ext} = \sum_{j=1}^M \frac{Z_j}{|\vec{r} - \vec{R}_j|}, \quad (2.19)$$

$V_H$  is the Hartree potential, given by

$$V_H[n(\vec{r})] = \int \frac{n(\vec{r}')}{|\vec{r} - \vec{r}'|} d\vec{r}', \quad (2.20)$$

and  $V_{XC}$  in the exchange-correlation potential, given by

$$V_{XC}[n(\vec{r})] = \frac{\delta E_{XC}[n(\vec{r})]}{\delta n(\vec{r}')}. \quad (2.21)$$

All these functional derivatives that enter in the Kohn-Sham equation depend on the density, and therefore on the KS orbitals. The Kohn-Sham equations are solved self-consistently.

### 2.2.1 The exchange-correlation functional

The quality of DFT depends on the form of the unknown XC functional  $E_{XC}$ . The simplest approximation for the XC functional was proposed in the paper of Kohn-Sham [4] and it is called the local density approximation (LDA), where the XC functional is written as,

$$E_{XC}^{LDA}[n(\vec{r})] = \int n(\vec{r}) \epsilon_{XC}^{LDA}(n(\vec{r})) d\vec{r}, \quad (2.22)$$

where  $\epsilon_{XC}^{LDA}$  is the XC energy per electron of the homogeneous electron gas (HEG) with the electron density  $n(\vec{r})$ . In the LDA, the XC energy of a system depends locally on the electron density.  $\epsilon_{XC}^{LDA}$  is usually separated into exchange and correlation contributions

$$\epsilon_{XC}^{LDA}(n(\vec{r})) = \epsilon_X^{HEG}(n(\vec{r})) + \epsilon_C^{LDA}(n(\vec{r})). \quad (2.23)$$

There is an exact solution for the exchange energy in the HEG, and it is given by

$$\epsilon_X^{HEG}(n(\vec{r})) = -\frac{3}{4} \left( \frac{3n(\vec{r})}{\pi} \right)^{\frac{1}{3}}. \quad (2.24)$$

However, the correlation energy is not known analytically and needs to be approximated. The accurate calculation of the correlation part is possible

based on Quantum Monte Carlo data by Ceperley and Alder [5]. Several popular approximations for the LDA correlation functional are given in references [6–8]. Although LDA functionals are simple, they work rather well in simulating many bulk and surface systems. For systems which have an electron density far away from the HEG, *i.e.* systems with strongly varying densities, LDA usually does not perform very well. This is the case for molecules and for the interaction of a molecule with a metal surface, for which LDA does not describe barriers to dissociation accurately, so that for various strongly activated H<sub>2</sub>-metal surface systems no or only a very small barrier to dissociation is found [9, 10].

A more advanced level of XC functionals is formed by the generalized gradient approximation (GGA) XC functionals [11, 12]. In the GGA, the XC energy not only depends on the electron density, but also on the gradient of electron density  $\nabla n(\vec{r})$ , *i.e.*:

$$E_{XC}^{GGA}[n(\vec{r})] = \int n(\vec{r}) \epsilon_{XC}^{GGA}(n(\vec{r}), \nabla n(\vec{r})) d\vec{r}. \quad (2.25)$$

Such a functional is often called a semi-local functional, because of the added density gradient dependence. The XC energy  $E_{XC}^{GGA}$  is split into an exchange and a correlation contribution,  $E_X^{GGA}$  and  $E_C^{GGA}$ , respectively, as for the LDA. The exchange part of  $E_{XC}^{GGA}$  is always expressed as

$$E_X^{GGA}[n(\vec{r})] = \int n(\vec{r}) \epsilon_X^{HEG}(n(\vec{r})) F_X(s) d\vec{r}, \quad (2.26)$$

where  $F_X(s)$  is generally called the exchange enhancement factor, which is commonly written as a function of the reduced density gradient  $s$ :

$$s = \frac{|\nabla n(\vec{r})|}{2(3\pi^2)^{\frac{1}{3}} n^{\frac{4}{3}}(\vec{r})}. \quad (2.27)$$

$s$  is dimensionless due to the exponent of the density in the denominator. We note that all traditional GGA functionals exploit an equation like Equation 2.26 to express the exchange part of the XC energy, so that Peverati and Truhlar [13] used this expression to define the GGA. However, Peverati and Truhlar also defined a non-separable gradient approximation (NGA), in which the electron density and its gradient is employed to represent both exchange and correlation in a non-separable term [13, 14]. This new kind of functional approximation includes both exchange and correlation in a

non-separable way by a new functional type that has the form of a non-separable gradient enhancement of HEG exchange; it also includes a more conventional correlation term [13].

Many different GGA functional forms exist. The functional significantly improves over LDA results in many cases, and it is relatively accurate for a large range of systems. The most famous and most used functional in the surface science community is the PBE [15] functional. The exchange enhancement factor for the PBE XC functional is given by:

$$F_X(s) = 1 + \kappa - \frac{\kappa}{1 + \mu s^2 / \kappa}, \quad (2.28)$$

where  $\kappa$  and  $\mu$  are derived from physical constants (not semi-empirical parameters). Another functional frequently used for gas-surface systems is RPBE [16], in which the exchange enhancement factor is given by:

$$F_X(s) = 1 + \kappa \cdot (1 - e^{-\mu s^2 / \kappa}). \quad (2.29)$$

Unfortunately, for molecules interacting with metals the GGA is not always very accurate. For instance, for such systems, it is observed that often RPBE yields too high reaction barriers, while the PBE functional is too attractive (yields too low barriers) at the same time, but mixing these two functionals can provide the required accuracy for the system [17]. Implementation and references for a large number of other GGA functionals can be found in Ref. [18]. Construction of new GGA functionals is still an active research field in the surface science community.

The next step upward from the GGA level on "Jacob's ladder" proposed by Perdew and Schmidt [19] is the meta-generalized gradient approximation (meta-GGA), which depends on the kinetic energy density and /or the Laplacian of the density in addition to the gradient of the density. This functional provides the opportunity of a better incorporation of exact quantum mechanical constraints, and in many cases a somewhat higher accuracy can be achieved compared to GGA results. Popular meta-GGA functionals are TPSS [20] and revTPSS [21]. The additional variable in the meta-GGA functional yields an advantage for surface science, by allowing a better distinction between molecules and solids [21].

The next step on the ladder is the "hyper-GGA" level, in which exact Hartree-Fock exchange is added into the GGA functional to improve it. A well-known hybrid functional in the molecular chemistry community is

B3LYP [19, 22, 23] which gives very good descriptions for energetic and structural properties of isolated molecular systems. In spite of the good performance of hybrid functionals in molecular chemistry, they are not so common in solid state physics and surface science, especially for molecule-metal systems. The evaluation of the exact exchange functional for metals in which electrons are de-localized, is computationally very costly and difficult to achieve for molecule-surface interaction where the goal is to obtain a full PES [24–26].

An important limitation of all local or semi-local (*i.e.*, up to meta-GGA level) functionals is that they can not describe long range electronic correlations (which give rise to long range interactions), such as van der Waals (vdW) interaction. Various methods have been proposed to overcome this problem, some more or some less applicable to problems involving metals surfaces. A popular approach is adding a pairwise potential based on  $C_6$  coefficients computed from time-dependent density functional theory (TD-DFT) in the DFT-D3 method by Grimme *et al.* [27].  $C_6$  coefficients obtained from the mean-field ground state electron density in other methods have been reported by Tkatchenko and Scheffler [28]. Very significant progress was achieved by introducing the non-local correlation density functional vdW-DF, which has been reported by Dion *et al.* [29]. Since then, further refinements of vdW-DF functional provided very satisfying results for many systems [30–32] and other functionals have been reported by improving over the original vdW-DF functional, by either changing the exchange functional, the correlation functional or both. The computational method of Román-Pérez and Soler [33] has allowed the vdW-DF [29] and vdW-DF2 [34] correlation functional to be evaluated efficiently.

### Specific reaction parameter density functional

The so-called specific reaction parameter (SRP) approach to DFT is a semi-empirical approach to optimizing the unknown XC functional, which in its original version was developed by Truhlar and co-workers [35] for reactions in the condensed phase. This approach is based on fitting one or a few parameters in the XC functional to a set of experimental data. The functional is optimized for describing a specific reaction, then the fitted functional is tested against at least one other set of experimental data for the same system. Diaz *et al.* [17] applied an implementation of this approach to a gas-surface reaction by fitting a weighted average of two GGA functionals

to one set of experimental data, which is very sensitive to minimum barrier height, for  $\text{H}_2 + \text{Cu}(111)$ . It has been shown that this new semi-empirical functional is able to reproduce a large range of experimental data for the  $\text{H}_2 + \text{Cu}(111)$  [17] system within chemical accuracy, and is transferable to  $\text{H}_2$  interacting with another crystal face of the Cu metal, *i.e.*,  $\text{Cu}(100)$  [36]. In this thesis, our main focus lies on this method and we apply the SRP methodology to our selected systems. In the next chapters we discuss more about how SRP density functionals are derived and can be transferable from one system to another system.

## 2.3 Density functional theory for periodic systems

A metal surface is infinite but periodic. When performing calculations on a molecule interacting with a metal surface, it is necessary to take into account the periodicity of the surface to avoid edge effects. DFT is very suitable for representing an infinite surface. For a periodic system, the potential of the system should represent this periodicity. In solid state physics, the Bloch theorem [37] applies to the solution of the Schrödinger equation of an electron in a periodic potential. This theorem says that an eigenfunction for an electron in a periodic potential can be written as a plane wave multiplied with a periodic function with the same periodicity as the potential. Therefore, to build the periodicity into the DFT calculation a periodic basis set can be used. Based on the Bloch theorem the eigen-states, in this case the KS orbitals, can be written as

$$\phi_{i,k}(\vec{r}) = u_k(\vec{r})e^{i\vec{k}\cdot\vec{r}}, \quad (2.30)$$

where  $\vec{k}$  is a wave-vector in the first Brillouin zone and  $u_{i,k}$  is a function with the same periodicity ( $\vec{R}$ ) as the potential,

$$u_{i,k}(\vec{r}) = u_{i,k}(\vec{r} + \vec{R}). \quad (2.31)$$

By expanding  $u_{i,k}$  in the plane wave basis set (Fourier series), the KS orbitals can be written as

$$\phi_{i,k} = N \sum_G c_{i,k}(\vec{G}) e^{i(\vec{k}+\vec{G})\cdot\vec{r}}, \quad (2.32)$$

where  $\vec{G}$  is a reciprocal lattice vector,  $c_{i,k}(G)$  is an expansion coefficient and  $N$  is a normalization factor.

When performing the actual calculations, the number of plane waves that represent the wave function can not be infinite. The size of the basis set is specified by the maximum kinetic energy  $E_{cut-off}$ . In Equation 2.32, the plane wave  $e^{i(\vec{k}+\vec{G})\cdot\vec{r}}$  is included in the basis set if:

$$\frac{1}{2}|\vec{k} + \vec{G}|^2 \leq E_{cut-off}. \quad (2.33)$$

To determine a suitable  $E_{cut-off}$  one should perform several calculations with increasing  $E_{cut-off}$  to ensure that the property of interest (*e.g.*, energy) is converged with respect to  $E_{cut-off}$ . Also in the calculations, continuous sampling of the first Brillouin zone is computationally problematic and it has to be sampled by a discrete (and finite) number of grid points (the *k*-points). A particularly useful scheme for generation of *k*-points grids that will be used in this thesis, was devised by Monkhorst and Pack [38].

The plane wave basis has some advantages. First, they are orthogonal and easy to use to control the completeness of the basis set. Also, they are independent of the atomic positions so with plane waves, there is no basis set superposition error. Furthermore, a computational advantage arises from the fact that a fast algorithm exist to operate with them and convert the wave function between real space and momentum space (fast Fourier transforms (FFTs)). The use of plane waves as a basis set also has some downsides. To represent core electron orbitals, which are rapidly varying functions due to their localization close to the nucleus, and also valence electron orbitals very close to nuclei, which can assume a highly-oscillating behaviour, a prohibitively large number of plane wave is necessary. However, core electrons described by these wave functions do not participate in the interaction with the other atoms, since the rearrangement of the valence electrons is mainly responsible for bonding. Therefore, it is possible to remove these electrons and replace them by effective potentials named pseudopotentials. The name of pseudopotentials comes from the fact that the strong Coulomb potential of a bare nucleus is replaced with a softer potential of a pseudo-atom. The pseudo-atom includes nuclei, core electrons and interaction among them including relativistic effects.

The pseudopotential can be constructed in such a way that the potential and resulting pseudo-wave functions are as smooth as possible inside the cut-off radius  $r_c$  close to the nucleus and that they are almost exactly the

same as the real potential and wave function outside the cut-off radius. In the pseudopotential approach, the pseudo-wave functions are smoother than the corresponding all electron wave functions which oscillate rapidly in the core region, while they reproduce the all electron wave functions beyond a distance from the nucleus  $r_c$ . Ultrasoft pseudopotentials were introduced by Vanderbilt (1990) [39]; these allow calculations to be performed with a low cutoff energy. A more general approach is provided by the projector-augmented waves (PAW) method [40, 41], which also allows for calculation of all-electron observables and which is used in the calculations presented in this thesis.

In plane wave DFT, there is periodicity in three dimensions in contrast to the two dimensional periodicity of the surface. To tackle this problem, a supercell approach [42] is used to treat molecule on surface systems, which actually have 2D periodicity. A large vacuum space is introduced along the dimension perpendicular to the surface so that the unit cell is partitioned into regions of solid (slab) and vacuum [43]. The slab [44] is periodic in the directions parallel to the surface and contains enough atomic layers in the direction perpendicular to the surface to converge the molecule-surface interaction energy. To minimize the artificial interaction between periodic images (interaction between the slab and its periodic image) a thick enough vacuum space is needed. In the construction of the supercell all these factors should be taken into account to keep the computational cost (number of atoms) as low as possible, while still obtaining accurate results.

## 2.4 Construction of potential energy surfaces

In the previous section we described the electronic structure methods that provide the data that one needed to obtain the PES on which the nuclear motion is propagated. A continuous PES is needed to solve the Schrödinger equation for nuclear motion, Equation 2.10. To obtain a continuous PES, the approach is to perform a number of DFT single point calculations for a set of selected configurations of the system and then interpolate them using some sort of fitting scheme. For the PES of a diatomic molecule interacting with a frozen metal surface a rather efficient interpolation method is available, which was proposed by Busnengo *et al.* [45, 46] and is called the corrugation reducing procedure (CRP). The CRP method will be used as an interpolation method through out this thesis and will be described here.

The main problem in the interpolation of the molecule-surface potential near to a surface is that it is highly corrugated, *i.e.*, a large variation in the potential exists when a small change happens in the molecular coordinates. The idea behind the CRP method is to reduce this corrugation to a manageable level. It is known that the interaction of the individual atoms with the surface causes most of the corrugation in the potential. Therefore, the CRP interpolation method, for example for  $\text{H}_2$  interacting with a surface, reduces the corrugation near the surface by subtracting the H atom-surface interactions from the total interaction to obtain a smoother function. Then the interpolation is carried out of the smoother function and the H-surface potential is added back to obtain the final full 6D potential. First let us define the coordinate system of a  $\text{H}_2$  molecule on a surface. As mentioned in Section 1.2.1, the geometry of the  $\text{H}_2$  molecule relative to the surface can be described by the motion of (the center of mass (COM) of) the  $\text{H}_2$  molecule in three dimensions ( $(X, Y, Z) \equiv R$ ), and the internal motion of the molecule ( $(r, \theta, \phi) \equiv q$ ), *i.e.*, the interatomic distance  $r$ , the angle between the molecular axis and the surface normal  $\theta$ , and the angle  $\phi$  between the projection of the molecular axis on the surface and the  $X$  axis, respectively. In the CRP method, the six-dimensional (6D) PES is written as

$$V^{6D}(\vec{R}, \vec{q}) = I^{6D}(\vec{R}, \vec{q}) + \sum_{i=1}^2 V_i^{3D}(\vec{r}_i), \quad (2.34)$$

in which  $V^{6D}$  is the full 6D PES of the  $\text{H}_2$ /surface system and  $I^{6D}$  is the so-called 6D interpolation function of the  $\text{H}_2$ /surface system, which still depends on the center of mass coordinates ( $\vec{R}$ ) with respect to the surface and the internal coordinates of the  $\text{H}_2$  molecule ( $\vec{q}$ ).  $V_i^{3D}$  is the three-dimensional (3D) PES of the H/surface system, with  $\vec{r}_i$  the vector representing the coordinates of the  $i$ th H atom with respect to the surface. For the interpolation of the 3D H/surface system PES, the CRP is again applied using

$$V_i^{3D}(\vec{r}_i) = I_i^{3D}(\vec{r}_i) + \sum_j^N V^{1D}(R_{ij}), \quad (2.35)$$

where  $I_i^{3D}$  is the 3D interpolation function describing the H/surface system, and  $N$  is the number of surface atoms to take into account in the summation. The interaction of a hydrogen atom with a single surface atom is represented by a one-dimensional (1D) function  $V^{1D}$  depending on the distance between



the hydrogen atom  $i$  and surface atom  $j$  ( $R_{ij}$ ). The  $V^{1D}$  function reduces the corrugation of  $V_i^{3D}$ .

The first step in this procedure is to calculate the DFT points for a grid of geometries. To reduce the computational cost, it is very useful to include the most symmetric molecular configurations. This is because a periodic lattice is considered and additional symmetry is usually present in the form of mirror planes and rotation axes. Furthermore, in the case of a homonuclear diatomic molecule, or when the molecule is above a high symmetry site of the surface, even more symmetry can be present. Therefore, several symmetric  $X, Y$  positions are selected and for each of these positions several orientations  $(\theta, \phi)$  are chosen. Finally for each set of  $(X, Y, \theta, \phi)$ , a grid of  $(r, Z)$  values is chosen. The DFT calculations are performed for each  $(X, Y, Z, r, \theta, \phi)$  geometry. Then the CRP approach is applied to these DFT points. The 3D potentials of each atom of the molecule are subtracted from the 6D molecule-surface potential points. The remaining interpolation function  $I^{6D}$  is smooth enough to use standard numerical interpolation methods to interpolate it. In this step typically the 6D problem is decoupled into four two-dimensional (2D) interpolation steps [47]. For each calculated  $(X, Y, \theta, \phi)$  configuration, 2D cubic splines interpolation method is used to interpolate the calculated  $(r, Z)$  grid of energy points. Once the interpolated values of  $(r, Z)$  grid points are obtained, the  $(\theta, \phi)$  interpolation for each  $(X, Y)$  combination is carried out. Usually a Fourier interpolation method is used with basis functions (sines and cosines) incorporating the symmetry of the system. Finally, the interpolation is performed for the remaining  $(X, Y)$  coordinates. In this step a symmetry adapted Fourier expansion or 2D periodic cubic splines can be used. After interpolating the interpolation function the 3D potentials are again added to obtain the continuous 6D potential.

In the CRP scheme, the individual 3D atom potentials have to be calculated. They are obtained in a similar way as the 6D PES. First the DFT values are obtained for a grid of positions of the H-atom  $(X, Y, Z)$ . The 3D PES is also corrugated and its corrugation is reduced by subtraction of the 1D pair potentials. Then the 3D interpolation function can be interpolated using 3D cubic splines. The interpolation is performed in two steps. First, for each calculated  $(X, Y)$  configuration, 1D cubic spline interpolation is performed to interpolate the calculated  $(Z)$  grid of energy points. Then a Fourier interpolation is performed in the  $(X, Y)$  coordinates, using symmetry adopted sine and cosine functions. For  $V^{1D}$  the spline interpolation

of the interaction of the H atom above  $X = 0, Y = 0$  is used.

## 2.5 Molecular dynamics

Once the 6D PES is constructed one can perform the dynamics calculations either classically or quantum mechanically. Computing the dynamical properties gives us the opportunity to understand and compare to the experimental measurements.

### 2.5.1 Quasi-classical dynamics

The classical trajectory calculations are performed by solving Newton's equations of motion for the 6 molecular DOFs as

$$M_i \frac{d^2 R_i}{dt^2} = -\nabla_i V^{6D}(R_i, R_j), \quad i \neq j \quad (2.36)$$

where  $i, j$  are the indexes of the atoms in the diatomic molecule. To integrate the equations of motion, different propagators exist and can be used, such as the (velocity) Verlet propagator [48], the Beeman propagator [49], etc.

The Quasi-classical trajectory (QCT) method usually gives more accurate results for  $H_2$ -surface reactions than the purely classical method because in a QCT calculation the initial vibrational zero point energy (ZPE) is modelled using an ensemble of initial conditions for the internal motion of the molecule that forms a classical microcanonical distribution [50]. The vibrational states of the molecule are calculated using the Fourier grid Hamiltonian (FGH) method [51]. In the QCT calculations based on the CRP interpolated PES, Hamilton's equations of motion are integrated with the predictor-corrector method of Bulirsch and Stoer [52].

At the beginning of each trajectory calculation the initial conditions have to be set, *i.e.*, the initial positions, and velocities of the particles. In modeling  $H_2$  dissociation on a surface, the molecule is initially positioned far away from the surface, where the potential does not yet depend on  $Z$ . The molecule with a particular velocity towards the surface corresponds to the perpendicular incidence energy  $E_{\perp}$ . The impact site on the surface is chosen randomly and, if off-normal incidence is considered, a velocity vector is set up according to the parallel incidence energy  $E_{\parallel}$ , the polar incidence angle  $\theta_i$ , and the azimuthal incidence angle  $\phi_i$ .

Reaction or scattering probabilities, for each initial incidence energy and initial rovibrational state ( $E_i$ ,  $\nu_i$  and  $j_i$ ) are calculated as an average over molecular initial conditions (position of the molecular center of mass over the surface unit cell, molecular orientations and orientation of the initial angular momentum vector) where these initial conditions of the  $\text{H}_2$  molecule are selected using a standard Monte Carlo method. To obtain  $m_j$  resolved reaction probabilities, the initial angular momentum  $L$  of the  $\text{H}_2$  molecule is fixed by  $L = \sqrt{j(j+1)}\hbar$  and its orientation is chosen randomly with the constraint  $\cos(\theta_L) = m_j/\sqrt{j(j+1)}$ , where  $\theta_L$  is the angle between the angular momentum vector and the surface normal.

After the propagation over a certain number of time steps, the trajectories are analyzed to determine whether a specific outcome has been reached. When the interatomic distance of the molecule reaches a particular value, the molecule is considered to have reacted. When the distance between the molecule and the surface becomes larger than a certain value where no interaction is present, the molecule is considered to have scattered. The molecule is considered to be trapped if neither outcome has occurred.

The reaction probability  $P_r$  can be obtained from

$$P_r = \frac{N_r}{N_{total}}, \quad (2.37)$$

where  $N_r$  is the number of reacted trajectories and  $N_{total}$  is the total number of trajectories. Certain observables such as molecular beam sticking probabilities or degeneracy averaged reaction probabilities can be computed using the QCT method.

### 2.5.2 Quantum dynamics

For the quantum dynamics (QD) calculations, a time-dependent wave packet (TDWP) method [53] was used, where the time dependent Schrödinger equation is solved to generate scattering and reaction probabilities. The wave packet is represented in a discrete variable representation (DVR) [54] for  $Z, r, X, Y$  and a finite basis representation (FBR) [55, 56] has been used to describe the angular DOFs. Fast Fourier transforms [57] and discrete associated Gauss-Legendre transforms [55, 56] were used to transform the wave function from FBR space to DVR space, and *vice versa*. The wave packet is propagated in time using the Split Operator method [58]. The

initial wave packet, which is placed far away from the surface on a specular grid (sp), where the interaction with the surface is negligibly small, is written as a product of a Gaussian wave packet to describe motion perpendicular to the surface, plane waves to describe motion parallel to the surface, and a rovibrational wave function describing the initial state of the molecule according to

$$\psi_0(X, Y, Z, r, \theta, \phi) = \phi_{\nu,j}(r) Y_{jm_j}(\theta, \phi) \frac{1}{\sqrt{A}} e^{ik_0^{X,Y} \cdot \mathcal{R}} \int dk^Z \beta(k_0^Z) \frac{1}{2\pi} e^{ik_0^Z Z}. \quad (2.38)$$

Here  $\phi_{\nu,j}(r)$  and  $Y_{jm_j}(\theta, \phi)$  are, respectively, the vibrational and rotational eigenfunction of the  $\text{H}_2$  molecule in the gas phase with vibrational, rotational and magnetic rotational quantum number  $\nu$ ,  $j$  and  $m_j$ . The initial parallel motion of the wave packet along  $X$  and  $Y$  is described by  $\frac{1}{\sqrt{A}} e^{ik_0^{X,Y} \cdot \mathcal{R}}$ , in which  $A$  is a normalization factor (the surface area of the unit cell),  $k_0^{X,Y}$  is the initial parallel momentum and  $\mathcal{R}$  is the position vector  $(X, Y)$ . The wave packet describing motion in the  $Z$  direction is a function of the initial momentum  $k_0^Z$  and is Gaussian shaped and centered on  $Z_0$ :

$$\beta(k_0^Z) = \left( \frac{2\sigma^2}{\pi} \right)^{1/4} e^{-\sigma^2(\bar{k}-k_0^Z)^2} e^{i(\bar{k}-k_0^Z)Z_0}. \quad (2.39)$$

Here  $\bar{k}$  is the average momentum in  $Z$  and  $\sigma$  is a half width parameter. To ensure that the wave packet moves towards the surface with a range of translational energies,  $\bar{k}$  is chosen to be negative. When the wave packet enters the region where it interacts with the surface, it is transferred from the specular grid to the regular grid using a projection operator formalism [59, 60]. The part of the wave packet which returns from the surface, is analyzed using the scattering amplitude formalism [61–63] at  $Z_\infty$  where the molecule and surface (in principle) no longer interact and is integrated over time to obtain the state-to-state scattering S-matrix elements for all open vibration, rotation and diffraction channels. Beyond  $Z_\infty$  or large  $r$ , optical potentials [64] are used to adsorb the reacted part of the wave packet and the reflected part of the wave packet.

Scattering probabilities as a function of energy were obtained from S-matrix elements over the entire range of energies present in the wave packet. The fully initial state resolved reaction probability is defined as 1 minus the

sum of the scattering probabilities:

$$P_r(\nu, j, m_j) = 1 - \sum_{\nu', j', m'_j, n, m} P_{scat}(\nu, j, m_j \rightarrow \nu', j', m'_j, n, m), \quad (2.40)$$

where  $P_{scat}(\nu, j, m_j \rightarrow \nu', j', m'_j, n, m)$  are the state to state scattering probabilities.  $\nu(\nu')$ ,  $j(j')$ ,  $m_j(m'_j)$  ss are the initial(final) vibrational, rotational and magnetic rotational quantum number, respectively, and  $n$  and  $m$  are the quantum numbers for diffraction. For more details about this method see Ref. [65].

### 2.5.3 Computation of observables

#### Initial state resolved reaction probabilities

Initial state resolved reaction probabilities  $P_{deg}(E; v, j)$  are obtained by degeneracy averaging the fully initial state resolved reaction probabilities  $P_r(E; v, j, m_j)$  according to

$$P_{deg}(E; v, j) = \frac{\sum_{m_j=0}^{m_j=j} (2 - \delta_{m_j,0}) \cdot P_r(E; v, j, m_j)}{2j + 1}, \quad (2.41)$$

where  $P_r$  is the fully initial state-resolved reaction probability,  $\delta$  is the Kronecker delta, and  $\nu$ ,  $j$  and  $m_j$  are the initial vibrational, rotational and magnetic rotational quantum number of the  $\text{H}_2$  molecule, respectively.

#### Molecular beam sticking probabilities

In order to make a meaningful comparison of computed reaction probabilities with measured sticking probability results, we have performed simulations of the molecular beam conditions, used in the experiments. For this one has to take into account two things. First, the initial state resolved reaction probabilities should be averaged over all rovibrational states which have a significant population in the molecular beam. Second, it is necessary to consider the spread of incidence energies present in the molecular beam. Therefore we need to compute the molecule's monoenergetic reaction probabilities  $P_{mono}(E_i, T_n)$ , which depend on the collision energy  $E_i$  and on the

nozzle temperature  $T_n$ , and thus, on the rovibrational state populations. The monoenergetic reaction probability can be written as :

$$P_{mono}(E_i, T_n) = \sum_{\nu, j} F_B(\nu, j; T_n) P_{deg}(E_i; \nu, j), \quad (2.42)$$

where  $P_{deg}(E_i; \nu, j)$  is the monoenergetic initial state-resolved reaction probability and  $F_B(\nu, j; T_n)$  is the Boltzmann weight of the  $(\nu, j)$  state. The factor  $F_B(\nu, j; T_n)$  is given by:

$$F_B(\nu, j; T_n) = (2j + 1) e^{[-E_{vib}(\nu, j)/k_B T_n]} \times e^{[-E_{rot}(\nu, j)/0.8k_B T_n]} \times N(j), \quad (2.43)$$

where  $N(j)$  is the normalization factor which takes into account the correct nuclear spin statistics for hydrogen and is given by :

$$N(j) = \frac{w(j)}{\sum_{\nu', j' \equiv j \pmod{2}} (2j' + 1) e^{[-E_{vib}(\nu', j')/k_B T_n]} \times e^{[-E_{rot}(\nu', j')/0.8k_B T_n]}}. \quad (2.44)$$

In Equation 2.44, the summation runs only over the values of  $j'$  which have the same parity as  $j$ . Furthermore,  $E_{vib}$  and  $E_{rot}$  are the vibrational and rotational energy of the rovibrational state, respectively, and  $k_B$  is the Boltzmann constant. Because there are three parallel nuclear spin states and only one anti-parallel spin state for  $H_2$ , for the molecular beam at thermal equilibrium at high temperature (room temperature or higher), which is the usual case in the experiments, a ratio between ortho (odd  $j$ )- and para-hydrogen of 3:1 is expected. At very low temperature, it is expected that only the  $\nu = 0$  and  $j = 0$  rovibrational state is occupied. Therefore, the molecular beam in the thermal equilibrium should consist of pure para-hydrogen at very low temperature. However, the conversion of ortho- to para-hydrogen is very slow and does not happen on the time scale of the experiment. The  $H_2$  is then either (vibrationally or rotationally) cooled or heated by the nozzle, but without the possibility of a nuclear spin flip. Therefore, the 3:1 ortho-para ratio in the  $N(j)$  factor ( $w(j)$ ) is, for practical purposes, independent of the nozzle temperature. For  $H_2(D_2)$ ,  $w(j)$  is equal to  $1/4(2/3)$  for even  $j$  values, and  $3/4(1/3)$  for odd  $j$  values.

In the Equations 2.43 and 2.44, the experimental rotational distributions can be described by a rotational temperature  $T_{rot}$ , which is assumed to be lower than the nozzle temperature ( $T_{rot} = 0.8T_n$ ) [66, 67]. Once the

monoenergetic reaction probabilities have been computed, one can compute reaction probabilities convoluted over the incidence energy or velocity distribution of the experimental molecular beam, according to the expression [68] :

$$P_{beam}(T_n) = \frac{\int_{\nu_i=0}^{\nu_i=\infty} f(\nu_i; T_n) P_{mono}(E_i; T_n) d\nu_i}{\int_{\nu_i=0}^{\nu_i=\infty} f(\nu_i; T_n) d\nu_i}, \quad (2.45)$$

where  $E_i = 1/2Mv_i^2$ ,  $v_i$  being the velocity of the molecule, and  $f(\nu_i; T_n)$  the flux weighted velocity distribution for a nozzle temperature  $T_n$  given by:

$$f(\nu_i; T_n) d\nu_i = C v_i^3 \exp[-(v_i - v_s)^2 / \alpha^2] d\nu_i. \quad (2.46)$$

In this equation,  $C$  is a constant and  $T_n$  is the nozzle temperature used in the corresponding molecular beam experiment. Furthermore, the parameter  $v_s$  is the stream velocity and  $\alpha$  is the parameter that characterizes the width of the velocity distribution. Note that the parameters  $C$ ,  $v_s$  and  $\alpha$  again parametrically depend on the nozzle temperature. The parameters can be obtained by fitting the experimental time-of-flight (TOF) spectra, using the Levenberg-Marquardt algorithm [69], to

$$G(t; T_n) = c_1 + c_2 \cdot v^4 \exp[-(v - v_s/\alpha)^2], \quad (2.47)$$

where  $c_1$  and  $c_2$  are constants. In Equation 2.47,  $v$  is taken as  $L/t$  where  $L$  is the length of the flight path.

### Vibrational efficacy

The vibrational efficacy is used to investigate how efficiently vibrational energy can be used to promote reaction relative to translational energy. It can be computed by

$$\eta_\nu(P) = \frac{E_i^{\nu=0,j}(P) - E_i^{\nu=1,j}(P)}{E_{vib}(\nu = 1, j) - E_{vib}(\nu = 0, j)}, \quad (2.48)$$

where  $E_{vib}(\nu, j)$  is the vibrational energy corresponding to a particular state of the gas-phase molecule and  $E_i^{\nu,j}(P)$  is the incidence energy at which the the initial state-resolved reaction probability becomes equal to  $P$  for  $H_2$  ( $D_2$ ) initially in its  $(\nu, j)$  state. In evaluating Equation 2.48  $j$  is typically taken as 0.

### Diffraction probabilities

To study diffraction, a quantum phenomenon, quantum dynamics calculations should be performed. In the diffractive scattering process, the molecule's translational momentum parallel to the surface can only change by discrete amounts. In order to compare with the experimental diffraction probabilities [70], as we will see in Chapter 6, the rovibrationally elastic diffraction probabilities are computed by

$$P_{nm}(\nu, j, m_j) = \sum_{m_j''=-j}^j P_{scat}(\nu, j, m_j \rightarrow \nu' = \nu, j' = j, m_j'', n, m), \quad (2.49)$$

where  $P_{nm}$  is the rovibrationally elastic probability for scattering into diffraction state denoted by the  $n$  and  $m$  quantum numbers. These probabilities are degeneracy averaged by

$$P_{nm}(\nu, j) = \sum_{m_j=0}^j (2 - \delta_{m_j,0}) P_{nm}(\nu, j, m_j) / (2j + 1). \quad (2.50)$$



## References

1. Schrödinger, E. An Undulatory Theory of the Mechanics of Atoms and Molecules. *Physical Review* **28**, 1049–1070 (1926).
2. Born, M. & Oppenheimer, R. Zur Quantentheorie der Molekeln. *Annalen der Physik* **389**, 457–484 (1927).
3. Hohenberg, P. & Kohn, W. Inhomogeneous Electron Gas. *Physical Review* **136**, B864–B871 (1964).
4. Kohn, W. & Sham, L. J. Self-Consistent Equations Including Exchange and Correlation Effects. *Physical Review* **140**, A1133–A1138 (1965).
5. Ceperley, D. M. & Alder, B. J. Ground State of the Electron Gas by a Stochastic Method. *Physical Review Letters* **45**, 566–569 (1980).
6. Vosko, S. H., Wilk, L. & Nusair, M. Accurate Spin-Dependent Electron Liquid Correlation Energies for Local Spin Density Calculations: A Critical Analysis. *Canadian Journal of Physics* **58**, 1200–1211 (1980).
7. Perdew, J. P. *et al.* Atoms, Molecules, Solids, and Surfaces: Applications of The Generalized Gradient Approximation for Exchange and Correlation. *Physical Review B* **46**, 6671–6687 (1992).
8. Perdew, J. P. & Zunger, A. Self-Interaction Correction to Density-Functional Approximations for Many-Electron Systems. *Physical Review B* **23**, 5048–5079 (1981).
9. Hammer, B., Jacobsen, K. W. & Nørskov, J. K. Role of Nonlocal Exchange Correlation in Activated Adsorption. *Physical Review Letters* **70**, 3971–3974 (1993).
10. White, J. A., Bird, D. M., Payne, M. C. & Stich, I. Surface Corrugation in the Dissociative Adsorption of H<sub>2</sub> on Cu(100). *Physical Review Letters* **73**, 1404–1407 (1994).
11. Langreth, D. C. & Mehl, M. J. Beyond the Local-Density Approximation in Calculations of Ground-State Electronic Properties. *Physical Review B* **28**, 1809–1834 (1983).
12. Becke, A. D. Density-Functional Exchange-Energy Approximation with Correct Asymptotic Behavior. *Physical Review A* **38**, 3098–3100 (1988).

13. Peverati, R. & Truhlar, D. G. Quest for a Universal Density Functional: the Accuracy of Density Functionals Across a Broad Spectrum of Databases in Chemistry and Physics. *Philosophical Transactions of the Royal Society A: Mathematical, Physical and Engineering Sciences* **372**, 20120476 (2014).
14. Peverati, R. & Truhlar, D. G. An Improved and Broadly Accurate Local Approximation to the Exchange-Correlation Density Functional: The MN12-L Functional for Electronic Structure Calculations in Chemistry and Physics. *Physical Chemistry Chemical Physics* **14**, 13171–13174 (2012).
15. Perdew, J. P., Burke, K. & Ernzerhof, M. Generalized Gradient Approximation Made Simple. *Physical Review Letters* **77**, 3865–3868 (1996).
16. Hammer, B., Hansen, L. B. & Nørskov, J. K. Improved Adsorption Energetics within Density-Functional Theory Using Revised Perdew-Burke-Ernzerhof Functionals. *Physical Review B* **59**, 7413–7421 (1999).
17. Díaz, C. *et al.* Chemically Accurate Simulation of a Prototypical Surface Reaction: H<sub>2</sub> Dissociation on Cu(111). *Science* **326**, 832–834 (2009).
18. Libxc: A Library of Exchange and Correlation Functionals for Density Functional Theory. *Computer Physics Communications* **183**, 2272–2281 (2012).
19. Perdew, J. P. & Schmidt, K. Jacob’s Ladder of Density Functional Approximations for the Exchange-Correlation Energy. *AIP Conference Proceedings* **577**, 1–20 (2001).
20. Tao, J., Perdew, J. P., Staroverov, V. N. & Scuseria, G. E. Climbing the Density Functional Ladder: Nonempirical Meta-Generalized Gradient Approximation Designed for Molecules and Solids. *Physical Review Letters* **91**, 146401 (2003).
21. Perdew, J. P., Ruzsinszky, A., Csonka, G. I., Constantin, L. A. & Sun, J. Workhorse Semilocal Density Functional for Condensed Matter Physics and Quantum Chemistry. *Physical Review Letters* **103**, 026403 (2009).
22. Becke, A. D. Density-Functional Thermochemistry. III. The Role of Exact Exchange. *Journal of Chemical Physics* **98**, 5648–5652 (1993).

23. Stephens, P. J., Devlin, F. J., Chabalowski, C. F. & Frisch, M. J. *Ab Initio* Calculation of Vibrational Absorption and Circular Dichroism Spectra Using Density Functional Force Fields. *Journal of Physical Chemistry* **98**, 11623–11627 (1994).
24. Paier, J. *et al.* Screened Hybrid Density Functionals Applied to Solids. *Journal of Chemical Physics* **124**, 154709 (2006).
25. Stroppa, A., Termentzidis, K., Paier, J., Kresse, G. & Hafner, J. CO Adsorption on Metal Surfaces: A Hybrid Functional Study with Plane-Wave Basis Set. *Physical Review B* **76**, 195440 (2007).
26. Kroes, G. J. & Díaz, C. Quantum and Classical Dynamics of Reactive Scattering of H<sub>2</sub> from Metal Surfaces. *Chemical Society Reviews* **45**, 3658–3700 (2016).
27. Grimme, S. Semiempirical GGA-Type Density Functional Constructed with a Long-Range Dispersion Correction. *Journal of Computational Chemistry* **27**, 1787–1799 (2006).
28. Tkatchenko, A. & Scheffler, M. Accurate Molecular van der Waals Interactions from Ground-State Electron Density and Free-Atom Reference Data. *Physical Review Letters* **102**, 073005 (2009).
29. Dion, M., Rydberg, H., Schröder, E., Langreth, D. C. & Lundqvist, B. I. van der Waals Density Functional for General Geometries. *Physical Review Letters* **92**, 246401 (2004).
30. Berland, K. *et al.* Van der Waals Forces in Density Functional Theory: a Review of the vdW-DF Method. *Reports on Progress in Physics* **78**, 066501 (2015).
31. Klimeš, J. & Michaelides, A. Perspective: Advances and Challenges in Treating Van der Waals Dispersion Forces in Density Functional Theory. *Journal of Chemical Physics* **137** (2012).
32. Hyldgaard, P., Berland, K. & Schröder, E. Interpretation of van der Waals Density Functionals. *Physical Review B* **90**, 075148 (2014).
33. Román-Pérez, G. & Soler, J. M. Efficient Implementation of a van der Waals Density Functional: Application to Double-Wall Carbon Nanotubes. *Physical Review Letters* **103**, 096102 (2009).
34. Lee, K., Murray, É. D., Kong, L., Lundqvist, B. I. & Langreth, D. C. Higher-Accuracy van der Waals Density Functional. *Physical Review B* **82**, 081101 (2010).

35. Chuang, Y.-Y., Radhakrishnan, M. L., Fast, P. L., Cramer, C. J. & Truhlar, D. G. Direct Dynamics for Free Radical Kinetics in Solution: Solvent Effect on the Rate Constant for the Reaction of Methanol with Atomic Hydrogen. *Journal of Physical Chemistry A* **103**, 4893–4909 (1999).
36. Sementa, L. *et al.* Reactive Scattering of H<sub>2</sub> from Cu(100): Comparison of Dynamics Calculations Based on the Specific Reaction Parameter Approach to Density Functional Theory with Experiment. *Journal of Chemical Physics* **138** (2013).
37. Bloch, F. Über die Quantenmechanik der Elektronen in Kristallgittern. *Zeitschrift für Physik* **52**, 555–600 (1929).
38. Monkhorst, H. J. & Pack, J. D. Special Points for Brillouin-Zone Integrations. *Physical Review B* **13**, 5188–5192 (1976).
39. Laasonen, K., Car, R., Lee, C. & Vanderbilt, D. Implementation of Ultrasoft Pseudopotentials in *Ab Initio* Molecular Dynamics. *Physical Review B* **43**, 6796–6799 (1991).
40. Kresse, G. & Joubert, D. From Ultrasoft Pseudopotentials to the Projector Augmented-Wave Method. *Physical Review B* **59**, 1758–1775 (1999).
41. Blöchl, P. E. Projector Augmented-Wave Method. *Physical Review B* **50**, 17953–17979 (1994).
42. Neugebauer, J. & Scheffler, M. Adsorbate-Substrate and Adsorbate-Adsorbate Interactions of Na and K Adlayers on Al(111). *Physical Review B* **46**, 16067–16080 (1992).
43. Sun, W. & Ceder, G. Efficient Creation and Convergence of Surface Slabs. *Surface Science* **617**, 53–59 (2013).
44. Te Velde, G. & Baerends, E. Slab Versus Cluster Approach for Chemisorption Studies. CO on Cu (100). *Chemical Physics* **177**, 399–406 (1993).
45. Busnengo, H. F., Salin, A. & Dong, W. Representation of the 6D Potential Energy Surface for a Diatomic Molecule Near a Solid Surface. *Journal of Chemical Physics* **112**, 7641–7651 (2000).
46. Olsen, R. A. *et al.* Constructing Accurate Potential Energy Surfaces for a Diatomic Molecule Interacting With a Solid Surface: H<sub>2</sub>+Pt(111) and H<sub>2</sub>+Cu(100). *Journal of Chemical Physics* **116**, 3841–3855 (2002).

47. Bukas, V. J., Meyer, J. & Alducin, M. Ready, Set and no Action: A Static Perspective on Potential Energy Surfaces commonly used in Gas-Surface Dynamics. *Zeitschrift für Physikalische Chemie* **227**, 1523–1542 (2013).
48. Verlet, L. Computer "Experiments" on Classical Fluids. I. Thermodynamical Properties of Lennard-Jones Molecules. *Physical Review* **159**, 98–103 (1967).
49. Beeman, D. Some Multistep Methods for Use in Molecular Dynamics Calculations. *Journal of Computational Physics* **20**, 130–139 (1976).
50. Díaz, C., Olsen, R. A., Busnengo, H. F. & Kroes, G. J. Dynamics on Six-Dimensional Potential Energy Surfaces for H<sub>2</sub>/Cu(111): Corrugation Reducing Procedure versus Modified Shepard Interpolation Method and PW91 versus RPBE. *Journal of Physical Chemistry C* **114**, 11192–11201 (2010).
51. Marston, C. C. & Balint-Kurti, G. G. The Fourier Grid Hamiltonian Method for Bound State Eigenvalues and Eigenfunctions. *Journal of Chemical Physics* **91**, 3571–3576 (1989).
52. J. Stoer, R. B. *Introduction to Numerical Analysis* (Springer: New York, 1980).
53. Kosloff, R. Time-Dependent Quantum-Mechanical Methods for Molecular Dynamics. *Journal of Physical Chemistry* **92**, 2087–2100 (1988).
54. Light, J. C., Hamilton, I. P. & Lill, J. V. Generalized Discrete Variable Approximation in Quantum Mechanics. *Journal of Chemical Physics* **82**, 1400–1409 (1985).
55. Corey, G. C. & Lemoine, D. Pseudospectral Method for Solving the Time-Dependent Schrödinger Equation in Spherical Coordinates. *Journal of Chemical Physics* **97**, 4115–4126 (1992).
56. Lemoine, D. The Finite Basis Representation as the Primary Space in Multidimensional Pseudospectral Schemes. *Journal of Chemical Physics* **101**, 10526–10532 (1994).
57. Kosloff, D. & Kosloff, R. A Fourier Method Solution for the Time Dependent Schrödinger Equation as a Tool in Molecular Dynamics. *Journal of Computational Physics* **52**, 35–53 (1983).

58. Feit, M., Fleck, J. & Steiger, A. Solution of the Schrödinger Equation by a Spectral Method. *Journal of Computational Physics* **47**, 412–433 (1982).
59. Pijper, E., Kroes, G. J., Olsen, R. A. & Baerends, E. J. Reactive and Diffractive Scattering of H<sub>2</sub> from Pt(111) Studied Using a Six-Dimensional Wave Packet Method. *Journal of Chemical Physics* **117**, 5885–5898 (2002).
60. Kroes, G. J., Baerends, E. J. & Mowrey, R. C. Six-Dimensional Quantum Dynamics of Dissociative Chemisorption of H<sub>2</sub> on Cu(100). *Journal of Chemical Physics* **107**, 3309–3323 (1997).
61. Balint-Kurti, G. G., Dixon, R. N. & Marston, C. C. Time-Dependent Quantum Dynamics of Molecular Photofragmentation Processes. *Journal of Chemical Society, Faraday Transactions* **86**, 1741–1749 (1990).
62. Balint-Kurti, G. G., Dixon, R. N. & Marston, C. C. Grid Methods for Solving the Schrödinger Equation and Time Dependent Quantum Dynamics of Molecular Photofragmentation and Reactive Scattering Processes. *International Reviews in Physical Chemistry* **11**, 317–344 (1992).
63. Mowrey, R. C. & Kroes, G. J. Application of an Efficient Asymptotic Analysis Method to Molecule–Surface Scattering. *Journal of Chemical Physics* **103**, 1216–1225 (1995).
64. Vibok, A. & Balint-Kurti, G. G. Parametrization of Complex Absorbing Potentials for Time-Dependent Quantum Dynamics. *Journal of Physical Chemistry* **96**, 8712–8719 (1992).
65. Kroes, G. J. & Somers, M. F. Six-Dimensional Dynamics of Dissociative Chemisorption of H<sub>2</sub> on Metal Surfaces. *Journal of Theoretical and Computational Chemistry* **04**, 493–581 (2005).
66. Rettner, C. T., Michelsen, H. A. & Auerbach, D. J. Quantum-State-Specific Dynamics of the Dissociative Adsorption and Associative Desorption of H<sub>2</sub> at a Cu(111) Surface. *Journal of Chemical Physics* **102**, 4625–4641 (1995).
67. Rendulic, K., Anger, G. & Winkler, A. Wide Range Nozzle Beam Adsorption Data for the Systems H<sub>2</sub>/Nickel and H<sub>2</sub>/Pd(100). *Surface Science* **208**, 404–424 (1989).

68. Díaz, C., Olsen, R. A., Auerbach, D. J. & Kroes, G. J. Six-Dimensional Dynamics Study of Reactive and Non Reactive Scattering of H<sub>2</sub> from Cu(111) Using a Chemically Accurate Potential Energy Surface. *Physical Chemistry Chemical Physics* **12**, 6499–6519 (2010).
69. Marquardt, D. W. An Algorithm for Least-Squares Estimation of Non-linear Parameters. *Journal of the Society for Industrial and Applied Mathematics* **11**, 431–441 (1963).
70. Nieto, P. *et al.* Reactive and Nonreactive Scattering of H<sub>2</sub> from a Metal Surface Is Electronically Adiabatic. *Science* **312**, 86–89 (2006).





CHAPTER

3

# Chemically Accurate Simulation of Dissociative Chemisorption of $D_2$ on Pt(111)

This chapter is based on:

Elham Nour Ghassemi, Mark Wijzenbroek, Mark F. Somers and Geert-Jan Kroes. *Chemical Physics Letters* **683**, 329-335, 2017.



## Abstract

Using semi-empirical density functional theory and the quasi-classical trajectory (QCT) method, a specific reaction parameter (SRP) density functional is developed for the dissociation of dihydrogen on Pt(111). The validity of the QCT method was established by showing that QCT calculations on reaction of D<sub>2</sub> with Pt(111) closely reproduce quantum dynamics results for reaction of D<sub>2</sub> in its rovibrational ground state. With the SRP functional, QCT calculations reproduce experimental data on D<sub>2</sub> sticking to Pt(111) at normal and off-normal incidence with chemical accuracy. The dissociation of dihydrogen on Pt(111) is non-activated, exhibiting a minimum barrier height of -8 meV.

## 3.1 Introduction

The availability of accurate barriers for reactions of molecules on metal surfaces is of central importance to chemistry. Catalysis is used to make more than 80% of the chemicals produced worldwide [1], and the accurate calculation of the rate of a heterogeneously catalyzed process requires accurate barriers for the elementary surface reactions involved [2]. This is especially true for the rate controlling steps [3, 4], which often are dissociative chemisorption reactions.

Chemistry would thus benefit enormously from the availability of implementations of first principles methods that would enable the chemically accurate (*i.e.*, to within 1 kcal/mol) calculation of barriers for reactions of molecules with metal surfaces. However, presently such implementations do not yet exist [5]. Also, density functional theory (DFT) using functionals at the gradient approximation (GA) or meta-GA level, which can be used to map out potential energy surfaces (PESs) for molecules interacting with metals, is not yet capable of predicting reaction barriers for gas-phase reactions with chemical accuracy [6]. This accuracy problem of DFT is reflected in the limited accuracy with which absolute rates of heterogeneously catalyzed processes over model catalysts can now be computed with empirically optimized density functionals (*e.g.*, 2 orders of magnitude for ammonia production over Ru catalysts [7]).

Currently, the most viable route to chemically accurate barriers for molecules with metal surfaces uses implementations [8, 9] of specific reaction parameter DFT (SRP–DFT [10]). In this semi-empirical version of DFT, usually a single adjustable parameter in the density functional is fitted to reproduce an experiment that is particularly sensitive to the reaction barrier height for the specific system considered. Next, the quality of the functional is tested by checking that the candidate SRP density functional for the system also reproduces other experiments on the same system, which differ from the experiment the functional was fitted to in a non-trivial way [8, 9]. Using SRP–DFT we have recently started with an effort to develop a database of chemically accurate barriers for molecules reacting with metals, which can be used to benchmark implementations of first principles methods with a claim to chemical accuracy. This database now contains data for  $H_2 + Cu(111)$  [8],  $H_2 + Cu(100)$  [11], and  $CH_4 + Ni(111)$  [9].

The goal of this chapter is to extend the development of SRP density functionals, and the database, with a result for a weakly activated dissociative chemisorption reaction of  $H_2$  with a transition metal surface. For this, we have selected the  $H_2 + Pt(111)$  system. Reasons for selecting this system are that Pt is an important hydrogenation catalyst [12], and that the interaction of  $H_2$  with Pt(111) and other Pt surfaces has been investigated in a number of experimental [13–21] and theoretical [18, 22–29] studies.

Here, we fit an SRP density functional for  $H_2 + Pt(111)$  to dissociative chemisorption probabilities for  $D_2 + Pt(111)$  obtained from molecular beam measurements performed at normal incidence by Luntz *et al.* [15]. The quality of the functional is confirmed by showing that the functional also allows reaction probabilities to be reproduced with chemical accuracy for experiments performed at off-normal incidence [15]. This is a non-trivial result, as the reaction probability for  $D_2 + Pt(111)$  does not obey normal energy scaling [15], *i.e.*, it also depends on the component of the incidence energy parallel to the surface. This dependence arises from a particular type of correlation between the height of the barriers and their distance to the surface [23], the lowest barrier being furthest from the surface [25]. In view of the successes previously achieved for systems exhibiting a van der Waals well affecting the reactivity [9, 30], we adopt a SRP density functional in which the correlation functional [31] allows at least a qualitatively accurate description of the attractive part of the van der Waals interaction. The PBE $\alpha$  exchange functional [32] was adopted, which allows one not only to interpolate between the well-known RPBE [33] and PBE [34] functionals,

but also between PBE and a functional approximating the Wu-Cohen (WC) functional [35], which turned out to be important for the present case.

This chapter is set up as follows. In Section 3.2.1 we describe the dynamical model we used, and in Section 3.2.2 how the PES for  $\text{H}_2 + \text{Pt}(111)$  was obtained. Section 3.2.3 describes the dynamics methods employed, and Section 3.2.4 gives computational details. Section 3.3.1 describes the PES obtained with the SRP density functional. Section 3.3.2 considers the accuracy of the QCT method [36] with the PES employed, and the accuracy that might be achieved by performing dynamics calculations only for the rovibrational ground state of  $\text{D}_2$ , rather than performing a complete molecular beam simulation. In Section 3.3.3 we discuss how a candidate SRP density functional was derived for  $\text{H}_2 + \text{Pt}(111)$  through comparison to normal incidence data. In Section 3.3.4 we confirm the quality of the SRP functional through comparison of calculated sticking probabilities with experiments performed for off-normal incidence. Section 3.4 presents our conclusions and a brief outlook.

## 3.2 Method

### 3.2.1 Dynamical model

The calculations use the so-called Born-Oppenheimer static surface (BOSS) model [8]. As discussed in for instance Ref. [29], this model allows accurate calculations on reactive scattering of  $\text{H}_2$  from metal surfaces. With the model, the calculation of reaction probabilities is split in two parts: First, the PES is calculated (Section 3.2.2), and next the PES is used in dynamics calculations (Section 3.2.3). In the PES and the dynamics calculations, only the six molecular degrees of freedom of the  $\text{H}_2$  molecule are taken into account. The coordinates to describe the motion of the molecule are shown in Figure 3.1 (a).

### 3.2.2 Calculation of the PES

The ground state PES was calculated using DFT. The exchange-correlation (XC) functional used to compute the PES may be written as

$$E_{XC} = E_X^{PBE\alpha} + E_C^{vdW-DF2}, \quad (3.1)$$

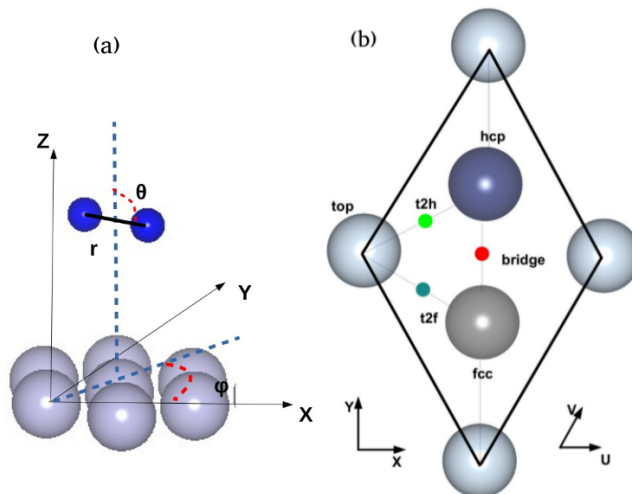


Figure 3.1: (a) The center of mass coordinate system used for the description of the  $H_2$  molecule relative to the static Pt(111) surface. (b) The surface unit cell and the sites considered for the Pt(111) surface, and the relationship with the coordinate system chosen for  $H_2$  relative to Pt(111). The origin  $(X, Y, Z) = (0, 0, 0)$  of the center of mass coordinates is located in the surface plane at a top site. Polar and azimuthal angles  $\theta$  and  $\phi$  are chosen such that  $(\theta = 90^\circ, \phi = 0^\circ)$  corresponds to molecules parallel to the surface along the  $X$  (or equivalently  $U$ ) direction.

*i.e.*, we use the  $PBE_\alpha$  exchange functional [32], with  $\alpha$  being the adjustable parameter, and the van der Waals DF2 functional of Langreth and Lundqvist and co-workers [31]. With the choice  $\alpha = 1$  the  $PBE_\alpha$  functional corresponds [32] to the PBE functional [34], while for  $\alpha \rightarrow \infty$  the  $PBE_\alpha$  functional corresponds [32] to the RPBE functional [33]. For  $\alpha = 0.52$  a functional is obtained that closely resembles [32] the WC functional that performs well in solid state calculations [35]. The use of  $PBE_\alpha$  in semi-empirical applications would seem to be especially advantageous if interpolation is required between PBE and a less repulsive exchange functional; if the goal is to interpolate between PBE and RPBE exchange we suggest using a weighted average of these two [9, 37], as using  $\alpha \rightarrow \infty$  in  $PBE_\alpha$  to

obtain the RPBE limit is a bit awkward for this purpose.

To obtain a global expression for the PES, the accurate corrugation reducing procedure (CRP) [38] was used to interpolate points calculated on a grid with DFT. The procedure used is exactly the same as used in Ref. [29]. The p3m1 plane group symmetry [39] associated with the Pt(111) surface was used.

### 3.2.3 Dynamics calculations of reaction probabilities

Reaction probabilities were calculated for the ( $\nu = 0, j = 0$ ) state of D<sub>2</sub> with the time-dependent wave packet (TDWP) method [40] in an implementation for dihydrogen scattering from surfaces with hexagonal symmetry that is fully described in Ref. [25]. Dissociation probabilities of D<sub>2</sub> colliding with Pt(111) for comparison with molecular beam experiments on the same system [15] were calculated with the QCT method [36] in an implementation described in Ref. [29]. Earlier calculations predicted that even for the lighter H<sub>2</sub> molecule the QCT method yields dissociative chemisorption probabilities for hydrogen dissociation on Pt(111) that are in excellent agreement with quantum dynamics results [24]. For the best comparison with experiments, the calculations include Monte-Carlo averaging over the velocity distributions of the hydrogen beams, and Boltzmann averaging over the rovibrational states of hydrogen, as fully described in Ref. [29]. An important assumption made in our calculations is that the molecular beams used in the experiments of Luntz *et al.* [15] are quite similar to hydrogen beams produced in experiments of Juurlink and co-workers [41], and we used the beam parameters presented in table 3 of Ref. [30] to simulate D<sub>2</sub> beams in our work on the basis of this assumption.

### 3.2.4 Computational details

The DFT calculations were performed with the VASP (version 5.2.12) programme [42–44]. Standard projector augmented wave (PAW) potentials [45] were used. First, the bulk fcc lattice constant was determined in the same manner as used previously for H<sub>2</sub> + Au(111) [46], using a  $20 \times 20 \times 20$   $\Gamma$ -centered grid of k-points. With the optimized SRP density functional (using  $\alpha = 0.57$ , see Section 3.3) a lattice constant of 4.015 Å was obtained, in reasonable agreement with the experimental value of 3.91 Å. Next, a relaxed 5-layer slab was obtained, again in the same manner as

used before for H<sub>2</sub> + Au(111) [46], using a 20 × 20 × 1  $\Gamma$ -centered grid of k-points. After having obtained the relaxed slab, single point calculations were carried out on H<sub>2</sub> + Pt(111), using a 9 × 9 × 1  $\Gamma$ -centered grid of k-points, and a plane wave cut-off of 400 eV, in a super cell approach in which 13 Å of vacuum length was used for the spacing between the Pt(111) slabs and a (2 × 2) surface unit cell. The grid of the points for which the H<sub>2</sub> + Pt(111) calculations were done, and other details of the calculations, were taken the same as in Ref. [29]. The CRP PES was extrapolated to the gas-phase potential of H<sub>2</sub> in the same way as used in Ref. [29].

In the QCT calculation of dissociative chemisorption probabilities for comparison with molecular beam experiments, 10000 trajectories were run for each ( $\nu, j$ ) state with the vibrational quantum number  $\nu \leq 3$  and the rotational quantum number  $j \leq 20$ . For each  $j$ , uniform sampling was performed of the magnetic rotational quantum number  $m_j$ . The centre-of-mass of H<sub>2</sub> was originally placed at  $Z = 9$  Å, with the velocity directed towards the surface and sampled from appropriate velocity distributions for D<sub>2</sub> beams (see table 3 of Ref. [30]). The molecule is considered dissociated once  $r > 2.25$  Å, and considered scattered once  $Z > 9$  Å. Other computational details of the QCT calculations are the same as in Ref. [29]. The surface lattice constant (*i.e.*, the nearest neighbor Pt–Pt distance) used in the QCT calculations (and in the TDWP calculations) was taken as the computed Pt lattice constant divided by  $\sqrt{2}$  (*i.e.*, as 2.84 Å).

In the TDWP calculations on ( $\nu = 0, j = 0$ ) D<sub>2</sub> + Pt(111), two separate wave packet calculations were performed to cover the collision energy range  $E_i = 0.05 - 0.55$  eV. This procedure avoids problems that may arise from the interaction of the low energy components of the wave packet with optical potentials if only one broad wave packet is used to cover a very large translational energy range. The input parameters we used in the TDWP calculations are listed in table 3.1. Convergence tests carried out suggest that, with the use of these parameters, the reaction probabilities computed for ( $\nu = 0, j = 0$ ) D<sub>2</sub> are converged to within better than 2 % of their values (*i.e.*, relative errors  $\leq 2$  %).



Table 3.1: Input parameter for the quantum dynamical calculations of  $D_2$  dissociating on  $Pt(111)$ . All values are given in atomic units. The abbreviation "sp" refers to the specular grid used to bring in the initial wave function.

Parameter	Description	Value	Value
$E_i$	normal incidence range in $Z$	[0.05-0.20]eV	[0.15-0.55]eV
$N_X = N_Y$	no. of grid points in $X$ and $Y$	16	16
$N_Z$	no. of grid points in $Z$	256	128
$N_{Z(sp)}$	no. of specular grid points	256	256
$\Delta Z$	spacing of $Z$ grid points	0.135	0.135
$Z_{min}$	minimum value of $Z$	-1.0	-1.0
$N_r$	no. of grid points in $r$	40	48
$\Delta r$	spacing of $r$ grid points	0.2	0.17
$r_{min}$	minimum value of $r$	0.4	0.4
$j_{max}$	maximum $j$ value in basis set	24	24
$m_{jmax}$	maximum $m_j$ value in basis set	16	16
$\Delta t$	time step	5	5
$T_{tot}$	propagation time	82000	22000
$Z_0$	center of initial wave packet	16.955	16.955
$Z_{inf}$	location of analysis line	12.5	12.5
$Z_{start}^{opt}$	start of optical potential in $Z$	12.5	12.5
$Z_{end}^{opt}$	end of optical potential in $Z$	33.425	16.145
$A_Z$	optical potential strength in $Z$	0.00072	0.0045
$r_{start}^{opt}$	start of optical potential in $r$	4.2	4.2
$r_{end}^{opt}$	end of optical potential in $r$	8.2	8.4
$A_r$	optical potential strength in $r$	0.0096	0.0096
$Z(sp)_{start}^{opt}$	start of optical potential in $Z(sp)$	22.355	22.355
$Z(sp)_{end}^{opt}$	end of optical potential in $Z(sp)$	33.425	33.425
$A_{Z(sp)}$	optical potential strength in $Z(sp)$	0.0035	0.0035

Table 3.2: Barrier heights ( $E_b$ ), the distance to the surface of the barrier ( $Z_b$ ), and the H–H distance at the barrier ( $r_b$ , in Å) are given for four different dissociation geometries defined by the impact site and the angle  $\phi$  (see Figure 3.1), for dissociation of H<sub>2</sub> over Pt(111) with H<sub>2</sub> parallel to the surface ( $\theta = 90^\circ$ ). The results have been obtained with the PBE $\alpha$ -vdW-DF2 functional with  $\alpha = 0.57$ . For the top site, results are given for two barrier geometries. The  $E_b$  values in brackets correspond to the 6D PES computed with the Becke-Perdew functional (see Ref. [25]).

site	$\phi$ (degrees)	$E_b$ (eV)	$r_b$ (Å)	$Z_b$ (Å)
<b>top, early</b>	0	-0.008 (0.06)	0.769	2.202
<b>top, late</b>	0	-0.055	1.096	1.549
<b>bridge</b>	0	0.275 (0.27)	0.837	1.777
<b>hcp</b>	30	0.462 (0.42)	0.874	1.586
<b>t2h</b>	120	0.200 (0.20)	0.837	1.679

### 3.3 Results and discussion

#### 3.3.1 Potential energy surface

Two-dimensional cuts (so-called elbow plots) through the PES used in the dynamics calculations on H<sub>2</sub> + Pt(111) are shown in Figure 3.2, in all cases for H<sub>2</sub> oriented parallel to the surface. With the optimized SRP density functional (using  $\alpha = 0.57$ , see Section 3.3.3), the dissociation is non-activated in the sense that the transition state has an energy that is 8 meV below the gas-phase minimum energy of H<sub>2</sub> (the early barrier for dissociation above the top site, see also table 3.2, which lists the geometries and barrier heights corresponding to the results shown in Figure 3.2). With the functional used, the barrier height ( $E_b$ ) shows a larger energetic corrugation (*i.e.*, a greater variation with impact site) than previously obtained with the Becke-Perdew functional (Ref. [25] and references therein). This is what should be expected for a functional accurately describing the experiments on dissociative chemisorption of D<sub>2</sub> on Pt(111) [15], as the previously computed sticking probability vs. incident translational energy curve was too steep [18, 24]. Note that previous experience with H<sub>2</sub>-metal systems suggests that the use of Lundqvist-Langreth van der Waals cor-

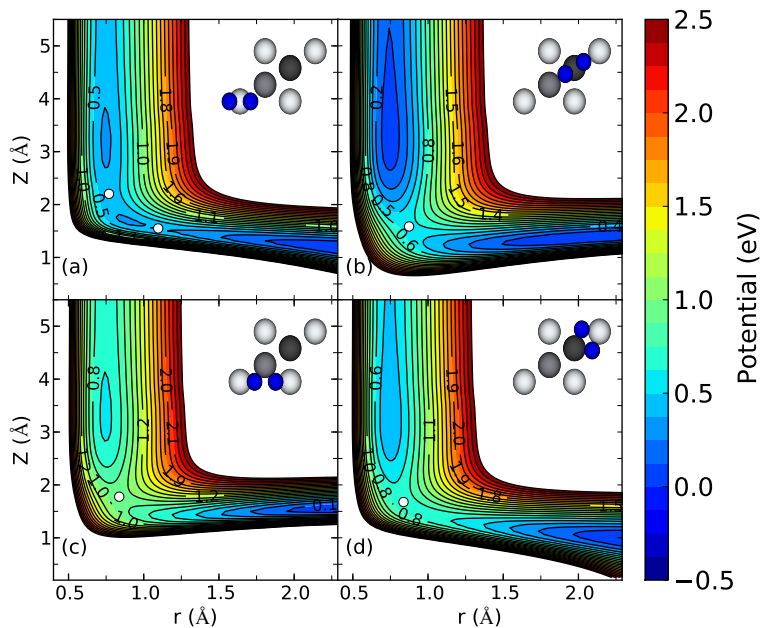


Figure 3.2: Elbow plots (*i.e.*  $V(Z, r)$ ) resulting from the  $H_2 + Pt(111)$  PES computed with the  $PBE_{\alpha}\text{-vdW-DF2}$  functional with  $\alpha = 0.57$ , and interpolated with the CRP method for four high symmetry configurations with the molecular axis parallel to the surface ( $\theta = 90^\circ$ ), for (a) the top site and  $\phi = 0^\circ$ , (b) the hcp site and  $\phi = 30^\circ$ , (c) the bridge site and  $\phi = 0^\circ$  (bridge-to-top), and (d) the t2h site and  $\phi = 120^\circ$  (see also Figure 3.1). Barrier geometries are indicated with white circles, and the corresponding barrier heights are given in table 3.2.

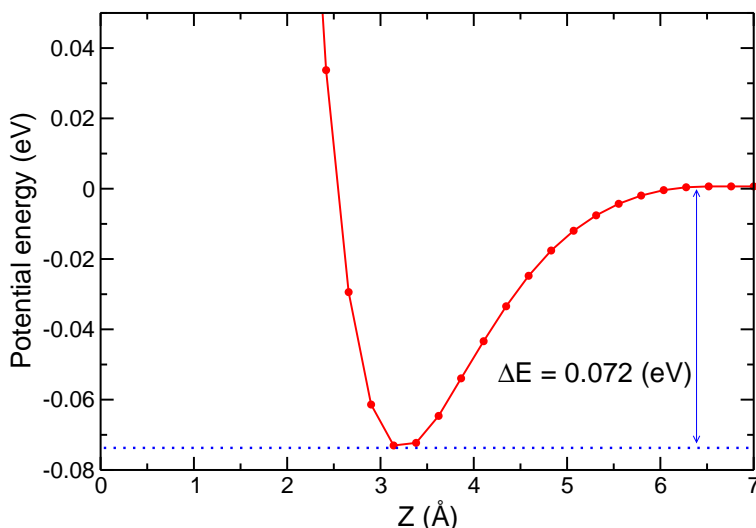


Figure 3.3: The potential for H<sub>2</sub> + Pt(111) is shown as a function of the molecule-surface distance, for  $r = r_e$  after averaging over the four remaining molecular degrees of freedom. The results are for the PES computed with the PBE $\alpha$ -vdW-DF2 functional with  $\alpha = 0.57$ .

relation functionals, as employed here, yield PESs with larger energetic corrugation than ordinary generalized gradient approximation (GGA) correlation functionals [29, 30].

Figure 3.3 shows a plot of the potential at  $r = r_e$ , after averaging over  $X, Y, \theta$ , and  $\phi$ , with  $r_e$  being the minimum H–H distance of gas-phase H<sub>2</sub>. This averaged potential curve shows a van der Waals minimum well depth of 72 meV, in excellent agreement with the range of values found in experiments (*i.e.*, 55 meV [14, 18], and 76 meV [47]). Getting the van der Waals attractive interaction right may be important to obtaining a correct value for the energy of the "early" transition state (which occurs at  $Z = 2.2$  Å, see table 3.2) and is probably also important to the calculation of probabilities for diffractive scattering, for which detailed experimental results are available [18] (see also Chapter 6).

### 3.3.2 Quantum vs. quasi-classical dynamics, and the importance of simulating the molecular beam

Figure 3.4 (a) shows a comparison of reaction probabilities computed for  $D_2$  in its initial ( $\nu = 0, j = 0$ ) state for specific incidence energies with quantum dynamics and with quasi-classical dynamics. The calculations used the optimized SRP density functional (*i.e.*, with  $\alpha = 0.57$ , see Section 3.3.3). Even in the absence of averaging over initial rovibrational states and over the distribution of energies, as would be appropriate for comparisons with molecular beam experiments, the quantum and QCT results are in excellent agreement with one another. In the following, we will therefore use the QCT method to compute sticking probabilities for comparison to the molecular beam experiments of Luntz *et al.* [15].

Figure 3.4 (b) shows a comparison of reaction probabilities computed with the QCT method for  $D_2$  in its initial ( $\nu = 0, j = 0$ ) state for specific incidence energies with QCT results obtained with full averaging over the rovibrational state populations and velocity distributions that are typical for molecular beam experiments using pure  $D_2$  beams [30, 41]. The comparison of Figure 3.4 (b) suggests that it should not really be necessary to take the effect of the velocity distribution and the rovibrational state distribution into account, in broad agreement with an earlier theoretical study of  $H_2 + Pt(111)$  [27]. This is in sharp contrast with findings for the highly activated  $H_2 + Cu(111)$  reaction [8, 48]; for this system, taking into account the velocity distribution is necessary for accurate results, because the reactivity may come entirely from incidence energies above the average incidence energy of the beam, and above the high reaction threshold. Even though taking into account the beam conditions should be much less important for  $D_2 + Pt(111)$ , in the following we will always represent computational results with full averaging over the incidence energy and rovibrational state population of the  $D_2$  beams, to obtain the best possible comparison with the molecular beam experiments of Luntz *et al.* [15].

### 3.3.3 Fit of the SRP density functional to molecular beam data for normal incidence

Before the SRP functional for  $H_2 + Pt(111)$  could be fit, a choice had to be made concerning which experimental dataset for normal incidence theoretical results should be compared with. In the literature at the time

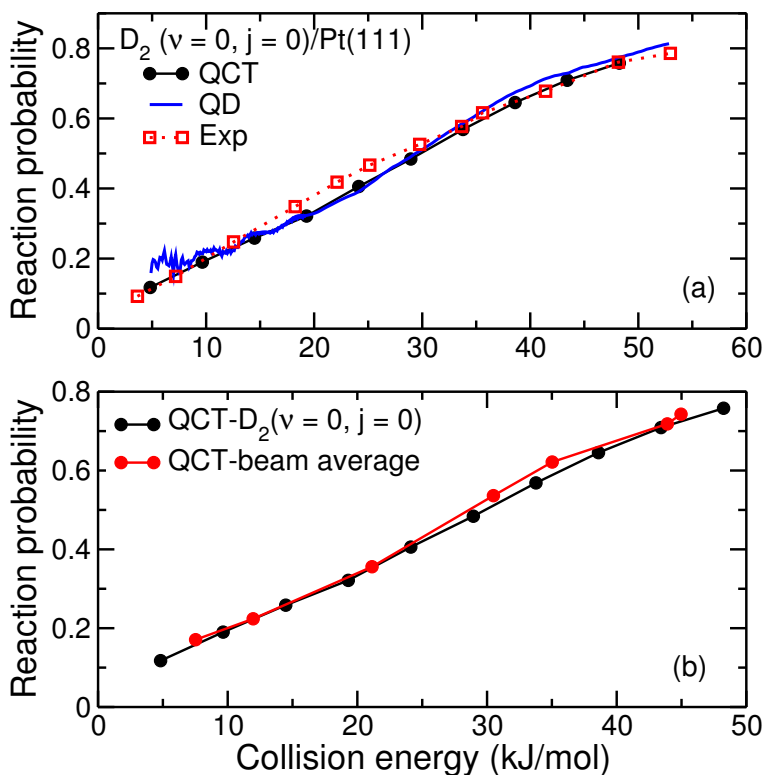


Figure 3.4: (a) Dissociation probabilities computed for  $(\nu = 0, j = 0)$   $D_2 + Pt(111)$  with quantum dynamics and with the QCT method are shown as a function of the collision energy, for normal incidence. The results are compared with sticking probabilities measured for  $D_2 + Pt(111)$  [15] and shown as a function of average incidence energy. (b) Dissociation probabilities computed for  $(\nu = 0, j = 0)$   $D_2 + Pt(111)$  with the QCT method for specific collision energies are compared with sticking probabilities computed for  $D_2 + Pt(111)$  with full averaging over the rovibrational state populations and velocity distributions of typical molecular beams of pure  $D_2$ .

our research was performed, two sets of molecular beam data were available for dihydrogen normally incident on Pt(111), *i.e.*, those of Luntz *et al.* [15] and those of Samson *et al.* [16]. The work of Luntz *et al.* focused on the dihydrogen + Pt(111) system, looking at the effects of the angle of incidence  $\theta_i$ , surface temperature  $T_s$ , isotopic mass, and nozzle temperature  $T_n$  in great detail, and producing data for  $D_2 + Pt(111)$  at  $T_s = 300$  K for a large range of incidence energies  $E_i$  by also using seeding of  $D_2$  in  $H_2$  to achieve high  $E_i$ . In contrast, Samson *et al.* only published data for  $D_2 + Pt(111)$  for normal incidence, for one value of  $T_s$  (150 K), for the more limited range of  $E_i$  available with pure  $D_2$  beams only, in a paper focused on how alloying varying amounts of Sn into the surface affects the sticking. Furthermore, Luntz *et al.* explicitly stated that their "incidence energies" (labeled  $E_i$  in their work) were energy averaged over the TOF<sup>1</sup> distribution of the beams they used, whereas Samson *et al.* simply assumed that the average incidence energy (which we will label as  $\langle E_i \rangle$ ) is given by  $\langle E_i \rangle = 2.75 k_B T_n$ . For these reasons, we have chosen to fit our SRP functional to the normal incidence data of Luntz *et al.*, assuming that these would represent the most accurate dataset.

The assumption that the dataset of Luntz *et al.* is best for benchmarking purposes is important. Although Samson *et al.* stated that their  $D_2 + Pt(111)$  data closely reproduce the prior results of Luntz *et al.*, plotting the datasets together reveals that the data of Samson *et al.* are displaced along the energy axis by 1 to 1.5 kcal/mol relative to the Luntz *et al.* data, towards higher energies (not shown in this chapter). The data of Samson *et al.* therefore suggest a somewhat less reactive surface. If our assumption is incorrect, or if our interpretation of the meaning of  $\langle E_i \rangle$  in the experiments of Luntz *et al.* would be incorrect (we obtain the average by averaging incidence energy over the flux weighted velocity distribution given by equation 3 in the Supporting Information to Ref. [8]) this should be reflected in the accuracy of the extracted SRP functional and minimum barrier height. Problems with the interpretation of results of molecular beam experiments due to lacking or incomplete specification of the velocity distributions have hampered efforts to obtain accurate SRP functionals and benchmark data before [49]. However, the problem noted here for  $H_2 + Pt(111)$  is not as severe as for  $H_2 + Pd(111)$  [49]. See also Chapter 6 for a detailed discussion of the experiments of the two different groups, and the

---

<sup>1</sup>time-of-flight

quality of the SRP functional in describing these experiments.

To obtain an SRP functional, first tests were performed combining the PBE functional for exchange [34] with the Lundqvist-Langreth functional of Dion *et al.* (vdW-DF1) [50]. With this functional, the van der Waals well was too deep compared with experimental results, and the computed reaction probabilities were shifted to too high energies and did not exhibit chemical accuracy (results not shown). For these reasons, we switched to the improved Lundqvist-Langreth functional of Lee *et al.* (vdW-DF2) [31], and to the PBE $\alpha$  functional [32], adjusting  $\alpha$  by trial and error to obtain agreement with the sticking experiments of Luntz *et al.* [15]. By choosing  $\alpha = 0.57$ , agreement with the experiments for normal incidence could be obtained to within chemical accuracy, by which we mean that the computed sticking probabilities are displaced along the energy axis from the interpolated experimental curve by no more than 1 kcal/mol (see Figure 3.5). The resulting SRP–DFT PES shows a minimum barrier height of -8 meV ( $\approx 1$  kJ/mol), suggesting the reaction to be non-activated if the molecule hits the surface at the right site (the top site, see table 3.2). The "activated appearance" of the reaction probability curve comes from the molecule also hitting the surface at other impact sites and orientations for which higher barriers are encountered (see for instance table 3.2 and Figure 3.2), as already suggested by Luntz *et al.* at the time of their work [15].

### 3.3.4 Confirming the quality of the SRP density functional by comparison to molecular beam data for off-normal incidence

Strictly speaking, the functional obtained in Section 3.3.4 is, at this stage, only a "candidate SRP functional": to become an SRP functional, dynamics calculations with the functional should also be able to reproduce other experiments on the same system, which differ from the experiments the functional was fit to in a non-trivial way [8, 9]. For this, we chose to use the datasets obtained by Luntz *et al.* for off-normal incidence [15]. For H<sub>2</sub> + Pt(111) more recent, detailed data on molecular diffraction are also available [18], but recent work on H<sub>2</sub> + Ru(0001) suggests that accurately reproducing diffraction data is fraught with difficulties [30] (see also Chapter 6). This is most likely related to the need to extrapolate the experimental data to a low temperature or even static surface regime using Debye-Waller attenuation, or to simulate the effect of surface temperature



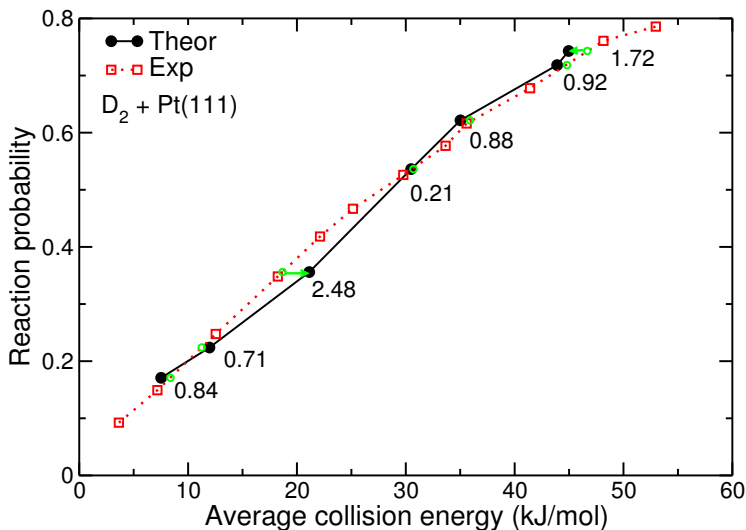


Figure 3.5: Reaction probabilities computed for  $D_2 + Pt(111)$  with the SRP density functional (see text) are shown as a function of  $\langle E_i \rangle$ , comparing to the molecular beam results of Luntz *et al.* [15]. The results are for normal incidence. The arrows and accompanying numbers show the collision energy spacing (in kJ/mol, 1 kcal/mol  $\approx$  4.2 kJ/mol) between the computed sticking probabilities and the interpolated experimental sticking probability data (green circles).

in accurate quantum dynamics calculations [30].

Reaction probabilities computed for  $\theta_i = 30^\circ$  and  $45^\circ$  agree with the experimental values to within chemical accuracy (Figure 3.6). Larger displacements than 1 kcal/mol of the computed reaction probabilities from the interpolated experimental sticking curve are observed for  $\theta_i = 60^\circ$ , but we argue that for this large an incidence angle our operational definition of chemical accuracy may not be appropriate. The slope of the measured sticking curve as a function of total incidence energy is small, so that a small error in the measured reaction probability could have a large effect on the energy displacement of the computed reaction probability to the interpolated experimental curve. In this context, we note that error bars on the measured sticking probabilities were lacking [15]. In view of the positive results for  $\theta_i = 30^\circ$  and  $45^\circ$ , we argue that our PBE $\alpha$ -vdW-DF2 functional

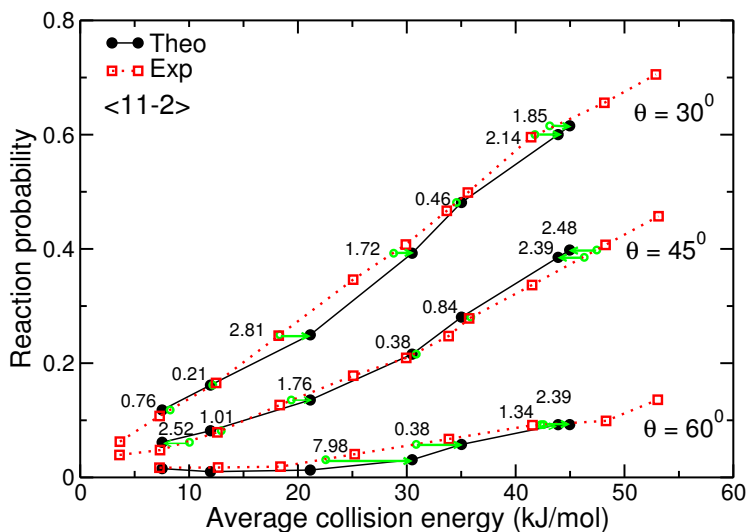


Figure 3.6: Reaction probabilities computed for  $D_2 + Pt(111)$  with the SRP density functional (see text) are shown as a function of , comparing to the molecular beam results of Luntz *et al.* [15]. The results are for off-normal incidence at the indicated incidence angles  $\theta_i$  of  $30^\circ$ ,  $45^\circ$  and  $60^\circ$ , along the  $\langle 11-2 \rangle$  incidence direction. The arrows and accompanying numbers show the collision energy spacing (in kJ/mol,  $1 \text{ kcal/mol} \approx 4.2 \text{ kJ/mol}$ ) between the computed sticking probabilities and the interpolated experimental sticking probability data (green circles).

is an SRP functional for  $H_2 + Pt(111)$ , and that the minimum barrier data (and the barriers obtained for other impact sites shown in table 3.2) can be used for benchmark purposes, *i.e.*, they can be included in an emerging database with chemically accurate barriers for molecules interacting with transition metals [5].

Luntz *et al.* did not specify the incidence plane used in their experiments on off-normal incidence [15]. The computed data shown in Figure 3.6 are for incidence along the  $\langle 11 - 2 \rangle$  direction, which corresponds to the vector bisecting the  $U$  and  $V$  vectors in Figure 3.1. However, for incidence along the  $\langle 10 - 1 \rangle$  direction (corresponding to the direction of  $U$  in Figure 3.1), the computed sticking probabilities closely reproduce the values computed for the  $\langle 11 - 2 \rangle$  direction, and they likewise reproduce the experimental

data, for  $\theta_i = 30^\circ$  and  $45^\circ$  (not shown). For  $\theta_i = 60^\circ$  and incidence along the  $\langle 10 - 1 \rangle$  direction, the computed sticking probabilities do not quite reproduce the values computed for the  $\langle 11 - 2 \rangle$  direction (in agreement with earlier theoretical work on  $\text{H}_2 + \text{Pt}(111)$  [25]), but the result that for this incidence direction and large angle the computed data do not reproduce the experiments with chemical accuracy is also obtained for the  $\langle 10 - 1 \rangle$  direction.

### 3.4 Conclusions and outlook

We have obtained an SRP density functional for  $\text{H}_2 + \text{Pt}(111)$  by adjusting the  $\alpha$  parameter in the  $\text{PBE}\alpha\text{-vdW-DF2}$  functional until reaction probabilities computed with the QCT method reproduced sticking probabilities measured for normally incident  $\text{D}_2$  with chemical accuracy. In the QCT calculations, the rovibrational state populations and the velocity distributions of the incident beams were taken into account. Also, the appropriateness of the use of the QCT method for the purpose of accurately calculating reaction probabilities for  $\text{D}_2 + \text{Pt}(111)$  was established by a comparison with quantum dynamics calculations for the initial ( $\nu = 0$ ,  $j = 0$ ) state of  $\text{D}_2$ . The quality of the SRP functional was confirmed by showing that QCT calculations using the functional also reproduced data for off-normal incidence for  $\theta_i = 30^\circ$  and  $45^\circ$ , for which the computed reaction probabilities show no dependence on the plane of incidence. The minimum barrier height obtained for the reaction is -8 meV, in agreement with the experimental observation of no, or only a small energetic threshold to reaction [15]. This value can be entered into a small [5], but growing [9] database with barriers of reactions of molecules with metal surfaces, for which chemical accuracy is claimed.

Our conclusion depends on the assumption that the data of Luntz *et al.* are accurate and the validity of our interpretation of the average incidence energy in their experiments [15] (see Section 3.3.3). To confirm this, accurate new experiments on reaction of  $\text{H}_2$  or  $\text{D}_2$  with  $\text{Pt}(111)$  for varying incidence angles and well-defined molecular beam velocity distributions and incidence plane would be welcomed. Experiments that were done [51] after the research presented in this chapter only suggested small differences between reaction probabilities measured for the  $\langle 10 - 1 \rangle$  and  $\langle 11 - 1 \rangle$  incidence directions and  $\theta_i = 50^\circ$ .

Future computational work could address the question of how the dynamical model may have to be extended to accurately reproduce the detailed molecular diffraction data available for H<sub>2</sub> + Pt(111) [18] (see also Chapter 6). Once such a model is available it could be used in further tests of the SRP density functional for H<sub>2</sub> + Pt(111) by comparison to these data, and in tests of the candidate SRP density functional for H<sub>2</sub> + Ru(0001), for which detailed diffraction data are also available [30]. We also suggest that the SRP functional be used to model data on the reaction of H<sub>2</sub> with stepped Pt surfaces [20, 21], to check whether SRP functionals developed for a low index transition metal surface exhibit transferability to systems in which the same molecule interacts with a vicinal or stepped surface of that metal. This question will be considered for Pt(211) in Chapter 5.

## References

1. Noyori, R. Synthesizing Our Future. *Nature Chemistry*, 5–6 (2009).
2. Xu, Y. *et al.* In Silico Search for Novel Methane Steam Reforming Catalysts. *New Journal of Physics* **15**, 125021 (2013).
3. Wolcott, C. A., Medford, A. J., Studt, F. & Campbell, C. T. Degree of Rate Control Approach to Computational Catalyst Screening. *Journal of Catalysis* **330**, 197–207 (2015).
4. Sabbe, M. K., Reyniers, M.-F. & Reuter, K. First-Principles Kinetic Modeling in Heterogeneous Catalysis: An Industrial Perspective on Best-Practice, Gaps and Needs. *Catalysis Science & Technology* **2**, 2010–2024 (2012).
5. Kroes, G. J. Toward a Database of Chemically Accurate Barrier Heights for Reactions of Molecules with Metal Surfaces. *Journal of Physical Chemistry Letters* **6**, 4106–4114 (2015).
6. Peverati, R. & Truhlar, D. G. Quest for a Universal Density Functional: the Accuracy of Density Functionals Across a Broad Spectrum of Databases in Chemistry and Physics. *Philosophical Transactions of the Royal Society A: Mathematical, Physical and Engineering Sciences* **372**, 20120476 (2014).
7. Medford, A. J. *et al.* Assessing the Reliability of Calculated Catalytic Ammonia Synthesis Rates. *Science* **345**, 197–200 (2014).
8. Díaz, C. *et al.* Chemically Accurate Simulation of a Prototypical Surface Reaction: H<sub>2</sub> Dissociation on Cu(111). *Science* **326**, 832–834 (2009).
9. Nattino, F. *et al.* Chemically Accurate Simulation of a Polyatomic Molecule-Metal Surface Reaction. *Journal of Physical Chemistry Letters* **7**, 2402–2406 (2016).
10. Chuang, Y.-Y., Radhakrishnan, M. L., Fast, P. L., Cramer, C. J. & Truhlar, D. G. Direct Dynamics for Free Radical Kinetics in Solution: Solvent Effect on the Rate Constant for the Reaction of Methanol with Atomic Hydrogen. *Journal of Physical Chemistry A* **103**, 4893–4909 (1999).

11. Sementa, L. *et al.* Reactive Scattering of H<sub>2</sub> from Cu(100): Comparison of Dynamics Calculations Based on the Specific Reaction Parameter Approach to Density Functional Theory with Experiment. *Journal of Chemical Physics* **138** (2013).
12. D. Navalikhina, M. & V. Krylov, O. Heterogeneous Catalysts of Hydrogenation. *Russian Chemical Review* **67**, 587–616 (1998).
13. Cowin, J. P., Yu, C., Sibener, S. J. & Hurst, J. E. Bound Level Resonances in Rotationally Inelastic HD/Pt (111) Surface Scattering. *Journal of Chemical Physics* **75**, 1033–1034 (1981).
14. Cowin, J. P., Yu, C., Sibener, S. J. & Wharton, L. HD Scattering from Pt(111): Rotational Excitation Probabilities. *Journal of Chemical Physics* **79**, 3537–3549 (1983).
15. Luntz, A. C., Brown, J. K. & Williams, M. D. Molecular Beam Studies of H<sub>2</sub> and D<sub>2</sub> Dissociative Chemisorption on Pt(111). *Journal of Chemical Physics* **93**, 5240–5246 (1990).
16. Samson, P., Nesbitt, A., Koel, B. E. & Hodgson, A. Deuterium Dissociation on Ordered Sn/Pt(111) Surface Alloys. *Journal of Chemical Physics* **109**, 3255–3264 (1998).
17. Gee, A. T., Hayden, B. E., Mormiche, C. & Nunney, T. S. The Role of Steps in the Dynamics of Hydrogen Dissociation on Pt(533). *Journal of Chemical Physics* **112**, 7660–7668 (2000).
18. Nieto, P. *et al.* Reactive and Nonreactive Scattering of H<sub>2</sub> from a Metal Surface Is Electronically Adiabatic. *Science* **312**, 86–89 (2006).
19. Poelsema, B., Lenz, K. & Comsa, G. The Dissociative Adsorption of Hydrogen on Pt(111): Actuation and Acceleration by Atomic Defects. *Journal of Chemical Physics* **134** (2011).
20. Groot, I. M. N., Kleyn, A. W. & Juurlink, L. B. F. The Energy Dependence of the Ratio of Step and Terrace Reactivity for H<sub>2</sub> Dissociation on Stepped Platinum. *Angewandte Chemie International Edition* **50**, 5174–5177 (2011).
21. Groot, I. M. N., Kleyn, A. W. & Juurlink, L. B. F. Separating Catalytic Activity at Edges and Terraces on Platinum: Hydrogen Dissociation. *Journal of Physical Chemistry C* **117**, 9266–9274 (2013).

22. Halstead, D. & Holloway, S. Quantum-Mechanical Scattering of H<sub>2</sub> from Metal Surfaces: Diffraction and Dissociative Adsorption. *Journal of Chemical Physics* **88**, 7197–7208 (1988).
23. Darling, G. R. & Holloway, S. The Role of Parallel Momentum in the Dissociative Adsorption of H<sub>2</sub> at Highly Corrugated Surfaces. *Surface Science* **304**, L461–L467 (1994).
24. Pijper, E. *et al.* Six-Dimensional Quantum Dynamics of Scattering of (v=0, j=0) H<sub>2</sub> from Pt(1 1 1): Comparison to Experiment and to Classical Dynamics Results. *Chemical Physics Letters* **347**, 277–284 (2001).
25. Pijper, E., Kroes, G. J., Olsen, R. A. & Baerends, E. J. Reactive and Diffractive Scattering of H<sub>2</sub> from Pt(111) Studied Using a Six-Dimensional Wave Packet Method. *Journal of Chemical Physics* **117**, 5885–5898 (2002).
26. Pijper, E., Kroes, G. J., Olsen, R. A. & Baerends, E. J. Dissociative and Diffractive Scattering of H<sub>2</sub> from Pt(111): A Four-Dimensional Quantum Dynamics Study. *Journal of Chemical Physics* **116**, 9435–9448 (2002).
27. Vincent, J., Olsen, R., Kroes, G. J. & Baerends, E. Dissociative Chemisorption of H<sub>2</sub> on Pt(1 1 1): Isotope Effect and Effects of the Rotational Distribution and Energy Dispersion. *Surface Science* **573**, 433–445 (2004).
28. Ludwig, J. & Vlachos, D. G. *Ab Initio* Molecular Dynamics of Hydrogen Dissociation on Metal Surfaces Using Neural Networks and Novelty Sampling. *Journal of Chemical Physics* **127** (2007).
29. Wijzenbroek, M., Klein, D. M., Smits, B., Somers, M. F. & Kroes, G. J. Performance of a Non-Local van der Waals Density Functional on the Dissociation of H<sub>2</sub> on Metal Surfaces. *Journal of Physical Chemistry A* **119**, 12146–12158 (2015).
30. Wijzenbroek, M. & Kroes, G. J. The Effect of the Exchange-Correlation Functional on H<sub>2</sub> Dissociation on Ru(0001). *Journal of Chemical Physics* **140** (2014).
31. Lee, K., Murray, É. D., Kong, L., Lundqvist, B. I. & Langreth, D. C. Higher-Accuracy van der Waals Density Functional. *Physical Review B* **82**, 081101 (2010).

32. Madsen, G. K. H. Functional Form of the Generalized Gradient Approximation for Exchange: The PBE $\alpha$  Functional. *Physical Review B* **75**, 195108 (2007).
33. Hammer, B., Hansen, L. B. & Nørskov, J. K. Improved Adsorption Energetics within Density-Functional Theory Using Revised Perdew-Burke-Ernzerhof Functionals. *Physical Review B* **59**, 7413–7421 (1999).
34. Perdew, J. P., Burke, K. & Ernzerhof, M. Generalized Gradient Approximation Made Simple. *Physical Review Letters* **77**, 3865–3868 (1996).
35. Wu, Z. & Cohen, R. E. More Accurate Generalized Gradient Approximation for Solids. *Physical Review B* **73**, 235116 (2006).
36. Karplus, M., Porter, R. N. & Sharma, R. D. Exchange Reactions with Activation Energy. I. Simple Barrier Potential for (H, H<sub>2</sub>). *Journal of Chemical Physics* **43**, 3259–3287 (1965).
37. Nattino, F., Díaz, C., Jackson, B. & Kroes, G. J. Effect of Surface Motion on the Rotational Quadrupole Alignment Parameter of D<sub>2</sub> Reacting on Cu(111). *Physical Review Letters* **108**, 236104 (2012).
38. Busnengo, H. F., Salin, A. & Dong, W. Representation of the 6D Potential Energy Surface for a Diatomic Molecule Near a Solid Surface. *Journal of Chemical Physics* **112**, 7641–7651 (2000).
39. Frankcombe, T. J., Collins, M. A. & Zhang, D. H. Modified Shepard Interpolation of Gas-Surface Potential Energy Surfaces with Strict Plane Group Symmetry and Translational Periodicity. *Journal of Chemical Physics* **137** (2012).
40. Kosloff, R. Time-Dependent Quantum-Mechanical Methods for Molecular Dynamics. *Journal of Physical Chemistry* **92**, 2087–2100 (1988).
41. Groot, I. M. N., Ueta, H., van der Niet, M. J. T. C., Kleyn, A. W. & Juurlink, L. B. F. Supersonic Molecular Beam Studies of Dissociative Adsorption of H<sub>2</sub> on Ru(0001). *Journal of Chemical Physics* **127**, 244701 (2007).
42. Kresse, G. & Furthmüller, J. Efficient Iterative Schemes for *Ab Initio* Total-Energy Calculations Using a Plane-Wave Basis Set. *Physical Review B* **54**, 11169–11186 (1996).
43. Kresse, G. & Furthmüller, J. Efficiency of *Ab-Initio* Total Energy Calculations for Metals and Semiconductors Using a Plane-Wave Basis Set. *Computational Materials Science* **6**, 15–50 (1996).



44. Kresse, G. & Hafner, J. *Ab Initio* Molecular Dynamics for Liquid Metals. *Physical Review B* **47**, 558–561 (1993).
45. Kresse, G. & Joubert, D. From Ultrasoft Pseudopotentials to the Projector Augmented-Wave Method. *Physical Review B* **59**, 1758–1775 (1999).
46. Wijzenbroek, M., Helstone, D., Meyer, J. & Kroes, G. J. Dynamics of H<sub>2</sub> Dissociation on the Close-Packed (111) Surface of the Noblest Metal: H<sub>2</sub> + Au(111). *Journal of Chemical Physics* **145**, 144701 (2016).
47. Poelsema, B., Lenz, K. & Comsa, G. The Dissociative Adsorption of Hydrogen on Defect-'Free' Pt(111). *Journal of Physics: Condensed Matter* **22**, 304006 (2010).
48. Kroes, G. J. & Díaz, C. Quantum and Classical Dynamics of Reactive Scattering of H<sub>2</sub> from Metal Surfaces. *Chemical Society Reviews* **45**, 3658–3700 (2016).
49. Boereboom, J. M., Wijzenbroek, M., Somers, M. F. & Kroes, G. J. Towards a Specific Reaction Parameter Density Functional for Reactive Scattering of H<sub>2</sub> from Pd(111). *Journal of Chemical Physics* **139** (2013).
50. Dion, M., Rydberg, H., Schröder, E., Langreth, D. C. & Lundqvist, B. I. van der Waals Density Functional for General Geometries. *Physical Review Letters* **92**, 246401 (2004).
51. Cao, K., van Lent, R., Kleyn, A. & Juurlink, L. A Molecular Beam Study of D<sub>2</sub> Dissociation on Pt(111): Testing SRP-DFT Calculations. *Chemical Physics Letters* **706**, 680–683 (2018).



**Test of the Transferability of  
the Specific Reaction  
Parameter Functional for  
 $\text{H}_2 + \text{Cu}(111)$  to  
 $\text{D}_2 + \text{Ag}(111)$**

This chapter is based on:

Elham Nour Ghassemi, Mark Somers, and Geert-Jan Kroes. *The Journal of Physical Chemistry C* **122**(40), 22939-22952, 2018.



## Abstract

The accurate description of the dissociative chemisorption of a molecule on a metal surface requires a chemically accurate description of the molecule-surface interaction. Previously, it was shown that the specific reaction parameter approach to density functional theory (SRP-DFT) enables accurate descriptions of the reaction of dihydrogen with metal surfaces in, for instance  $\text{H}_2 + \text{Pt}(111)$ ,  $\text{H}_2 + \text{Cu}(111)$  and  $\text{H}_2 + \text{Cu}(100)$ . SRP-DFT likewise allowed a chemically accurate description of dissociation of methane on  $\text{Ni}(111)$  and  $\text{Pt}(111)$ , and the SRP functional for  $\text{CH}_4 + \text{Ni}(111)$  was transferable to  $\text{CH}_4 + \text{Pt}(111)$ , where Ni and Pt belong to the same group. Here we investigate whether the SRP density functional derived for  $\text{H}_2 + \text{Cu}(111)$  also gives chemically accurate results for  $\text{H}_2 + \text{Ag}(111)$ , where Ag belongs to the same group as Cu. To do this, we have performed quasi-classical trajectory calculations using the six-dimensional PES of  $\text{H}_2 + \text{Ag}(111)$  within the Born-Oppenheimer static surface approximation. The computed reaction probabilities are compared with both state-resolved associative desorption and molecular beam sticking experiments. Our results do not yet show transferability, as the computed sticking probabilities and initial-state selected reaction probabilities are shifted relative to experiment to higher energies by about 2.0–2.3 kcal/mol. The lack of transferability may be due to the different character of the SRP functionals for  $\text{H}_2 + \text{Cu}$  and  $\text{CH}_4 +$  group 10 metals, the latter containing a van der Waals correlation functional and the former not.

## 4.1 Introduction

The benchmark system of  $\text{H}_2$  interacting with a metal surface is very important to understand and accurately model elementary reactions on metal surfaces. This is relevant to heterogeneous catalysis, which is employed in the majority of reactive processes in the chemical industry [1]. Breaking heterogeneously catalyzed processes into elementary steps is one way to describe them. Dissociative chemisorption, in which a bond in the molecule impacting on a surface is broken and two new chemical bonds are formed by

the fragments to the surface, is an elementary and often the rate-limiting step [2, 3], for example in ammonia synthesis [4].

It is essential to have an accurate potential energy surface (PES) and obtain an accurate barrier for the reaction to accurately perform calculations on dissociation of a molecule on a surface. Although there is no direct way to measure barrier heights experimentally, a close comparison of molecular beam experiments and dynamics calculations reproducing the reaction probabilities may enable this determination to within chemical accuracy (1 kcal/mol) [5, 6].

The most efficient electronic structure method to compute the interaction of a molecule with a metal surface is density functional theory (DFT). However, there are limitations to the accuracy of the exchange-correlation (XC) functional, where the XC functional is usually taken at the generalized gradient approximation (GGA) [6] level. For barriers of gas phase reactions, it has been shown that mean absolute errors of GGA functionals are greater than 3 kcal/mol [7]. To address the problem of the accuracy with DFT, an implementation of the specific reaction parameter approach to DFT (SRP–DFT) was proposed [5]. Fitting of a single adjustable parameter of this semi-empirical version of the XC functional to a set of experimental data for a molecule interacting with a surface may allow the production of an accurate PES [6]. The quality of the derived XC functional is tested by checking that this XC-functional is also able to reproduce other experiments on the same system, to which it was not fitted [5, 6]. The SRP–DFT methodology has provided the possibility to develop a database of chemically accurate barriers for molecules reacting on metal surfaces. Results are now available for  $H_2 + Cu(111)$  [5, 6],  $H_2 + Cu(100)$  [6, 8],  $H_2 + Pt(111)$  [9],  $CH_4 + Ni(111)$  [10],  $CH_4 + Pt(111)$  and  $CH_4 + Pt(211)$  [11]. However, this effort is at an early stage and demands more efforts to extend the database.

In a previous study, it was shown that the SRP–DFT XC functional can be transferable among systems in which one molecule interacts with metals from the same group in the periodic table. Nattino *et al.* [10] demonstrated the accurate description of dissociation of methane on Ni(111) with an SRP functional. Migliorini *et al.* [11] showed the transferability of the derived SRP functional for this system to the methane + Pt(111) system.

The goal of this chapter is to check the transferability of the SRP48 functional [12] for  $H_2 + Cu(111)$  to a system in which  $H_2$  interacts with a (111) surface of another group 11 element. The SRP48 functional was selected to investigate whether it would allow a chemically accurate de-

description of the dissociative adsorption of  $D_2$  on the (111) surface of silver, as it yields a chemically accurate description of a range of experiments on  $H_2/D_2 + Cu(111)$  [12]. A previous study using the SRP48 functional computed initial-state selected reaction probabilities for  $H_2 + Au(111)$  using quasi-classical dynamics [13]. Subsequent associative desorption experiments measured initial-state selected reaction probabilities that were shifted to substantially lower translational energies [14]. These results suggest that the SRP48 functional is not transferable from  $H_2 + Cu(111)$  to  $H_2 + Au(111)$ . The experimentalists also suggested that the dissociation of  $H_2$  on  $Au(111)$  should be affected by electron-hole pair excitation. However, molecular beam sticking experiments are not yet available for the  $H_2 + Au(111)$  system.

Here quasi-classical trajectory (QCT) [15] calculations are performed using a  $H_2 + Ag(111)$  PES based on DFT calculations with the SRP48 functional. Comparison is made with available molecular beam experiments and associative desorption experiments to evaluate the accuracy of the SRP DF extracted for  $H_2 + Cu(111)$  for the  $H_2 + Ag(111)$  system. Our calculations used the Born-Oppenheimer static surface (BOSS) model, in which non-adiabatic effects, *i.e.*, electron-hole pair excitations, and phonon inelastic scattering were neglected. The recent theoretical study of the  $H_2-Ag(111)$  system by Maurer *et al.* [16] has provided evidence for a strong mode dependence of nonadiabatic energy loss, with loss especially occurring along the  $H_2$  bond stretch coordinate. However, work performed after the research in this chapter was published suggests that the sticking curve should shift upward in energy by less than 0.5 kcal/mol due to electron-hole pair excitation [17]. Moreover, for a variety of chemical reactions on surfaces, chemicurrents have been observed due to the nonadiabaticity in the recombination reaction, leading to transfer of energy to the substrate electronic degrees of freedom [18–20].

Despite the experimental and the latest theoretical evidence, most of the theoretical works based on a purely adiabatic approximation can accurately describe the reactive and non-reactive scattering of  $H_2$  from metal surfaces and dissociation on surfaces such as  $Cu(111)$  [5] and  $Ru(0001)$  [21]. Furthermore, a study on  $H_2/Pt(111)$  using a single PES has shown that employing the Born-Oppenheimer (BO) approximation, *i.e.* neglecting electron-hole pair excitations, could describe both reaction and diffractive scattering [22]. Based on these studies, it has been suggested that the BO approximation is reliable enough to accurately describe  $H_2$  reaction on and scattering from

metal surfaces. This expectation is born out by theoretical studies that have directly addressed the effect of electron-hole pair excitation on reaction of  $H_2$  on metal surfaces using electron friction, and have without exception found the effect to be small [23–27].

The validity of the static surface approximation and the neglect of surface motion and surface temperature have been discussed elsewhere (see for instance Ref. [28]). Due to the large mass mismatch between  $H_2$  and the surface atoms, and because molecular beam experiments are typically performed for low surface temperatures, the static surface approximation usually yields good results for activated sticking [9, 12, 29]. For associative desorption experiments, which tend to use high surface temperatures, the width of the reaction probability curve may be underestimated with the static surface approximation, but the curve should be centered on the correct effective reaction barrier height [5, 29].

There have been a few studies on  $H_2 + Ag(111)$ . The studies showed that the dissociative chemisorption of  $H_2$  on silver is highly activated and does not proceed at room temperature [30–32]. The observation of dissociative chemisorption of molecular  $D_2$  on  $Ag(111)$  was reported for the first time by Hodgson and co-workers, using molecular beam scattering at translational energies above 220 meV and nozzle temperatures above 940 K [33, 34]. They reported that the sticking coefficient of  $D_2$  to  $Ag(111)$  at low incidence energy is very small. These experimental studies also suggested that the dissociative chemisorption of  $H_2/D_2$  on the  $Ag(111)$  surface is an endothermic activated process. Furthermore, the sticking probability is sensitive to the internal temperature, or state distribution, of the  $D_2$  beam. Specifically, the population of highly vibrationally excited states enhances the dissociative chemisorption probability. The molecular beam experiments were able to measure sticking probabilities up to 0.02 for average incidence energies up to about 0.48 eV using a pure  $D_2$  beam. Achieving higher incidence energies (up to 0.8 eV) was possible, by seeding the  $D_2$  beam in  $H_2$  and using the King and Wells technique for detection [35], but the experimentalists reported that the reaction could not be observed with this technique [33, 34], indicating a  $D_2$  sticking probability  $< 0.05$  for energies up to 0.8 eV. Thus, the activation barrier for  $D_2$  ( $\nu = 0$ ) dissociation was reported to be  $> 0.8$  eV [33].

Due to the large activation barrier height for dissociation of  $D_2$  on  $Ag(111)$  surface, the adsorption process is not so accessible to experiment. In this situation, recombinative desorption provides a useful method to in-



investigate the adsorption dynamics by employing the principle of detailed balance [36–38]. Hodgson and co-workers measured the energy release into translational motion for D<sub>2</sub> recombinative desorption from Ag(111) for specific rovibrational D<sub>2</sub> states and various surface temperatures. They found that surface temperature can affect the form of the translational energy distribution and thereby the sticking probability curve, where it is derived by applying detailed balance. At higher surface temperature, the energy distribution in recombinative desorption broadens. Therefore, the initial-state selected sticking probability broadens with increasing surface temperature. At the surface temperature of 570 K the translational energy distribution for H<sub>2</sub>/D<sub>2</sub> ( $\nu = 0$ ) [37, 38] becomes bimodal and shows a peak at high translational energy. The large energy release in recombination is due to the large activation barrier to the reverse process, *i.e.*, direct activated dissociation. At higher surface temperature, at low translational energy the sticking probability increases rapidly with surface temperature and shows an energy-independent behavior [38]. The sticking probability curves can be reproduced using an error function at higher translational energies. However, this model cannot reproduce the low energy tail of the sticking probability curve, and describe the bimodal energy distribution. In this paper the focus will be on the high energy tail of the reaction probability.

Jiang and Guo [39] examined the reactivity in the H<sub>2</sub>–Ag(111) system. They showed that the reactivity in this system is controlled not only by the height of the reaction barrier but also by the topography of the PES in the strongly interacting region. They reported a reaction barrier height of 1.15 eV for H<sub>2</sub> dissociation on Ag(111) using the PBE functional [40]. While they compared computed initial-state selected reaction probabilities with results of associative desorption experiments, no comparison was made with the molecular beam experiments of Hodgson and co-workers [33, 34]. For the associative desorption experiments, good agreement was reported with the PBE theory at the higher incidence energies.

This chapter is organized as follows. Section 4.2.1 describes the dynamical model, and Section 4.2.2 the construction of the PES. The dynamics methods that are used here to study H<sub>2</sub> + Ag(111) are explained in Section 4.2.3. Section 4.2.4 describes how we calculate the observables. Section 4.2.5 provides computational details. In Section 4.3 the results of the calculations are shown and discussed. Section 4.3.1 describes the computed PES, and Section 4.3.2 provides results on vibrationally inelastic scattering, initial vibrational state selected reaction, and sticking in molecular beam

experiments. Conclusions are provided in Section 4.4.

## 4.2 Method

### 4.2.1 Dynamical model

In our calculations, the BOSS model [5] is used. There are two approximations in this model. In the Born-Oppenheimer approximation, it is considered that the reaction occurs on the ground state PES and that electron-hole pair excitation does not affect the reaction probability. The second approximation is that the surface atoms are static and occupy their ideal, relaxed 0 K lattice configuration positions at the (111) surface of the fcc structure of the metal. As a result, motion in the six molecular degrees of freedom is taken into account in our dynamical model. Figure 4.1 (a) shows the coordinate system used for our study, and Figure 4.1 (b) shows the surface unit cell for the Ag(111) surface and the symmetric sites relative to the coordinates used for  $H_2$ .

### 4.2.2 Construction of potential energy surface

A full six-dimensional (6D) PES was constructed using DFT with the SRP48 functional being a weighted average of two functionals [12] ( $0.48 \times$  RPBE [41] +  $0.52 \times$  PBE [40]). The DFT procedure and the way the data are interpolated are almost entirely the same as used before for  $H_2 + Au(111)$  [13]. Here we only describe the most important aspects and provide the few details on which the present procedure differs from that used earlier.

For the interpolation of the 6D PES, in total 28 configurations were used, spread over the 6 different sites on the surface unit cell indicated in Figure 4.1 (b). The accurate corrugation reducing procedure (CRP) method [42] was used to interpolate DFT data, which were computed on grids of points. All our calculations were carried out for interatomic distances  $r$  in the range 0.3–2.3 Å. The low starting value of  $r$  was needed because high initial vibrational states are involved in the Boltzmann sampling of the molecular beam simulations. We extended the H–H distance to a lower bound than used for  $H_2 + Au(111)$  [13] to guarantee the accurate calculation of higher vibrationally excited states (see below). In all other aspects the procedure followed to produce the DFT data on grids of points and to interpolate the points with the CRP is entirely analogous to that used earlier for  $H_2 +$

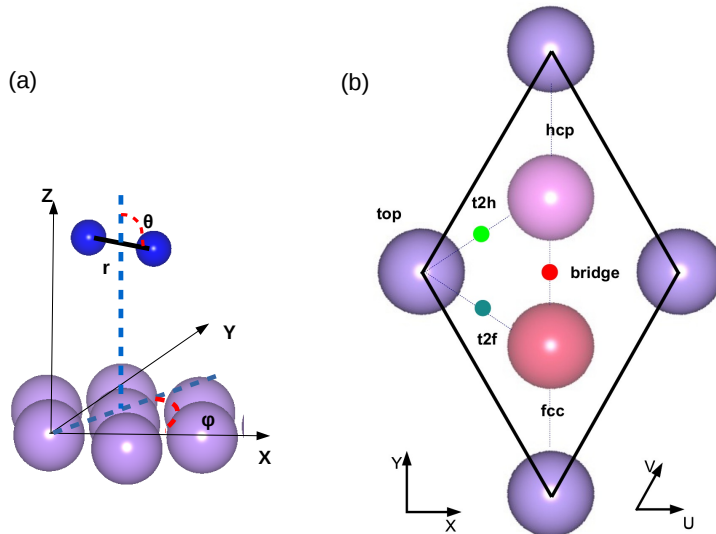


Figure 4.1: (a) The coordinate system used to describe the H<sub>2</sub> molecule relative to the static Ag(111) surface. (b) Top view of the surface unit cell and the sites considered for the Ag(111) surface. The center of mass (of H<sub>2</sub>) coordinate system is centered on a top site (a surface atom). The hcp site corresponds to a second layer atom and the fcc site to a third layer atom.

Au(111). For more detailed information, the reader is referred to Refs. [13] and [21]. In the interpolation procedure to obtain the PES from DFT data on the six sites in Figure 4.1 (b), the p3ml plane group symmetry [43] is used. Tests to confirm the accuracy of the interpolation for additional DFT data not included in the interpolation data set were done and confirmed the quality of the procedure. As a check on the accuracy of the PES, we compare two different DFT data sets, which were not used in the construction of the PES, with the corresponding CRP interpolated values. In method 1, 300 geometries of H<sub>2</sub> + Ag(111) were selected completely at random, with the only restrictions being  $0.3 \text{ \AA} \leq r \leq 2.3 \text{ \AA}$  and  $0.25 \text{ \AA} \leq Z \leq 4.0 \text{ \AA}$ . In method 2 only dynamically relevant points in the barrier region were selected: 300 randomly selected points were taken from QCT calculations,

from  $10^4$  trajectories, a further restriction being  $0.7 \text{ \AA} \leq r \leq 2.3 \text{ \AA}$  and  $0.9 \text{ \AA} \leq Z \leq 3.5 \text{ \AA}$ . (For more details we refer the reader to Ref. [44].)

### 4.2.3 Dynamics methods

#### Quasi-classical dynamics

The QCT method [15] was used to compute dynamical observables, so that the initial zero-point-energy (ZPE) of  $H_2$  is taken into account. To calculate the initial state resolved reaction probabilities, the molecule is initially placed at  $Z = 7 \text{ \AA}$  with a velocity normal towards the surface that corresponds to the specific initial incidence energy. To obtain accurate results, for each computed point on the reaction probability curves at least  $10^4$  trajectories were calculated; more trajectories were computed to obtain a sufficiently small error bar for low sticking probabilities. In all cases the maximum propagation time was 2 ps. The method of Stoer and Bulirsh [45] was used to propagate the equations of motion.

The Fourier grid Hamiltonian (FGH) method [46] was used to determine the bound state rotational-vibrational eigenvalues and eigenstates of gas-phase  $H_2$  by solving the time-independent Schrödinger equation. This method was used to compute the rovibrational levels of the hydrogen molecule in the gas phase. Other initial conditions are randomly chosen. The orientation of the molecule,  $\theta$ , and  $\phi$ , is chosen also based on the selection of the initial rotational state. The magnitude of the classical initial angular momentum is fixed by  $L = \sqrt{j(j+1)}/\hbar$ , and its orientation, while constrained by  $\cos \Theta_L = m_j/\sqrt{j(j+1)}$ , is otherwise randomly chosen as described in [13, 21]. Here,  $j$  is the rotational quantum number,  $m_j$  is the magnetic rotational quantum number and  $\Theta_L$  is the angle between the angular momentum vector and the surface normal. The impact sites are chosen at random. The amount of vibrational energy corresponding to a particular vibrational and rotational level is initially given to the  $H_2$  molecule. The bond distance and the vibrational velocity of the molecule are randomly sampled from a one-dimensional quasi-classical dynamics calculation of a vibrating  $H_2$  molecule for the corresponding vibrational energy [13].

#### Quantum dynamics

For quantum dynamics (QD) calculations the time-dependent wave packet (TDWP) method was used [47, 48]. To represent the wave packet in  $Z, r, X$

and  $Y$ , a discrete variable representation (DVR) [49] was used. To represent the angular wave function a finite base representation (FBR) was employed [50, 51]. To propagate the wave packet according to the time-dependent Schrödinger equation, the split operator method [52] was used (See Ref. [48] for more details).

The wave packet is initially located far away from surface. The initial wave packet is written as a product of a Gaussian wave packet describing motion of the molecule towards the surface, a plane wave for motion parallel to the surface, and a rovibrational wave function to describe the initial vibrational and rotational states of the molecule. At  $Z = Z_\infty$ , analysis of the reflected wave packet is done using the scattering amplitude formalism [53–55],  $Z_\infty$  being a value of  $Z$  where the molecule and surface no longer interact.  $S$  matrix elements for state to state scattering are obtained in this way and used to compute scattering probabilities. An optical potential is used to absorb the reacted ( $r$ ) or scattered ( $Z$ ) wave packet for large values of  $r$  and  $Z$  [56]. Full details of the method are presented in Ref. [48].

#### 4.2.4 Computation of the observables

##### Degeneracy averaged reaction probabilities

In the QCT calculations of the reaction probabilities, the molecule is considered dissociated when its interatomic distance becomes greater than 2.5 Å. The reaction probability is computed from  $P_r = N_r/N_{total}$ , in which  $N_r$  is the number of reactive trajectories and  $N_{total}$  is the total number of trajectories. For a particular initial vibrational state  $\nu$  and rotational state  $j$ , the degeneracy averaged reaction probability can be computed by

$$P_{deg}(E_i; \nu, j) = \sum_{m_j=0}^j (2 - \delta_{m_j 0}) P_r(E_i; \nu, j, m_j) / (2j + 1), \quad (4.1)$$

where  $P_r$  is the fully initial state-resolved reaction probability. In the quantum dynamics, the fully initial state-resolved reaction probability is defined as

$$P_r(E_i; \nu, j, m_j) = 1 - \sum_{\substack{\nu', j', m'_j, \\ n, m}} P_{scat}(E_i; \nu, j, m_j \longrightarrow \nu', j', m'_j, n, m). \quad (4.2)$$

In this equation, the  $P_{scat}(E_i; \nu, j, m_j \rightarrow \nu', j', m'_j, n, m)$  are the state to state scattering probabilities. Initial (final) vibrational, rotational and magnetic rotational quantum numbers are denoted by  $\nu$  ( $\nu'$ ),  $j$  ( $j'$ ),  $m_j$  ( $m'_j$ ), respectively.  $n$  and  $m$  are the quantum numbers for diffraction. Vibrationally inelastic scattering probabilities can be obtained from

$$P_{scat}(E_i; \nu, j \rightarrow \nu') = \sum_{\substack{j', m'_j, m'_j, \\ n, m}} P_{scat}(E_i; \nu, j, m_j \rightarrow \nu', j', m'_j, n, m) / (2j+1). \quad (4.3)$$

### Vibrational efficacy

The vibrational efficacy  $\eta_{\nu=0 \rightarrow 1}(P)$  is another interesting quantity in our study. The vibrational efficacy describes how efficiently vibrational energy can be used to promote reaction relative to translational energy [29, 57]. It is typically computed by

$$\eta_\nu(P) = \frac{E_i^{\nu=0, j}(P) - E_i^{\nu=1, j}(P)}{E_{vib}(\nu = 1, j) - E_{vib}(\nu = 0, j)}, \quad (4.4)$$

where  $E_{vib}(\nu, j)$  is the vibrational energy corresponding to a particular state of the gas-phase molecule and  $E_i^{\nu, j}(P)$  is the incidence energy at which the the initial state-resolved reaction probability becomes equal to  $P$  for  $H_2$  ( $D_2$ ) initially in its  $(\nu, j)$  state. In evaluating Equation 4.4,  $j$  is typically taken as 0.

### Molecular beam sticking probabilities

In the molecular beam, the population of the rovibrational levels depends on the nozzle temperature. The rovibrational levels of the hydrogen molecule approaching to the surface are assumed populated according to a Boltzmann distribution at the nozzle temperature used in the experiment. The monoenergetic reaction probabilities  $R_{mono}(E_i; T_n)$  are computed via Boltzmann averaging over all rovibrational states populated in the molecular beam with a nozzle temperature  $T_n$  at a collision energy  $E_i$  [28]

$$R_{mono}(E_i; T_n) = \sum_{\nu, j} F_B(\nu, j; T_n) P_{deg}(E_i, \nu, j). \quad (4.5)$$

Here,  $F_B(\nu, j; T_n)$  is the Boltzmann weight of each  $(\nu, j)$  state. The factor  $F_B(\nu, j; T_n)$  is described by

$$F_B(\nu, j; T_n) = \frac{F(\nu, j; T_n)}{\sum_{\nu, j} F(\nu, j; T_n)}, \quad (4.6)$$

in which

$$F(\nu, j; T_n) = (2j + 1)e^{-\frac{E_{vib}(\nu)}{k_B T_{vib}}} w(j)e^{-\frac{E_{rot}(j)}{(k_B T_{rot})}}. \quad (4.7)$$

In this equation  $E_{vib}$  and  $E_{rot}$  are the vibrational and rotational energy, respectively and  $k_B$  is the Boltzmann constant. The factor  $w(j)$  describes the nuclear spin statistics of  $\text{H}_2$  and  $\text{D}_2$ . With even  $j$ ,  $w(j)$  is 1 (2) for  $\text{H}_2$  ( $\text{D}_2$ ) and with odd values  $w(j)$  is 3 (1) for  $\text{H}_2$  ( $\text{D}_2$ ). The vibrational temperature of the molecule is assumed to be equal to the nozzle temperature ( $T_{vib} = T_n$ ). However, in the molecular beam simulation, it is assumed that the rotational temperature of the molecule in the beam is lower than the nozzle temperature ( $T_{rot} = 0.8T_n$ ) [58].

The experimentalist showed that vibrational excitation promotes dissociation of  $\text{D}_2$  on  $\text{Ag}(111)$  [33] and suggested that sticking is dominated by higher vibrational states [34]. In the theoretical simulation of the molecular beam, we have to consider the Boltzmann factor of the populated vibrational states. To ensure a proper contribution of the higher rotational and vibrational states in the QCT calculations, the highest populated vibrational state is allowed to be up to 5 and the highest rotational state to be up to 25. The threshold of the Boltzmann weight for an initial rovibrational state to be considered is  $4 \times 10^{-6}$ . The convergence of the sticking probability with respect to this threshold was checked.

To extract the sticking probability from the theoretical model, in principle flux weighted incidence energy distributions should be used. Subsequently, the reaction probability on sticking probability is computed via averaging over the incident velocity distribution of the experimental molecular beam<sup>1</sup>, according to the expression [59]

$$R_{beam}(\bar{E}; T_n) = \frac{\int_0^\infty f(v_i; T_n) R_{mono}(E_i; T_n) dv_i}{\int_0^\infty f(v_i; T_n) dv_i}, \quad (4.8)$$

---

<sup>1</sup> $\bar{E} = \langle E_i \rangle$

where  $f(v_i; T_n)$  is the flux weighted velocity distribution given by [60]

$$f(v_i; T_n)dv_i = Cv_i^3 e^{-(v_i-v_s)^2/\alpha^2} dv_i. \quad (4.9)$$

Here,  $C$  is a constant,  $v_i$  is the velocity of the molecule ( $E_i = \frac{1}{2}Mv_i^2$ ),  $v_s$  is the stream velocity and  $\alpha$  is a parameter that describes the width of the velocity distribution.

According to the experimentalists, the mean translational energies obtained from TOF distributions for the pure  $D_2$  beam were related to the nozzle temperature by  $\langle E_i \rangle = 2.7 k_B T_n$ . This indicates a slight rotational cooling of the incident molecular beam ( $T_{rot} \approx 0.8T_n$ ). However, they could not detect any relaxation of the incident vibrational state distributions. To simulate the molecular beam with our dynamical model, we use energy distributions, which have been fitted by the experimentalists [A. Hodgson, private communication] with the exponentially modified Gaussian function of the form,

$$G(E) = \sqrt{2\pi\sigma} \exp\left(\frac{-(E - \langle E \rangle)^2}{2\sigma}\right). \quad (4.10)$$

Here,  $\sigma$  is defined by :

$$\sigma = 5.11e^{-3}\langle E \rangle + 1.3184e^{-4}, \quad (4.11)$$

and the nozzle temperature  $T_n$  (in K) is related to  $\langle E \rangle$  by

$$T(K) = 3935.8\langle E \rangle + 99.4, \quad (4.12)$$

with  $\langle E \rangle$  given in eV. Hereafter we refer to these energy distributions (Equation 4.10) as  $G(E)$ . While we will use the  $G(E)$  provided by the experimentalist, we note that these do not correspond to the usual asymmetry flux weighted distributions defined in terms of the stream velocity  $v_s$  and the width parameter  $\alpha$  giving by Equation 4.9. Using the energy distribution  $G(E)$ , the reaction probability is then described by

$$R_{beam}(\bar{E}; T_n) = \frac{\int_0^\infty G(E_i; T_n) R_{mono}(E_i; T_n) dE_i}{\int_0^\infty G(E_i; T_n) dE_i}. \quad (4.13)$$

The experimentally measured reaction probabilities and the corresponding average translational energies for  $D_2 + Ag(111)$  are listed in table 4.1, which also presents the values of  $T_n$  and  $\sigma$ . Figure 4.2 shows the experimental incident energy distributions for different average incidence energies.



Table 4.1: Average energies and experimental sticking coefficient  $S_0$ .  $T_n$  shows the nozzle temperatures. The data were obtained from A. Hodgson (private communication).

Average energy (eV)	$\sigma$ (meV <sup>2</sup> )	$S_0$	$T_n$ (K)
0.221	1.26	$7.6 \times 10^{-8}$	969
0.274	1.53	$3.9 \times 10^{-6}$	1177
0.304	1.68	$8.6 \times 10^{-6}$	1295
0.336	1.85	$8.6 \times 10^{-5}$	1421
0.376	2.05	$3.9 \times 10^{-4}$	1579
0.424	2.30	$3.1 \times 10^{-3}$	1768
0.452	2.44	$9.2 \times 10^{-3}$	1878
0.486	2.62	$2.0 \times 10^{-2}$	2012

In order to obtain statistically reliable QCT results, we did convergence tests on the number of trajectories for each set of incidence conditions. To simulate molecular beam experiments, at least  $10^6$  trajectories were computed for each incidence condition. To simulate the molecular beam experiments we also used the beam parameters presented in table S9 of the supporting material of Ref. [5], which describe the D<sub>2</sub> pure beams produced in experiments of Auerbach and co-workers [57] in terms of the flux weighted velocity distributions (Equation 4.9).

#### 4.2.5 Computational details

The DFT calculations were performed with the VASP software package (version 5.2.12). Standard VASP ultrasoft pseudopotentials were used, as done originally for H<sub>2</sub> + Cu(111) [5]. First the bulk fcc lattice constant was computed in the same manner as used previously for H<sub>2</sub> + Au(111) [13], using a  $20 \times 20 \times 20$   $\Gamma$ -centered grid of k-points. The distance between the nearest neighbor Ag atoms in the top layer was obtained as  $a = a_{3D}/\sqrt{2} = 2.97$  Å with the SRP48 functional, where  $a_{3D}$  is the bulk lattice constant. With the SRP48 functional a bulk lattice constant  $a_{3D}$  of 4.20 Å was computed. It is in reasonable agreement with the computed value of 4.16 Å of the PBE functional [39]. Compared to the experimental value (4.08 Å) [61, 62], the SRP48 functional overestimates the lattice constant

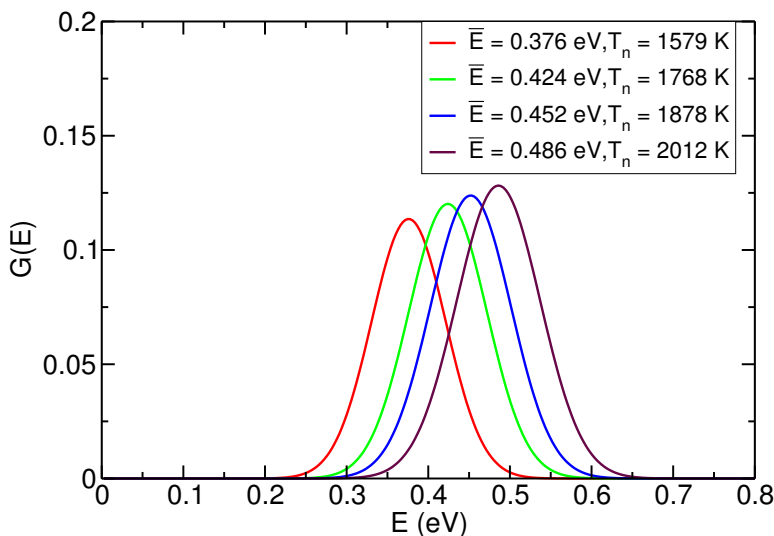


Figure 4.2: Incident energy distributions  $G_{H-dis}(E)$  for different values of  $T_n$  data from [A. Hodgson, private communication].

by about 3 %.

A  $(2 \times 2)$  surface unit cell has been used to model the  $H_2/Ag(111)$  system. The slab consisted of 4 layers. A relaxed 4-layer slab was generated again in the same manner as used before for  $H_2 + Au(111)$  [13], using  $20 \times 20 \times 1$   $\Gamma$ -centered grid of k-points. The inter-layer distances computed with the SRP48 functional were  $d_{12} = 2.41$  Å,  $d_{23} = 2.40$  Å, and  $d_{34}$  was taken as the SRP48 bulk inter-layer spacing (2.41 Å).

After having obtained the relaxed slab, the single point calculations for the PES were carried out using a  $11 \times 11 \times 1$   $\Gamma$ -centered grid of k-points, and a plane wave cut-off of 400 eV. In the super cell approach, a 13 Å vacuum length between the periodic Ag(111) slabs was used. Other details of the calculations were the same as in Ref. [28]. With the computational set-up used, we estimate that the molecule-surface interaction energy is converged to within 30 meV [13].

For the quantum dynamics calculations on reaction, wave packets were propagated to obtain results for the energy range of [0.5–1.0] eV. Table 4.2 collects the parameters which were used. Figure 4.3 (a) shows convergence tests of using different numbers of grid points on the surface unit cell for

Table 4.2: Input parameters for the quantum dynamical calculations of  $D_2$  ( $\nu = 2$ ,  $j = 0$ ) dissociating on Ag(111). For different vibrational states the same input parameters could be used, aside from the number of grid points in  $X$  and  $Y$ . They are listed in parentheses for  $\nu = 1$  and  $\nu = 3$ , respectively. All values are given in atomic units (except the parameters  $P$  for the quadratic optical potentials, which are given in eV). The abbreviation "sp" refers to the specular grid used to bring in the initial wave function.

Parameter	Description	Value
$E_i$	normal incidence range in $Z$	[0.5-1.0] (eV)
$N_X = N_Y$	no. of grid points in $X$ and $Y$	24 (20, 32)
$N_Z$	no. of grid points in $Z$	154
$N_{Z(sp)}$	no. of specular grid points	256
$\Delta Z$	spacing of $Z$ grid points	0.1
$Z_{min}$	minimum value of $Z$	-1.0
$N_r$	no. of grid points in $r$	42
$\Delta r$	spacing of $r$ grid points	0.15
$r_{min}$	minimum value of $r$	0.4
$j_{max}$	maximum $j$ value in basis set	24
$m_{jmax}$	maximum $m_j$ value in basis set	16
$\Delta t$	time step	2
$T_{tot}$	Total propagation time	20000
$Z_0$	center of initial wave packet	15.8
$Z_{inf}$	location of analysis line	12.5
$Z_{start}^{opt}$	start of optical potential in $Z$	12.5
$Z_{end}^{opt}$	end of optical potential in $Z$	14.3
$P_Z$	optical potential in $Z$	0.4
$r_{start}^{opt}$	start of optical potential in $r$	4.15
$r_{end}^{opt}$	end of optical potential in $r$	6.55
$P_r$	optical potential in $r$	0.3
$Z(sp)_{start}^{opt}$	start of optical potential in $Z(sp)$	20.0
$Z(sp)_{end}^{opt}$	end of optical potential in $Z(sp)$	24.5
$P_{Z(sp)}$	optical potential in $Z(sp)$	0.3

Table 4.3: Barrier heights ( $E_b$ ), positions ( $Z_b, r_b$ ) for dissociative chemisorption of  $H_2$  on  $Ag(111)$  above different sites in which  $H_2$  is parallel to the surface ( $\theta = 90^\circ$ ). The results are provided for the SRP48 PES.

configuration	$\phi^\circ$	$Z_b$ (Å)	$r_b$ (Å)	$E_b$ (eV)
<b>top</b>	0	1.51	1.57	1.69
<b>bridge</b>	90	1.10	1.27	1.38
<b>t2f</b>	120	1.34	1.45	1.58
<b>fcc</b>	0	1.34	1.67	1.70

quantum dynamics calculations on  $D_2(\nu = 2, j = 0)$ . Taking the number of grid points in  $X$  and  $Y$  equal to  $N_X = N_Y = 28$ , the results of the quantum dynamics calculations are in good agreement with quantum dynamics results with  $N_X = N_Y = 32$ . Convergence could thus be achieved with  $N_X = N_Y = 28$  (see Figure 4.3 (a)). By repetition of the same procedure, we found that the numbers of  $X$  and  $Y$  grid points  $N_X = N_Y = 20$  and  $N_X = N_Y = 32$  are sufficient to obtain converged quantum dynamics results for  $D_2(\nu = 1, j = 0)$  and  $D_2(\nu = 3, j = 0)$ , respectively. We also checked convergence with the highest rotational level  $j_{max}$  and  $m_{jmax}$  for the angular part of the wave packet, see Figure 4.3 (b). As can be seen convergence is achieved with  $j_{max} = 24$  and  $m_{jmax} = 16$ .

## 4.3 Results and discussion

### 4.3.1 The potential energy surface

Figure 4.4 shows elbow plots of the PES computed with the SRP48 functional for different configurations. Table 4.3 shows the geometries and heights of the barrier to dissociation found for impact on the top, bridge, fcc hollow, and t2f sites. In all cases  $H_2$  is positioned parallel to the  $Ag(111)$  surface. The minimum barrier height (1.38 eV) is found for bridge-to-hollow dissociation (see Figure 4.4 (b)), similar to  $H_2 + Cu(111)$  [5]. Comparing the reaction paths in the 2D elbow plots, we suggest that impact on the fcc site is most likely relevant for vibrationally inelastic scattering and for the dissociation of vibrationally excited  $H_2$ . The 2D elbow plot for this site displays a large curvature of the reaction path. The minimum barrier

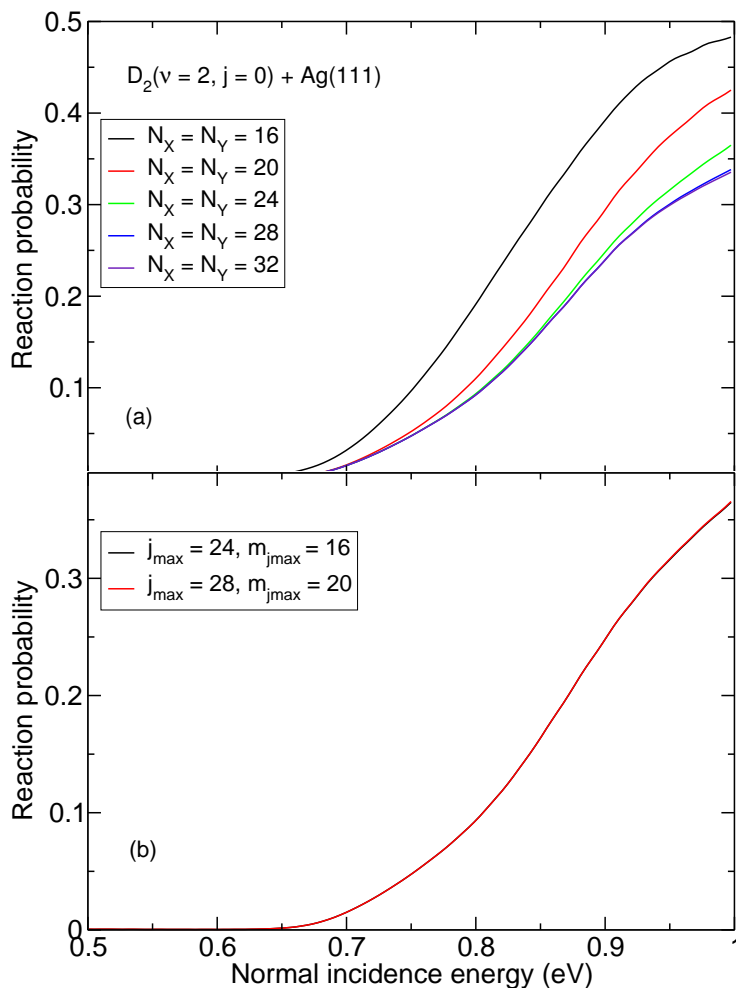


Figure 4.3: Convergence test for reaction of  $D_2(\nu = 2, j = 0)$  on  $Ag(111)$  for (a) the number of grid points in the X and Y coordinates and (b) the highest  $j_{max}$  and  $m_{jmax}$  in the basis sets.

position for that site also shows a large inter-molecular distance  $r$ , *i.e.*, a later barrier. It is known that these two characteristics promote vibrationally inelastic scattering and vibrational enhanced dissociation [63, 64]. The lowest curvature of the reaction path in front of the barrier was found for the bridge site. Due to the lower reaction barrier height for the bridge site,

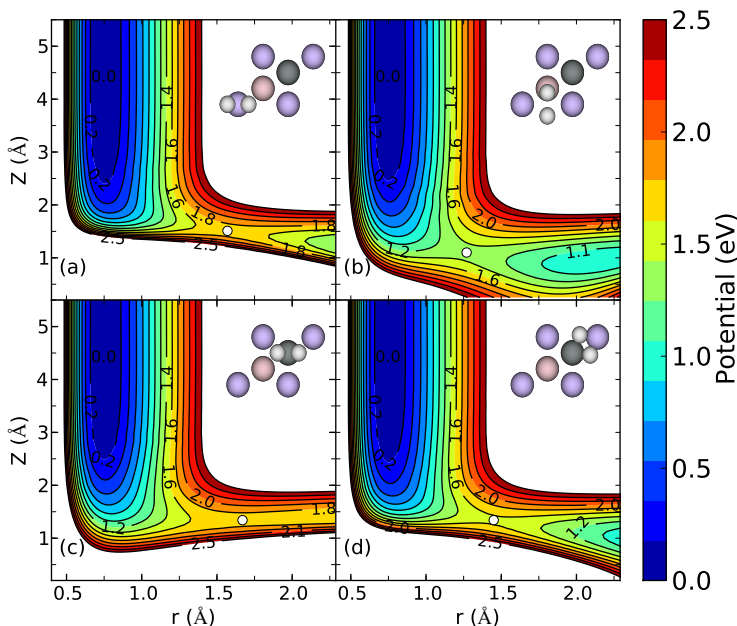


Figure 4.4: Elbow plots (*i.e.*,  $V(Z, r)$ ) of the  $H_2 + Ag(111)$  PES computed with the SRP48 functional and interpolated with the CRP method for four high symmetry configurations with the molecular axis parallel to the surface ( $\theta = 90^\circ$ ) as depicted by the insets, for (a) the top site and  $\phi = 0^\circ$ , (b) the bridge site and  $\phi = 90^\circ$ , (c) the fcc site and  $\phi = 0^\circ$ , and (d) the t2f site and  $\phi = 120^\circ$ . Barrier geometries are indicated with white circles, and corresponding barrier heights and geometries are given in table 4.3.

we predict that the reaction occurs mostly above this site for  $\nu = 0$   $H_2$ .

To carefully check the accuracy of the interpolation method (the CRP), additional electronic structure single point calculations have been performed using VASP, for molecular configurations centered on a symmetric site bridge ( $X = 0.5 a$ ,  $Y = 0.0$ , where  $a$  is the lattice constant). Figure 4.5 presents the results of a comparison between DFT results not included in the input database for the interpolation and the CRP interpolated PES

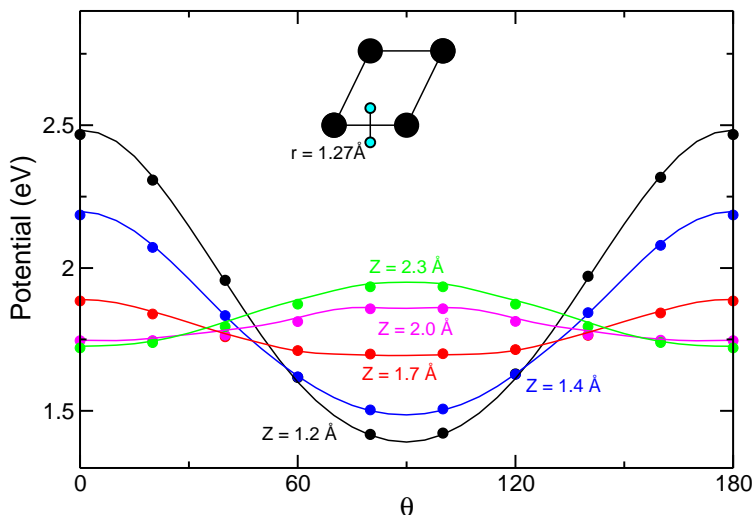


Figure 4.5: The  $\theta$ -dependence of the  $\text{H}_2 + \text{Ag}(111)$  SRP48 PES is shown for molecular configurations centered on a bridge site ( $X = 1/2a$ ;  $Y = 0$ ),  $\phi = 90^\circ$  and  $r_b = 1.27 \text{ \AA}$ , where  $a$  is the surface lattice constant. Full lines: interpolated PES; symbols: DFT results. The values of  $Z$  corresponding to different curves and sets of symbols are provided with matching color.

along  $\theta$  on this site, with  $\phi = 90^\circ$  and  $r = 1.27 \text{ \AA}$ . The black curve and symbols ( $r = 1.27 \text{ \AA}$ , and  $Z = 1.2 \text{ \AA}$ ) present the  $\theta$ -variation of the PES around a point near the minimum barrier position. The curves show that  $\text{H}_2$  prefers to change its orientation from perpendicular to parallel when it approaches the surface. The interpolated PES faithfully reproduces the DFT results. The same finding was obtained for interpolation in  $X$  (see Figure 4.6). Hence, the accuracy in the interpolation of the PES guarantees that the comparison of our dynamical results to experiments should reflect the accuracy of the electronic structure results and the computational model.

As described in Section 4.2.2, we also evaluate the accuracy of the CRP interpolated PES using two additional methods. We evaluate interpolation errors by comparing DFT data points with corresponding CRP values and computing the root mean square error (RMSE), mean absolute error (MAE) and mean signed error (MSE, obtained by subtracting DFT energies from CRP energies). To test the accuracy of the PES in more detail, we chose

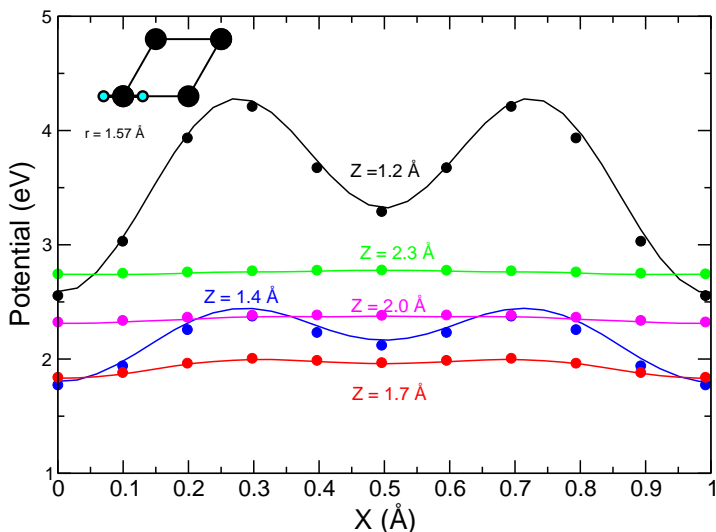


Figure 4.6: The  $X$ -dependence of the  $H_2 + Ag(111)$  SRP48 PES is shown for molecular configurations including the top site ( $X = 0.0$ ;  $Y = 0.0$ ), for  $\phi = 0^\circ$ ,  $\theta = 90^\circ$  and  $r_b = 1.57 \text{ \AA}$ . Full lines: interpolated PES; symbols: DFT results. The values of  $Z$  corresponding to different curves and sets of symbols are provided with matching color.

three different energy ranges: 1 -  $[0-0.69] \text{ eV}$  (less than 1/2 times the minimum barrier height) 2 -  $[0.69-1.38] \text{ eV}$  (between half times the minimum barrier height and the minimum barrier height) 3 -  $[1.38-2.07] \text{ eV}$  (larger than the minimum barrier height but smaller than 1.5 times the barrier height). The corresponding values for both data sets ((1) data selected in a completely random way and (2) data from QCT calculations) are listed in table 4.4. Importantly, the errors for the dynamically selected dataset are in all cases less than 1 kcal/mol ( $\approx 43 \text{ meV}$ ).

### 4.3.2 Dynamics

#### Scattering

In Figure 4.7 vibrationally elastic and inelastic excitation probabilities  $P(\nu = 2, j = 0 \rightarrow \nu = \nu')$  are presented as a function of the initial normal incidence energy. At an incidence energy of 0.5 eV, the probability for vi-



Table 4.4: Accuracy of the 6D PES in comparison to DFT calculations. All energies are in eV, with the zero of energy take as the gas phase  $\text{H}_2$  minimum energy. N is the number of data points. The number in brackets behind the error refers to method used to evaluate the error in Section 4.2.2.

Energy	N	RMSE (1)	RMSE (2)	MAE (1)	MAE (2)	MSE (1)	MSE (2)
[0.0 – 0.69]	100	0.024	0.009	0.012	0.007	0.006	0.007
[0.69 – 1.38]	100	0.086	0.021	0.044	0.020	0.008	0.020
[1.38 – 2.07]	100	0.132	0.036	0.069	0.031	0.015	0.031

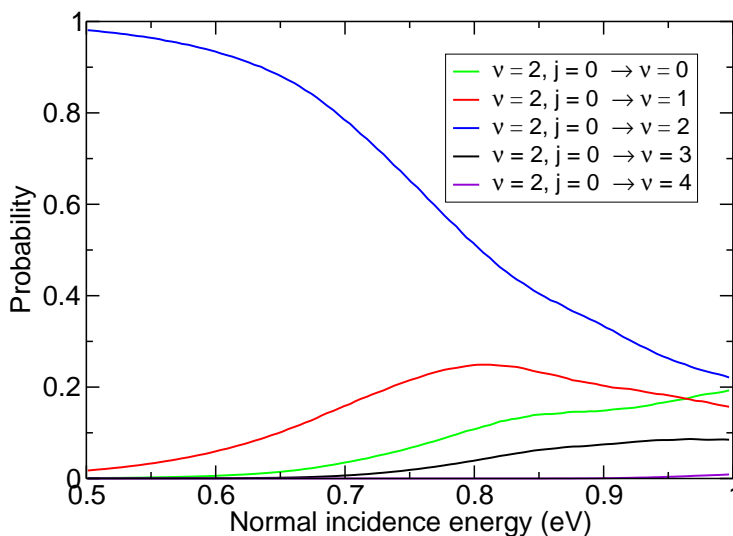


Figure 4.7: The vibrationally elastic and inelastic scattering probabilities are shown as a function of the normal incidence energy for scattering of  $D_2$  ( $\nu = 2, j = 0$ ) from  $Ag(111)$  using the SRP48 PES.

brationally elastic scattering is about 1. At higher incidence energies, the sizeable  $P(\nu = 2, j = 0 \rightarrow \nu \neq \nu')$  indicate a substantial competition between vibrationally elastic and inelastic scattering on the one hand and reaction on the other hand for all energies shown. This behavior can result from a PES that describes reaction paths with especially late barriers with a high degree of curvature in  $r$  and  $Z$  (see Section 4.3.1) [63, 64], leading to a coupling between molecular vibration and motion towards the surface. This explains why we see reaction probabilities no larger than about 0.8 for the highest incidence energy  $E_i$  we employed.

### Initial-state resolved reaction

The comparison between the calculated and measured results for  $H_2$  ( $\nu = 0, j = 3$ ),  $D_2(\nu = 0, j = 2)$ , and  $D_2(\nu = 1, j = 2)$  is shown in Figures 4.8 and 4.9. The theoretical results were obtained by degeneracy averaging the fully initial state resolved reaction probabilities. The experimental results were extracted from associative desorption experiments [37, 38]. In the figure, the symbols show the experimental data and the solid curves show the

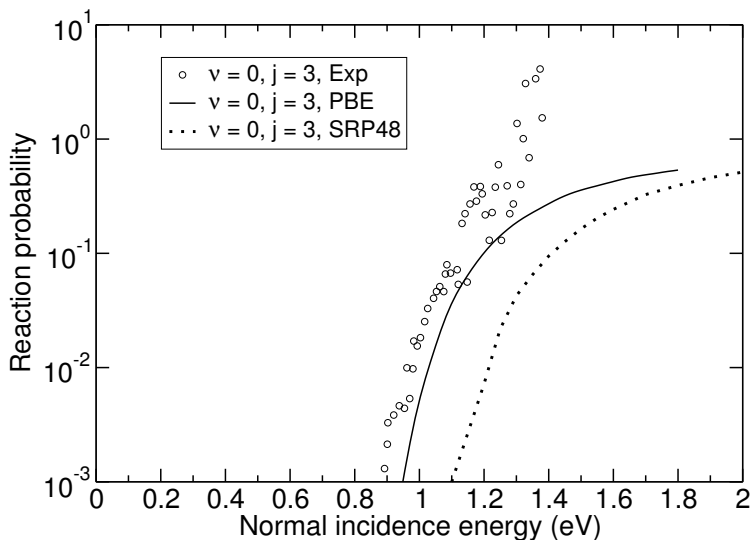


Figure 4.8: Comparison of experimental and computed reaction probabilities as a function of the incidence energy  $E_i$  for  $\text{H}_2$  in the  $(\nu = 0, j = 3)$  state, dissociating on  $\text{Ag}(111)$ . The experimental data were reported in Ref. [37]. The quantum dynamics results obtained for the PBE functional were obtained in Ref. [39].

theoretical results based on a PES computed with the PBE functional by Jiang *et al.* [39]. The dotted lines show our theoretical results obtained with the SRP48 functional. One thing to keep in mind is that our calculated reaction probabilities saturate at high  $E_i$  at about 0.8. In contrast, fits made by the experimentalists assumed the reaction probability to saturate at 1 (this condition was not imposed on the data shown). The agreement of theory and experiment is good at high translational energies for the results of the Jiang *et al.* group. However, the initial state resolved reaction probabilities obtained with the SRP48 functional underestimate the experimental reaction probabilities. Jiang *et al.* obtained a minimum barrier height of 1.16 eV with the PBE functional, while we computed a value of 1.38 eV with the SRP48 functional. The comparison suggests that the SRP48 functional overestimates the reaction barrier height, so that, the computed reaction probabilities are too low.

Other initial state  $(\nu, j)$  resolved reaction probabilities for several vibra-

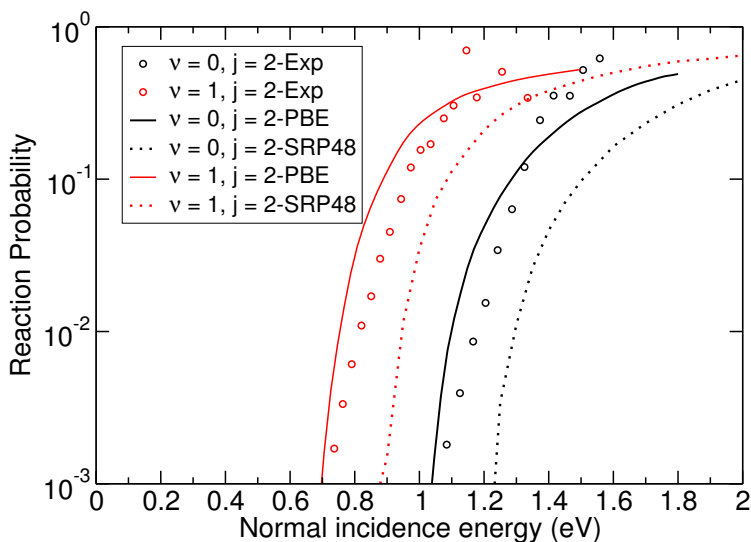


Figure 4.9: Comparison of experimental and computed reaction probabilities as a function of the incidence energy  $E_i$  for  $D_2$  in the  $(\nu = 0 - 1, j = 2)$  states, dissociating on  $Ag(111)$ . The experimental data were reported in Ref. [38]. The quantum dynamics results obtained for the PBE functional were obtained in Ref. [39].

tional states and  $j = 0$  of  $H_2$  and  $D_2$  have also been computed for the SRP48 PES using QCT. They are presented as a function of incidence energy  $E_i$  in Figure 4.10 (a) for the  $H_2$  ( $\nu = 0, 1, 2, 3, 4, 5, j = 0$  states). Figure 4.10 (b) shows the results for  $D_2$ .

The theoretical vibrational efficacy computed from our results for  $H_2(D_2)$  ( $\nu = 0, j = 0$ ) and  $H_2(D_2)$  ( $\nu = 1, j = 0$ ) is greater than 1. For example, at a reaction probability of 0.24, the calculated shift between the  $\nu = 0$  and  $\nu = 1$   $D_2$  reaction probability curves is about 0.504 eV, while the vibrational excitation energy is 0.37 eV for  $D_2$  ( $\nu = 0 \rightarrow 1$ ), yielding a vibrational efficacy of 1.37.

Vibrational promotion of reaction with vibrational efficacies up to 1 may be explained conceptually through a picture in which the molecule moves along the reaction path in a potential elbow in the two dimensions  $r$  and  $Z$ . Analyzing the effect based on the vibration perpendicular to the reaction path, the reaction may be promoted by increasing  $\nu$  if the frequency of

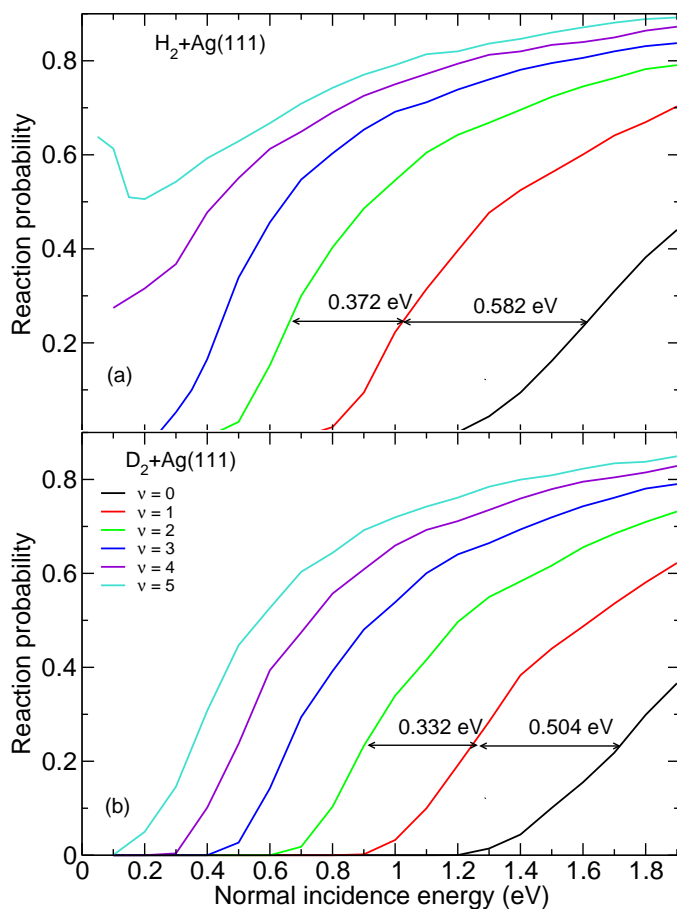


Figure 4.10: Reaction probabilities as a function of incidence energy  $E_i$  for  $\text{H}_2$  (a) and  $\text{D}_2$  (b) in the  $(\nu = 0 - 5, j = 0)$  states. Horizontal arrows and the number above these indicate the energy spacing between the reaction probability curves for the  $(\nu = 0 - 2, j = 0)$  states for a reaction probability equal to 0.24.

motion perpendicular to the path is decreased. This can be done through a mass effect (leading to larger vibrational efficacies for later barriers [65, 66], the Polanyi rules [67]) or by a decrease of the force constant for this motion [68, 69], when the molecule moves towards the barrier (vibrationally

elastic enhancement) in both cases. It is also possible that the vibration discussed is de-excited before the molecule gets to the barrier [64], possibly leading to a vibrational efficacy somewhat greater than 1.0 (vibrationally inelastic enhancement). However, vibrational efficacies greater than 1.0, as found here, can also be explained if the assumption is made that for low  $\nu$  (and high incident energy) the molecule cannot follow the minimum energy path and slides off it [70, 71] (this has also been called a bobsled effect in the past [72]).

Comparison between the reaction threshold energy of  $D_2$  ( $\nu = 0, j = 0$ ) and  $H_2$  ( $\nu = 0, j = 0$ ) shows that this energy for  $D_2$  is at a somewhat higher incidence energy than for  $H_2$ . This is known as a zero-point energy effect [73], where  $H_2$  has more energy in zero-point vibrational motion, so that more of this energy can be converted to energy along the reaction coordinate (via softening of the H–H bond).

Figure 4.10 (a) also shows an interesting effect: at the highest  $\nu$ , the reaction probability curve takes on the shape of a curve affected by trapping mediated dissociation at low incident energies, *i.e.*, the reaction becomes non-activated for the highest  $\nu$  for  $H_2$ . The same effect was observed by Laurent *et al.* [74], who investigated reaction in five different  $H_2$  metal systems, and found that for high enough  $\nu$  the reaction probability curve takes on this shape, with the value of  $\nu$  at which this effect occurs depending on how activated the dissociation is. They attributed the non-monotonic dependence on incidence energy as being due to an increased ability of the highly vibrationally excited molecule to reorient itself to a favorable orientation for reaction.

The experimentalists [34] used a model to fit the molecular beam sticking data, assuming that dissociation is independent of molecular rotation, being the sum of contributions from dissociation of the molecule in different initial vibrational states  $\nu$  described by a sticking function

$$S_0(E_i, \nu) = \frac{A}{2} \left\{ 1 + \tanh \frac{(E_i - E_0(\nu))}{w(\nu)} \right\}. \quad (4.14)$$

Here,  $E_0$  is the translational energy required for the sticking probability to reach half of its maximum value,  $w$  is the width of the function, and  $A$  is the saturation parameter. In this model, the molecular sticking probability is assumed to be a function of the incidence energy and the vibrational state. All parameters are assumed to be dependent on the initial vibrational state as well.  $E_i$  is the normal incidence energy. We use this model

to check whether we reproduce the deconvoluted initial vibrational state resolved sticking probability for  $D_2$  on  $Ag(111)$ . The experimentally determined parameters can be found in Ref. [34].

The comparison between the experimentally fitted results and our computed initial state resolved reaction probabilities for  $D_2$  ( $\nu = 1 - 4$ ,  $j = 0$ ) is presented in Figure 4.11 (a). Figure 4.11 (b) also shows the computed sticking probability as a function of collision energy, in which Boltzmann averaging is performed over all rotational states for each specific vibrational state and specific incidence energy of  $D_2$ . This figure shows that also considering higher rotationally excited states ( $> j = 0$ ) in our calculations may considerably enhance the vibrational state resolved reaction probabilities. In particular, it is clear that the sticking probability for the  $j = 0$  rotational level is smaller than the sticking probability obtained by averaging over the rotational distribution of the molecular beam at  $T_n = 2012$  K. Also as a result of this rotational state averaging effect, our computed vibrational state resolved reaction probabilities have a much larger width  $w$  than the experimentally extracted data. The QCT results indicate that the saturation value of the reaction probability is approximately equal to 0.8 and not 1 as was assumed in extracting  $w$  from experimental data using Equation 4.14.

To check the accuracy of the QCT results and to investigate the possible quantum effects in the dissociation of a small and light molecule on the surface, quantum dynamics calculations were performed. In Figure 4.12 the initial state resolved reaction probability for  $D_2$  dissociating on  $Ag(111)$  obtained from QCT calculations is compared to QD calculations for the initial ( $\nu = 1 - 3$ ,  $j = 0$ ) states. We found an excellent agreement between these two dynamical methods (QCT and QD) giving us enough confidence to use the QCT results for the molecular beam sticking simulations. The results for  $\nu = 1$  suggest that the comparison with experiment in Figure 4.9 should be accurate for the  $\nu = 1$ ,  $j = 2$  state of  $D_2$ , at least for probabilities larger than 0.01. The comparison between QCT and QD results for ( $\nu = 0$ ,  $j = 0$ )  $H_2 + Ag(111)$  presented in Figure 6 of Ref. [75] on the other hand would suggest that using QD would move the computed reaction probability curve to higher energies by a few tens of meV for  $\nu = 0$ , which would slightly worsen the agreement between the present theory and experiment for  $\nu = 0$  in Figure 4.9.

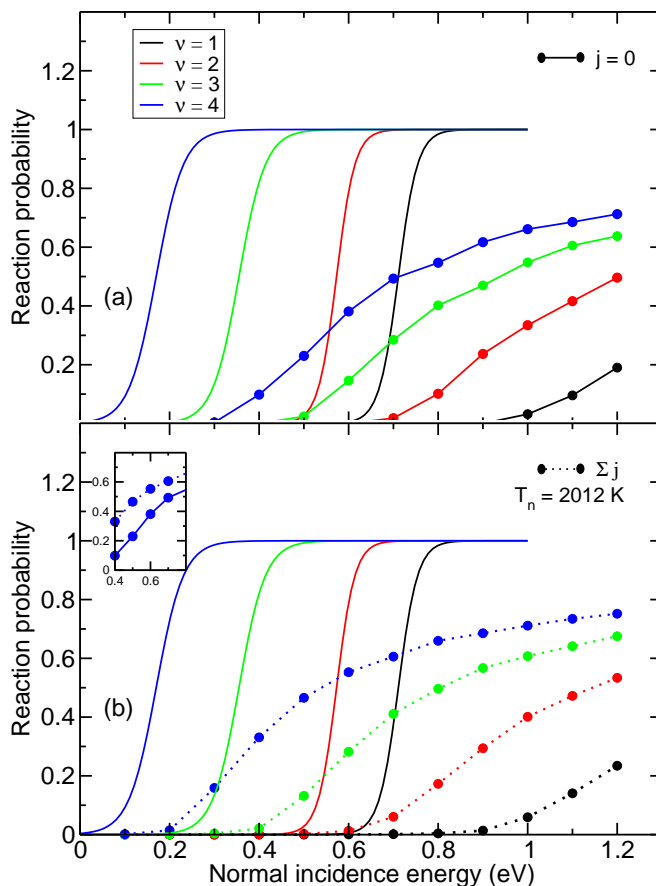


Figure 4.11: (a) Deconvoluted sticking function  $S_0(E_i, \nu)$  for  $D_2$  at  $Ag(111)$  (lines) [34] and the computed initial state resolved reaction probabilities for the  $(\nu = 1 - 4, j = 0)$  states (symbols with matching color). (b) The same functions  $S_0(E_i, \nu)$  resulting from the experimental analyses [34] are compared with computed initial vibrational state selected reaction probabilities with Boltzmann averaging over the rotational states using  $T_n = 2012$  K. Comparison between the computed initial state resolved reaction probabilities and initial vibrational state resolved reaction probabilities is also shown for the  $\nu = 4$  state.



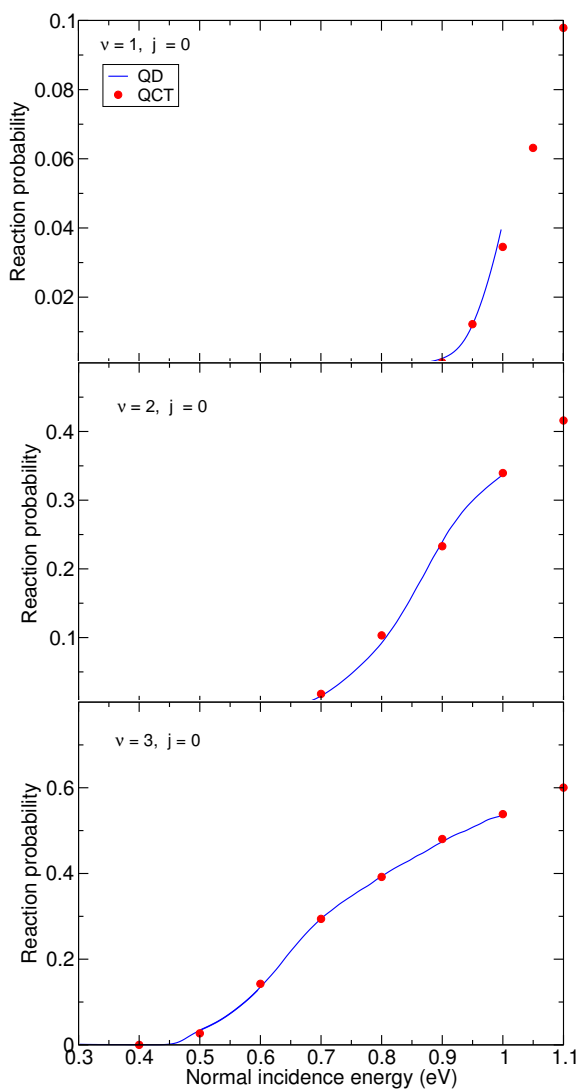


Figure 4.12: Comparison between the initial state resolved reaction probability calculated with QD and QCT calculations for ( $\nu = 1 - 3$ ,  $j = 0$ )  $D_2$  dissociating on Ag(111).

## Molecular beam sticking

In Figure 4.13, the computed sticking probabilities are shown as a function of the average collision energy for  $D_2$  dissociation on  $Ag(111)$ . A comparison is made with available experimental results of Cottrell *et al.* [34]. Calculations were performed for two set of beam parameters corresponding to different velocity distributions.

The experimentalists claimed that the sticking of all vibrational levels  $\nu < 4$  may be significant and must be included in modeling the experimental data [34]. Our calculations show that the contributions of the initial vibrational states in the  $D_2$  molecule dissociating on the surface are 3% for  $\nu = 1$ , 8% for  $\nu = 2$ , 52% for  $\nu = 3$ , 31% for  $\nu = 4$  and 5% for  $\nu = 5$ , when the average incidence energy of the beam is 0.486 eV and  $T_n = 2012$  K. This theoretical result is in agreement with that experimental expectation.

The sticking probabilities are plotted as a function of average incidence energy in Figure 4.13 (a). Here, the black symbols show the experimental data measured by Cottrell *et al.* [34]. The dotted line presents the interpolation of the experimental data. The red symbols are our computed beam simulation results, averaging over translational energy distributions according to the formula provided by the experimentalists and described above, and Boltzmann averaging over the initial rovibrational states of  $D_2$  molecule in the beam according to the nozzle temperatures given in table 4.1. The energy differences between the computed data and the spline interpolated experimental curve are in the range 87–100 meV (2–2.3 kcal/mol). Therefore, our theoretical results do not agree with the experimental results to within chemical accuracy (1 kcal/mol  $\approx$  43 meV). The discrepancy should not be due to the use of the QCT method instead of quantum dynamics. As discussed above, at even the largest average collision energy in the experiment the dominant contributions to the QCT reaction probabilities come from  $\nu \geq 3$ . These probabilities are not expected to exhibit large errors due to zero-point energy violation (see Figure 4.12). The QCT reaction probabilities for lower  $\nu$  (especially for  $\nu = 0$ ) may exhibit larger zero-point energy violation errors (see for instance Figure 6 of Ref. [75] for  $\nu = 0$   $H_2 + Ag(111)$ ), but in any case their contribution should be small at all energies. Furthermore, their contribution would lead to (small) overestimates by the computed reaction probabilities rather than underestimates, as zero-point energy violation tends to increase the reaction probability (see again Figure 6 of Ref. [75]). Therefore, correcting for zero-point energy violation errors

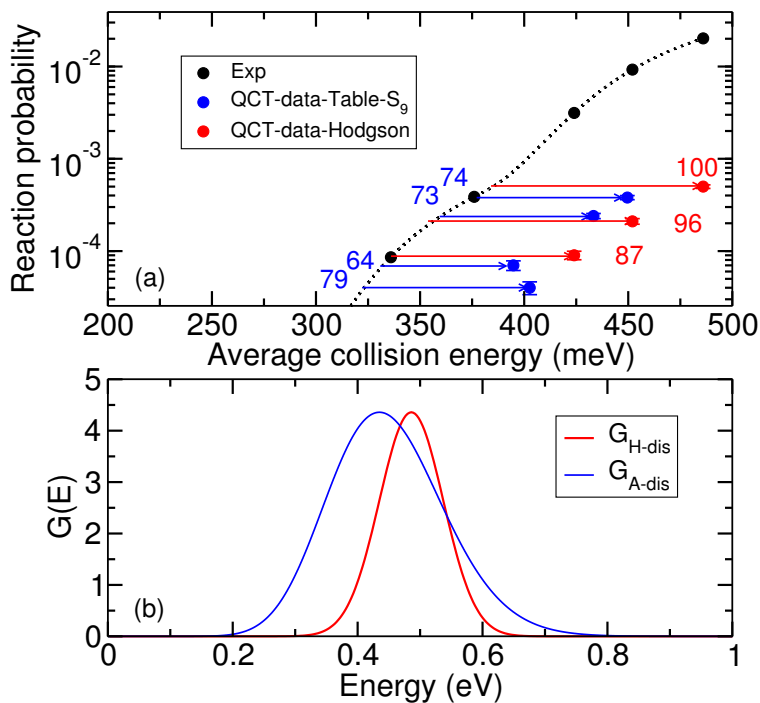


Figure 4.13: (a) Reaction probability for molecular beams of  $D_2$  dissociating on  $Ag(111)$  computed with the SRP48 functional. For comparison, experimental results [34] are plotted. Horizontal arrows and the number above these indicate the energy spacing between the theoretical reaction probability results and the interpolated experimental curve. (b) Energy distributions for two different set of beam parameters. The red curve shows the energy distribution ( $G_{H-dis}$ ,  $\bar{E} = 0.486$  eV,  $\sigma = 2.61 \times 10^{-3}$  eV) at the nozzle temperature 2012 K, and the blue curve presents the flux weighted velocity distributions  $G_{A-dis}$ , for  $\bar{E} = 0.449$  eV, at the nozzle temperature 1975 K.

should not improve the agreement with experiment, and would only lead to small changes.

The discrepancy between the molecular beam sticking probabilities and the QCT results is also not due to the neglect of non-adiabatic effects (electron-hole pair excitation). Work on reaction of  $H_2$  on copper surfaces (Refs. [23–25] and [27]) and on  $H_2 + Ag(111)$  [17, 76] suggests that including these effects would lead to a minor reduction of the reaction probability, increasing the disagreement with experiment further. Inclusion of phonon effects, however, could somewhat increase the reaction probability at the low energy sides of the reaction probability curves for specific  $\nu$  contributing to the sticking probability if there is a mechanical coupling to the surface phonons (if the barrier position moves with a phonon coordinate) [77], as in the surface oscillator model [78]. Additionally, the sticking probability could be increased somewhat if there is an electronic (or energetic) coupling with the surface phonons (if the barrier height changes with the phonon displacement coordinate) [77]. However, these effects are expected to be small, as there is a large mass mismatch between  $H_2$  and Ag, and the surface temperature in the molecular beam experiments was very low (100 K) [34]. Also, the mechanical and electronic couplings for  $H_2$  - metal surface interactions tend to be small [79] compared to the case of methane interacting with transition metal surfaces, for which the effects may be large [77]. Future research could show how large these effects are, but we note that including both effects is not likely to increase the agreement between the molecular beam experiment and calculations using the SRP48 functional.

The comparison of computed initial-state selected reaction probabilities and probabilities extracted from associative desorption experiments in Figures 4.8 and 4.9 suggests that using the PBE functional might lead to better agreement with the molecular beam experiments than the SRP48 functional. Thus, the PBE functional (or a PBE/RPBE mixture with a much lower RPBE weight than presently used (0.48)) might be a good starting point for the development of an SRP functional for  $H_2 + Ag(111)$ .

The lack of agreement found between the present calculations and the molecular beam sticking probabilities is at odds with the finding of transferability between  $CHD_3 + Ni(111)$  and  $Pt(111)$  [11]. A possible reason for the lack of transferability found is that the SRP48 functional is not based on a van der Waals correlation functional [80], as was the case for  $CHD_3 + Ni(111)$  and  $Pt(111)$  [11]. The only case [11] for which transferability has been established among systems in which one specific molecule interacts

with surfaces of different transition metals belonging to the same group so far involved a SRP functional incorporating a van der Waals correlation functional. For  $\text{H}_2 + \text{Cu}(111)$  such an SRP functional has already been identified [28], which gave a somewhat better overall description of experiments than the SRP48 functional, although the minimum barrier height obtained with the new functional exceeded that of the SRP48 functional by 76 meV [28].

The blue symbols in Figure 4.13 (a) show the computed results based on energy distributions and nozzle temperatures of pure  $\text{D}_2$  beams from the experiments on  $\text{D}_2 + \text{Cu}(111)$  reported by Auerbach *et al.* [5]. We call these energy distributions (*i.e.* the flux-weighted velocity distribution)  $G_{A-dis}$ . The energy differences between these computed results and the interpolated experimental curve are in the range 64–79 meV (1.5–1.8 kcal/mol). The theoretical sticking probabilities are therefore in somewhat better agreement with experiment if the more asymmetric incidence energy distributions of Auerbach and co-workers are used.

In Figure 4.13 (b), the energy distribution  $G_{A-dis}$  is wider and shows a longer tail towards high energies than  $G_{H-dis}$ . As a result, more molecules should be able to overcome the reaction barrier. As the  $G_{A-dis}$  curves should be more realistic, a better comparison between theory and experiment would be possible if we acquire more information on the experimental translational energy distributions, and in particular regarding their high energy tails.

Our finding that the initial state resolved reaction probabilities computed with the SRP48 functional are shifted to somewhat higher energies (by about 0.1 eV for  $\text{D}_2$ , see Figure 4.9) is consistent with our comparison for the molecular beam sticking measurements.

## 4.4 Conclusions

In order to investigate whether the SRP functional derived for the  $\text{H}_2 + \text{Cu}(111)$  system is transferable to the  $\text{H}_2 + \text{Ag}(111)$  system, where Ag is the same group as Cu, we have performed calculations on the dissociative chemisorption of  $\text{H}_2/\text{D}_2$  on  $\text{Ag}(111)$ .

The raw DFT data have been computed by the VASP software package and an accurate fitting method (the CRP) has been used to map out the 6D PES based on the SRP48 functional. The minimum barrier heights and geometries have been reported.

We have discussed the dynamics methods within the BOSS model. The QCT method has been used to compute the initial-state resolved reaction probabilities for several rovibrational states of  $D_2$  and  $H_2$ . The reliability of the QCT method, to accurately calculate the reaction probabilities for  $D_2 + Ag(111)$ , has been tested by a comparison with quantum dynamics calculations for the  $\nu = 1 - 3$ ,  $j = 0$  states of  $D_2$ . It was found that QCT reproduces the QD results very well.

Results for vibrationally (in)elastic scattering, *i.e.*, probabilities  $P(\nu = 2, j = 0 \rightarrow \nu = \nu')$  as function of incidence energy, have been presented and discussed. These calculations serve for better understanding of why we see reaction probabilities no larger than about 0.8 for high incidence energy. A clear competition was shown between vibrational inelastic scattering and reaction at higher incidence energies resulting in reaction probabilities saturating at 0.8 instead of what was assumed to be 1.0 in the fitting procedures of the experimental data [34].

A comparison of our computed initial-state resolved reaction probabilities with the computed state-specific reaction probabilities of the Jiang *et al.* group [39] and with the experimental associative desorption results of Hodgson and co-workers [37, 38] extracted by application of the detailed balance principle, has been presented. The comparison suggests that the barrier heights in the SRP48 PES are too high. Also, a non-monotonic dependence on incidence energy has been observed in our results for  $H_2$  dissociation at the highest  $\nu$  ( $\nu = 5$ ). A vibrational efficacy  $\eta_{\nu=0 \rightarrow 1}(P)$  greater than 1 has been reported for  $H_2(D_2)(\nu = 0, j = 0)$  and also for  $H_2(D_2)(\nu = 1, j = 0)$ . Such a high vibrational enhancement suggests that for low  $\nu$  (and high incidence energy) the molecule is not able to stay on the minimum energy path for reaction.

The computed reaction probabilities for several  $D_2$  vibrational states and  $j = 0$ , have been compared with data used to analyze the molecular beam experiments and reaction probabilities that were Boltzmann averaged over  $j$ . The comparison suggests that the rotational state averaging effect contributes to a larger width  $w$  in our computed vibrational state resolved reaction probabilities than found for the experimentally extracted reaction probability curves for specific  $\nu$ .

Finally, using the obtained QCT results, we have also simulated molecular beam sticking probabilities and compared with the experimental results of Cottrell *et al.* [34]. We have reported the energy differences between the computed data and the spline interpolated experimental curve to be in

the range of 2–2.3 kcal/mol. Thus, no chemical accuracy was achieved in our theoretical results. Theoretical calculations using flux weighted velocity distributions with the beam parameters taken from  $D_2 + Cu(111)$  experiment [5] have also been shown. We have found that these calculations are in somewhat better agreement with the experiment and energy differences between the computed results and interpolated experimental curve shrink to 1.5–1.8 kcal/mol. It has been suggested that the asymmetric incidence energy distributions should be more realistic and a better comparison between theory and experiment might result if more information about the experimental energy distributions of the beam would become available. The present comparison suggests that the PBE functional (or a PBE/RPBE mixture with a much lower RPBE weight than presently used (0.48)) might be a better starting point for the development of an SRP functional for  $H_2 + Ag(111)$  than the SRP48 functional.

Our finding of a vibrational efficacy greater than one suggests that a trial-and-error procedure involving dynamics calculations will be required to obtain a new SRP functional for  $H_2 + Ag(111)$ , as the  $H_2$  molecule is apparently unable to follow the minimum energy path. This would seem to disqualify a procedure based solely on static energy profiles. Ultimately, our results for reaction based on the SRP48 functional systematically underestimate the available experimental results. Therefore it is concluded that a chemically accurate description of the dissociative chemisorption of  $D_2$  on  $Ag(111)$  is not yet obtained with the SRP48 DFT functional. Despite the chemically accurate description of dissociative chemisorption of  $H_2$  on  $Cu(111)$  with the SRP48 functional, it is not transferable to the  $H_2 + Ag(111)$  system, although  $Cu$  and  $Ag$  belong to the same group.

## References

1. Noyori, R. Synthesizing Our Future. *Nature Chemistry*, 5–6 (2009).
2. Wolcott, C. A., Medford, A. J., Studt, F. & Campbell, C. T. Degree of Rate Control Approach to Computational Catalyst Screening. *Journal of Catalysis* **330**, 197–207 (2015).
3. Sabbe, M. K., Reyniers, M.-F. & Reuter, K. First-Principles Kinetic Modeling in Heterogeneous Catalysis: An Industrial Perspective on Best-Practice, Gaps and Needs. *Catalysis Science & Technology* **2**, 2010–2024 (2012).
4. Ertl, G. Primary Steps in Catalytic Synthesis of Ammonia. *Journal of Vacuum Science & Technology A* **1**, 1247–1253 (1983).
5. Díaz, C. *et al.* Chemically Accurate Simulation of a Prototypical Surface Reaction:  $H_2$  Dissociation on  $Cu(111)$ . *Science* **326**, 832–834 (2009).
6. Kroes, G. J. Toward a Database of Chemically Accurate Barrier Heights for Reactions of Molecules with Metal Surfaces. *Journal of Physical Chemistry Letters* **6**, 4106–4114 (2015).
7. Peverati, R. & Truhlar, D. G. An Improved and Broadly Accurate Local Approximation to the Exchange-Correlation Density Functional: The MN12-L Functional for Electronic Structure Calculations in Chemistry and Physics. *Physical Chemistry Chemical Physics* **14**, 13171–13174 (2012).
8. Sementa, L. *et al.* Reactive Scattering of  $H_2$  from  $Cu(100)$ : Comparison of Dynamics Calculations Based on the Specific Reaction Parameter Approach to Density Functional Theory with Experiment. *Journal of Chemical Physics* **138** (2013).
9. Ghassemi, E. N., Wijzenbroek, M., Somers, M. F. & Kroes, G. J. Chemically Accurate Simulation of Dissociative Chemisorption of  $D_2$  on  $Pt(111)$ . *Chemical Physics Letters* **683**. Ahmed Zewail (1946-2016) Commemoration Issue of Chemical Physics Letters, 329–335 (2017).
10. Nattino, F. *et al.* Chemically Accurate Simulation of a Polyatomic Molecule-Metal Surface Reaction. *Journal of Physical Chemistry Letters* **7**, 2402–2406 (2016).



11. Migliorini, D. *et al.* Surface Reaction Barriometry: Methane Dissociation on Flat and Stepped Transition-Metal Surfaces. *Journal of Physical Chemistry Letters* **8**, 4177–4182 (2017).
12. Nattino, F., Díaz, C., Jackson, B. & Kroes, G. J. Effect of Surface Motion on the Rotational Quadrupole Alignment Parameter of D<sub>2</sub> Reacting on Cu(111). *Physical Review Letters* **108**, 236104 (2012).
13. Wijzenbroek, M., Helstone, D., Meyer, J. & Kroes, G. J. Dynamics of H<sub>2</sub> Dissociation on the Close-Packed (111) Surface of the Noblest Metal: H<sub>2</sub> + Au(111). *Journal of Chemical Physics* **145**, 144701 (2016).
14. Shuai, Q., Kaufmann, S., Auerbach, D. J., Schwarzer, D. & Wodtke, A. M. Evidence for Electron-Hole Pair Excitation in the Associative Desorption of H<sub>2</sub> and D<sub>2</sub> from Au(111). *Journal of Physical Chemistry Letters* **8**, 1657–1663 (2017).
15. Karplus, M., Porter, R. N. & Sharma, R. D. Exchange Reactions with Activation Energy. I. Simple Barrier Potential for (H, H<sub>2</sub>). *Journal of Chemical Physics* **43**, 3259–3287 (1965).
16. Maurer, R. J., Jiang, B., Guo, H. & Tully, J. C. Mode Specific Electronic Friction in Dissociative Chemisorption on Metal Surfaces: H<sub>2</sub> on Ag(111). *Physical Review Letters* **118**, 256001 (2017).
17. Zhang, Y., Maurer, R. J., Guo, H. & Jiang, B. Hot-Electron Effects during Reactive Scattering of H<sub>2</sub> from Ag(111): the Interplay between Mode-Specific Electronic Friction and the Potential Energy Landscape. *Chemical Science* **10**, 1089–1097 (2019).
18. Hasselbrink, E. Non-Adiabaticity in Surface Chemical Reactions. *Surface Science* **603**. Special Issue of Surface Science dedicated to Prof. Dr. Dr. h.c. mult. Gerhard Ertl, Nobel-Laureate in Chemistry 2007, 1564–1570 (2009).
19. Gergen, B., Nienhaus, H., Weinberg, W. H. & McFarland, E. W. Chemically Induced Electronic Excitations at Metal Surfaces. *Science* **294**, 2521–2523 (2001).
20. Schindler, B., Diesing, D. & Hasselbrink, E. Electronically Nonadiabatic Processes in the Interaction of H with a Au Surface Revealed Using MIM Junctions: The Temperature Dependence. *Journal of Physical Chemistry C* **117**, 6337–6345 (2013).

21. Wijzenbroek, M. & Kroes, G. J. The Effect of the Exchange-Correlation Functional on  $H_2$  Dissociation on Ru(0001). *Journal of Chemical Physics* **140** (2014).
22. Nieto, P. *et al.* Reactive and Nonreactive Scattering of  $H_2$  from a Metal Surface Is Electronically Adiabatic. *Science* **312**, 86–89 (2006).
23. Luntz, A. C. & Persson, M. How Adiabatic Is Activated Adsorption/Associative Desorption? *Journal of Chemical Physics* **123**, 074704 (2005).
24. Muzas, A. S. *et al.* Vibrational Deexcitation and Rotational Excitation of  $H_2$  and  $D_2$  Scattered from Cu(111): Adiabatic Versus Non-adiabatic Dynamics. *Journal of Chemical Physics* **137**, 064707 (2012).
25. Juaristi, J. I., Alducin, M., Muiño, R. D., Busnengo, H. F. & Salin, A. Role of Electron-Hole Pair Excitations in the Dissociative Adsorption of Diatomic Molecules on Metal Surfaces. *Physical Review Letters* **100**, 116102 (2008).
26. Fücksel, G., Schimka, S. & Saalfrank, P. On the Role of Electronic Friction for Dissociative Adsorption and Scattering of Hydrogen Molecules at a Ru(0001) Surface. *Journal of Physical Chemistry A* **117**, 8761–8769 (2013).
27. Spiering, P. & Meyer, J. Testing Electronic Friction Models: Vibrational De-Excitation in Scattering of  $H_2$  and  $D_2$  from Cu(111). *Journal of Physical Chemistry Letters* **9**, 1803–1808 (2018).
28. Wijzenbroek, M., Klein, D. M., Smits, B., Somers, M. F. & Kroes, G. J. Performance of a Non-Local van der Waals Density Functional on the Dissociation of  $H_2$  on Metal Surfaces. *Journal of Physical Chemistry A* **119**, 12146–12158 (2015).
29. Kroes, G. J. & Díaz, C. Quantum and Classical Dynamics of Reactive Scattering of  $H_2$  from Metal Surfaces. *Chemical Society Reviews* **45**, 3658–3700 (2016).
30. Yu, C.-f., Whaley, K. B., Hogg, C. S. & Sibener, S. J. Selective Adsorption Resonances in the Scattering of n- $H_2$  p- $H_2$  n- $D_2$  and o- $D_2$  from Ag(111). *Physical Review Letters* **51**, 2210–2213 (1983).
31. Horne, J. M., Yerkes, S. C. & Miller, D. R. An Experimental Investigation of the Elastic Scattering of He and  $H_2$  from Ag(111). *Surface Science* **93**, 47–63 (1980).

32. Asada, H. Specular Reflection of Helium and Hydrogen Molecular Beams from the (111) Plane of Silver. *Surface Science* **81**, 386–408 (1979).
33. Healey, F., Carter, R., Worthy, G. & Hodgson, A. Endothermic Dissociative Chemisorption of Molecular D<sub>2</sub> on Ag(111). *Chemical Physics Letters* **243**, 133–139 (1995).
34. Cottrell, C., Carter, R. N., Nesbitt, A., Samson, P. & Hodgson, A. Vibrational State Dependence of D<sub>2</sub> Dissociation on Ag(111). *Journal of Chemical Physics* **106**, 4714–4722 (1997).
35. King, D. A. & Wells, M. G. Reaction Mechanism in Chemisorption Kinetics: Nitrogen on the 100 Plane of Tungsten. *Proceedings of the Royal Society of London A: Mathematical, Physical and Engineering Sciences* **339**, 245–269 (1974).
36. Healey, F., Carter, R. & Hodgson, A. The Recombinative Desorption of D<sub>2</sub> from Ag(111): Temperature-Programmed Desorption and Low Energy Electron Diffraction. *Surface Science* **328**, 67–79 (1995).
37. Murphy, M. J. & Hodgson, A. Translational Energy Release in the Recombinative Desorption of H<sub>2</sub> from Ag(111). *Surface Science* **390**, 29–34 (1997).
38. Murphy, M. J. & Hodgson, A. Role of Surface Thermal Motion in the Dissociative Chemisorption and Recombinative Desorption of D<sub>2</sub> on Ag(111). *Physical Review Letters* **78**, 4458–4461 (1997).
39. Jiang, B. & Guo, H. Six-Dimensional Quantum Dynamics for Dissociative Chemisorption of H<sub>2</sub> and D<sub>2</sub> on Ag(111) on a Permutation Invariant Potential Energy Surface. *Physical Chemistry Chemical Physics* **16**, 24704–24715 (2014).
40. Perdew, J. P., Burke, K. & Ernzerhof, M. Generalized Gradient Approximation Made Simple. *Physical Review Letters* **77**, 3865–3868 (1996).
41. Hammer, B., Hansen, L. B. & Nørskov, J. K. Improved Adsorption Energetics within Density-Functional Theory Using Revised Perdew-Burke-Ernzerhof Functionals. *Physical Review B* **59**, 7413–7421 (1999).
42. Busnengo, H. F., Salin, A. & Dong, W. Representation of the 6D Potential Energy Surface for a Diatomic Molecule Near a Solid Surface. *Journal of Chemical Physics* **112**, 7641–7651 (2000).

CHAPTER 4. TEST OF THE TRANSFERABILITY OF THE  
SPECIFIC REACTION PARAMETER FUNCTIONAL FOR  
 $H_2 + CU(111)$  TO  $D_2 + AG(111)$

126

43. Frankcombe, T. J., Collins, M. A. & Zhang, D. H. Modified Shepard Interpolation of Gas-Surface Potential Energy Surfaces with Strict Plane Group Symmetry and Translational Periodicity. *Journal of Chemical Physics* **137** (2012).
44. Fücksel, G. *et al.* Anomalous Dependence of the Reactivity on the Presence of Steps: Dissociation of  $D_2$  on  $Cu(211)$ . *Journal of Physical Chemistry Letters* **9**, 170–175 (2018).
45. J. Stoer, R. B. *Introduction to Numerical Analysis* (Springer: New York, 1980).
46. Marston, C. C. & Balint-Kurti, G. G. The Fourier Grid Hamiltonian Method for Bound State Eigenvalues and Eigenfunctions. *Journal of Chemical Physics* **91**, 3571–3576 (1989).
47. Kosloff, R. Time-Dependent Quantum-Mechanical Methods for Molecular Dynamics. *Journal of Physical Chemistry* **92**, 2087–2100 (1988).
48. Pijper, E., Kroes, G. J., Olsen, R. A. & Baerends, E. J. Reactive and Diffractive Scattering of  $H_2$  from  $Pt(111)$  Studied Using a Six-Dimensional Wave Packet Method. *Journal of Chemical Physics* **117**, 5885–5898 (2002).
49. Light, J. C., Hamilton, I. P. & Lill, J. V. Generalized Discrete Variable Approximation in Quantum Mechanics. *Journal of Chemical Physics* **82**, 1400–1409 (1985).
50. Corey, G. C. & Lemoine, D. Pseudospectral Method for Solving the Time-Dependent Schrödinger Equation in Spherical Coordinates. *Journal of Chemical Physics* **97**, 4115–4126 (1992).
51. Lemoine, D. The Finite Basis Representation as the Primary Space in Multidimensional Pseudospectral Schemes. *Journal of Chemical Physics* **101**, 10526–10532 (1994).
52. Feit, M., Fleck, J. & Steiger, A. Solution of the Schrödinger Equation by a Spectral Method. *Journal of Computational Physics* **47**, 412–433 (1982).
53. Balint-Kurti, G. G., Dixon, R. N. & Marston, C. C. Time-Dependent Quantum Dynamics of Molecular Photofragmentation Processes. *Journal of Chemical Society, Faraday Transactions* **86**, 1741–1749 (1990).

54. Balint-Kurti, G. G., Dixon, R. N. & Marston, C. C. Grid Methods for Solving the Schrödinger Equation and Time Dependent Quantum Dynamics of Molecular Photofragmentation and Reactive Scattering Processes. *International Reviews in Physical Chemistry* **11**, 317–344 (1992).
55. Mowrey, R. C. & Kroes, G. J. Application of an Efficient Asymptotic Analysis Method to Molecule–Surface Scattering. *Journal of Chemical Physics* **103**, 1216–1225 (1995).
56. Vibok, A. & Balint-Kurti, G. G. Parametrization of Complex Absorbing Potentials for Time-Dependent Quantum Dynamics. *Journal of Physical Chemistry* **96**, 8712–8719 (1992).
57. Michelsen, H. A., Rettner, C. T., Auerbach, D. J. & Zare, R. N. Effect of Rotation on the Translational and Vibrational Energy Dependence of the Dissociative Adsorption of D<sub>2</sub> on Cu(111). *Journal of Chemical Physics* **98**, 8294–8307 (1993).
58. Rettner, C. T., Michelsen, H. A. & Auerbach, D. J. Quantum-State-Specific Dynamics of the Dissociative Adsorption and Associative Desorption of H<sub>2</sub> at a Cu(111) Surface. *Journal of Chemical Physics* **102**, 4625–4641 (1995).
59. Díaz, C., Olsen, R. A., Auerbach, D. J. & Kroes, G. J. Six-Dimensional Dynamics Study of Reactive and Non Reactive Scattering of H<sub>2</sub> from Cu(111) Using a Chemically Accurate Potential Energy Surface. *Physical Chemistry Chemical Physics* **12**, 6499–6519 (2010).
60. Michelsen, H. A. & Auerbach, D. J. A Critical Examination of Data on the Dissociative Adsorption and Associative Desorption of Hydrogen at Copper Surfaces. *Journal of Chemical Physics* **94**, 7502–7520 (1991).
61. Swanson, H. E. & Tatge, E. Standard X-ray Diffraction Powder Patterns. *National Bureau of Standard (US) Circular* **1**, 23–24 (1953).
62. Liu, L. & Bassett, W. A. Compression of Ag and Phase Transformation of NaCl. *Journal of Applied Physics* **44**, 1475–1479 (1973).
63. Darling, G. R. & Holloway, S. Translation-to-Vibrational Excitation in the Dissociative Adsorption of D<sub>2</sub>. *Journal of Chemical Physics* **97**, 734–736 (1992).

64. Darling, G. & Holloway, S. Dissociation Thresholds and the Vibrational Excitation Process in the Scattering of  $H_2$ . *Surface Science* **307**, 153–158 (1994).
65. Hand, M. & Holloway, S. The Scattering of  $H_2$  and  $D_2$  From  $Cu(100)$ : Vibrationally Assisted Dissociative Adsorption. *Surface Science* **211-212**, 940–947 (1989).
66. Hand, M. R. & Holloway, S. A Theoretical Study of the Dissociation of  $H_2/Cu$ . *Journal of Chemical Physics* **91**, 7209–7219 (1989).
67. Polanyi, J. C. Some Concepts in Reaction Dynamics. *Science* **236**, 680–690 (1987).
68. Gross, A. & Scheffler, M. Influence of Molecular Vibrations on Dissociative Adsorption. *Chemical Physics Letters* **256**, 417–423 (1996).
69. Pijper, E., Kroes, G. J., Olsen, R. A. & Baerends, E. J. The Effect of Corrugation on the Quantum Dynamics of Dissociative and Diffractive Scattering of  $H_2$  from  $Pt(111)$ . *Journal of Chemical Physics* **113**, 8300–8312 (2000).
70. Díaz, C. & Olsen, R. A. A Note on the Vibrational Efficacy in Molecule-Surface Reactions. *Journal of Chemical Physics* **130**, 094706 (2009).
71. Smith, R. R., Killelea, D. R., DelSesto, D. F. & Utz, A. L. Preference for Vibrational Over Translational Energy in a Gas-Surface Reaction. *Science* **304**, 992–995 (2004).
72. Levine, R. D. in (Cambridge University Press: Cambridge, 2005).
73. Darling, G. R. & Holloway, S. The Dissociation of Diatomic Molecules at Surfaces. *Reports on Progress in Physics* **58**, 1595 (1995).
74. Laurent, G., Daz, C., Busnengo, H. F. & Martn, F. Nonmonotonic Dissociative Adsorption of Vibrationally Excited  $H_2$  on metal surfaces. *Physical Review B* **81**, 161404 (2010).
75. Hu, X., Jiang, B., Xie, D. & Guo, H. Site-Specific Dissociation Dynamics of  $H_2/D_2$  on  $Ag(111)$  and  $Co(0001)$  and the Validity of the Site-Averaging Model. *Journal of Chemical Physics* **143**, 114706 (2015).
76. Maurer, R. J., Jiang, B., Guo, H. & Tully, J. C. Mode Specific Electronic Friction in Dissociative Chemisorption on Metal Surfaces:  $H_2$  on  $Ag(111)$ . *Physical Review Letters* **118**, 256001 (2017).

77. Nave, S., Tiwari, A. K. & Jackson, B. Dissociative Chemisorption of Methane on Ni and Pt Surfaces: Mode-Specific Chemistry and the Effects of Lattice Motion. *Journal of Physical Chemistry A* **118**, 9615–9631 (2014).
78. Hand, M. & Harris, J. Recoil Effects in Surface Dissociation. *Journal of Chemical Physics* **92**, 7610–7617 (1990).
79. Bonfanti, M., Díaz, C., Somers, M. F. & Kroes, G. J. Hydrogen Dissociation on Cu(111): the Influence of Lattice Motion. Part I. *Physical Chemistry Chemical Physics* **13**, 4552–4561 (2011).
80. Dion, M., Rydberg, H., Schröder, E., Langreth, D. C. & Lundqvist, B. I. van der Waals Density Functional for General Geometries. *Physical Review Letters* **92**, 246401 (2004).





**Transferability of the  
Specific Reaction Parameter  
Density Functional for  
 $\text{H}_2 + \text{Pt}(111)$  to  
 $\text{H}_2 + \text{Pt}(211)$**

This chapter is based on:

Elham Nour Ghassemi, Egidius W. F. Smeets, Mark F. Somers, Geert-Jan Kroes, Irene M. N. Groot, Ludo B. F. Juurlink, and Gernot Fuchs. *The Journal of Physical Chemistry C* **123**(5), 2973-2986, 2019.



## Abstract

The accurate description of heterogeneously catalyzed reactions may require the chemically accurate evaluation of barriers for reactions of molecules at edges of metal nanoparticles. It was recently shown that a semi-empirical density functional describing the interaction of a molecule dissociating on a flat metal surface ( $\text{CHD}_3 + \text{Pt}(111)$ ) is transferable to the same molecule reacting on a stepped surface of the same metal ( $\text{Pt}(211)$ ). However, validation of the method for additional systems is desirable. To address the question whether the specific reaction parameter (SRP) functional that describes  $\text{H}_2 + \text{Pt}(111)$  with chemical accuracy is capable of also accurately describing  $\text{H}_2 + \text{Pt}(211)$ , we have performed molecular beam simulations with the quasi-classical trajectory (QCT) method, using the SRP functional developed for  $\text{H}_2 + \text{Pt}(111)$ . Our calculations used the Born-Oppenheimer static surface (BOSS) model. The accuracy of the QCT method was assessed by comparison with quantum dynamics (QD) results for reaction of the ro-vibrational ground state of  $\text{H}_2$ . The theoretical results for sticking of  $\text{H}_2$  and  $\text{D}_2$  on  $\text{Pt}(211)$  are in quite good agreement with experiment, but uncertainties remain due to a lack of accuracy of the QCT simulations at low incidence energies, and possible inaccuracies in the reported experimental incidence energies at high energies. We also investigated the non-adiabatic effect of electron-hole pair excitation on the reactivity using the molecular dynamics with electronic friction (MDEF) method, employing the local density friction approximation (LDFA). Only small effects of electron-hole pair excitation on sticking are found.

## 5.1 Introduction

The heterogeneous catalysis community is highly interested in stepped surfaces because structure-sensitive catalyzed reactions often occur at edges of nanoparticles. These edges contain low-coordinated surface atoms, which resemble the atoms present at step edges of stepped surfaces. Consequently, a number of experiments have addressed dissociative chemisorption reactions of molecules on stepped surfaces, such as NO at steps on defective Ru(0001) [1],  $\text{H}_2$  on stepped Pt surfaces [2–8],  $\text{N}_2$  at steps on defective

Ru(0001) [9, 10], and methane on Pt surfaces [11, 12], to name but a few examples. A much lower number of theoretical dynamics studies have addressed dissociative chemisorption on stepped surfaces, and these studies have looked at  $H_2 + Pt(211)$  [13–17],  $H_2 + Cu(211)$  [18, 19],  $H_2$  dissociation on defective Pd(111) [20], and at  $CHD_3 + Pt(211)$  [12, 21–24].

In view of the importance of dissociative chemisorption reactions on stepped surfaces to heterogeneous catalysis, it would obviously be useful to have a predictive procedure in place for accurately evaluating the interaction between a molecule and a stepped surface. Recent experimental work suggests that such a procedure may be based on experiments and dynamics calculations based on semi-empirical density functional theory (DFT) for the electronic structure, for the same molecule interacting with a low-index, flat surface of the same metal [12]. As has now been established for several systems, dynamics calculations based on electronic structure calculations with the specific reaction parameter approach to DFT (SRP–DFT) are able to reproduce sticking measurements on such systems with chemical accuracy [12, 25–28]. Very recently, it has been shown that the SRP density functional (SRP–DF) for  $CHD_3$  interacting with the flat Pt(111) system is transferable to the same molecule interacting with the stepped Pt(211) system [12] (transferability of the SRP DF from  $H_2 + Cu(111)$  [12] to  $H_2 + Cu(100)$  [26], *i.e.*, among systems in which the same molecule interacts with different flat, low-index surfaces, had been established earlier [26]). However, this finding just concerned only one specific system, and it is important to check whether this finding also holds for other systems. The main goal of this work is to investigate whether the SRP–DF recently determined for  $H_2 + Pt(111)$  [28] is also capable of yielding chemically accurate results for  $H_2 + Pt(211)$ .

The system of interest to our study ( $H_2 + Pt(211)$ ) has first been studied theoretically. Olsen *et al.* [13] computed a six-dimensional (6D) potential energy surface (PES) for the system with DFT, using the GGA functional due to Becke [29] and Perdew [30] (BP), and interpolating the DFT results with the corrugation reducing procedure (CRP) [31]. They next performed classical trajectory studies on this PES within the Born-Oppenheimer and static surface (BOSS) approximations. On the basis of these calculations, they were able to show that a trapping mechanism contributes a component to the sticking probability which is high at low incidence energy ( $E_i$ ) and decreases monotonically with  $E_i$  [13]. In this mechanism,  $H_2$  gets trapped at an unreactive site, *i.e.*, at the bottom of the step, and then diffuses to

an atom at the top of the step edge, where it subsequently reacts.

Next, McCormack *et al.* also analyzed the other contributing mechanisms to the sticking of H<sub>2</sub> on Pt(211) [14]. Their classical trajectory calculations using the same PES as used before showed two additional mechanisms. A mechanism in which H<sub>2</sub> reacts directly at the step is non-activated and contributes equally at all  $E_i$ . In an additional mechanism, H<sub>2</sub> reacts on the terrace. In this mechanism the reaction is activated, yielding a contribution to the sticking that rises monotonically with increasing  $E_i$ . By scaling the contributions from the different mechanisms according to the different lengths of the (111) terraces in the Pt(211) and Pt(533) surfaces (both exhibiting (111) terraces and (100) steps), they [14] were able to obtain good agreement with previous experiments on H<sub>2</sub> + Pt(533) [6].

In two subsequent studies using the same PES, Luppi *et al.* [15] investigated rotational effects with classical trajectory calculations, while Olsen *et al.* [17] made a comparison between quantum dynamics and classical dynamics results for reaction of ( $\nu = 0, j = 0$ ) H<sub>2</sub>. According to the classical trajectory studies of Luppi *et al.*, the trapping-mediated contribution to the reaction, which leads to a high sticking probability at low  $E_i$ , but which contribution then quickly decreases with  $E_i$ , should be present for low rotational states ( $j = 0$  and 1), but should disappear for states with intermediate  $j$ . The reason they provided is that energy transfer to rotation should cause trapping for  $j = 0$  and  $j = 1$ , while energy transfer from rotation should instead hinder trapping. Olsen *et al.* found that QCT calculations were in good agreement with quantum dynamics results for high  $E_i$  (in excess of 0.1 eV). However, the QCT study overestimated the trapping-mediated contribution to the reaction at low  $E_i$ , which was attributed to one mechanism operative for trapping in the classical calculations (excitation of the rotation) not being allowed in quantum dynamics, as the trapping well should not support rotationally excited bound states for their PES [17].

H<sub>2</sub> + Pt(211) has also been studied experimentally by Groot *et al.* [7, 8, 32]. Their molecular beam sticking probabilities [7] were in reasonable agreement with the quantum dynamics results for ( $\nu = 0, j = 0$ ) H<sub>2</sub> of Olsen *et al.* [17], although the quantum dynamics results based on the BP functional overestimated the sticking at high  $E_i$ . Likewise, there were discrepancies at low  $E_i$ , with the computed trapping-mediated contribution to the sticking being too low compared to the experimental result. In two subsequent papers, Groot *et al.* showed that the sticking on surfaces with longer (111) terraces and (100) steps (Pt(533) and Pt(755)) can successfully

be modeled based on the contributing mechanisms to sticking at the step and at the terrace on Pt(211) [8, 32], much like McCormack *et al.* had done before for Pt(533) [14]. They also used their results to analyze the contributions of facets and edges of Pt nanoparticles to  $H_2$  dissociation proceeding on these nanoparticles [8].

The goal of this chapter is to test whether the SRP–DF for  $H_2 + Pt(111)$  is transferable to  $H_2 + Pt(211)$ . For this reason, we will put emphasis on the comparison of sticking probabilities computed with a PES obtained with the SRP–DF for  $H_2 + Pt(111)$  with the experimental results of Ref. [8], taking the experimental conditions (velocity distributions of the beams, nozzle temperatures  $T_n$  used) into account as fully as possible. Our calculations are done within the BOSS model, and mainly use the QCT method for the dynamics. We will not reanalyze the mechanisms contributing to the reaction, simply noting that the dependence of the computed sticking probabilities on  $E_i$  is in accordance with conclusions arrived at earlier by Olsen *et al.* [13] and McCormack *et al.* [14]. We find that, overall, the computed sticking probability is in good agreement with experiment for both  $H_2$  and  $D_2 + Pt(211)$ , suggesting that the transferability may well hold. However, at present this conclusion is not yet certain due to uncertainties in the parameters needed to describe the molecular beams used in the experiments. Our results suggest that, once more precisely defined experimental results become available, the comparison with experiment should be revisited on the basis of quantum dynamics calculations.

This chapter is set up as follows. Section 5.2.1 describes the dynamical model, and Section 5.2.2 and Section 5.2.3 describe the construction of the PES and the PES interpolation method. The dynamics methods used here are explained in Section 5.2.4 and Section 5.2.5. Section 5.2.6 describes how we calculate the observables. Section 5.2.7 provides computational details. In Section 5.3, the results of the calculations are shown and discussed. Section 5.3.1 describes the computed PES. In Section 5.3.2, we compare the QCT results with the QD results. The isotope effect of the QCT results for reaction of ( $\nu = 0, j = 0$ )  $H_2$  and  $D_2$  is shown and discussed in Section 5.3.3. Section 5.3.4 provides theoretical results on molecular beam sticking probabilities and comparison with the experimental data. In Section 5.3.5, the effect of electron-hole pair excitation on the reactivity is discussed and the MDEF results are compared with the MD results for sticking. Conclusions are provided in Section 5.4.

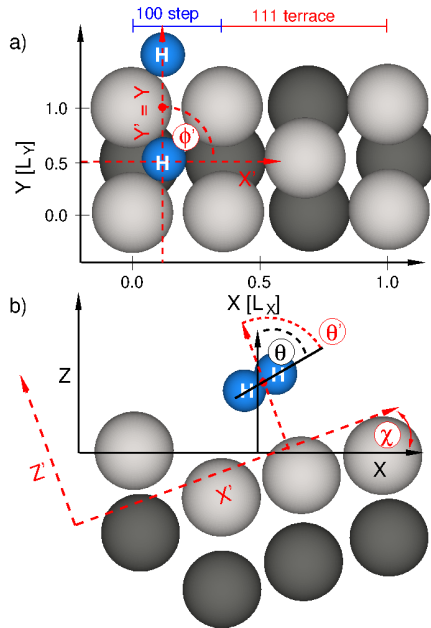


Figure 5.1: Coordinate systems for H<sub>2</sub> on Pt(211). (a) Top view of the (1×1) unit cell showing also the dissociated reference geometry of H<sub>2</sub> used to converge the computational setup with respect to the adsorption energy  $E_{ads}$ . First and second layer Pt atoms are in silver and dark gray, respectively. H atoms are blue colored. (b) Side view of the slab model. The Z-axis (molecule-surface distance) in the standard coordinate system drawn in black is aligned with the normal to the macroscopic surface. X and Y are the lateral components of the COM position of H<sub>2</sub> indicated by a red dot. Furthermore,  $r$  is the interatomic H–H distance (not shown) and the angular orientation is specified by the polar angle  $\theta \in [0, \pi]$  and the azimuthal angle  $\phi \in [0, 2\pi]$  (not shown). The angular orientation of H<sub>2</sub> in the internal coordinate system is defined with respect to the normal of the (111) terrace, as shown in red. The two coordinate systems include an angle  $\chi$  of 20°. The corresponding angular coordinates are  $\{\theta', \phi'\}$ . The surface lattice constants are  $L_X = 6.955 \text{ \AA}$  and  $L_Y = 2.839 \text{ \AA}$ .

## 5.2 Theoretical methodology

### 5.2.1 Dynamical model

The dynamics simulations presented in the following approach the true reaction dynamics of the system by assuming the reaction to take place on an ideal rigid Pt(211) surface at zero coverage. During the entire dynamics, the surface atoms are fixed at their initial equilibrium positions as obtained from DFT calculations. The dynamical degrees of freedom (DOF) treated here are the six DOF of  $H_2$ . These are the center-of-mass (COM) position given by Cartesian coordinates  $X, Y, Z$  relative to a surface atom, the interatomic H–H distance  $r$  and the angular orientation of the molecule defined with respect to the macroscopic surface plane. As usual,  $X, Y$  are the lateral components of the COM position and  $Z$  is the molecule-surface distance. The orientation of the molecule is specified by the polar angle  $\theta \in [0, \pi]$  and the azimuthal angle  $\phi \in [0, 2\pi]$ . The corresponding coordinate system is visualized in Figure 5.1.

### 5.2.2 Electronic structure calculations

In this work, electronic structure calculations are carried out using periodic DFT as implemented in the *Vienna Ab Initio Simulation Package* (VASP) [33–36]. Specifically, we employ an exchange-correlation functional of the form:

$$E_{XC} = E_X^{PBE\alpha} + E_C^{vdW-DF2} \quad (5.1)$$

which contains PBE $\alpha$  exchange [37] and the vdW-DF2-functional of Lundquist and Langreth and co-workers [38]. The latter accounts for long-range van der Waals interactions. The  $\alpha$ -value was set to 0.57 according to our previous work [28] where we have determined this value to be suitable in order to bring computed and measured [39] sticking probabilities for  $D_2$  on Pt(111) in quantitative agreement, see also Chapter 3. At first sight, the strategy of fitting a DFT functional to an experiment performed on a particular system might lead to a functional that is too specific to be accurate also for other systems, even though they might appear very similar chemically. However, recent theoretical work on the dissociation of molecular hydrogen on different facets of Cu [25, 26] and methane dissociation on nickel [27] and platinum [12] surfaces have shown that so-optimized functionals may indeed be transferable among different but chemically similar systems. This sug-



gests that the SRP functional designed for the  $D_2 + \text{Pt}(111)$  system might be of similar accuracy for the  $D_2(\text{H}_2) + \text{Pt}(211)$  system.

The DFT calculations on the  $D_2 + \text{Pt}(211)$  system presented here are based on a  $\text{Pt}(211)$  slab model with four layers using a  $(1 \times 2)$  supercell. As often done for hydrogen + metal systems, we here assume effects resulting from surface atom motion on the dissociation dynamics to be negligible at the relevant experimental conditions to which we will compare our simulations. Consequently, we content ourselves with a representation of the interaction potential for a frozen  $\text{Pt}(211)$  surface. The surface atom positions of the three uppermost layers are initially optimized by relaxing the  $\text{Pt}$  slab, but then kept frozen for all subsequent calculations on the system. We took care that the mirror axis was not affected by the geometry optimization of the slab. The resulting slab model obeys the symmetry of the  $p1m1$  plane group [18]. This is helpful in reducing the computational burden associated with the construction of the 6D PES, as we will show below. Similar to Ref. [18], the vacuum gap separating periodic slab images is about 16.2 Å. We use a  $\Gamma$ -centered  $7 \times 7 \times 1$  k-point mesh generated according to the Monkhorst grid scheme [40]. The energy cut-off,  $E_{\text{PAW}}$ , used in the projector augmented wave (PAW) method was set to 450 eV. We employ Fermi smearing with a width of 0.1 eV. The optimal number of k-points and surface layers, and the optimal  $E_{\text{PAW}}$  value were determined by convergence calculations as summarized in table 5.1. There, we list the adsorption energy  $E_{\text{ads}}$  computed as difference between the minimum energy of  $\text{H}_2$  at its equilibrium distance  $r_{\text{eq}} \approx 0.74$  Å in the gas phase (here about 6 Å away from the surface, and parallel to the surface) and the dissociatively adsorbed configuration of  $\text{H}_2$  on  $\text{Pt}(211)$  as depicted in Figure 5.1.  $E_{\text{ads}}$ -values are listed in table 5.1 for different slab thicknesses, k-point meshes, and cut-off energies. The lattice constants of the rectangular  $(1 \times 1)$  surface unit cell are  $L_X = 6.955$  Å along the  $X$ -axis and  $L_Y = 2.839$  Å along the  $Y$ -axis, corresponding to a bulk lattice constant  $D$  of 4.016 Å. The latter value compares reasonably well with the experimental value ( $D = 3.916$  Å [41]).

### 5.2.3 Representation of the potential energy surface

In order to construct a continuous electronic ground state PES for molecular hydrogen interacting with a rigid  $\text{Pt}(211)$  system, we adopt the CRP [31] which allows for a fast and accurate interpolation of DFT data points. The

Table 5.1: Adsorption energies  $E_{ads}$  in eV for  $H_2$  on Pt(211) computed using different k-point meshes, cut-off energies  $E_{\text{PAW}}$  and number of layers in the slab. The  $E_{ads}$ -value obtained with a converged computational setup is marked by an asterisk. The reference geometry of dissociated  $H_2$  used to determine  $E_{ads}$  is shown in Figure 5.1.

$E_{\text{PAW}}$ [eV]	4 layer slab				5 layer slab			
	350	400	450	500	350	400	450	500
$5 \times 5 \times 1$	0.951	0.940	0.934	0.931	0.951	0.939	0.934	0.931
$6 \times 6 \times 1$	0.952	0.941	0.935	0.932	0.951	0.940	0.934	0.931
$7 \times 7 \times 1$	0.962	0.952	0.945*	0.943	0.962	0.951	0.945	0.942
$8 \times 8 \times 1$	0.963	0.953	0.947	0.944	0.953	0.952	0.946	0.943

six-dimensional PES accounts only for the six DOF of molecular hydrogen as shown in Figure 5.1. Details about the CRP algorithm and its implementation in our in-house computer code are presented elsewhere [18]. In the following, only a few principles of the CRP will be explained, and a few details will be presented concerning the structure of the DFT data set. The interpolation of realistic globally defined PESs can become considerably error-prone when small geometrical alterations lead to strong changes of the system’s potential energy. Using the CRP, this problem can be avoided by first reducing large differences within the original DFT data points,  $V^{DFT}$ . The resulting reduced data set,  $I^{DFT}$ ,

$$I^{DFT}(\vec{Q}_i) = V^{DFT}(\vec{Q}_i) - V^{ref}(\vec{Q}_i) \quad (5.2)$$

is better suited for an interpolation which will yield the smooth function  $I(\vec{Q})$  used to compute the final PES according to:

$$V(X, Y, Z, r, \theta, \phi) := V(\vec{Q}) = I(\vec{Q}) + V^{ref}(\vec{Q}). \quad (5.3)$$

Here,  $\vec{Q}_i = (X_{i_1}, Y_{i_2}, Z_{i_3}, r_{i_4}, \theta_{i_5}, \phi_{i_6})^T$  is a discrete coordinate vector, labeled with the multidimensional index  $i$ , in the 6D space  $\vec{Q} = (X, Y, Z, r, \theta, \phi)^T$ . For the reference function,  $V^{ref}(\vec{Q})$ , we are here using the sum of the two H + Pt(211) interaction potentials which are also obtained via the CRP. They describe most of the repulsive features of the PES, and are therefore

particularly suitable for reducing the corrugation of the PES in the CRP as explained in Ref. [18] and Ref. [31].

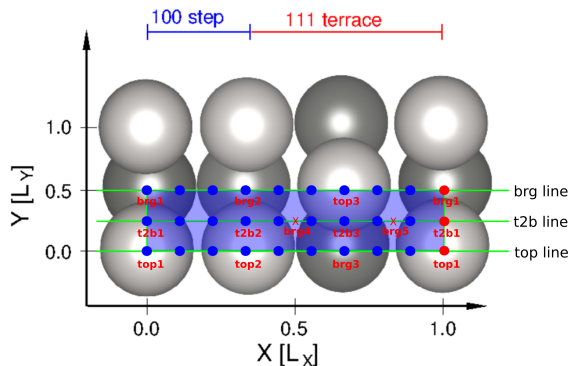


Figure 5.2: Top view of a  $(1 \times 1)$  unit cell of Pt(211). Indicated is the irreducible wedge by a blue plane and the blue dots represent the positions of H and of the center of mass of  $H_2$ , respectively, at which DFT energy points were calculated in order to construct the 3D/6D PES. A few selected sites are labeled with top, brg (bridge) and t2b (top to bridge) and are further distinguished by numbers. Red dots indicate periodic images at the edge of the irreducible wedge.

In order to keep the number of DFT points to be computed as low as possible, we perform DFT calculations for specific angular orientations of  $H_2$  labeled by  $\{\theta', \phi'\}$  in the following. They are defined in a modified coordinate system which is aligned with the vector normal to the (111) terrace, and not with the vector normal to the macroscopic surface as is the case for the angular coordinates  $\{\theta, \phi\}$ . The corresponding transformations between the two coordinate systems were previously presented in the supplementary information of Ref. [18] and in Ref. [42]. In tables 5.2 and 5.3, we list details about the DFT grid representation of the PES for the H(D) + Pt(211) system as well as for the  $H_2(D_2)$  + Pt(211) system. The former is required to provide the reference PES  $V^{ref}(\vec{Q})$  in Equations (5.2) and (5.3). Note that, with the coordinate system chosen for the DFT calculations, for H + Pt(111) a low minimum value of  $Z$  is needed to map out the interaction of H with Pt(211) at the bottom of the step (see table 5.2). In

Table 5.2: Specification of the DFT grid used to represent the atomic reference  $H + \text{Pt}(211)$  interaction potential. The grid along  $Y$  is defined for the irreducible wedge (IW) which makes up only the half of the  $\text{Pt}(211)(1 \times 1)$  unit cell, see Figure 5.2.

quantity	value	unit	remark
grid range along $X$ on IW	$[0, L_X]$	Å	
grid range along $Y$ on IW	$[0, L_Y/2]$	Å	
grid range along $Z$	$[-3.65, 7.05]$	Å	
$N_X$ number of grid points in $X$ on IW	18		equidistant
$N_Y$ number of grid points in $Y$ on IW	3		equidistant
$N_Z$ number of grid points in $Z$	109		equidistant
$\Delta X$ grid spacing along $X$	$L_X/18$	Å	
$\Delta Y$ grid spacing along $Y$	$L_Y/4$	Å	
$\Delta Z$ grid spacing along $Z$	0.1	Å	
representation of $V^{\text{top}}$ reference potential			
grid range along $Z$	$[0, 7.05]$	Å	
$N_Z^{\text{top}}$ number of grid points in $Z$	576		non-equidistant

the CRP, this is required in order to remove the repulsive interaction in the  $\text{H}_2 + \text{Pt}(211)$  PES over the whole interpolation range before interpolation is carried out. Due to the (100) step, the surface roughness is increased and small molecule-surface distances need to be taken into account (here,  $Z_{\min} = -2.2 \text{ \AA}$ ). The reasons are that we also describe molecular configurations in which  $\text{H}_2$  stands perpendicular to the surface and that we represent large interatomic distances ( $r_{\max} = 2.5 \text{ \AA}$ ), atomic repulsions must then also be represented for small atom-surface distances, down to  $Z = -3.45 \text{ \AA}$ .

We apply the following interpolation order to generate a smooth function  $I^{DFT}(\vec{Q})$ . First, we interpolate along the interatomic H–H distance  $r$  and the molecule-surface distance  $Z$  using a two-dimensional spline interpolation. Second, we interpolate along the polar angle  $\theta'$  using a trigonometric interpolation. Finally, we interpolate along the lateral positions  $X, Y$  and the azimuthal angle  $\phi'$  using a symmetry-adapted three-dimensional Fourier interpolation. The resulting PES is smooth, fast to evaluate and provides analytical forces.

#### 5.2.4 Molecular dynamics simulations

In this chapter, the dissociation dynamics of molecular hydrogen on Pt(211) is modeled using the QCT method [43], *i.e.*, with molecular dynamics (MD) simulations. The quantum mechanical ro-vibrational energy of incident  $\text{H}_2/\text{D}_2$  is sampled by a Monte-Carlo procedure outline in Ref. [44] and the occupation of the associated ro-vibrational levels is determined by the molecular beam parameters, as discussed below. We distinguish between standard MD simulations and molecular dynamics simulations with electronic friction (MDEF) [45]. The latter method allows one to study non-adiabatic effects on the dissociation dynamics due to the creation of electron-hole pairs in the surface region. For a N-dimensional system, the general equation to be solved in the following is the Langevin equation [46] which reads:

$$-m_i \frac{d^2 q_i}{dt^2} = -\frac{\partial V(q_1, \dots, q_N)}{\partial q_i} - \sum_j \eta_{ij}(q_i, \dots, q_N) \frac{dq_j}{dt} + R(T). \quad (5.4)$$

Here,  $m_i$  is the mass associated with a generalized coordinate  $q_i$ ,  $\eta_{ij}$  is an element of the friction tensor which yields a dissipative term due to the coupling of the nuclear DOF of molecular hydrogen with the electronic DOF of the Pt(211) surface. Finally,  $R(T)$  is a white noise random force

Table 5.3: Specification of the DFT grid used to represent the  $H_2(D_2) + Pt(211)$  interaction potential. The grid along  $Y$  is specified for the irreducible wedge which equals here the lower half of the  $Pt(211)(1 \times 1)$  unit cell, see Figure 5.2. Due to symmetry, the  $\phi'$ -dependence of the PES along the *top* and the *brg* line can be represented with three points (here at  $\phi' = 0, 45$  and  $90^\circ$ ). Due to the absence of a mirror axis associated with the *t2b* line, we needed an additional point (here at  $\phi' = 315^\circ$ ) to sample the PES along  $\phi'$ .

quantity	value	unit	remark
range of $X$	$[0, L_X[$	Å	
range of $Y$	$[0, L_Y/2]$	Å	
range of $Z$	$[-2.2, 6.6]$	Å	
range of $r$	$[0.4, 2.5]$	Å	
range of $\theta'$	$[0, \pi/2]$	rad	
range of $\phi'$	$[-\pi/4, \pi/2]$	rad	
$N_X$ number of grid points along $X$	9		equidistant
$N_Y$ number of grid points along $Y$	3		equidistant
$N_Z$ number of grid points along $Z$	53		equidistant
$N_r$ number of grid points along $r$	22		equidistant
$N_{\theta'}$ number of grid points along $\theta'$	2		equidistant
$N_{\phi'}$ number of grid points along $\phi'$	3-4 <sup>(*)</sup>		equidistant
$\Delta X$ grid spacing of $X$	$L_X/9$	Å	
$\Delta Y$ grid spacing of $Y$	$L_Y/4$	Å	
$\Delta Z$ grid spacing of $Z$	0.15	Å	
$\Delta r$ grid spacing of $r$	0.1	Å	
$\Delta \theta'$ grid spacing of $\theta'$	$\pi/2$	rad	
$\Delta \phi'$ grid spacing of $\phi'$	$\pi/4$	rad	

resulting from the electronic bath at temperature  $T := T_{el} = T_s$ , which here corresponds to the surface temperature  $T_s$ . At  $T = 0$  K, the random force disappears and only the frictional force remains in the dissipative part of Equation (5.4). In the absence of electronic friction ( $\eta = 0$ ), the Langevin equation obeys Newton's equation of motion and the evolution of the system depends then only on the gradient of the PES. The methodology used to

solve Equation (5.4) is described in Refs. [44, 47].

The position-dependent friction coefficients in Equation (5.4) are computed using the local-density friction approximation (LDFA) with the use of the independent atom approximation (IAA) [48]. As a consequence only the diagonal elements of the friction tensor  $\underline{\eta}$  remain and off-diagonal elements vanish. In the LDFA model,  $\eta$  is a function of the electron density  $\rho(x, y, z)$  embedding the ion with position  $(x, y, z)$ . In accordance with previous results [49], we assume that the embedding density corresponds to a good approximation to the unperturbed electron density of the bare Pt(211) surface which is here obtained from a single DFT calculation. To compute the friction coefficient for the H(D) atom, we adopt the relation [44]

$$\eta^{LDFA}(r_s) = ar_s^b \exp(-cr_s), \quad (5.5)$$

where the parameters are  $a = 0.70881 \hbar/a_0^{b+2}$ ,  $b = 0.554188$ ,  $c = 0.68314 a_0^{-1}$  and were previously fitted in Ref. [44] to *ab initio* data [50]. The Wigner-Seitz radius  $r_s = (3/(4\pi\rho))^{1/3}$  depends on the density  $\rho(x, y, z)$  embedding the hydrogen at position  $(x, y, z)$ . It is convenient to solve Equation (5.4) in Cartesian coordinates, and to use proper coordinate transformations to compute the potential and forces as functions of the six molecular coordinates presented in Figure 5.1.

Following previous studies on the reactive scattering of diatomic molecules from metal surfaces [44, 51], the effect of electron-hole pair excitation on the reaction of H<sub>2</sub>(D<sub>2</sub>) on Pt(211) can also be studied by scaling the LDFA-IAA friction coefficients. Here, we consider a scaling factor of 1 ( $\eta = \eta^{LDFA}$ ) and 2 ( $\eta = 2 \times \eta^{LDFA}$ ). We investigate what happens if the friction coefficients are multiplied by a factor two because the LDFA-IAA friction model is approximate, ignoring the possible effects of the electronic structure of the molecule. Friction coefficients computed with the orbital dependent friction model tend to come out larger [52–54]. In the former case we have performed calculations for  $T_s = T_{el} = 0$  K and 300 K, while in the latter case, we only performed calculations at  $T_s = T_{el} = 0$  K, that is, in the absence of random forces.

### 5.2.5 Quantum dynamics simulations

Six-dimensional quantum dynamics calculations are performed with the time-dependent wave packet method [55, 56] using our in-house wave packet

propagation code by solving the time-dependent Schrödinger equation

$$i\hbar \frac{d\Psi(\vec{Q}; t)}{dt} = \hat{H}\Psi(\vec{Q}; t). \quad (5.6)$$

Here,  $\Psi(\vec{Q}; t)$  is the corresponding nuclear wave function of molecular hydrogen at time  $t$ . The Hamilton operator used in Equation (5.6) accounts for the motion in the six molecular DOF of  $H_2$  and reads:

$$\hat{H} = -\frac{\hbar^2}{2M} \vec{\nabla}^2 - \frac{\hbar^2}{2\mu} \frac{\partial^2}{\partial r^2} + \frac{\hbar^2}{2\mu r^2} \hat{J}^2(\theta, \phi) + V(\vec{Q}), \quad (5.7)$$

where  $\vec{\nabla}$  is the Nabla operator, and  $\hat{J}(\theta, \phi)$  the angular momentum operator for the hydrogen molecule,  $M$  is the molecular mass and  $\mu$  is the reduced mass of  $H_2(D_2)$ . The initial nuclear wave function is represented as a product of a wave function describing initial translational motion and a ro-vibrational eigenfunction  $\Phi_{\nu, j, m_j}(r, \theta, \phi)$  of gaseous  $H_2(D_2)$  characterized by the vibrational quantum numbers  $\nu$ , the angular momentum quantum number  $j$  and the angular momentum projection quantum number  $m_j$ . Therefore, the initial wave function reads

$$\Psi(\vec{Q}; t_0) = \psi(\vec{k}_0, t_0) \Phi_{\nu, j, m_j}(r, \theta, \phi), \quad (5.8)$$

where  $\vec{k}_0 = (k_0^X, k_0^Y, k_0^Z)^T$  is the initial wave vector. The wave function describing initial translational motion is given by:

$$\psi(\vec{k}_0, t_0) = e^{i(k_0^X X_0 + k_0^Y Y_0)} \int_{-\infty}^{\infty} \beta(k_0^Z) e^{ik_0^Z Z_0} dk_Z. \quad (5.9)$$

Here, the initial wave packet  $\beta(k_0^Z)$  is characterized by a half-width parameter  $\sigma$  according to

$$\beta(k_0^Z) = \left(\frac{2\sigma^2}{\pi}\right)^{-\frac{1}{4}} e^{-\sigma^2(\bar{k} - k_0^Z)} e^{-i(\bar{k} - k_0^Z)Z_0}, \quad (5.10)$$

with  $\bar{k}$  being the average momentum and  $Z_0$  the position of the center of the initial wave packet.

The equations of motion were solved using the split-operator method [57]. The motion in  $X, Y, Z$ , and  $r$  was represented using Fourier grids. Quadratic optical potentials [58] were used to absorb the wave function at the edges



of the grid in  $r$  and  $Z$ . A non-direct product finite basis representation was used to describe the rotational motion of  $\text{H}_2$  [59, 60]. To compute reaction probabilities, first S-matrix elements were computed for diffractive and ro-vibrationally elastic and inelastic scattering, using the scattering matrix formalism of Balint-Kurti *et al.* [61]. These were used to compute probabilities for diffractive and ro-vibrationally elastic and inelastic scattering. The sum of these probabilities yield the reflection probability, and subtracting from 1 then yields the reaction probability.

### 5.2.6 Computation of observables

Using the quasi-classical method, we aim to model the sticking of  $\text{H}_2(\text{D}_2)$  on Pt(211) at conditions present in experiments we compare with by taking into account the different translational and ro-vibrational energy distributions characterizing the different molecular beams. At a nozzle temperature  $T_n$ , the probability  $P_{beam}$  of finding molecular hydrogen in a specific ro-vibrational state  $\nu, j$  with a velocity  $v + dv$  in the beam is:

$$P_{beam}(v, \nu, j; T_n)dv = P_{int}(\nu, j, T_n) \times f_{vel}(v; T_n)dv, \quad (5.11)$$

where the flux-weighted velocity distribution

$$f_{vel}(v; T_n)dv = Cv^3 \exp(-(v - v_s)^2/\alpha^2)dv \quad (5.12)$$

is normalized by a normalization constant  $C$  and characterized by a width parameter  $\alpha$  and the stream velocity  $v_s$ . The ro-vibrational state distribution is given by

$$P_{int}(\nu, j, T_n) = \frac{w(j)F(\nu, j, T_n)}{\sum_{\nu', j' \equiv j \pmod{2}} F(\nu', j', T_n)}. \quad (5.13)$$

The weight  $w(j)$  accounts for the different nuclear spin configurations of ortho- and para hydrogen molecules. For  $\text{H}_2$ ,  $w(j) = 1/4$  ( $3/4$ ) for even (odd)  $j$ -values and, for  $\text{D}_2$ ,  $w(j) = 2/3$  ( $1/3$ ) for even (odd) values of  $j$ . The function  $F(\nu, j, T_n)$  is defined as

$$F(\nu, j, T_n) = (2j+1) \underbrace{\exp(-(E_{\nu,0} - E_{0,0})/k_B T_n)}_{\text{vibrational energy distribution}} \underbrace{\exp(-(E_{\nu,j} - E_{\nu,0})/0.8k_B T_n)}_{\text{rotational energy distribution}}. \quad (5.14)$$

The appearance of a factor 0.8 in the rotational energy distribution reflects that rotational and nozzle temperatures assume the relation  $T_{rot} = 0.8 T_n$  due to rotational cooling upon expansion of the gas in the nozzle [62]. The experimental beam parameters for the  $H_2/D_2 + Pt(211)$  systems are listed in table 5.4 and table 5.5.

The quasi-classical initial conditions are prepared using a Monte Carlo procedure described in Ref. [44] and sample directly the probability distribution  $P_{beam}$ . The resulting probability  $P_i$  for dissociative adsorption, scattering and non-dissociative trapping of an ensemble of molecules is determined by the ratio:

$$P_i = \frac{N_i}{N}, \quad (5.15)$$

where  $N_i$  stands for the number of adsorbed, dissociated or trapped trajectories ( $N_{ads}$ ,  $N_{diss}$ ,  $N_{trap}$ ) and  $N$  is the total number of trajectories computed for a specific energy point  $\langle E_i \rangle$ , where  $\langle E_i \rangle$  denotes the average translational incidence energy of the molecule.

### 5.2.7 Computational details

The time-integration of Equation (5.4) is done in Cartesian coordinates using a time step of  $\Delta t = 2.0\hbar/E_h$  ( $\approx 0.0484$  fs) with the stochastic Ermak-Buckholz propagator [64], which also works accurately in the non-dissipative case. Further technical details are given in Ref. [44, 47]. The maximal allowed propagation time for each trajectory is  $t_f = 10$  ps. In the non-dissipative case, our QCT setup usually leads to an energy conservation error of smaller than 1 meV. All trajectories start at a molecule-surface distance of 7 Å and initially sample the ensemble properties of the experimental molecular beam, that is, we model the ro-vibrational state distribution according to the nozzle temperature as well as the translational energy distribution of the incidence beam. The parameters characterizing the molecular beam are given in table 5.4 and table 5.5 and details about their experimental determination are given in the supporting information of Ref. [63]. The initial conditions used in the quasi-classical simulations are determined using the Monte-Carlo algorithm explained in Ref. [44].

We compute  $N = 10,000$  trajectories per energy point and count trajectories as dissociatively adsorbed if they assume an interatomic H–H distance larger than 2.5 Å during the dynamics. Scattered trajectories are characterized by a sign change in the  $Z$ -component of the total momentum vector

Table 5.4: Parameters used for the molecular beam simulations of H<sub>2</sub> on Pt(211). The parameters were obtained from fitting the experimental time-of-flight (TOF) data to equation 6 in the supporting information of Ref. [63]. For pure H<sub>2</sub> beams, we also provide  $n$  in  $\langle E_i \rangle = nk_B T_n$  and the corrected average incidence energy  $\langle E_{corr} \rangle = 2.7k_B T_n$ .

	$\langle E_i \rangle$ [eV]	$v_s$ [m/s]	$\alpha$ [m/s]	$T_n$ [K]	$n$ in $\langle E_i \rangle = nk_B T_n$	$\langle E_{corr} \rangle$ [eV]
	0.004	626.5	55.9	293	-	-
	0.009	943.5	127.8	293	-	-
	0.013	1085.1	111.6	293	-	-
	0.014	1145.2	118.7	293	-	-
	0.025	1531.4	96.6	293	-	-
	0.035	1747.5	293.9	293	-	-
	0.043	2031.2	80.6	293	-	-
H <sub>2</sub>	0.132	3392.1	578.0	500	3.07	0.116
	0.181	3959.8	690.8	700	3.00	0.163
	0.169	4009.0	185.2	1300	-	-
	0.233	4442.8	862.5	900	3.00	0.210
	0.282	4838.8	1022.9	1100	2.98	0.255
	0.338	5223.2	1215.6	1300	3.02	0.302
	0.413	5617.0	1535.8	1500	3.20	0.348
	0.454	5790.7	1711.3	1700	3.10	0.395

Table 5.5: Parameters used for the molecular beam simulations of  $D_2$  on  $Pt(211)$ . The parameters were obtained from fitting the experimental time-of-flight (TOF) data to equation 6 in the supporting information of Ref. [63]. For pure  $D_2$  beams, we also provide  $n$  in  $\langle E_i \rangle = nk_B T_n$  and the corrected average incidence energy  $\langle E_{corr} \rangle = 2.7k_B T_n$ .

	$\langle E_i \rangle$ [eV]	$v_s$ [m/s]	$\alpha$ [m/s]	$T_n$ [K]	$n$ in $\langle E_i \rangle = nk_B T_n$	$\langle E_{corr} \rangle$ [eV]
	0.008	626.8	49.8	293	—	—
	0.027	1103.2	134.9	293	—	—
	0.040	1379.2	75.5	293	—	—
	0.054	1555.6	218.1	600	—	—
	0.076	1860.0	237.5	800	—	—
	0.110	2239.9	267.3	1100	—	—
$D_2$	0.130	2430.7	311.9	500	3.03	0.116
	0.140	2531.1	294.5	1100	—	—
	0.234	3191.0	548.1	900	3.02	0.209
	0.276	3628.1	160.3	1300	—	—
	0.346	3814.8	772.0	1300	3.09	0.303
	0.457	4304.1	989.4	1700	3.12	0.395

and have to pass a molecule-surface distance of  $Z_{sc} = 7.1 \text{ \AA}$ . We call a trajectory trapped if the total propagation time of 10 ps is reached and neither dissociation nor scattering has occurred.

The dissociative chemisorption of  $\text{H}_2(\nu = 0, j = 0)$  on Pt(211) is investigated quantum mechanically over a translational energy range of  $E_i \in [0.05, 0.75] \text{ eV}$  using two different wave packet propagations. The analysis line used to evaluate the scattered fraction of the wave packet was put at  $Z_{start}^{CAP} = 6.6 \text{ \AA}$ . This is a suitable value since the PES is  $r$ -dependent only for all values  $Z \geq 6.6 \text{ \AA}$ , so it allows representing the wave function on a smaller grid using  $N_Z$  points in  $Z$  for all channels but the channel representing the initial state (called the specular state, and represented on a larger grid called the specular grid, using  $N_{Z_{spec}}$  points). These parameters, and other parameters discussed below, are presented in table 5.6.

The grids in  $Z$  start at  $Z = Z_{start}$  and share the same grid spacing. The grid in  $r$  is described in a similar way by the parameters  $r_{start}$ ,  $N_r$ , and  $\Delta r$ . The numbers of grid points used in  $X$  and  $Y$  ( $N_X$  and  $N_Y$ ) are also provided, as are the maximum value of  $j$  and  $m_j$  used in the basis set ( $j_{max}$  and  $m_{j_{max}}$ ). The optical potentials used (also called complex absorbing potentials (CAPs)) are characterized by the value of the coordinate at which they start and end, and the value of the kinetic energy for which they should show optimal absorption [58]; these values were taken differently for the regular and the specular grid in  $Z$ . The time step  $\Delta t$  used in the split operator propagation and the total propagation time  $t_f$  are also provided. The initial wave packet is centered on  $Z_0$  and is constructed in such a way that 95% of the norm of the initial wave function is associated with kinetic energies in motion towards the surface between  $E_{min}$  and  $E_{max}$ , as also provided in table 5.6.

## 5.3 Results and discussion

### 5.3.1 Static DFT calculations

Before we come to the dynamics calculations, we here first present general features of the interaction potential of atomic and molecular hydrogen and a Pt(211) surface. In Figure 5.3, we plot the minimum potential energy values for atomic H assuming the optimal atom-surface distance  $Z$  over the full  $(1 \times 1)$  unit cell. The resulting H-Pt(211) PES resembles the PES earlier developed by Olsen *et al.* [42] on the basis of DFT energy point

Table 5.6: Characterization of the two different wave packet (WP) calculations for  $(\nu = 0, j = 0)H_2$  incident normally on Pt(211) for translational energies of  $E_i \in [0.05, 0.75]$  eV. Specified are the grid parameters for the wave function and the PES, and parameters defining the complex adsorbing potential in  $r$  and  $Z$ , the center position  $Z_0$  of the initial wave packet, and the corresponding translational energy range  $E_i$  covered.

Property	WP1	WP2	unit
WP grid parameters			
Range of $X$	$[0, L_X[$	$[0, L_X[$	$a_0$
$N_X$ grid points in $X$	36	36	
Range of $Y$	$[0, L_Y[$	$[0, L_Y[$	$a_0$
$N_Y$ grid points in $Y$	12	12	
Range of $Z$	$[-2.0, 19.45]$	$[-2.0, 17.10]$	$a_0$
$N_Z$	144	192	
$\Delta Z$	0.15	0.10	$a_0$
$N_{Z_{spec}}$	210	220	
Range of $r$	$[0.80, 9.05]$	$[0.80, 7.85]$	$a_0$
$N_r$	56	48	
$\Delta r$	0.15	0.15	$a_0$
$j_{max} = m_{j_{max}}$	22	32	
Complex absorbing potentials			
$Z^{CAP}$ range	$[12.55, 19.45]$	$[12.50, 16.90]$	$a_0$
$Z^{CAP}$ Optimum	0.05	0.08	eV
Specular grid			
$Z_{spec}^{CAP}$ start	22.75	16.10	$a_0$
$Z_{spec}^{CAP}$ end	29.35	19.90	$a_0$
$Z_{spec}^{CAP}$ optimum	0.05	0.08	eV
$r^{CAP}$ range	$[4.10, 9.05]$	$[4.55, 7.85]$	$a_0$
$r^{CAP}$ optimum	0.05	0.20	eV
Propagation			
$\Delta t$	2.00	2.00	$\hbar/E_h$
$t_f$	3870.21	1741.60	fs
Initial wave packet			
Energy range, $E_i$	$[0.05, 0.25]$	$[0.20, 0.75]$	eV
Center of WP, $Z_0$	16.45	14.30	$a_0$

calculations using a B88P86 functional [29, 30]. For example, the most

stable adsorption site for a single hydrogen atom on Pt(211) is located near the brg1 position at the step edge, see also Figure 5.2. Additional minima are found close to the top2 and the top3 sites. In agreement with Olsen *et al.* [42], we also obtain the largest diffusion barrier to be  $\approx 0.60$  eV above the global minimum in the vicinity of the brg2 site. The specific position of the global minimum for H adsorption suggests the minimum barrier for  $H_2$  dissociation to be on top of the step edge at the top1 site because the top1-to-brg1 path represents a short route for H atoms to assume their most

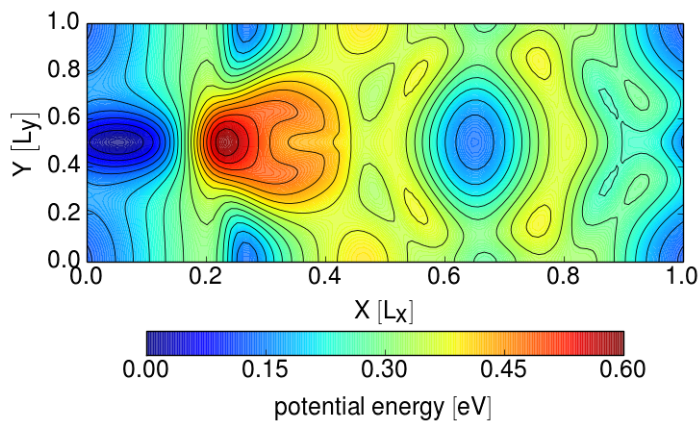


Figure 5.3: Minimum potential energy for H on Pt(211) for geometry optimized atom-surface distances  $Z_{opt}$  on a  $(1 \times 1)$  supercell. The energies are given relative to the most stable configuration of H on Pt(211) which is here near to the brg1 position (see Figure 5.2). Since our DFT calculations do not include spin-polarization, the corresponding highest adsorption energy of 3.74 eV for a single H atom should to our experience be overestimated by  $\sim 0.7$  eV. The contour line spacing is 0.03 eV.

favorable geometry on the surface. In general, the abstraction of atomic hydrogen from Pt(211) requires large amounts of energies as is known also for other H + transition metal systems [65, 66]. The value of  $E_{ads} \approx 3.7$  eV computed here is, however, overestimated by  $\sim 0.7 - 1.0$  eV since we did not perform spin-polarized DFT calculations, which are not relevant to the comparison with the work of Olsen *et al.* [42], to the reaction paths for  $H_2$  dissociation, and to the dynamics of  $H_2$  dissociation.

In Figure 5.4, we present different two-dimensional (2D) PES cuts along

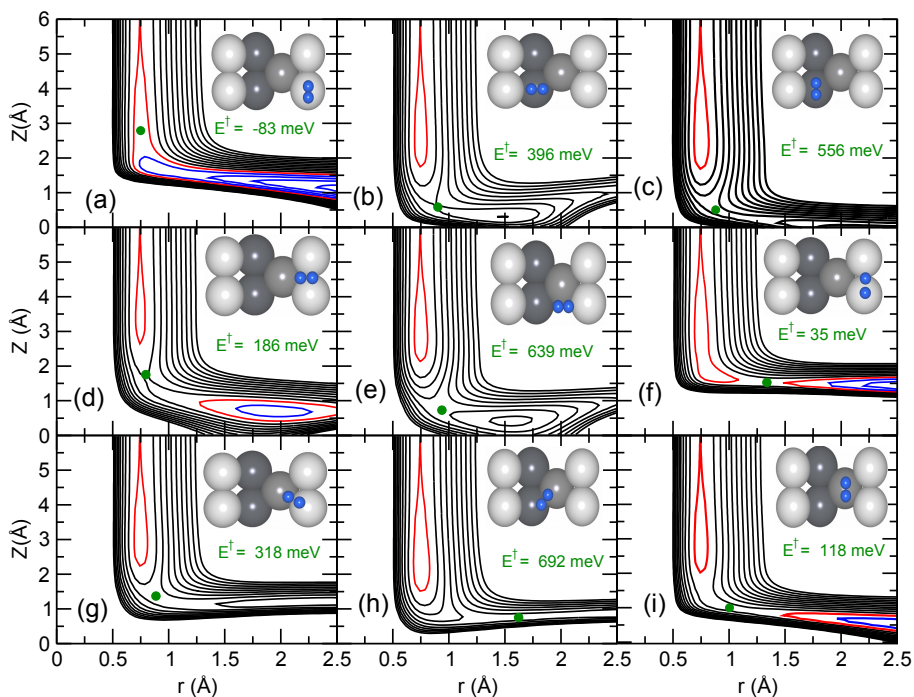


Figure 5.4: 2D potential cuts through the 6D PES for dissociative adsorption of  $H_2$  on Pt(211) along  $r$  and  $Z$  at the nine different sites on the  $(1 \times 1)$  unit cell. In all cases  $H_2$  approaches parallel to the macroscopic surface ( $\theta = 90^\circ$ ). Top views of the molecular configurations are shown as insets. Contour levels are given in the energy range of  $[-1, 2]$  eV with a spacing of 0.2 eV. The zero-value of the PES is set equal to the gas phase minimum energy. Negative (positive) valued contour lines are plotted in blue (black) and the zero-valued contour line is shown in red. Green circles indicate the position of the reaction barrier, and barrier heights  $E^\ddagger$  are also shown.



the H–H and the molecule-surface distances ( $r, Z$ ) for  $\text{H}_2$  approaching Pt(211) with orientations parallel to the surface at different impact sites, and azimuthal orientations as shown in the insets of the figure. As can be seen from Figure 5.4 (a), the dissociation of  $\text{H}_2$  proceeds indeed non-activated directly over the top1 site, that is, over a Pt atom at the step edge. Following the colour code of the figure,  $\text{H}_2$  can spontaneously dissociate after passing an early, but shallow barrier of  $E^\ddagger = -83 \text{ meV}^1$  (barrier is below the classical gas phase minimum) in the entrance channel. The two H atoms are then accommodated exothermally on the surface. This result is in agreement with previous work of McCormack *et al.* [14] where a non-activated route to dissociation was revealed for impacts near the top1 site and with H atoms dissociating to brg1 sites. This result also matches up with the above analysis of the topology of the H on Pt(211) PES that suggested the lowest barrier to be close to the top1 site. Furthermore, the associated barrierless path enables the contribution of a direct non-activated mechanism for reaction at all incidence energies, as found experimentally [8] as well as theoretically [14]. Interestingly, already small changes of the molecular geometry lead to significant changes of the topology of the PES. For example, moving  $\text{H}_2$  from the step edge to the bottom of the step while retaining its orientation, as shown in Figure 5.4 (c), yields a 2D-PES that has a large activation barrier of  $E^\ddagger = 556 \text{ meV}$  and dissociation appears to be endothermic. Aligning now the molecular axis with the  $X$ -axis of the surface unit cell, as shown in Figure 5.4 (b), reduces somewhat the barrier but the PES becomes strongly repulsive for very large values of  $r$  ( $r > 2 \text{ \AA}$ ). This suggests that the dissociation of  $\text{H}_2$  on Pt(211) may be accompanied by a strong angular reorientation dynamics, but also that associative desorption may set in after the molecule has experienced large interatomic stretches.

The different impact sites and initial orientations of the molecule do not only affect how large the barrier toward bond cleavage is and the length of the path towards a favorable adsorption state. They also influence the way in which vibrational and translational energy play in favor of reaction. Throughout the nine plots presented in Figure 5.4, one recognizes the typical elbow form of the PES along the  $r, Z$  coordinates. On the one hand, the curvature of the minimum energy paths in the elbows controls the vibration-translation (V-T) coupling [67], which may facilitate dissoci-

---

<sup>1</sup> $E^\ddagger = E_b$

Configuration	$r^\ddagger$ [Å]	$Z^\ddagger$ [Å]	$E^\ddagger$ [eV]
top1 ( $\phi = 90^\circ$ ), Fig.5.4(a)	0.75	2.79	-0.083
top2 ( $\phi = 0^\circ$ ), Fig.5.4(b)	0.90	0.59	0.396
top2 ( $\phi = 90^\circ$ ), Fig.5.4(c)	0.88	0.51	0.556
top3 ( $\phi = 90^\circ$ ), Fig.5.4(i)	1.00	0.99	0.118
brg1 ( $\phi = 0^\circ$ ), Fig.5.4(d)	0.80	1.75	0.186
brg3 ( $\phi = 0^\circ$ ), Fig.5.4(e)	0.94	0.73	0.639
brg4 ( $\phi = 30^\circ$ ), Fig.5.4(h)	1.62	0.75	0.692
brg5 ( $\phi = 120^\circ$ ), Fig.5.4(g)	0.89	1.37	0.318
t2b1 ( $\phi = 90^\circ$ ), Fig.5.4(f)	1.34	1.53	0.035

Table 5.7: Barrier heights and geometries for  $H_2$  on Pt(211) for the geometries shown in Figure 5.4. Energies are given relative to the gas phase minimum energy of  $H_2$ .

ation in quasi-classical simulations artificially due to the zero-point energy conversion effect: the higher the curvature, the more coupling. On the other hand, the Polanyi rules [68] relate the efficiency of translational and vibrational excitation of the incident molecule for reaction to the position of the barrier. In late-barrier systems resembling the product state reaction is promoted vibrationally, while in early-barrier systems reaction is more enhanced by translational excitation. For the  $H_2 + Pt(211)$  system, vibrationally non-adiabatic V-T processes as well as the Polanyi rules are expected to come into play during the reaction dynamics. For example, we find relatively early barriers for impact situations shown in Figure 5.4 (b)-(d) suggesting a preference of translational excitation for reaction. Impact sites associated with a late barrier are shown in Figure 5.4 (f), (h) and (i). In impacts on these sites, reaction is more likely to be promoted by initial vibrational excitation.

Reaction barrier energies and associated geometries for the nine incidence situations outlined in Figure 5.4 are specified in table 5.7. While the barriers to dissociation could be decreased somewhat when optimized with respect to  $\theta$  for cases in which  $H_2$  does not dissociate parallel to the step (Figures 5.4 (b), (d), (e), (g), and (h)), Figure 5.4 and table 5.7 nevertheless provide a good view of the  $H_2$ -Pt(211) interaction. We find the latest ( $r^\ddagger = 1.62$  Å) and highest barrier ( $E^\ddagger = 692$  meV) for molecules incident at the brg4 site (see also Figure 5.4 (h)). This indicates a considerable range of

activation energies ( $\sim 700$  meV) for the dissociation process. The  $Z^\dagger$ -values reported in table 5.7 range from  $0.51 \text{ \AA}$  at the top2 site (bottom of the step) to  $2.79 \text{ \AA}$  at the top1 site (top of the step edge). This reflects to some extent the overall shape of the Pt(211) surface, since step-top and step-bottom Pt atoms are displaced by  $\Delta Z = 1.27 \text{ \AA}$ .

The vdW-DF2 functional employed here yields not only rather large activation energies for the direct dissociation process but also considerable physisorption wells of  $\sim 72$  meV located comparably far away from the surface. The presence of such wells may additionally contribute to the trapping dynamics of small molecules or may even increase the chance of redirecting the molecule toward non-dissociative pathways. Baerends and co-workers [13, 14] previously reported on the importance of trapping as a mechanism for indirect dissociation of  $\text{H}_2$  on Pt(211). They used a PES that was constructed on the basis of standard GGA-DFT calculations and the authors found only a shallow physisorption well for impacts at the bottom-step. When using the DF2-functional in the description of the dynamics of molecular hydrogen on Pt(211), as done in this work, the trapping mechanism may become more substantial, which may affect the computation of sticking probabilities for slow molecules.

### 5.3.2 Comparison QCT and QD dynamics

Figure 5.5 shows the comparison between the QCT and QD results for  $\text{H}_2(\nu = 0, j = 0)$ . As already discussed in the introduction, the shape of the reaction probability curve in both the QD and the QCT dynamics arises from the presence of a trapping mechanism, which yields a contribution to the reactivity that decreases with incidence energy, and an activated mechanism, the contribution of which increases with incidence energy. As a result, the reaction of the  $\text{H}_2$  molecule on Pt(211) exhibits a nonmonotonic behaviour as a function of the collision energy. The reaction probability curve shows very high dissociation probabilities at very low collision energies. The minimum value of the reaction probability is at an intermediate value of the collision energy and the slope of the reaction probability curve becomes positive at higher collision energies.

As noted by McCormack *et al.* [14], with a GGA PES non-activated indirect dissociation may occur when a molecule hits the lower edge of the step on a non-reactive site, which showed the presence of a shallow chemisorption well in their PES. A difference with our PES is that physisorption can

occur anywhere at the surface, due to the presence of van der Waals wells for the PES computed with the vdW-DF2 correlation functional.

The QCT calculations reproduce the QD results at the higher incidence energies reasonably well. At low and intermediate energies, in the QD results the trapping mechanism manifests itself by the occurrence of peaks in the reaction probabilities, with the peak energies corresponding to the energies of the associated metastable quantum resonance (trapped) states. The comparison suggests that at low and at intermediate energies (up to 0.2 eV) the QCT results tend to overestimate the reactivity a bit. This could be due to two reasons. First, the increase of the reaction probability with decreasing energy at the lower incidence energy is understood to occur as a result of trapping of molecules entering the potential well, in which energy from the motion perpendicular to the surface is transferred into rotation and translational motion parallel to the surface [17]. In the QD calculations trapping should only be due to energy transfer to the motion parallel to the surface [17]. However, classically it is also allowed that energy is transferred from the motion towards the surface to the rotational DOFs [17]. Second, the QCT calculations may suffer from an artificial effect called zero-point-energy (ZPE) leakage, *i.e.*, in QCT calculations the quantization of vibrational energy may be lost and the original vibrational zero point energy may be transferred to other degrees of freedom.

### 5.3.3 Isotope effects in QCT results for reaction of ( $\nu = 0$ , $j = 0$ ) $H_2$ and $D_2$

Comparison between the computed QCT reaction probability curves for  $H_2$  and  $D_2$  shows that the reaction probability of  $H_2$  is higher than that of  $D_2$  at the same incidence energy (see Figure 5.6). We attribute this to a zero-point energy effect.  $H_2$  has more energy in zero point vibrational motion than  $D_2$ , so there is a higher probability that a given amount of this energy is transferred to motion along the reaction coordinate. Gross and Scheffler [69] for  $H_2$  dissociation on Pd(100) showed that in classical dynamics (no initial zero-point energy) there is no isotope effect between  $H_2$  and  $D_2$  in the sticking probabilities. At first sight, one might expect that steering is less effective for  $D_2$  due to its higher mass and therefore less reaction for  $D_2$  than  $H_2$ . On the other hand,  $D_2$  is slower than  $H_2$  at the same kinetic energy, so there is more time for the steering force to redirect the  $D_2$  molecule to a non-activated path. However, they found the quantum

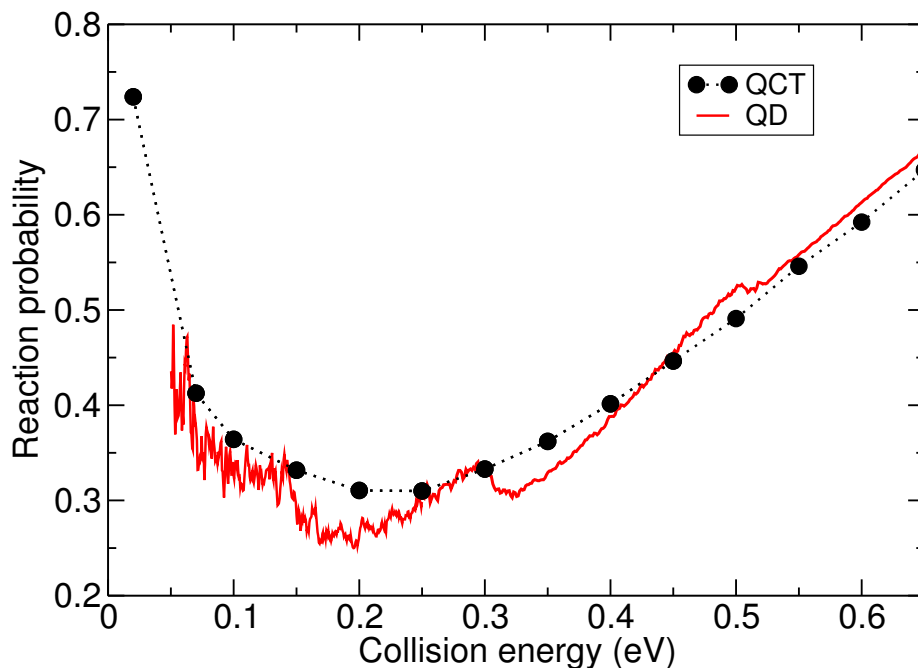


Figure 5.5: Initial-state resolved reaction probability for  $\text{H}_2$  ( $\nu = 0$ ,  $j = 0$ ) dissociation on Pt(211) calculated with QD in comparison with the QCT results.

dynamical sticking probabilities of  $\text{D}_2$  to be smaller than those of  $\text{H}_2$ . They suggested that this small difference should be a quantum dynamical effect and that the larger vibrational zero point energy of  $\text{H}_2$  can more effectively be used to cross the reaction barrier.

No isotopic dependence and also no surface temperature dependence for the sticking probability were reported by the experimentalists [8], as shown in Figure 5.7 where we show the sticking probability as a function of average incidence energy. (In Ref. [8] the sticking probabilities were shown as a function of the incidence energy corresponding to the most probable energy for a density-weighted incidence energy distribution, see the supporting information of Ref. [63].)

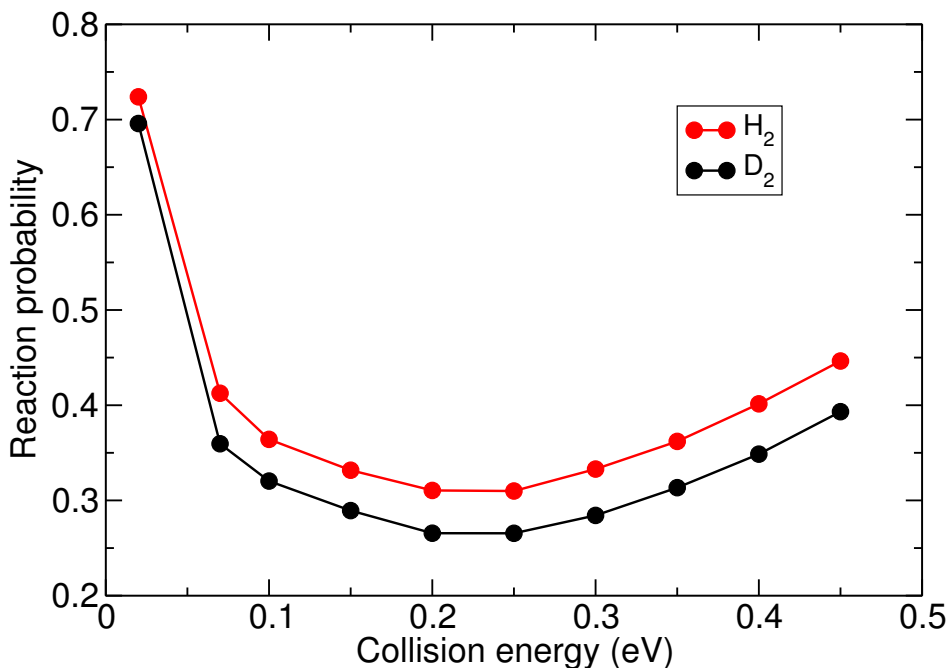


Figure 5.6: Initial-state-resolved reaction probabilities for the dissociation of  $H_2(D_2)$  on  $Pt(211)$  surface are shown with red (black) symbols for the ground rotational and vibrational state. The results are obtained with the QCT method.

### 5.3.4 Comparison of molecular beam sticking probabilities with experiment

Parameters used for the molecular beam sticking simulations (previously extracted from experiments as discussed in the supporting information of Ref. [63]) of  $H_2$  and  $D_2$  on  $Pt(211)$  are given in table 5.4 and table 5.5 .

The sticking probabilities extracted from molecular beam simulations for  $H_2$  dissociation on  $Pt(211)$  are shown in Figure 5.8 with a comparison to the experimental results. In the figure, the red circles show the theoretical results obtained from simulating the experimental beam conditions. The black circles display the experimental results reported by Groot *et al.* [8]. Figure 5.9 shows the same comparison for  $D_2$  dissociation on  $Pt(211)$ . In both cases, in the lower-energy regime, the theoretical results overestim-

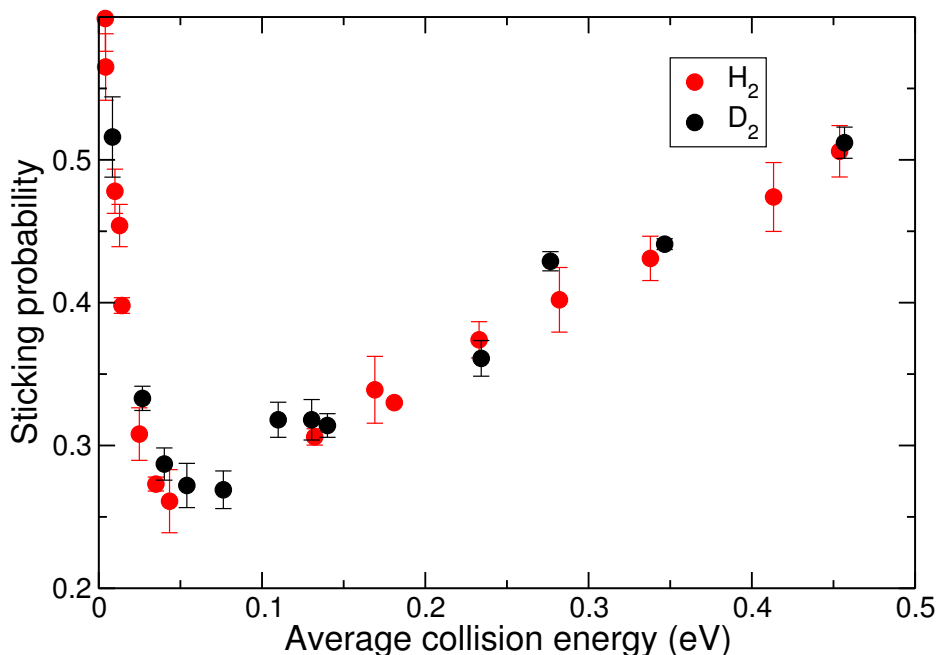


Figure 5.7: The experimental [8] sticking probability of H<sub>2</sub> (red symbols) and D<sub>2</sub> (black symbols) on Pt(211) as a function of average collision energy.

ate the experimental reaction probabilities. For H<sub>2</sub> on Pt(211), at higher energies the theoretical results also overestimate the experimental results. However, overestimation happens only at the highest incidence energy for D<sub>2</sub> + Pt(211). The energy shift (the distance along the energy axis between experimental data points and the interpolated theoretical curve) is [7–92] meV for H<sub>2</sub> + Pt(211) and [3–55] meV for D<sub>2</sub> + Pt(211). On this basis, our results for H<sub>2</sub> + Pt(211) do not yet agree with experiment to within chemical accuracy ( $\approx 43$  meV). To find the mean deviation of the theoretically calculated sticking probability curve from the experimental results, we also calculated the mean absolute error (MAE) and mean signed error (MSE). We obtained a MAE of 40.8 meV and a MSE of 9.8 meV for H<sub>2</sub> and a MAE of 32.4 meV and a MSE of -0.4 meV for D<sub>2</sub>. On this basis, the errors in the theoretical data in both cases are less than 1 kcal/mol  $\approx 43$  meV.

As already stated, the comparison between experiment and theoretical results is not yet good at the lower incidence energies. Two reasons might

be involved, which are related to there being an important contribution to sticking from a trapping-mediated mechanism. The first reason concerns the inability of the QCT method to describe the sticking probability accurately when trapping contributes to reaction. The QCT results overestimate the contribution of trapping due to translation-to-rotation energy transfer, which is not allowed in QD descriptions [70] (see Section 5.3.2). The quantum dynamics calculations of Figure 5.5 suggest that for reaction of  $H_2(\nu = 0, j = 0)$  the reaction probability decreases faster with energy at low incidence energies if quantum effects are included, which goes in the right direction for getting better agreement with experiment. The other effect that could be important is surface temperature, which we do not include in our calculations. The initial reaction probability was experimentally determined at the surface temperature of 300 K. However, the experimentalists did not observe any surface temperature dependence [8]. In our view this makes it unlikely that the static surface approximation we used here is responsible for the discrepancy with experiment at low incidence energy.

Especially for  $H_2$  our QCT results overestimate the experimental sticking probability at high average energies, as computed from the beam parameters available from fitting experimental TOF spectra (see the supporting information of Ref. [63]). One question we addressed is whether this could be due to errors arising from fitting these parameters, which is critically difficult especially at high incidence energies associated with short flight times. Now it is rather well known that for pure  $H_2$  beams the average translational energy should not exceed  $2.7 k_B T_n$ , as no vibrational cooling occurs, and only about 20% rotational cooling [62, 71, 72]. Comparing the average incidence energies of the pure  $H_2$  beams in table 5.4 with  $2.7 k_B T_n$ , we however find that in most cases the average incidence energies exceed  $3 k_B T_n$ , and this also holds true for pure  $D_2$  beams (see also table 5.5). This suggests that the experimental average incidence energies extracted from the beam parameters were too high. By re-plotting the experimental results using average incidence energies  $E_{corr}$  equal to  $2.7 k_B T_n$  we can redo the comparison with the computed sticking probabilities, if we assume that the computed values do not much depend on the nozzle temperature through altered ro-vibrational state distributions. This is likely to hold true for non-activated or weakly activated dissociation. As Figure 5.10 shows this approach tremendously improves the agreement with experiment for the higher incidence energies at which the sticking is dominated by activated dissociation, and for which the QCT results should be accurate (see Sec-



tion 5.3.2): The agreement with experiment is now within chemical accuracy for these energies and pure H<sub>2</sub> beam conditions. For D<sub>2</sub> the agreement is not as good as for H<sub>2</sub> for the lower incidence energies in the high-energy range (see Figure 5.11), which is perhaps due to the rotational cooling being somewhat more efficient for D<sub>2</sub> than for H<sub>2</sub>, due to the lower rotational constant of D<sub>2</sub>. This means that in Figure 5.11 the experimental data could move somewhat to the right (to higher energies), thereby improving the agreement with experiment. Note also that in principle the fits of the beam parameters are expected to be less error prone for H<sub>2</sub> than for D<sub>2</sub>, due to longer flight times of D<sub>2</sub>.

Another solution to the puzzle of why the average incidence energies calculated from the beam parameters did not correspond to  $2.7 k_B T_n$  for pure beams could be that the nozzle temperature was actually higher than measured. This could in principle be simulated by assuming that the nozzle temperature can be computed from the measured average incidence energy, instead of adapting the average incidence energy to the measured nozzle temperature. This was not pursued computationally, as it would only be expected to lead to a small increase of the computed sticking probability, and to somewhat larger discrepancies for H<sub>2</sub> + Pt(211), for which the agreement with experiment was worst to start with.

Above, we have suggested that the rotational cooling in a D<sub>2</sub> beam could be somewhat more efficient than in the H<sub>2</sub> beam (due to the rotational constant of D<sub>2</sub> being lower). If this were true, this would suggest that we could have plotted the experimental data for the pure D<sub>2</sub> beams as a function of  $\langle E_i \rangle = ck_B T_n$  with  $c$  somewhat larger than 2.7 (for instance, 2.75 or 2.8) in Figure 5.11. If this would be correct, this would increase the agreement between theory and experiment in this figure, as already discussed above. However, it should also alter the conclusion regarding the absence of an isotope effect drawn originally by the experimentalists: if this assumption would be correct, the sticking probabilities measured for H<sub>2</sub> should be somewhat higher than those for D<sub>2</sub>, at least for the results from the pure H<sub>2</sub> and pure D<sub>2</sub> experiments. This would bring theory and experiment in agreement also regarding the qualitative conclusion on the isotope effect.

### 5.3.5 Comparison MD and MDEF results for sticking

Figures 5.12 and 5.13 show the results of MD and MDEF calculations for H<sub>2</sub> + Pt(211) and D<sub>2</sub> + Pt(211). At low energies adding electronic fric-

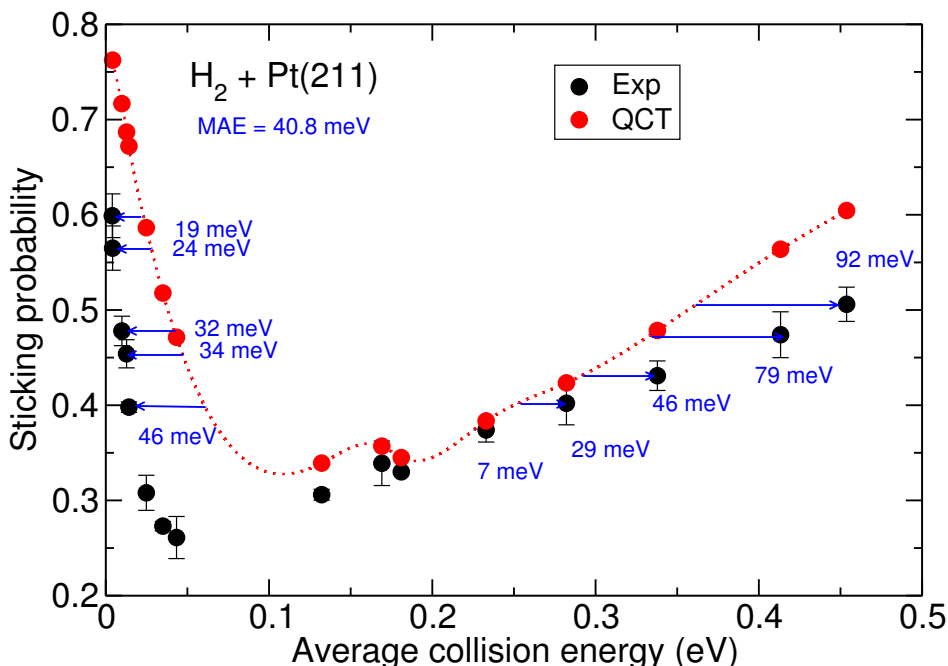


Figure 5.8: Sticking probability for molecular beam of  $H_2$  on Pt(211) simulated with QCT. For comparison experimental results reported by Groot *et al.* (Black symbols: experimental data from Ref. [8]) are plotted beside the theoretical results (red symbols). The arrows and accompanying numbers show the collision energy difference between the interpolated theoretical results and experimental data.

tion and doubling the friction coefficient increases the sticking probability for  $D_2$ . Doubling the electronic friction coefficient increases the sticking probabilities of  $H_2$  only at intermediate energies. At higher incidence energies adding electronic friction decreases the sticking probability a little bit. Adding this energy dissipation channel reduces sticking somewhat at higher incidence energies because energy in the bond stretch coordinate is nonadiabatically dissipated to electron-hole pair excitation. Also modeling the effect of the finite electronic temperature decreases the sticking probability at lower incidence energies, but there is no dramatic effect at higher incidence energies. The effect of  $T_{el}$  is negligible for  $\langle E_i \rangle > 0.13$  eV and very small at lower incidence energy. At the lowest incidence energies, the

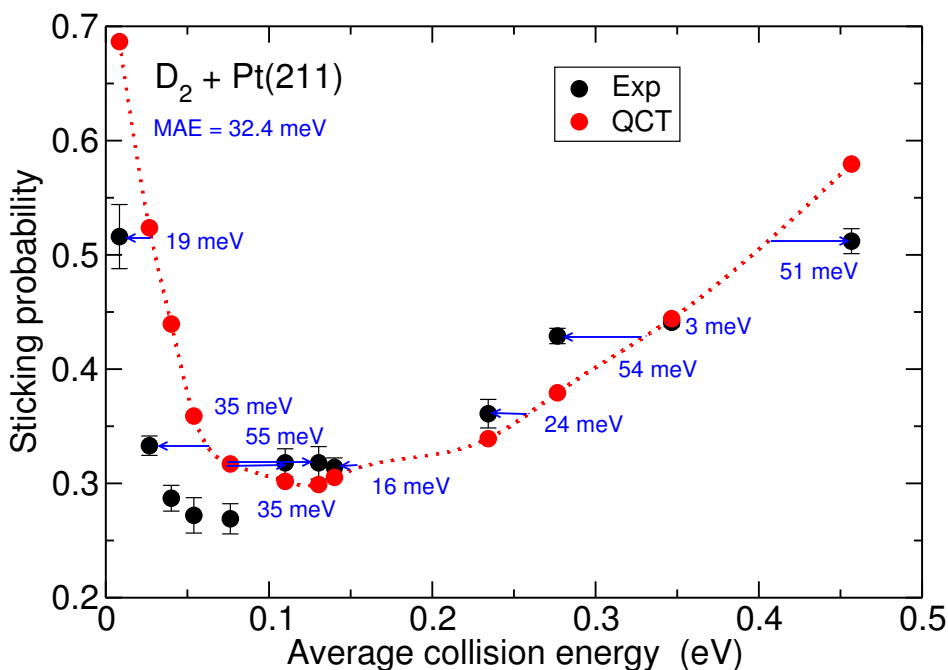


Figure 5.9: Sticking probability for molecular beam of  $D_2$  on Pt(211) simulated with QCT. For comparison experimental results reported by Groot *et al.* (Black symbols: experimental data from Ref. [8]) are plotted beside the theoretical results (red symbols). The arrows and accompanying numbers show the collision energy difference between the interpolated theoretical results and experimental data.

electronic dissipative channel enhances the trapping and, therefore, the dissociation probability [73]. The dissociation process is expected to increase in the presence of a trapping mechanism because once the molecule is trapped on the surface and starts to dissipate energy, it is difficult for the trapped molecule to recover the perpendicular translational energy to escape from the surface. The effect of including electron-hole pair excitations is therefore to increase the trapping-mediated contribution to the reactivity and thereby the reactivity. However, it keeps the direct mechanism almost unchanged. Raising the electronic temperature at lower incidence energies, *i.e.* through the presence of hot electrons, leads to collisions of the hot electrons with the molecule that can excite the molecular DOFs and provide the trapped mo-

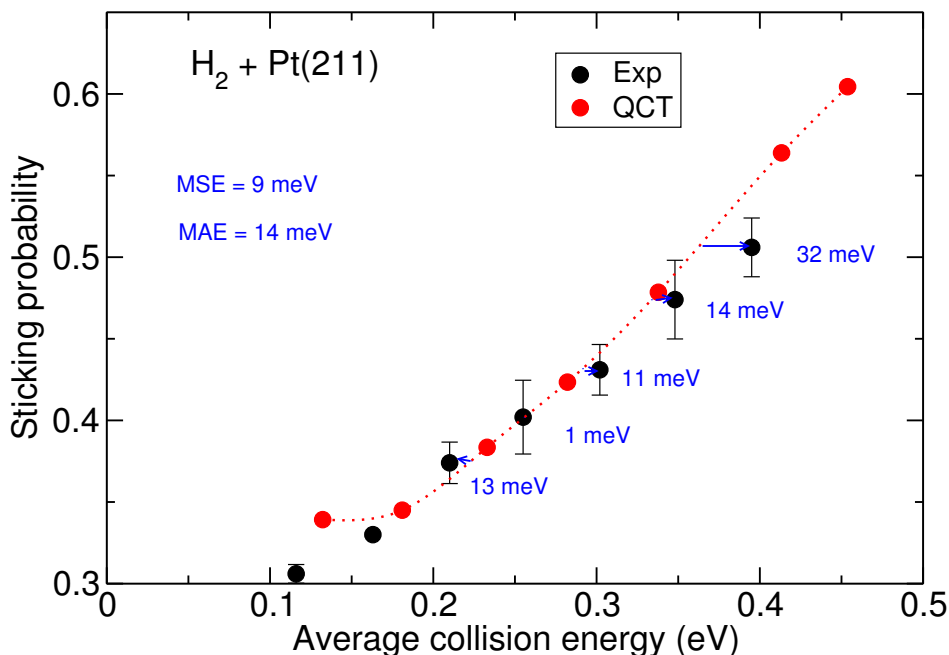


Figure 5.10: Sticking probability for molecular beam of  $H_2$  on Pt(211) simulated with QCT. For comparison experimental results reported by Groot *et al.* (Black symbols: experimental data from Ref. [8].) are plotted beside the theoretical results (red symbols). The arrows and accompanying numbers show the collision energy difference between the interpolated theoretical results and experimental data. In plotting the experimental results, we have assumed that the average incidence energy in the experiments was equal to  $2.7 k_B T_n$ .

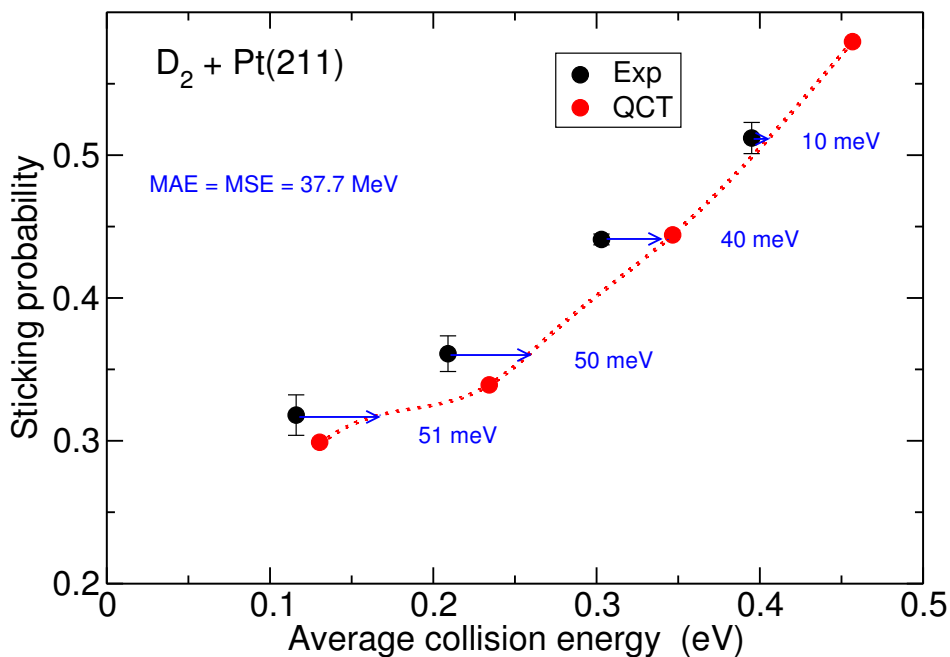


Figure 5.11: Sticking probability for molecular beam of D<sub>2</sub> on Pt(211) simulated with QCT. For comparison experimental results reported by Groot *et al.* (Black symbols: experimental data from Ref. [8].) are plotted beside the theoretical results (red symbols). The arrows and accompanying numbers show the collision energy difference between the interpolated theoretical results and experimental data. In plotting the experimental results, we have assumed that the average incidence energy in the experiments was equal to  $2.7 k_B T_n$ .

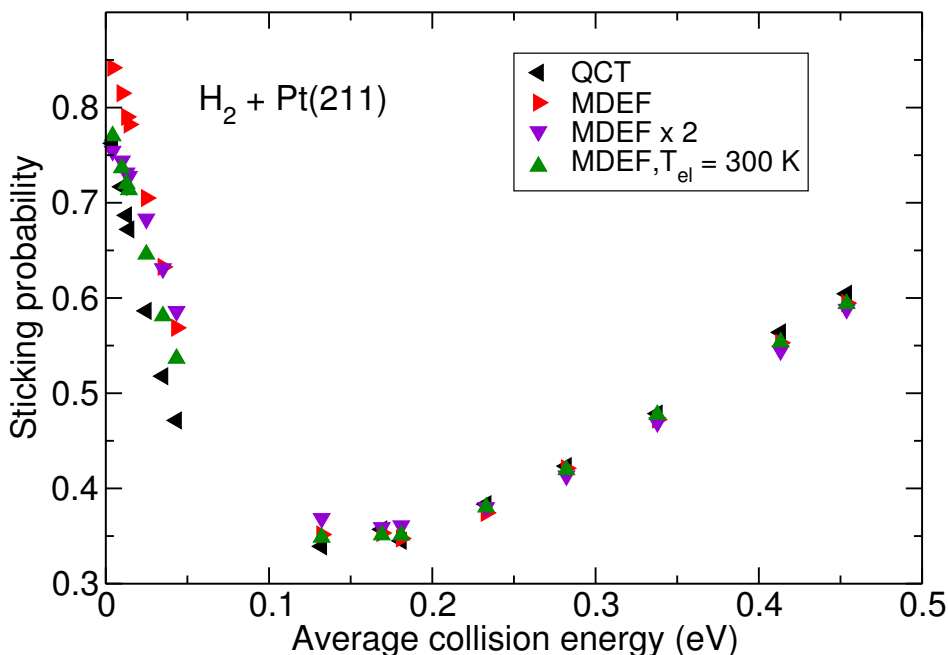


Figure 5.12: Sticking probability as a function of the average incidence energy obtained from MD and MDEF calculations. Black symbols show the MD, red and purple symbols show results of MDEF calculations using friction coefficient multiplied by different factors ( $\times 1$  and  $\times 2$  respectively) and green symbols show MDEF results using an electronic temperature  $T_{el} = 300$  K.

lecule with sufficiently high energy to get desorbed from the surface to the gas phase. Taking the electronic temperature in our calculations at lower incidence energies into account diminishes the trapping effect and therefore reduces the overall reactivity.

The good agreement between the MD and MDEF results at higher incidence energies confirms that the BOSS model, which does not consider electron-hole pair excitation, may accurately describe the dissociation of  $H_2$  and  $D_2$  on Pt(211) through the direct reaction mechanism at the terrace, and therefore, at higher incidence energies.

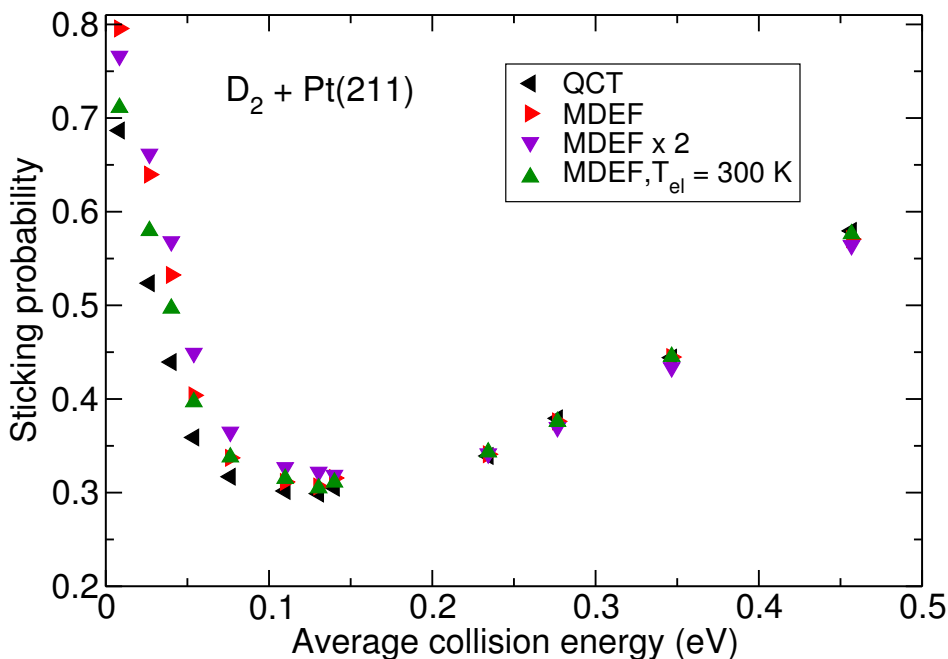


Figure 5.13: Sticking probability as a function of the average incidence energy obtained from MD and MDEF calculations. Black symbols show the MD, red and purple symbols show results of MDEF calculations using friction coefficient multiplied by different factors ( $\times 1$  and  $\times 2$  respectively) and green symbols show MDEF results using an electronic temperature  $T_{el} = 300$  K.

## 5.4 Conclusion

To address the question whether the SRP–DF functional derived for the  $\text{H}_2 + \text{Pt}(111)$  is transferable to the  $\text{H}_2 + \text{Pt}(211)$  system, we have performed calculations on the dissociation of  $\text{H}_2/\text{D}_2$  on the stepped  $\text{Pt}(211)$  surface. We used the VASP software package to compute the raw DFT data. The CRP interpolation method was used to accurately fit these data and construct the 6D PES based on the  $\text{PBE}\alpha\text{-vdW-DF2}$  functional with  $\alpha$  set to 0.57. The potential energy for H on  $\text{Pt}(211)$  for geometry optimized atom-surface distances on a  $(1\times 1)$  supercell was discussed and was compared with the previously developed PES of Olsen *et al.* [42]. We have also

discussed features of the PES for  $H_2$  dissociation on Pt(211) and reported on minimum barrier heights and associated geometries.

We have performed calculations within the BOSS model and within the MDEF model, in order to study non-adiabatic effects on the dissociation dynamics due to the creation of electron-hole pairs in the surface. The QCT method has been used to compute the initial-state resolved reaction probability and molecular beam sticking probability. The initial-state resolved reaction probability results obtained with the QCT method were compared with the results of QD calculations. The QCT calculations reproduced the QD results at the high energy range but not at the low energy range. The discrepancy between the results of these two dynamics methods at the low energy regime was discussed. We have also shown and discussed the isotope effect in the QCT results on the reaction probability of ( $\nu = 0, j = 0$ ) of  $H_2$  and  $D_2$ .

We have computed the sticking probabilities of molecular hydrogen and deuterium on Pt(211) and compared our theoretical results with the experimental data. Our theoretical results showed that the reactivity on Pt(211) is enhanced relative to Pt(111), in agreement with experiment. The lowest barrier height for reaction was found at the upper edge of the step. Reaction on the upper edge of the step is not activated. We have simulated molecular beam sticking probabilities and compared them with the experimental data of Groot *et al.* [8]. We have reported the energy shifts between the experimental data and the spline-interpolated theoretical data to be in this range [7–92] meV for  $H_2 + Pt(211)$  and [3–55] meV for  $D_2 + Pt(211)$ . Thus, in this sense chemical accuracy was not yet achieved in our theoretical results. However, it is well-known that the average energy of pure  $H_2$  beams should not exceed  $2.7 k_B T_n$  due to the absence of vibrational cooling and the occurrence of only about 20% rotational cooling for a pure beam. Nevertheless, we found that in most cases the average energies of the pure  $H_2$  and the pure  $D_2$  beams exceeded  $3 k_B T_n$ . Consequently, we have re-plotted the experimental results employing average energies equal to  $2.7 k_B T_n$  and re-done the comparison with computed sticking probabilities. With this modification, the agreement between experiment and theory tremendously improved for  $H_2$ . The agreement between theory and experiment for  $D_2$  was not as satisfactory as for  $H_2$  at the lower incidence energies in the high energy range. These results suggest that the experiments should be repeated and be reported for more accurately measured beam parameters to enable a better determination of the accuracy of the theoretical results.



Finally, we have presented the comparison of MD and MDEF results for the sticking probability for both H<sub>2</sub> and D<sub>2</sub> and discussed the effect of adding electronic friction and doubling the friction coefficient, and the effect of electronic temperature on the sticking at low and high incidence energies.

## References

1. Zambelli, T., Wintterlin, J., Trost, J. & Ertl, G. Identification of the "Active Sites" of a Surface-Catalyzed Reaction. *Science* **273**, 1688–1690 (1996).
2. Lu, K. & Rye, R. Flash Desorption and Equilibration of  $H_2$  and  $D_2$  on Single Crystal Surfaces of Platinum. *Surface Science* **45**, 677–695 (1974).
3. Bernasek, S. L. & Somorjai, G. A. Molecular Beam Study of the Mechanism of Catalyzed Hydrogen–Deuterium Exchange on Platinum Single Crystal Surfaces. *Journal of Chemical Physics* **62**, 3149–3161 (1975).
4. Christmann, K. & Ertl, G. Interaction of Hydrogen with Pt(111): The Role of Atomic Steps. *Surface Science*. **60**, 365–384 (1976).
5. Poelsema, B., Mechttersheimer, G. & Comsa, G. The Interaction of Hydrogen with Platinum(s)-9(111)  $\times$  (111) Studied with Helium Beam Diffraction. *Surface Science* **111**, 519–544 (1981).
6. Gee, A. T., Hayden, B. E., Mormiche, C. & Nunney, T. S. The Role of Steps in the Dynamics of Hydrogen Dissociation on Pt(533). *Journal of Chemical Physics* **112**, 7660–7668 (2000).
7. Groot, I. M. N., Schouten, K. J. P., Kleyn, A. W. & Juurlink, L. B. F. Dynamics of Hydrogen Dissociation on Stepped Platinum. *Journal of Chemical Physics* **129**, 224707 (2008).
8. Groot, I. M. N., Kleyn, A. W. & Juurlink, L. B. F. The Energy Dependence of the Ratio of Step and Terrace Reactivity for  $H_2$  Dissociation on Stepped Platinum. *Angewandte Chemie International Edition* **50**, 5174–5177 (2011).
9. Dahl, S. *et al.* Role of Steps in  $N_2$  Activation on Ru(0001). *Physics Review Letters* **83**, 1814–1817 (1999).
10. Honkala, K. *et al.* Ammonia Synthesis from First-Principles Calculations. *Science* **307**, 555–558 (2005).
11. Gee, A. T., Hayden, B. E., Mormiche, C., Kleyn, A. W. & Riedmüller, B. The Dynamics of the Dissociative Adsorption of Methane on Pt(533). *Journal of Chemical Physics* **118**, 3334–3341 (2003).

12. Migliorini, D. *et al.* Surface Reaction Barriometry: Methane Dissociation on Flat and Stepped Transition-Metal Surfaces. *Journal of Physical Chemistry Letters* **8**, 4177–4182 (2017).
13. Olsen, R., McCormack, D. & Baerends, E. How Molecular Trapping Enhances the Reactivity of Rough Surfaces. *Surface Science* **571**, L325–L330 (2004).
14. McCormack, D. A., Olsen, R. A. & Baerends, E. J. Mechanisms of H<sub>2</sub> Dissociative Adsorption on the Pt(211) Stepped Surface. *Journal of Chemical Physics* **122**, 194708 (2005).
15. Luppi, M., McCormack, D. A., Olsen, R. A. & Baerends, E. J. Rotational Effects in the Dissociative Adsorption of H<sub>2</sub> on the Pt(211) Stepped Surface. *Journal of Chemical Physics* **123**, 164702 (2005).
16. Ludwig, J., Vlachos, D. G., van Duin, A. C. T. & Goddard, W. A. Dynamics of the Dissociation of Hydrogen on Stepped Platinum Surfaces using the ReaxFF Reactive Force Field. *Journal of Physical Chemistry B* **110**, 4274–4282 (2006).
17. Olsen, R. A., McCormack, D. A., Luppi, M. & Baerends, E. J. Six-Dimensional Quantum Dynamics of H<sub>2</sub> Dissociative Adsorption on the Pt(211) Stepped Surface. *Journal of Chemical Physics* **128**, 194715 (2008).
18. Fücksel, G. *et al.* Anomalous Dependence of the Reactivity on the Presence of Steps: Dissociation of D<sub>2</sub> on Cu(211). *Journal of Physical Chemistry Letters* **9**, 170–175 (2018).
19. Cao, K., Fücksel, G., Kleyn, A. W. & Juurlink, L. B. F. Hydrogen Adsorption and Desorption from Cu(111) and Cu(211). *Physical Chemistry Chemical Physics* **20**, 22477–22488 (2018).
20. Huang, X., Yan, X. & Xiao, Y. Effects of Vacancy and Step on Dissociative Dynamics of H<sub>2</sub> on Pd(111) Surfaces. *Chemical Physics Letters* **531**, 143–148 (2012).
21. Fuhrmann, T. *et al.* Activated Adsorption of Methane on Pt(111) -an in Situ XPS Study. *New Journal of Physics* **7**, 107 (2005).
22. Chadwick, H., Gutiérrez-González, A., Migliorini, D., Beck, R. D. & Kroes, G. J. Incident Angle Dependence of CHD<sub>3</sub> Dissociation on the Stepped Pt(211) Surface. *Journal of Physical Chemistry C* **122**, 19652–19660 (2018).

23. Chadwick, H. *et al.* Methane Dissociation on the Steps and Terraces of Pt(211) Resolved by Quantum State and Impact Site. *Journal of Chemical Physics* **148**, 014701 (2018).
24. Migliorini, D., Chadwick, H. & Kroes, G. J. Methane on a Stepped Surface: Dynamical Insights on the Dissociation of CHD<sub>3</sub> on Pt(111) and Pt(211). *Journal of Chemical Physics* **149**, 094701 (2018).
25. Díaz, C. *et al.* Chemically Accurate Simulation of a Prototypical Surface Reaction: H<sub>2</sub> Dissociation on Cu(111). *Science* **326**, 832–834 (2009).
26. Sementa, L. *et al.* Reactive Scattering of H<sub>2</sub> from Cu(100): Comparison of Dynamics Calculations Based on the Specific Reaction Parameter Approach to Density Functional Theory with Experiment. *Journal of Chemical Physics* **138** (2013).
27. Nattino, F. *et al.* Chemically Accurate Simulation of a Polyatomic Molecule-Metal Surface Reaction. *Journal of Physical Chemistry Letters* **7**, 2402–2406 (2016).
28. Ghassemi, E. N., Wijzenbroek, M., Somers, M. F. & Kroes, G. J. Chemically Accurate Simulation of Dissociative Chemisorption of D<sub>2</sub> on Pt(111). *Chemical Physics Letters* **683**. Ahmed Zewail (1946-2016) Commemoration Issue of Chemical Physics Letters, 329–335 (2017).
29. Becke, A. D. Density-Functional Exchange-Energy Approximation with Correct Asymptotic Behavior. *Physical Review A* **38**, 3098–3100 (1988).
30. Perdew, J. P. Density-Functional Approximation for the Correlation Energy of the Inhomogeneous Electron Gas. *Physical Review B* **33**, 8822–8824 (1986).
31. Busnengo, H. F., Salin, A. & Dong, W. Representation of the 6D Potential Energy Surface for a Diatomic Molecule Near a Solid Surface. *Journal of Chemical Physics* **112**, 7641–7651 (2000).
32. Groot, I. M. N., Kleyn, A. W. & Juurlink, L. B. F. Separating Catalytic Activity at Edges and Terraces on Platinum: Hydrogen Dissociation. *Journal of Physical Chemistry C* **117**, 9266–9274 (2013).
33. Kresse, G. & Hafner, J. *Ab Initio* Molecular Dynamics for Liquid Metals. *Physical Review B* **47**, 558–561 (1993).
34. Kresse, G. & Hafner, J. *Ab Initio* Molecular-Dynamics Simulation of the Liquid-Metal-Amorphous-Semiconductor Transition in Germanium. *Physical Review B* **49**, 14251–14269 (1994).

35. Kresse, G. & Furthmüller, J. Efficiency of *Ab-Initio* Total Energy Calculations for Metals and Semiconductors Using a Plane-Wave Basis Set. *Computational Materials Science* **6**, 15–50 (1996).
36. Kresse, G. & Furthmüller, J. Efficient Iterative Schemes for *Ab Initio* Total-Energy Calculations Using a Plane-Wave Basis Set. *Physical Review B* **54**, 11169–11186 (1996).
37. Madsen, G. K. H. Functional Form of the Generalized Gradient Approximation for Exchange: The PBE $\alpha$  Functional. *Physical Review B* **75**, 195108 (2007).
38. Lee, K., Murray, É. D., Kong, L., Lundqvist, B. I. & Langreth, D. C. Higher-Accuracy van der Waals Density Functional. *Physical Review B* **82**, 081101 (2010).
39. Luntz, A. C., Brown, J. K. & Williams, M. D. Molecular Beam Studies of H<sub>2</sub> and D<sub>2</sub> Dissociative Chemisorption on Pt(111). *Journal of Chemical Physics* **93**, 5240–5246 (1990).
40. Monkhorst, H. J. & Pack, J. D. Special Points for Brillouin-Zone Integrations. *Physical Review B* **13**, 5188–5192 (1976).
41. Materer, N. *et al.* Reliability of Detailed LEED Structural Analyses: Pt(111) and Pt(111)-p(2×2)-O. *Surface Science* **325**, 207–222 (1995).
42. Olsen, R. A., Bădescu, C., Ying, S. C. & Baerends, E. J. Adsorption and Diffusion on a Stepped Surface: Atomic Hydrogen on Pt(211). *Journal of Chemical Physics* **120**, 11852–11863 (2004).
43. Karplus, M., Porter, R. N. & Sharma, R. D. Exchange Reactions with Activation Energy. I. Simple Barrier Potential for (H, H<sub>2</sub>). *Journal of Chemical Physics* **43**, 3259–3287 (1965).
44. Füchsel, G., del Cueto, M., Díaz, C. & Kroes, G. J. Enigmatic HCl + Au(111) Reaction: A Puzzle for Theory and Experiment. *Journal of Physical Chemistry C* **120**, 25760–25779 (2016).
45. Head-Gordon, M. & Tully, J. C. Molecular Dynamics with Electronic Frictions. *Journal of Chemical Physics* **103**, 10137–10145 (1995).
46. Lemons, D. S. & Gythiel, A. Paul Langevin's 1908 paper "On the Theory of Brownian Motion" ["Sur la théorie du mouvement brownien," C. R. Acad. Sci. (Paris) 146, 530-533 (1908)]. *American Journal of Physics* **65**, 1079–1081 (1997).

47. Füchsel, G., Klamroth, T., Monturet, S. & Saalfrank, P. Dissipative Dynamics within the Electronic Friction Approach: the Femtosecond Laser Desorption of  $H_2/D_2$  from Ru(0001). *Physical Chemistry Chemical Physics* **13**, 8659–8670 (2011).
48. Juaristi, J. I., Alducin, M., Muiño, R. D., Busnengo, H. F. & Salin, A. Role of Electron-Hole Pair Excitations in the Dissociative Adsorption of Diatomic Molecules on Metal Surfaces. *Physical Review Letters* **100**, 116102 (2008).
49. Novko, D., Blanco-Rey, M., Alducin, M. & Juaristi, J. I. Surface Electron Density Models for Accurate *Ab Initio* Molecular Dynamics with Electronic Friction. *Physical Review B* **93**, 245435 (2016).
50. Puska, M. J. & Nieminen, R. M. Atoms Embedded in an Electron Gas: Phase Shifts and Cross Sections. *Physical Review B* **27**, 6121–6128 (1983).
51. Füchsel, G., Schimka, S. & Saalfrank, P. On the Role of Electronic Friction for Dissociative Adsorption and Scattering of Hydrogen Molecules at a Ru(0001) Surface. *Journal of Physical Chemistry A* **117**, 8761–8769 (2013).
52. Luntz, A. C. *et al.* Comment on “Role of Electron-Hole Pair Excitations in the Dissociative Adsorption of Diatomic Molecules on Metal Surfaces”. *Physical Review Letters* **102**, 109601 (2009).
53. Spiering, P. & Meyer, J. Testing Electronic Friction Models: Vibrational De-Excitation in Scattering of  $H_2$  and  $D_2$  from Cu(111). *Journal of Physical Chemistry Letters* **9**, 1803–1808 (2018).
54. Maurer, R. J., Jiang, B., Guo, H. & Tully, J. C. Mode Specific Electronic Friction in Dissociative Chemisorption on Metal Surfaces:  $H_2$  on Ag(111). *Physical Review Letters* **118**, 256001 (2017).
55. Kosloff, R. Time-Dependent Quantum-Mechanical Methods for Molecular Dynamics. *Journal of Physical Chemistry* **92**, 2087–2100 (1988).
56. Pijper, E., Kroes, G. J., Olsen, R. A. & Baerends, E. J. Reactive and Diffractive Scattering of  $H_2$  from Pt(111) Studied Using a Six-Dimensional Wave Packet Method. *Journal of Chemical Physics* **117**, 5885–5898 (2002).

57. Feit, M., Fleck, J. & Steiger, A. Solution of the Schrödinger Equation by a Spectral Method. *Journal of Computational Physics* **47**, 412–433 (1982).
58. Vibok, A. & Balint-Kurti, G. G. Parametrization of Complex Absorbing Potentials for Time-Dependent Quantum Dynamics. *Journal of Physical Chemistry* **96**, 8712–8719 (1992).
59. Corey, G. C. & Lemoine, D. Pseudospectral Method for Solving the Time-Dependent Schrödinger Equation in Spherical Coordinates. *Journal of Chemical Physics* **97**, 4115–4126 (1992).
60. Lemoine, D. The Finite Basis Representation as the Primary Space in Multidimensional Pseudospectral Schemes. *Journal of Chemical Physics* **101**, 10526–10532 (1994).
61. Balint-Kurti, G. G., Dixon, R. N. & Marston, C. C. Grid Methods for Solving the Schrödinger Equation and Time Dependent Quantum Dynamics of Molecular Photofragmentation and Reactive Scattering Processes. *International Reviews in Physical Chemistry* **11**, 317–344 (1992).
62. Rettner, C. T., Michelsen, H. A. & Auerbach, D. J. Quantum-State-Specific Dynamics of the Dissociative Adsorption and Associative Desorption of H<sub>2</sub> at a Cu(111) Surface. *Journal of Chemical Physics* **102**, 4625–4641 (1995).
63. Ghassemi, E. N. *et al.* Transferability of the Specific Reaction Parameter Density Functional for H<sub>2</sub> + Pt(111) to H<sub>2</sub> + Pt(211). *Journal of Physical Chemistry C* **123**, 2973–2986 (2019).
64. Ermak, D. L. & Buckholz, H. Numerical Integration of the Langevin Equation: Monte Carlo Simulation. *Journal of Computational Physics* **35**, 169–182 (1980).
65. Winkler, A. Interaction of Atomic Hydrogen with Metal Surfaces. *Applied Physics A* **67**, 637–644 (1998).
66. Kroes, G. J., Pavanello, M., Blanco-Rey, M., Alducin, M. & Auerbach, D. J. *Ab Initio* Molecular Dynamics Calculations on Scattering of Hyperthermal H Atoms from Cu(111) and Au(111). *Journal of Chemical Physics* **141**, 054705 (2014).

67. Darling, G. R. & Holloway, S. Translation-to-Vibrational Excitation in the Dissociative Adsorption of  $D_2$ . *Journal of Chemical Physics* **97**, 734–736 (1992).
68. Polanyi, J. C. Concepts in Reaction Dynamics. *Accounts of Chemical Research* **5**, 161–168 (1972).
69. Gross, A. Reactions at Surfaces Studied by *Ab Initio* Dynamics Calculations. *Surface Science Reports* **32**, 291–340 (1998).
70. Busnengo, H. F. *et al.* Six-Dimensional Quantum and Classical Dynamics Study of  $H_2(\nu = 0, J = 0)$  Scattering from Pd(111). *Chemical Physics Letters* **356**, 515–522 (2002).
71. Gallagher, R. J. & Fenn, J. B. Rotational Relaxation of Molecular Hydrogen. *Journal of Chemical Physics* **60**, 3492–3499 (1974).
72. Rendulic, K., Anger, G. & Winkler, A. Wide Range Nozzle Beam Adsorption Data for the Systems  $H_2$ /Nickel and  $H_2$ /Pd(100). *Surface Science* **208**, 404–424 (1989).
73. Goikoetxea, I., Juaristi, J. I., Alducin, M. & Muiño, R. D. Dissipative Effects in the Dynamics of  $N_2$  on Tungsten Surfaces. *Journal of Physical Condense Matter* **21**, 264007 (2009).



# CHAPTER 6

## Assessment of Two Problems of Specific Reaction Parameter Density Functional Theory : Sticking and Diffraction of H<sub>2</sub> on Pt(111)

This chapter is based on:

Elham Nour Ghassemi, Mark F. Somers, and Geert-Jan Kroes *The Journal of Physical Chemistry C* **123**(16), 10406-10418, 2019.



## Abstract

It is important that theory is able to accurately describe dissociative chemisorption reactions on metal surfaces, as such reactions are often rate controlling in heterogeneously catalyzed processes. Chemically accurate theoretical descriptions have recently been obtained on the basis of the specific reaction parameter (SRP) approach to density functional theory (DFT), allowing reaction barriers to be obtained with chemical accuracy. However, being semi-empirical this approach suffers from two basic problems. The first is that sticking probabilities (to which SRP density functionals (DFs) are usually fitted) might show differences across experiments, of which the origins are not always clear. The second is that it has proven hard to use experiments on diffractive scattering of  $\text{H}_2$  from metals for validation purposes, as dynamics calculations using a SRP–DF may yield a rather poor description of the measured data, especially if the potential used contains a van der Waals well. We address the first problem by performing dynamics calculations on three sets of molecular beam experiments on  $\text{D}_2 + \text{Pt}(111)$ , using four sets of molecular beam parameters to obtain sticking probabilities, and the SRP–DF recently fitted to one set of experiments on  $\text{D}_2 + \text{Pt}(111)$ . It is possible to reproduce all three sets of experiments with chemical accuracy with the aid of two sets of molecular beam parameters. The theoretical simulations with the four different sets of beam parameters allow one to determine for which range of incidence conditions the experiments should agree well, and for which conditions they should show specific differences. This allows one to arrive at conclusions about the quality of the experiments, and about problems that might affect the experiments. Our calculations on diffraction of  $\text{H}_2$  scattering from  $\text{Pt}(111)$  show both quantitative and qualitative differences with previously measured diffraction probabilities, which were Debye-Waller (DW) extrapolated to 0 K. We suggest that DW extrapolation, which is appropriate for direct scattering, might fail if the scattering is affected by the presence of a van der Waals well, and that theory should attempt to model surface atom motion for reproducing diffraction experiments performed for surface temperatures of 500 K and higher.

## 6.1 Introduction

Dissociative chemisorption reactions are important elementary surface reactions, in the sense that they often control the rate of heterogeneously catalyzed processes [1, 2], which are used in most of the reactive processes carried out by the chemical industry [3]. Well-known examples include  $N_2$  dissociation in ammonia synthesis [4] and the dissociative chemisorption of methane in the steam reforming reaction [5]. Simulating rate-controlling reactions accurately is crucial to the calculation of accurate rates of the overall catalyzed processes [6]. Therefore, it is important to be able to perform accurate calculations on dissociative chemisorption reactions.

At present, the best method to obtain accurate results (and in some cases predictions) for dissociative chemisorption reactions is based on a semi-empirical version of density functional theory, called the specific reaction parameter (SRP) approach to DFT (SRP–DFT). This method has now been applied successfully to three  $H_2$ -metal systems ( $H_2 + Cu(111)$  [7],  $H_2 + Cu(100)$  [8], and  $H_2 + Pt(111)$  [9]), and three  $CH_4$ -metal systems ( $CHD_3 + Ni(111)$  [10],  $CHD_3 + Pt(111)$  [11], and  $CHD_3 + Pt(211)$  [11]). The method is predictive to the extent that it is often possible to derive an accurate SRP density functional (SRP–DF) by simply taking the SRP–DF from a chemically related system: the SRP–DF for  $H_2 + Cu(111)$  accurately describes the dissociation of  $H_2$  on  $Cu(100)$  [8], and the SRP–DF for  $CH_4 + Ni(111)$  accurately describes  $CHD_3 + Pt(111)$  and  $Pt(211)$  [11].

However, being semi-empirical and in need of validation, the SRP–DFT approach is not without problems. The first problem is that the SRP–DFT approach is obviously no more accurate than the underlying experimental data are. This problem can become severe if different sets of measurements of the sticking probability for a specific system show widely differing results, as recently explored for  $H_2 + Pd(111)$  [12]. The second problem has to do with the demands put on SRP–DFs. For a density functional to be called a SRP–DF, a requirement put forward is that at least one set of experiments not used to derive the SRP–DF can be accurately reproduced with dynamics calculations based on that SRP–DF. This has recently been a problem for  $H_2 + Ru(0001)$ , where it was possible to accurately reproduce sticking experiments, but not diffraction experiments, with dynamics calculations based on two functionals also containing van der Waals correlation [13].

Here we address the above two problems for the dissociative chemisorption of deuterated dihydrogen on Pt(111). Platinum is an important hydro-

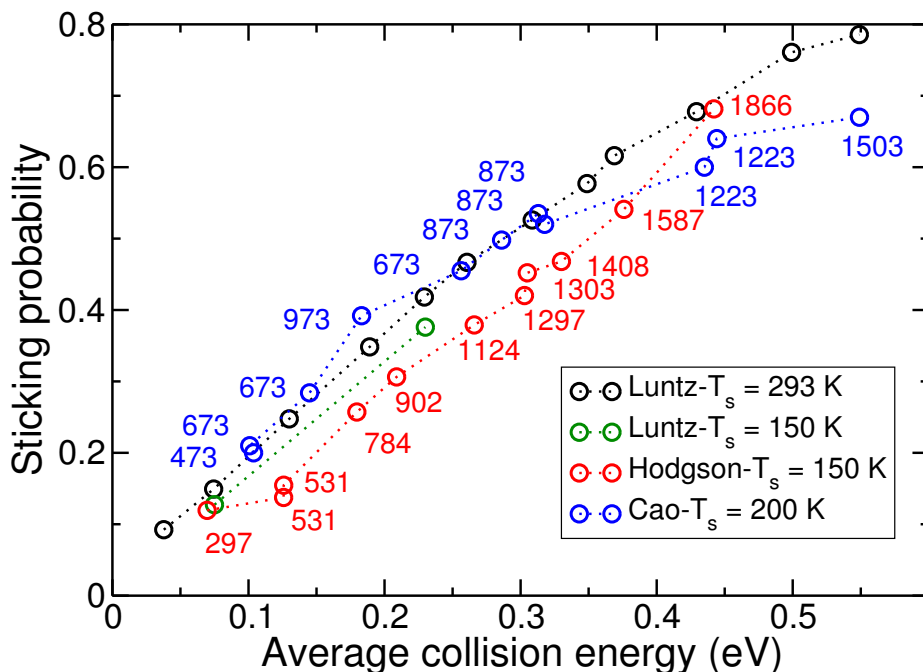


Figure 6.1: Comparison of the energy dependence of the sticking probability of  $D_2$  on Pt(111) for three different sets of experimental data from Hodgson and co-workers [16] (red circles), Luntz *et al.* [15] (black circles for a surface temperature  $T_s$  of 293 K, green circles for  $T_s \approx 150$  K), and Cao *et al.* [17] (blue circles). Nozzle temperatures  $T_n$  are indicated (in K) for the experiments of Hodgson and co-workers and of Cao *et al.*.

generation catalyst [14], and consequently the sticking of  $H_2$  on Pt(111) has been studied in molecular beam experiments by three different groups [15–17]. While the outcome of these experiments is not as varied as results for  $H_2 + Pd(111)$ , as discussed further below there are nevertheless considerable differences between the sets of sticking probabilities  $S_0$  measured in the three experiments (see also Figure 6.1).

Diffractive scattering of dihydrogen from Pt surfaces has been studied experimentally by Cowin *et al.* in the 1980s [18–20], and more recently by Nieto *et al.* who also looked at out-of-plane diffraction [21]. An SRP–DF for  $H_2 + Pt(111)$  [9] has been fitted to molecular beam experiments on stick-

ing at normal incidence [15], and validated against sticking measurements performed for off-normal incidence [15].

Several theoretical studies have addressed the reactive [9, 21–28] and the diffractive [21, 22, 25, 26] scattering of dihydrogen from  $Pt(111)$ . Dynamics calculations based on the B88P86 generalized gradient approximation (GGA) exchange-correlation (XC) functional [29, 30] were able to reproduce measured sticking probabilities and in-plane and out-of-plane diffraction probabilities semi-quantitatively [21]. This might be taken to suggest that an SRP–DF can be fitted to molecular beam experiments on sticking, and then validated by showing that, on the basis of the fitted SRP–DF, diffraction probabilities can be reproduced quantitatively. However, calculations on  $H_2 + Ru(0001)$  have shown that this may be problematic [13], although for this case the situation could be improved by assuming static disorder of the surface [31]. Furthermore, comparisons of quantum dynamics (QD) calculations and quasi-classical trajectory (QCT) calculations modeling motion in all six degrees of freedom (DOFs) of  $H_2$  have established that the reaction of ( $\nu = 0, j = 0$ )  $H_2$  [24] and of ( $\nu = 0, j = 0$ )  $D_2$  [9] can be accurately modeled with the QCT method. Finally, QD calculations on  $H_2 + Pt(111)$  [27] and QCT calculations on  $D_2 + Pt(111)$  [9] have suggested that in the simulation of  $S_0$  measured in molecular beam experiments it should already be a good approximation to simply compute the reaction probability for ( $\nu = 0, j = 0$ ) dihydrogen at the average incident energy  $\langle E_i \rangle$ , and to omit the averaging over the translational energy distribution and the rovibrational energy distribution of  $H_2$  in the beam. Here,  $\nu$  and  $j$  are the vibrational and rotational quantum numbers of  $H_2$ .

Here, we use the recently determined SRP–DF for  $D_2 + Pt(111)$  to simulate all three available sets of  $S_0$  measured in supersonic molecular beam experiments with QCT calculations. The question we address is whether it is possible to simulate all three experiments with chemical accuracy on the basis of one DF. A problem we address in this connection is that the experiments have not always been described in as much detail as theorists would like; for instance, the parameters characterizing the velocity distributions and rovibrational state distributions of the incident  $D_2$  are often poorly known. To address this, we will simulate all three sticking experiments using four different sets of molecular beam parameters. We also use the time-dependent wave packet (TDWP) method [25, 32] to compute diffraction probabilities on the basis of the SRP–DF, and compare these with the measured values for in-plane and out-of-plane diffraction of Nieto

*et al.* [21]. Here, the question addressed is whether the SRP–DF previously derived, on the basis of sticking probabilities and based on GGA exchange and van der Waals (non-local) correlation, allows the accurate modeling of diffraction of  $\text{H}_2$  from a metal surface.

This chapter is set up as follows. Section 6.2.1 gives an in-depth description of the three sets of supersonic molecular beam experiments that have been performed on sticking of  $\text{D}_2$  on Pt(111). Section 6.2.2 discussed the four sets of molecular beam parameters that we have used to simulate these experiments. Section 6.2.3 compares the outcome of the experiments, and discusses which set of molecular beam parameters should in principle be best for simulating each experiment. Section 6.3 discusses the methods we have used. Section 6.3.1 discusses the dynamical model used, Section 6.3.2 the potential energy surface based on the SRP–DF, Section 6.3.3 the dynamics methods employed, Section 6.3.4 the computation of the observables, and Section 6.3.5 provides computational details. Section 6.4 contains the results and discussion, with Section 6.4.1 addressing the simulation of the sticking measurements, and Section 6.4.2 the results for diffraction of  $\text{H}_2$ . Finally, conclusions are presented in Section 6.5.

## 6.2 Experiments and beam parameters used to simulate the experiments

In this section we provide a brief description of the three supersonic molecular beam experiments on  $\text{D}_2 + \text{Pt}(111)$  that have been published in the literature [15–17]. In all three publications, results were reported for normal incidence, which we focus on in the present work. We also give a brief description of the four different sets of molecular beam parameters that we have used to simulate the experiments. We finish with a brief discussion of how well the experiments agree with one another, and of which set of parameters should, in principle, be optimal for simulating the three different published experiments.

### 6.2.1 Molecular beam experiments on $\text{D}_2 + \text{Pt}(111)$

The first experiments reported on  $\text{D}_2 + \text{Pt}(111)$  were published by Luntz *et al.*, and we focus on the sticking probabilities  $S_0$  reported in figure 1 of their paper [15], which were measured at a surface temperature ( $T_s$ ) of

295 K. The sticking probabilities were measured with the King and Wells technique [33]. The beam energies were varied by both changing the nozzle temperature  $T_n$  (temperatures up to 1800 K were used) and by seeding D<sub>2</sub> in H<sub>2</sub> (thereby increasing its speed) or in Ne (decreasing its speed). According to the authors, the beam energies were measured with time-of-flight (TOF) techniques to approximately 2 % accuracy. The energies reported were energies averaged over flux weighted velocity distributions [34]. Luntz *et al.* did not report the actual parameters describing their velocity distributions. Luntz *et al.* also reported sticking probabilities for off-normal incidence, for varying polar incidence angles. They also measured the dependence of  $S_0$  on  $T_s$  in the range 100-300 K, and reported that for average incidence energies  $\langle E_i \rangle$  of 0.075 eV and 0.23 eV  $S_0$  shows only a very small increase with  $T_s$  [15].

Subsequently, sticking probabilities of D<sub>2</sub> on Pt(111) were published by Hodgson and co-workers, in the framework of a study on dissociation of D<sub>2</sub> on Sn/Pt(111) surface alloys. The sticking probabilities were reported in figure 5a of their paper, and were measured for a surface temperature of 150 K [16]. Sticking probabilities were measured using temperature programmed desorption measurements calibrated against King and Wells measurements at high incidence energies, and/or using King and Wells measurements directly [35]. The experiments used pure D<sub>2</sub> beams, varying  $T_n$  up to a temperature of 2100 K. The experimentalists reported [16] that translational energy distributions were measured with TOF techniques, and that the mean translational energies were related to  $T_n$  through  $\langle E_i \rangle = 2.75 k_B T_n$ , referring to Ref. [36] for the details of the expansion conditions used. In a private communication [35] Hodgson reported that the incidence energy ( $E$ ) distributions could be described approximately by exponentially modified Gaussian distributions

$$G(E) = \sqrt{2\pi\sigma} \exp\left(\frac{-(E - \langle E \rangle)^2}{2\sigma}\right), \quad (6.1)$$

with  $\sigma$  defined as

$$\sigma = 5.11e^{-3}\langle E \rangle + 1.3184e^{-4}. \quad (6.2)$$

With these definitions, the average incidence energy  $\langle E_i \rangle$  is simply equal to  $\langle E \rangle$ .

Finally, sticking probabilities of D<sub>2</sub> on Pt(111) were published by Cao *et al.* [17], in the framework of a comparison to previously published  $S_0$



computed on the basis of SRP–DFT [9]. We focus on the sticking probabilities  $S_0$  reported in figure 1 of their paper [17], which were measured at  $T_s = 200$  K. The sticking probabilities were measured with the King and Wells technique [33]. The beam energies were varied by both changing  $T_n$  (temperatures up to 1503 K were used) and by seeding  $D_2$  in  $H_2$  or in Ne,  $N_2$ , or Ar. In addition to measuring  $T_n$ , the authors conducted TOF experiments to determine the stream velocities  $v_s$  and velocity widths  $\alpha$ , and taken together with  $T_n$  these parameters fully characterize the molecular beams employed. The parameters  $v_s$  and  $\alpha$  together determine the flux weighted velocity distribution

$$f(v_i; T_n)dv_i = Cv_i^3 e^{-(v_i - v_s)^2 / \alpha^2} dv_i, \quad (6.3)$$

and average incidence energies  $\langle E_i \rangle$  can be determined by averaging incidence energy over this distribution of incident velocities. The parameters used in the experiments are reported in table 6.1. Cao *et al.* also reported sticking probabilities for off-normal incidence, for varying polar incidence angles and for two planes of incidence.

### 6.2.2 Sets of molecular beam parameters and their use in simulating molecular beam experiments

In this chapter, we have used four sets of molecular beam parameters to simulate molecular beam experiments. The first set is derived from experiments on  $D_2 + Ru(0001)$  [37]. In these experiments, measurements were taken on sticking using pure  $D_2$  beams for five different values of  $T_n$  (300, 500, 900, 1300, and 1700 K), and for  $D_2$  beams seeded in  $H_2$  with two different mixing ratios for  $T_n = 1700$  K. The values of  $v_s$ ,  $\alpha$ , and  $T_n$ , which are available from Ref. [38], have been reported in table 3 of Ref. [13]. With the aid of these parameters, sticking probabilities can be computed by velocity averaging (mono-energetic) Boltzmann averaged reaction probabilities  $R_{mono}(E_i; T_n)$  over the velocity distribution specified in Equation 6.3 according to

$$R_{beam}(\bar{E}; T_n) = \frac{\int_0^\infty f(v_i; T_n) R_{mono}(E_i; T_n) dv_i}{\int_0^\infty f(v_i; T_n) dv_i}, \quad (6.4)$$

with the incidence energy  $E_i$  simply given by the product of half the mass of  $D_2$  with  $v_i^2$ , where  $v_i$  is the incident velocity. In turn, the Boltzmann

averaged reaction probability can be computed from the initial  $(\nu, j)$  state selected reaction probability  $P_{deg}(E_i, \nu, j)$  according to

$$R_{mono}(E_i; T_n) = \sum_{\nu, j} F_B(\nu, j; T_n) P_{deg}(E_i, \nu, j). \quad (6.5)$$

with

$$F_B(\nu, j; T_n) = \frac{F(\nu, j; T_n)}{\sum_{\nu, j} F(\nu, j; T_n)}, \quad (6.6)$$

and

$$F(\nu, j; T_n) = (2j + 1) e^{-\frac{E_{vib}(\nu)}{k_B T_{vib}}} w(j) e^{-\frac{E_{rot}(j)}{(k_B T_{rot})}}. \quad (6.7)$$

Here,  $\nu$  is the vibrational, and  $j$  the rotational quantum number of D<sub>2</sub>, and  $w(j)$  is 2 for even  $j$  and 1 for odd  $j$ . For the rotational temperature, typically  $T_{rot} = 0.8 T_n$  is assumed [39, 40], based mostly on experiments by Gallagher and Fenn [41], and this is what we used to simulate the experiments of Luntz *et al.* [15] and of Cao *et al.* [17]. The assumption made by Hodgson and co-workers that  $\langle E_i \rangle = 2.75 k_B T_n$  corresponds to  $T_{rot} = 0.75 T_n$  and this was used to simulate their experiments [16]. The beam parameters of Groot *et al.* describe molecular beams that are comparatively broad in energy (with large  $\alpha$  parameters), as can be seen from figure 1 of Ref. [37].

The second set of parameters describes the beams that were actually used in the D<sub>2</sub> + Pt(111) experiments of Cao *et al.* [17]. As noted above, the values of  $v_s$ ,  $\alpha$ , and  $T_n$  are presented in table 6.1. They can be used with Equations 6.3–6.7 to compute sticking probabilities for  $\langle E_i \rangle$  in the range 0.10–0.55 eV, with the results corresponding to  $T_n$  in the range 490–1520 K. As these parameters describe experiments from the same group as the first set of parameters discussed above, they likewise describe molecular beams that are comparatively broad in energy. The third set of parameters are a set of  $\langle E \rangle$ ,  $\sigma$ , and  $T_n$  describing a set of experiments of Hodgson and co-workers on D<sub>2</sub> + Ag(111) [36] for which the expansion conditions were similar to the conditions prevalent in the experiments on D<sub>2</sub> + Pt(111) of the same group [16]. The parameters, which were collected in table 1 of Ref. [42] (see also table 4.1), can be used together with Equations 6.1, 6.2, 6.5–6.7 and

$$R_{beam}(\bar{E}; T_n) = \frac{\int_0^\infty G(E_i; T_n) R_{mono}(E_i; T_n) dE_i}{\int_0^\infty G(E_i; T_n) dE_i}. \quad (6.8)$$

Table 6.1: Parameters used for the molecular beam simulations of  $D_2$  on Pt(111). These parameters are derived from the  $D_2 + Pt(111)$  experiments of Cao *et al.* [17].

$\langle E_i \rangle$ (eV)	$v_s$ (m/s)	$\alpha$ (m/s)	$T_{\text{nozzle}}$ (K)
0.104	2004.6	528.7	473
0.101	2127.9	297.9	673
0.145	2256.8	741.8	673
0.183	2484.9	881.7	973
0.256	3204.7	766.3	673
0.286	3302.7	906.7	873
0.313	3449.1	955.3	873
0.318	3521.1	909.4	873
0.436	4015.0	1181.0	1223
0.444	4096.5	1151.1	1223
0.549	4039.3	1744.7	1503

to compute sticking probabilities for  $\langle E_i \rangle$  in the range 0.22–0.49 eV, with the results corresponding to  $T_n$  in the range 970–2012 K. For similar  $\langle E_i \rangle$  the parameters describe distributions that are symmetric in incidence energy, and beams that are narrower in incidence energy than the beams described by parameter sets 1 and 2 (see figure 2 of Ref. [42], comparing to figure 1 of Ref. [37]).

The fourth set of parameters are once again a set of values of  $v_s$ ,  $\alpha$ , and  $T_n$ . They describe molecular beams of a width comparable to the  $D_2$  beams of Hodgson and co-workers, but which do not suffer from the unphysical symmetry in incidence energy [43] present in parameter set 3, as discussed in Ref. [42]. The parameters were obtained from Ref. [44] and describe pure  $D_2$  beam experiments on  $D_2 + Cu(111)$  [45], and are collected in table 6.2. (A subset of these parameters were presented in table S9 of Ref. [7]). The parameters can be used to simulate experiments with  $E_i$  in the range 0.21–0.45 eV, with the results corresponding to  $T_n$  in the range 875–1975 K.

Table 6.2: Parameters used for the molecular beam simulations of D<sub>2</sub> on Pt(111). These parameters are derived from the pure D<sub>2</sub> beam experiments on D<sub>2</sub> + Cu(111) of Auerbach and co-workers [44].

$\langle E_i \rangle$ (eV)	$v_s$ (m/s)	$\alpha$ (m/s)	$T_{\text{nozzle}}$ (K)
0.207	3134.0	203.0	875
0.244	3392.0	278.0	1030
0.265	3553.0	218.0	1120
0.305	3805.0	259.0	1290
0.340	4014.0	299.0	1435
0.392	4196.0	614.0	1790
0.400	4337.0	371.0	1670
0.430	4374.0	685.0	1905
0.446	4461.0	687.0	1975

### 6.2.3 Comparison of the measured S<sub>0</sub>

The three sets of measured S<sub>0</sub> are shown as a function of  $\langle E_i \rangle$  and compared with one another in Figure 6.1. The S<sub>0</sub> of Luntz *et al.* [15] and of Cao *et al.* [17] are in quite good agreement with one another for  $\langle E_i \rangle$  up to about 0.32 eV, but for higher  $\langle E_i \rangle$  the S<sub>0</sub> measured by Luntz *et al.* [15] are larger. The S<sub>0</sub> of Hodgson and co-workers [16] are smaller than the S<sub>0</sub> measured by Luntz *et al.* [15] and by Cao *et al.* [17] for almost all  $\langle E_i \rangle$ , except for  $\langle E_i \rangle > 0.4$  eV where they exceed the values measured by Cao *et al.*

To be able to provide a more detailed comparison, we compare the experiments on a one-to-one basis in Figure 6.2. Figure 6.2 (a) shows again that the S<sub>0</sub> of Luntz *et al.* [15] are larger than those of Hodgson and co-workers [16] over the entire energy range. About the origin of this difference we can only speculate. Some of the difference could be due to the lower  $T_s$  value used by Hodgson and co-workers (150 K [16] vs. 295 K in the experiment of Luntz *et al.* [15]). Figure 6.1 also shows two results of Luntz *et al.* measured at or interpolated to  $T_s = 150$  K (see figure 2 of their paper [15]). The plotted data suggests that at least some of the difference could be due to the lower  $T_s$  of Hodgson and co-workers, but is not clear to us how accurately the dependence on  $T_s$  was measured by Luntz *et al.*, and

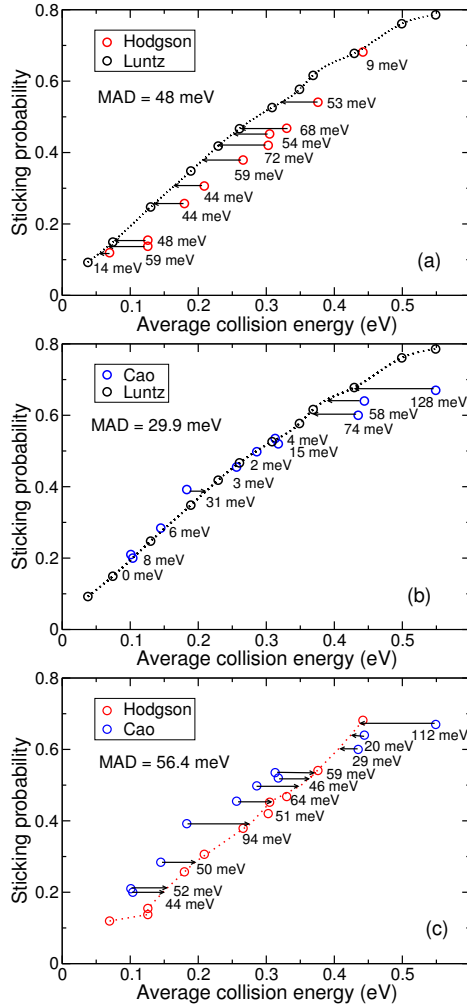


Figure 6.2: A one-to-one comparison of the experiments: (a) comparison of experimental data from Hodgson and co-workers [16] with experimental data from Luntz *et al.* [15], (b) comparison of experimental data from Cao *et al.* [17] with experimental data from Luntz *et al.* [15], and (c) comparison of experimental data from Hodgson and co-workers [16] with experimental data from Cao *et al.* [17]. In the all cases the horizontal arrows and the numbers indicate the energy spacings between the interpolated values of one experiment and the actual values of the other experiment. The dotted lines show the interpolated curve of one set of experimental data.

the  $T_s$  dependence of their data for  $\langle E_i \rangle = 0.23$  eV would seem rather large for weakly activated dissociation, also in view of the large mass mismatch between D<sub>2</sub> and Pt. We also note that the good agreement between the data of Luntz *et al.* ( $T_s = 293$  K) and the data of Cao *et al.* ( $T_s = 200$  K, see Figure 6.2 (b)) suggests a weak  $T_s$  dependence of sticking between  $T_s = 200$  K and 293 K. It is also possible that the difference is due to a calibration problem in the experiments of Hodgson and co-workers, who in some of the measurements used thermal desorption of D<sub>2</sub> to measure S<sub>0</sub>, and had to calibrate their measurement on a King and Wells measurement at high  $\langle E_i \rangle$ . It also seems possible that at least some of the differences are due to the use of seeding gasses in the experiments of Luntz *et al.* [15], whereas Hodgson and co-workers used pure D<sub>2</sub> beams [16]. Specifically, it is possible that  $T_n$  was higher in several experiments performed at similar  $\langle E_i \rangle$  by Luntz *et al.*, due to the use of a seeding gas that would slow H<sub>2</sub> down.

One way to quantify the discrepancy between the experiments (or between an experimental and a theoretical dataset) is to compute the mean average deviation (MAD) in the average incidence energy at which particular values of S<sub>0</sub> are achieved. This deviation has to be calculated between actual measured (or calculated) values in one experiment, and interpolated values in the other experiment (or calculation). The MAD between the data of Luntz *et al.* [15] and of Hodgson and co-workers [16] is 48 meV, which is larger than 1 kcal/mol ( $\approx 43$  meV). Using 1 kcal/mol as a measure of chemical accuracy, we can then say that the two datasets do not agree to within chemical accuracy.

The datasets of Luntz *et al.* [15] and of Cao *et al.* [17] agree much better with one another (MAD = 29.9 meV, chemical accuracy, see Figure 6.2 (b)), at least for  $\langle E_i \rangle$  up to 0.32 eV. This is not true for the larger  $\langle E_i \rangle$ , where the S<sub>0</sub> of Cao *et al.* are much smaller than those of Luntz *et al.*. It is not clear what this difference is due to. It is likely that for the highest  $\langle E_i \rangle$  H<sub>2</sub> was used as a seeding gas in both experiments. At these high incidence energies, the measurement of the beam parameters (and thereby the determination of the  $\langle E_i \rangle$ ) becomes difficult, and it is possible that the  $E_i$  was overestimated by Cao *et al.*, or was underestimated by Luntz *et al.*. Another common pitfall with the measurement of a high value of S<sub>0</sub> with the King and Wells method is that the measurement is taken over a time interval where the surface is already partly covered. This could also result in an underestimation of S<sub>0</sub> and could be taken as another indication that

perhaps the  $S_0$  of Cao *et al.* are underestimated as a function of  $\langle E_i \rangle$  at  $\langle E_i \rangle > 0.4$  eV.

The agreement between the datasets of Cao *et al.* [17] and of Hodgson and co-workers [16] is worst (MAD = 56.4 meV, Figure 6.2 (c)). At the highest values of  $\langle E_i \rangle$ , the discrepancies can be understood at least in part from the higher  $T_n$  values that had to be employed in the pure  $D_2$  beam experiments of Hodgson and co-workers to achieve high  $\langle E_i \rangle$  values. However, this is not true for intermediate  $E_i$  values, where the  $S_0$  of Cao *et al.* are higher than those of Hodgson and co-workers, even though the  $T_n$  values were lower in the experiments of Cao *et al.* [17] (see Figure 6.1). This, and the good agreement between the datasets of Luntz *et al.* [15] and Cao *et al.* for incidence energies up to 0.32 eV would seem to suggest that the measured  $S_0$  of Hodgson and co-workers are too low at least for the lower  $E_i$  range.

This also brings us to the question of which set of beam parameters can best be used to simulate the molecular beam experiments. The answer seems obvious for the experiments of Cao *et al.* [17]: for this, the best set of parameters should in principle be the set measured by them [46]. The answer is also fairly straightforward for the experiments of Hodgson and co-workers [16]: for this, the best choice should be the set of parameters available [35] from experiments on  $D_2 + Ag(111)$  [36], as they indicated [16] that the expansion conditions in these experiments were the same as in the  $D_2 + Pt(111)$  experiments. Also, an alternative would be to use beam parameters from the pure  $D_2$  beam experiments on  $D_2 + Cu(111)$  [44, 45], which describe beams with a similar width in incidence energy that possess the appropriate asymmetry with respect to incidence energy [42]. The answer is least obvious for the experiments of Luntz *et al.* [15]. However, the similarity of their results to those of Cao *et al.* [17] suggest that their molecular beam parameters [46] may well be best, with the beam parameters of Groot *et al.* [37] (see Ref. [13]) representing a good alternative, as these experiments [37] come from the same group as those of Cao *et al.*. However, below we will perform simulations using all four sets of beam parameters to describe each of the three experiments, and determine which set leads to the lowest MAD of theory with experiment. Here, it should be noted that the SRP-DF determined for  $H_2 + Pt(111)$  was fitted to the experiments of Luntz *et al.* [15], using the beam parameters [13] describing the experiments of Groot *et al.* on  $D_2 + Ru(0001)$  [37].

## 6.3 Method

### 6.3.1 Dynamical model

The Born-Oppenheimer Static Surface (BOSS) [7] model is used in this study, implying two approximations. First the Born-Oppenheimer (BO) approximation is made, in which the electronic motions are separated from the massive nuclei motions and the ground state potential energy surface (PES) is calculated. In this approximation, electron-hole pair excitation does not affect the reactivity. Second the static surface approximation is made, in which the frozen surface atoms occupy 0 K lattice configuration positions in the (111) surface of the face centered cubic (fcc) structure of the metal. Consideration of these approximations leads to taking 6 molecular degrees of freedom into account in the PES and dynamics calculations. Figure 6.3 (a) shows the coordinate system and Figure 6.3 (b) shows the surface unit cell for the Pt(111) surface and the symmetric sites. With our model we cannot obtain information on the surface temperature dependence of sticking or diffraction.

### 6.3.2 Potential energy surface

The DFT electronic structure method is used to map out the PES. To compute the PES, the SRP-DF was devised, with the combination of the PBE $\alpha$  [47] exchange functional with the adjustable parameter  $\alpha$  and the van der Waals DF2 correlation functional of Langreth and Lundqvist and co-workers [48] as :

$$E_{XC}^{SRP-DF} = E_X^{PBE\alpha} + E_C^{vdW-DF2}$$

where  $\alpha = 0.57$  [9]. In total, 29 different molecular configurations distributed over 6 different sites on the surface unit cell shown in Figure 6.3(b) were used to compute and to interpolate the 6D PES. The accurate corrugation reducing procedure (CRP) [49] method was used to interpolate the DFT data calculated on the grid. For more detailed information about the construction of the PES and the interpolation method the reader is referred to Ref. [9].



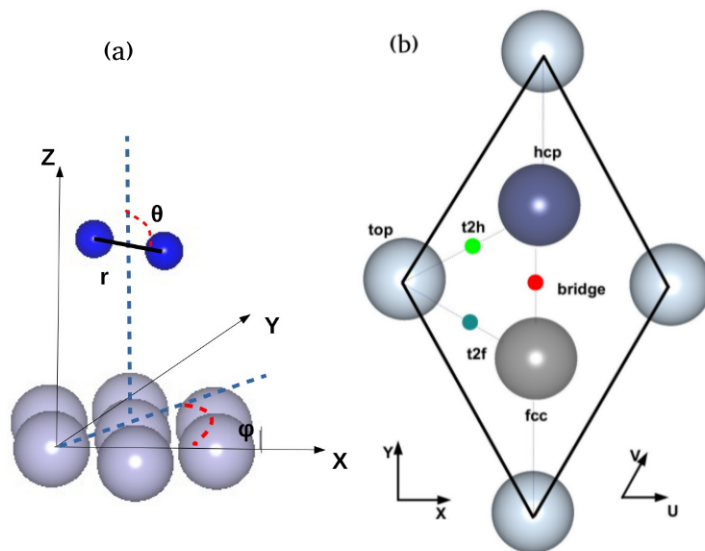


Figure 6.3: (a) The coordinate system for dissociation of H<sub>2</sub> on the Pt(111) surface. In the plot,  $X, Y, Z$  are the center of mass coordinates of H<sub>2</sub>,  $r$  is the H–H distance, and  $(\theta, \phi)$  are the polar and azimuthal angles specifying the orientation of the H–H bond with respect to the surface. (b) The schematic picture of the surface unit cell is indicated by a diamond shaped line connecting four top sites. The sites considered which are used for CRP interpolation, larger solid circles show the surface atoms and the small colored solid circles show the high symmetry sites. Two choices of coordinate system are indicated, a skewed coordinate system  $(U, V)$  and a Cartesian coordinate system  $(X, Y)$ . Light blue atoms are in the top layer, dark blue atoms are in the second layer, and gray atoms are in the third layer.

### 6.3.3 Dynamics methods

To compute dissociation probabilities for D<sub>2</sub> impinging on the Pt(111) surface the QCT method [50] was used. In this method the initial zero-point-energy (ZPE) of the molecule is taken into account, and the initial conditions are chosen with Monte Carlo sampling. The selection of the ori-

entation of the molecule,  $\theta$ , and  $\phi$ , is based on the selection of the initial rotational state. We used the fixed magnitude of the classical initial angular momentum according to  $L = \sqrt{j(j+1)}\hbar$ , and its orientation, while constrained by  $\cos \Theta_L = m_j/\sqrt{j(j+1)}$ , is otherwise randomly chosen as described in [13, 51]. Here,  $j$  is the rotational quantum number,  $m_j$  is the magnetic rotational quantum number and  $\Theta_L$  is the angle between the angular momentum vector and the surface normal. The impact sites are chosen at random.

The TDWP method was used to compute diffraction probabilities for H<sub>2</sub> scattering from Pt(111). This method is fully described in Ref. [25] (see also Section 2.5.2).

### 6.3.4 Computation of the observables

#### Initial state resolved reaction probabilities

Initial state resolved reaction probabilities  $P_{deg}(E; \nu, j)$  are obtained by degeneracy averaging the fully initial state resolved reaction probabilities  $P_r(E; \nu, j, m_j)$  according to

$$P_{deg}(E; \nu, j) = \frac{\sum_{m_j=0}^{m_j=j} (2 - \delta_{m_j,0}) \cdot P_r(E; \nu, j, m_j)}{(2j + 1)} \quad (6.9)$$

where  $P_r$  is the fully initial state-resolved reaction probability, and  $\delta$  is the Kronecker delta. Sections 6.2.1 and 6.2.2 have described how the degeneracy averaged sticking probabilities can be used to compute sticking probabilities for comparison with molecular beam experiments.

#### Diffraction probabilities

To study diffraction, a quantum phenomenon, quantum dynamics calculations should be performed as was done before for H<sub>2</sub> + Pt(111) [25]. In the diffractive scattering process, the molecules translational momentum parallel to the surface can only change by discrete amounts. In order to compare with the experimental diffraction probabilities [21], the rovibra-

tionally elastic diffraction probabilities are computed by

$$P_{nm}(E; \nu, j, m_j) = \sum_{m'_j=-j}^j P_{scat}(E; \nu, j, m_j \rightarrow \nu' = \nu, j' = j, m'_j, n, m), \quad (6.10)$$

where  $P_{nm}$  is the rovibrationally elastic probability for scattering into the diffraction state denoted by the  $n$  and  $m$  quantum numbers. These probabilities are degeneracy averaged by

$$P_{nm}(E; \nu, j) = \sum_{m_j=-j}^j P_{nm}(E; \nu, j, m_j)/(2j + 1). \quad (6.11)$$

The reciprocal lattice corresponding to the direct lattice is shown in Figure 6.4. The diffraction order  $O_d$  is also shown here. In the definition we use [21], the  $N^{th}$  diffraction order consists of all diffraction channels on the  $N^{th}$  concentric hexagon. The first order diffraction channels (1, 0), (-1, 0), (0, 1), (0, -1), (1, 1) and (-1, -1) correspond to a momentum change of one quantum  $\Delta k$ . We obtained probabilities for scattering of cold n-H<sub>2</sub> (20%  $j = 0$ , 75%  $j = 1$ , 5%  $j = 2$ ) [52] scattering from Pt(111) with an initial translational energy parallel to the surface of 0.055 eV.

### 6.3.5 Computational details

For the electronic structure calculations VASP (version 5.2.12) was used [53–56]. A plane wave basis set was used for the electronic orbitals and the XC functional used has been described and discussed in Section 6.3.2. Furthermore the standard PAW pseudopotentials [57] were used for the ion cores, and we used the scheme of Román-Pérez and Soler [58] to evaluate the vdW-DF2 correlation energy. Further details on the computation and interpolation of the PES have been provided in [9].

At least 10000 trajectories were computed in the QCT calculations for each initial set ( $E_i$ ,  $\nu_i$  and  $j_i$ ), sampled equally over the possible initial  $m_j$  states. In the calculation of the sticking probability and the Boltzmann averaging (Equation 6.5), the maximum vibrational quantum number was 3 and the maximum rotational quantum number was 20. The center of mass of the D<sub>2</sub> molecule was initially placed at  $Z = 9$  Å. If the D–D distance becomes larger than 2.25 Å the D<sub>2</sub> molecule is considered to be dissociated.

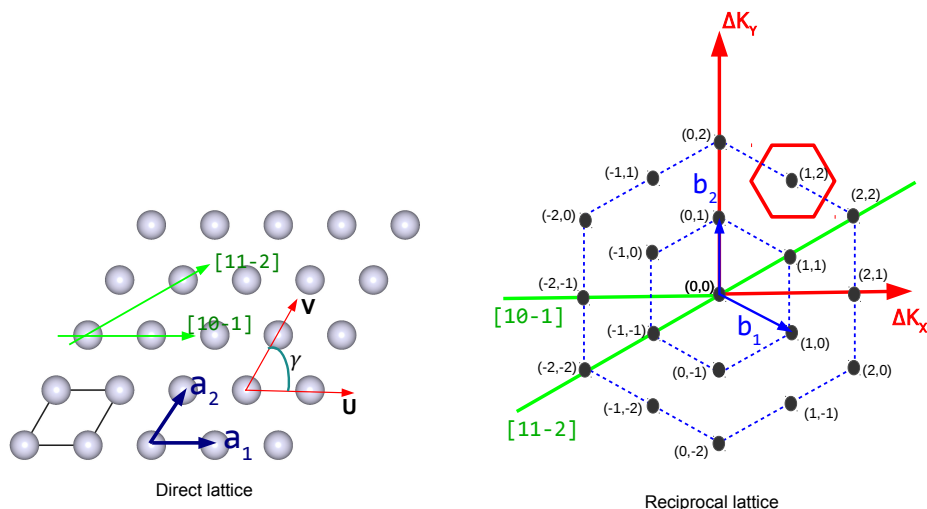


Figure 6.4: The direct (the left plot) and the reciprocal lattice (the right plot) for an fcc(111) surface. In the direct lattice  $\gamma$  is the skewing angle, and  $a_1$  and  $a_2$  are the primitive vectors that span the surface unit cell. Miller indices are shown in the reciprocal lattice to indicate the different diffraction channels. Red hexagon shows the 2D Wigner–Seitz cell. The concentric hexagons indicate how the diffraction order is defined for the (111) lattice. The  $\langle 10\bar{1} \rangle$  and  $\langle 11\bar{2} \rangle$  directions have been indicated in both figures in green.

Otherwise the  $D_2$  molecule is considered to be reflected from the surface to the gas phase when its distance to the surface in  $Z$  exceeds  $4.0 \text{ \AA}$  and  $D_2$  has a velocity towards the vacuum. The reaction probability was calculated as the ratio of the number of dissociated trajectories and the total number of trajectories run.

Table 6.3 lists the relevant parameters used in the 6D QD calculations for the scattering of ( $\nu = 0, j = 0$ )  $H_2$ . To cover the collision energy range  $E = 0.05 - 0.55 \text{ eV}$ , two wave packet calculations were performed for two separate energy ranges: 0.05 to 0.20 eV and 0.15 to 0.55 eV. This procedure

Table 6.3: Input parameters for the quantum dynamical calculations on H<sub>2</sub> dissociating on Pt(111) in the energy range of [0.05–0.20]eV. All values are given in atomic units. The abbreviation "sp" refers to the specular grid used to bring in the initial wave function.

Parameter	Description	Value
$N_X = N_Y$	no. of grid points in $X$ and $Y$	16
$N_Z$	no. of grid points in $Z$	256
$N_{Z(sp)}$	no. of specular grid points	256
$\Delta Z$	spacing of $Z$ grid points	0.135
$Z_{min}$	minimum value of $Z$	-1.0
$N_r$	no. of grid points in $r$	40
$\Delta r$	spacing of $r$ grid points	0.2
$r_{min}$	minimum value of $r$	0.4
$j_{max}$	maximum $j$ value in basis set	24
$m_{jmax}$	maximum $m_j$ value in basis set	16
$\Delta t$	time step	5
$T_{tot}$	total propagation time	82000
$Z_0$	center of initial wave packet	16.955
$Z_{inf}$	location of analysis line	12.5
$Z_{start}^{opt}$	start of optical potential in $Z$	12.5
$Z_{end}^{opt}$	end of optical potential in $Z$	33.425
$A_Z$	optical potential strength in $Z$	0.00072
$r_{start}^{opt}$	start of optical potential in $r$	4.2
$r_{end}^{opt}$	end of optical potential in $r$	8.2
$A_r$	optical potential strength in $r$	0.0096
$Z(sp)_{start}^{opt}$	start of optical potential in $Z(sp)$	22.355
$Z(sp)_{end}^{opt}$	end of optical potential in $Z(sp)$	33.425
$A_{Z(sp)}$	optical potential strength in $Z(sp)$	0.0035

avoids problems which may arise from the interaction of the optical potential with the low translational energy components of the wave packet, if only one broad Gaussian initial wave packet is used to cover the entire range.

## 6.4 Results and discussion

### 6.4.1 Sticking probabilities

To simulate the molecular beam sticking probabilities four different sets of molecular beam parameters are available. To distinguish these sets of parameters, here we introduce acronyms. As discussed in Section 6.2.2, the first set of parameters was extracted from experiments on  $D_2 + Ru(0001)$  [37], and we call this parameter set SBG, where S stands for seeded beams, B for broad in translational energy, and G for Groot *et al.* [37]. The second set of parameters is derived from the  $D_2 + Pt(111)$  experiments of Cao *et al.* [17], and we call this parameter set SBC. The third set of parameters (PNH) was reported in Ref. [42] to describe experiments of Hodgson and co-workers on  $D_2 + Ag(111)$  [16], and in this acronym P stand for pure  $D_2$  beam, N for narrow, and H for Hodgson and co-workers. The last set of parameters (PNA) describe pure  $D_2$  beam experiments on  $D_2 + Cu(111)$  using translationally narrow beams [44].

Figure 6.5 shows a comparison of the theoretical sticking probabilities for the four sets of parameters. The match between all sets of theoretical results is quite good for  $\langle E_i \rangle$  up to 0.32 eV. Based on the theory, we would then expect that there should be excellent agreement between the experiments of Cao *et al.* [17] (described by the parameter set SBC) and Hodgson and co-workers (parameter sets PNH and PNA) at  $\langle E_i \rangle$  up to 0.32 eV. However, the agreement between the  $S_0$  measured by these two groups is rather poor (see Figure 6.1 and Figure 6.2 (c)). Given that the two parameter sets SBC and PNH represent two extremes (of seeded beams that are broad in translational energy and pure beams that are narrow in energy), we should also expect good agreement of both of the experiments referred to above with the  $S_0$  measured by Luntz *et al.* [15], for which no beam parameters are available. The good agreement obtained of these  $S_0$  with the measurements of Cao *et al.* ( Figure 6.1 and Figure 6.2 (b)), and the poor agreement with the measurements of Hodgson and co-workers for  $\langle E_i \rangle \leq 0.32$  eV then suggests that for some reason the  $S_0$  measured by Hodgson and co-workers were too small.

A difference in the theoretical  $S_0$  appears at  $\langle E_i \rangle > 0.32$  eV between the results obtained with pure and narrow beams on the one hand, and with seeded and broad beams on the other hand ( Figure 6.5). The  $S_0$  computed with the parameter sets PNH and PNA exceed those computed with the

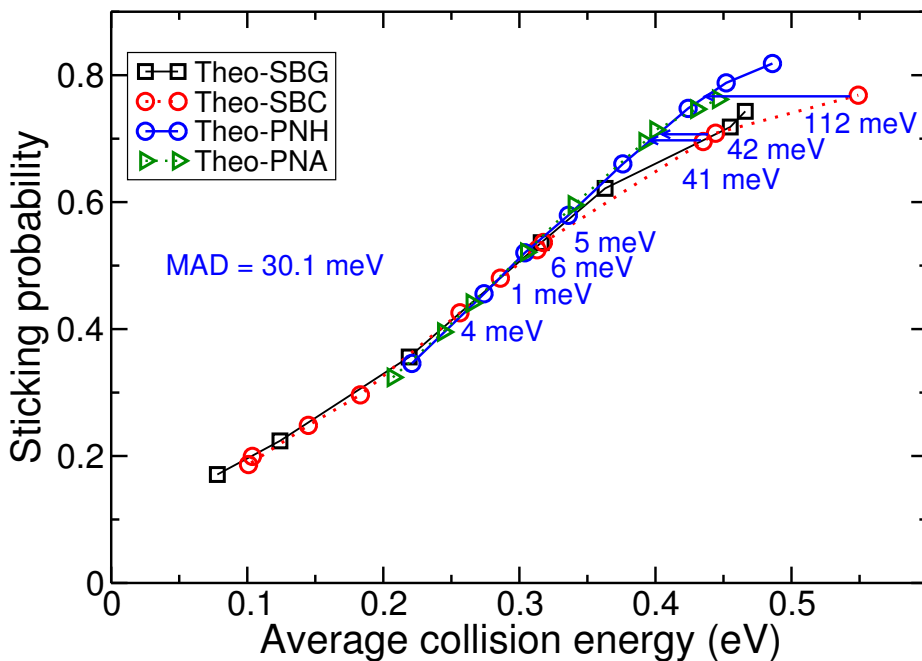


Figure 6.5: Comparison of sticking probabilities computed with different sets of parameters. Black symbols show the theoretical results obtained with the SBG parameters, red symbols the theoretical results with SBC. Blue and green symbols show the computed results obtained with the PNH and PNA parameters, respectively. The arrows and the numbers show the energy differences between the results obtained with the SBC parameters and interpolated values of the results obtained with the PNH parameters.

parameter sets SBG and SBC for higher energies. To understand the reason of the observed effect, we tested the effects of averaging the reaction probability over the translational energy distributions and over the rovibrational states separately. Boltzmann averaging the reaction probability based on nozzle temperature to obtain  $R_{mono}(E_i; T_n)$  similarly increases the reaction probability for the pure and for the seeded beams (see Figure 6.A.1 of the Appendix).

However, averaging over the translational energy decreases the reaction probability more for the broader energy distributions used in the seeded beam experiments than for the narrow energy distributions used in the

Table 6.4: MAD values in (eV) characterizing the agreement between three different sets of experimental results and the theoretical results obtained with four different sets of molecular beam parameters.

parameters	Exps	Luntz	Hodgson	Cao
<b>SBG</b>		13.5	34.6	37.4
<b>SBC</b>		13.3	35.6	36.9
<b>PNH</b>		35.1	45.0	54.0
<b>PNA</b>		26.1	47.0	54.5

pure  $D_2$  experiments (Figure 6.A.1). The reason for this is twofold: (i) at higher incidence energies  $E_i$  and for the weakly activated dissociative chemisorption problem under consideration, the slope of the reaction probability as a function of  $E_i$  becomes a decreasing function of  $E_i$ , and (ii) most molecules collide with the surface with  $E_i \leq \langle E_i \rangle$ . Therefore, averaging over the translational energy distribution decreases the measured  $S_0$ , and it does so more for translationally broader beams. Looking at the actual experimental results (Figure 6.1 and Figure 6.2 (a), and Figure 6.2 (c)) we see that the predicted trend is observed, although the  $\langle E_i \rangle$  at which the pure, narrow beam experiments yield higher  $S_0$  than in the seeded, broad beam experiments is shifted to higher energies, again suggesting that the  $S_0$  measured by Hodgson and co-workers are too small.

Figure 6.6 shows a comparison of the experimental data reported by Luntz *et al.* [15], for which no beam parameters were reported, and the results of our simulations with the SBG parameters. The sticking probabilities of Luntz *et al.* [15] are quite well described with this parameter set (well within chemical accuracy, MAD = 13.5 meV, see table 6.4). This experiment is also quite well described with the SBC set (MAD = 13.3 meV, see Figure 6.A.2 (a) and table 6.4).

The experimental data are also reproduced reasonably well with the parameter sets describing narrower beams (MAD = 26.1 meV for PNA and 35.1 meV for PNH, table 6.4 and Figures 6.A.2 (b) and (c)). However, the larger MADs obtained with the narrower beams suggests that the beams used by Luntz *et al.* were broad in translational energy, similar to the beams employed by Juurlink and co-workers. A caveat is that the SRP-DF was



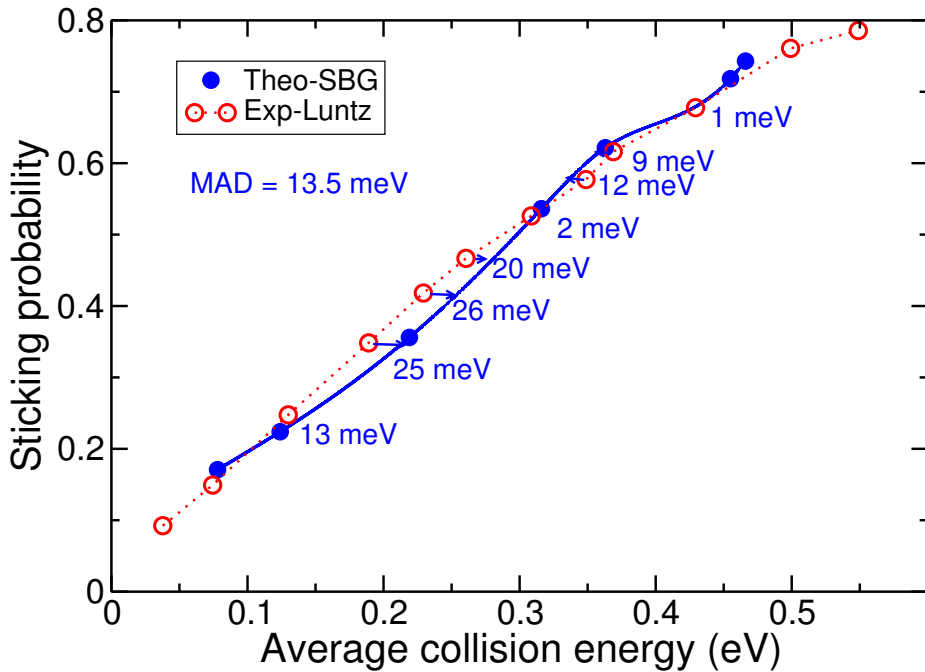


Figure 6.6: Computed sticking probabilities (blue symbols) are shown as a function of  $\langle E_i \rangle$  along with the experimental results (red symbols) of Luntz *et al.* [15]. The arrows and accompanying numbers show the energy differences between the experimental data and the interpolated theoretical sticking probability values.

fitted to the experiments of Luntz *et al.* using the SBG set of parameters, and this may affect the conclusion just arrived at, by biasing the SRP functional to yield better results for the broader beams.

The  $S_0$  measured by Hodgson and co-workers [16] are still described to within chemical accuracy with the SBG parameters ( Figure 6.7 (a)), albeit that the MAD (34.6 meV) is much higher than obtained for the experiment of Luntz *et al.* (13.5 meV, see table 6.4). A similar conclusion applies for the SBC parameter set (Figure 6.A.3 (a) and table 6.4).

However, with the two other sets of parameters, which should actually describe the beams used in the experiments of Hodgson and co-workers (see Section 6.2 ), our simulations cannot reproduce these experiments within

chemical accuracy ( Figure 6.7 (b) and Figure 6.A.3 (b)). Specifically, MAD values are obtained of 45.0 meV and 47.0 meV for the PNH and PNA sets, respectively. However, if we multiply the measured  $S_0$  with a factor 1.13, excellent agreement (MAD = 12.7 meV) with the theoretical  $S_0$  is obtained using the PNH set ( Figure 6.7 (c)). This finding represents additional evidence that the  $S_0$  measured by Hodgson and co-workers were too low, as it is unlikely that the effect is caused entirely by the use of a lower  $T_s$  (150 K) than employed by Luntz *et al.* (293 K) and Cao *et al.* (200 K, see Figure 6.1). A possible reason for this could be that at least in some of the experiments thermal desorption was used to measure the amount of adsorbed  $D_2$ , with calibration to values of  $S_0$  determined with one or more King and Wells measurements performed for high  $\langle E_i \rangle$  (see also Section 6.2). If the King and Wells measurements for some reason returned too low values of  $S_0$ , this should affect the subsequent thermal desorption measurements of  $S_0$  in a similar way. Possible reasons for King and Wells measurements returning too low  $S_0$  values include the use of a duty cycle that is too high, or the use of a time-interval in the King and Wells measurement that is too long, so that the sticking probability is determined for an already partially covered surface. These problems may become aggravated and lead to systematic errors if the King and Wells measurement is carried out only for a high  $\langle E_i \rangle$  for which  $S_0$  is high, and if the King and Wells measurement is carried out for calibration purposes.

The  $S_0$  measured by Cao *et al.* [17] are best described (and still to within chemical accuracy) with the beam parameter set SBC describing these experiments (MAD = 36.9 meV), Figure 6.8 and table 6.4). Figure 6.A.4 (a) shows similar agreement between the experiments of Cao *et al.* and the theoretical results obtained with the SBG set (MAD = 37.4 meV, table 6.4).

In both cases there are, however, large discrepancies between theory and experiments at the highest  $\langle E_i \rangle$ . The simulations using parameters describing narrow beams (PNH and PNA) cannot describe the experiments of Cao *et al.* with chemical accuracy (MAD values of 54.0 and 54.5 meV, respectively, see Figures 6.A.4 (b) and (c) and table 6.4). Also, much better descriptions of the experiments of Luntz *et al.* [15] than of the experiments of Cao *et al.* were obtained with the SBG and SBC parameter sets. This could be due to two reasons.

First of all, the SRP–DF has been fitted [9] to the experiments of Luntz *et al.* [15] using the SBG parameter set, and this could bias the SRP–DF to a better description of the experiments of Luntz *et al.*. Second, we suspect

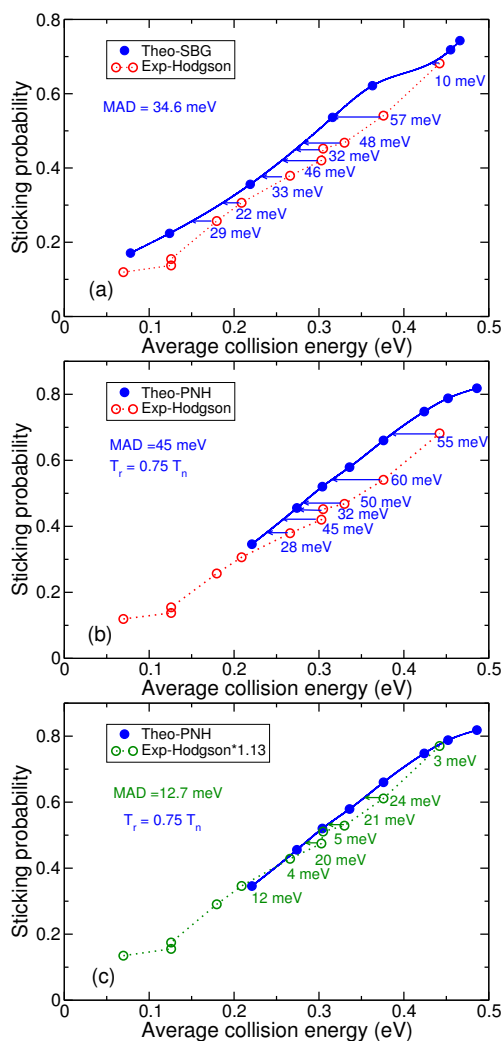


Figure 6.7: Comparison between the molecular beam sticking probabilities for the experiments of Hodgson and co-workers [16] and theoretical results obtained with two sets of parameters: (a) computed data with the SBG set of parameters (b) computed data with the PNH parameters. (c) The last panel shows the comparison between the experimental values of Hodgson and co-workers multiplied with 1.13 and the theoretical results obtained with the PNH set of parameters. The arrows with numbers show the energy spacings between the experimental values and the interpolated theoretical data. The blue curve shows the interpolated theoretical results in all cases.

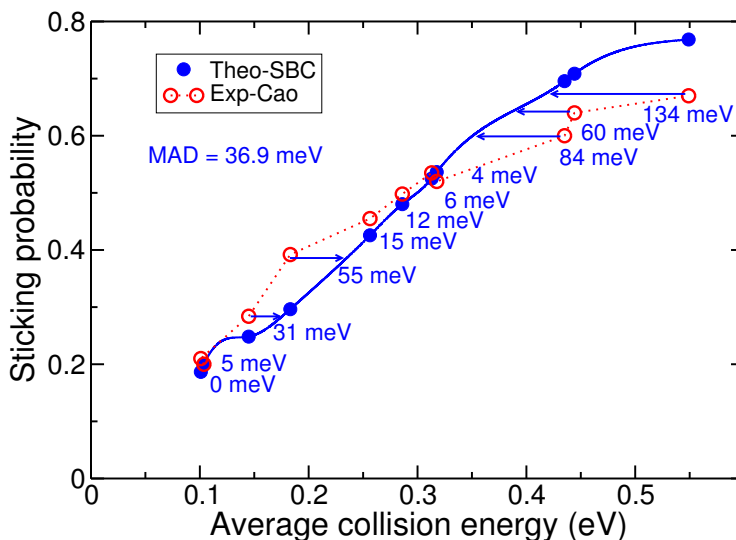


Figure 6.8: Comparison between the molecular beam sticking probabilities for the experiments of Cao *et al.* [17] and the theoretical results obtained with the set of parameters SBC. The arrows and numbers show the energy spacings between the experimental values and the interpolated theoretical data. The blue curve shows the interpolated theoretical results.

that the SBC beam parameters contain errors at the high  $\langle E_i \rangle$ . The reason for that is that, in recent experiments on  $H_2$  and  $D_2 + Pt(211)$  employing pure hydrogen beams, in most cases  $\langle E_i \rangle$  exceeded  $3k_B T_n$  rather than being approximately  $2.7k_B T_n$  [Ref. [59]], as would be expected for pure hydrogen beams [41]. As a result, the incidence energies were likely to be overestimated at high  $\langle E_i \rangle$  in these experiments. We suspect that the experiments of Cao *et al.* in figures 2 and 3 of their paper are similarly affected, and as a result for high  $\langle E_i \rangle$  the measured  $S_0$  should be underestimated. An explanation [Ref. [59]] is that parameters describing the translational energy distributions of hydrogen beams become progressively harder to determine accurately for higher  $\langle E_i \rangle$ , due to the corresponding shorter times of flight. An alternative explanation for  $\langle E_i \rangle > 2.7 k_B T_n$  in the experiments is that the actual  $T_n$  could have been higher than the measured value. However, this does not explain the sign of the difference between the simulated and measured  $S_0$ ; if we would underestimate the nozzle temperature in per-

forming the Boltzmann average, we would expect that the theory should underestimate the measured value of  $S_0$  at high  $\langle E_i \rangle$  (see Figure 6.A.1), but the opposite is the case (see Figure 6.8). On the other hand, the theory could overestimate the measured reaction probability at high  $\langle E_i \rangle$  if for some reason the expansion gas would not be fully equilibrated with the nozzle at the highest  $T_n$ , so that the gas temperature would be lower than  $T_n$ . It is not clear to us whether this might have been the case in the experiments of Cao *et al.*

### 6.4.2 Diffraction probabilities

The comparison of the theoretical results with the absolute diffraction probabilities extracted from the measured angular distributions by Nieto *et al.* [21] is shown in Figures 6.9 (a) and (b), and Figures 6.10 (a) and (b) for the  $\langle 1, 0, \bar{1} \rangle$  and  $\langle 1, 1, \bar{2} \rangle$  incidence directions, respectively. In these figures the diffraction probabilities are plotted against the total incidence energy for off-normal incidence for the PBE $\alpha$ vdW-DF2 XC functional. Increasing the impact energy increases the number of open diffraction channels and this appears to lead to a substantial drain of flux out of the specular channel in the experiment. However, a similar decrease is not observed in the calculations. Along the  $\langle 1, 0, \bar{1} \rangle$  incidence direction, as we can see in Figure 6.9 (b), the most important first order diffraction channel is made up by the two almost equivalent out-of-plane diffraction channels,  $(0, -1)$  and  $(0, 1)$  (see also Figure 6.4). The energy transfer into these two diffraction channels, *i.e.*  $(0, -1)$  and  $(0, 1)$ , is independent of the initial momentum because the parallel momentum change is perpendicular to the plane of incidence. For the other four diffraction channels, there is a component that is parallel to the incidence plane. Diffractive scattering probabilities for these diffraction channels are smaller because of the larger energy transfer involved [21, 60].

As shown in Figure 6.9, diffraction probability curves for the zero and first order diffraction channels do not show a dramatic change over the considered energy range. A quantitative comparison of the results displays that there is a large discrepancy between theory and experiment for  $P_0$ . However, comparing with experiment, the order of the size of the (sum of the) diffraction probabilities,  $P_0$  and  $[P(0, 1) + P(0, -1)]$ , is correctly described. In our calculations, the order in the size of  $[P(-1, 0) + P(-1, -1)]$  and  $[P(1, 1) + P(1, 0)]$  is not correctly described. Looking at  $[P(0, 1) + P(0, -1)]$ ,  $[P(-1, 0) + P(-1, -1)]$  and  $[P(1, 1) + P(1, 0)]$ , overall there is a

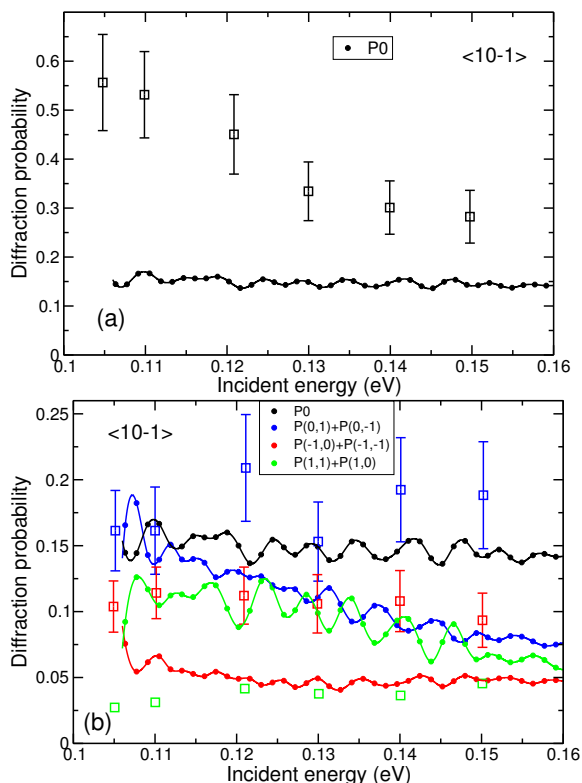


Figure 6.9: Diffraction probabilities for n-H<sub>2</sub> (20 %  $j = 0$ , 75 %  $j = 1$ , 5 %  $j = 2$ ) scattering : (a) Specular scattering (black) and (b) several first order out-of-plane diffractive scattering transitions from Pt(111) with an initial parallel energy of 55 meV along the  $\langle 1, 0, \bar{1} \rangle$  incidence direction computed with the PBE $\alpha$ -vdW-DF2 XC functional. For comparison, experimental results are shown (symbols with error bars). The probabilities for symmetry equivalent transitions are summed.

rather poor agreement between theory and experiment for these diffraction channels, regardless of the order in the size.

Figure 6.10 shows diffraction probabilities for scattering along the  $\langle 1, 1, \bar{2} \rangle$  incidence direction. The probability for specular scattering  $P_0$  (Figure 6.10 (a)) is larger than the first order in-plane diffraction probabilities  $P(1, 1)$ ,  $P(-1, -1)$  (Figure 6.10 (b)), the sum of the first order sideways backward diffraction probabilities [ $P(-1, 0) + P(0, -1)$ ], and the sum of the first or-

der sideways forward diffraction probabilities  $[P(1, 0) + P(0, 1)]$ . The results from the PBE $\alpha$ -vdW-DF2 XC functional underestimate the measured specular scattering probability  $P_0$ . In the experiment, the sums of the first order out-off-plane diffraction channels,  $[P(-1, 0) + P(0, -1)]$  and  $[P(1, 0) + P(0, 1)]$  show a higher probability than the first order in-plane diffraction channels,  $P(1, 1)$  and  $P(-1, -1)$ . The experiment also found smaller probabilities for in-plane and out-off-plane diffraction relative to specular scattering. In the intermediate energy range the sizes of  $[P(-1, 0) + P(0, -1)]$  and  $[P(1, 0) + P(0, 1)]$  are almost similar in both theory and experiment. Over most of the energy range the computed  $P(1, 1)$  is larger than the computed  $P(-1, -1)$  which is in disagreement with experiment and previous theoretical results [21]. Overall, the quantitative agreement between theory and experiment is rather poor, also for this incidence direction.

The agreement for diffraction compared to experiments is clearly not as good as the agreement obtained for the reaction probabilities. There are both qualitative and quantitative differences. The computed zero order diffraction probabilities are too low compared to the experiments. Another difference between our results and previous theoretical results by Nieto *et al.* [21] is that the older theoretical results, which were based on the B88P86 [29, 30] GGA functional, better reproduced the order in the first order diffraction probabilities [21].

Comparison of diffractive scattering of  $H_2$  from Cu(111) [61] obtained with PESs based on PW91 and RPBE functionals demonstrated that diffraction spectra are much more sensitive to the details of the PES than sticking probabilities. Therefore, the diffraction experimental data are very useful to test the accuracy of the PES and in turn the accuracy of the DFT functional. The present comparison between the theory and the experiment suggests that the SRP-DF for  $H_2 + Pt(111)$  may not yet be accurate enough to describe the diffraction in the  $H_2 + Pt(111)$  system.

We have previously discussed another potential source of discrepancy between measured diffraction probabilities and diffraction probabilities computed with a PES exhibiting a van der Waals well [13]. It is important to realize that the experimental diffraction probabilities shown in Figures 6.9 and 6.10 were not directly measured for a 0 K Pt(111) surface, and certainly not for a rigid surface, as assumed in the theory. Rather, these data were obtained by performing a DW extrapolation of data measured between 500 and 1000 K [21]. DW theory assumes direct scattering. However, our PES exhibits a van der Waals well of 72 meV, and at the normal incidence range

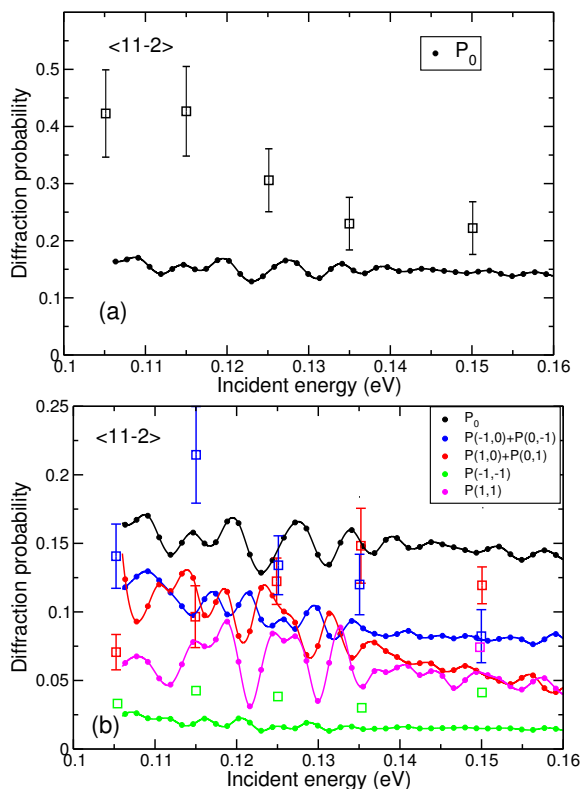


Figure 6.10: Comparison of the experimentally determined diffraction probabilities (symbols) with diffraction probabilities computed with the  $PBE\alpha$ -vdW-DF2 XC functional for (a) specular scattering (black) and (b) several first order out-of-plane (blue and red) and in-plane (green and pink) diffractive transitions for incidence along the  $\langle 1, 1, \bar{2} \rangle$  incidence direction for  $n$ - $H_2$  (20 %  $j = 0$ , 75 %  $j = 1$ , 5 %  $j = 2$ ) from  $Pt(111)$  with an initial parallel energy of 55 meV. The probabilities for symmetry equivalent transitions are summed.

of energies addressed here, part of the scattering should be indirect, as also indicated by the oscillatory behavior of the computed diffraction probabilities in Figures 6.9 and 6.10. If we were to take this into account in the DW attenuation, assuming that with each bounce on the surface there is again a probability of phonon excitation, this should lead to decreased "experimental" diffraction probabilities, by amounts that might differ among



the channels. In other words, it is possible that the theory is quite good for the hypothetical case of scattering from a 0 K surface, but that the experimental 0 K result is wrong because standard DW extrapolation to 0 K was not applicable. In this respect, GGA PESs might seem to give good results for diffraction (as observed in Ref. [21]) and for many other  $\text{H}_2$ -metal systems [62], because it applies to the hypothetical case of scattering from a surface with the van der Waals well discarded, for which DW attenuation should actually work reasonably well. This can be tested by computing diffraction probabilities for scattering from a thermal Pt(111) surface, allowing excitation of the phonons. Alternatively, it might be possible to test the corrugation of the repulsive part of the  $\text{H}_2 + \text{Pt}(111)$  PES by removing the van der Waals well to obtain a purely repulsive PES, and computing diffraction probabilities for this PES [31]. Finally it might be possible to model the attenuating effect of phonon excitation with the aid of an optical potential [63].

In previous work on  $\text{H}_2 + \text{Ru}(0001)$ , we found that the agreement between experiment and theory with inclusion of a van der Waals well in the PES could be improved by assuming a specific type of static surface disorder of the metal surface [31]. However, making this assumption will deteriorate rather than improve the agreement between theory and experiment. The reason is that making this assumption will lead to decreased computed diffraction probabilities, and this will worsen the already bad agreement for specular scattering even more.

## 6.5 Conclusions

This paper tackles two problems faced by the SRP–DFT approach. The first problem is that the SRP–DFT approach is obviously no more accurate than the underlying experimental data are. The second problem is that it is hard to validate a candidate SRP–DF on the basis of a comparison between theoretical and experimental diffraction probabilities for  $\text{H}_2$ -metal systems.

To address the first problem of the SRP–DFT approach, we have simulated all three sets of measurements of sticking probabilities available for  $\text{D}_2 + \text{Pt}(111)$ , using four different sets of molecular beam parameters. As discussed in the paper, substantial differences exist between the three sticking probability curves measured for  $\text{D}_2 + \text{Cu}(111)$ . We compared these experiments on a one-to-one basis. The comparison showed that the sticking

probability of Luntz *et al.* [15] are larger than those of Hodgson and co-workers [16] over the entire energy range. The datasets of Luntz *et al.* [15] and of Cao *et al.* [17] showed much better agreement at least for collision energies up to 0.32 eV, but not for larger collision energies. The agreement between the datasets of Cao *et al.* [17] and of Hodgson and co-workers [16] was poorest. We discussed the origin of these discrepancies and reported the MADs between the data of the experiments.

Next we described the four different sets of molecular beam parameters that we have used in our calculations to simulate the experiments. We also discussed the question of which set of beam parameters can best be used to simulate a particular set of molecular beam experiments.

To construct the PES, the CRP interpolation method was used to accurately fit DFT data based on the PBE $\alpha$ -vdW-DF2 functional with  $\alpha = 0.57$ . This functional was previously found to enable a chemically accurate description of the experiments of Luntz *et al.* [9]. We have performed calculations within the BOSS dynamical model. The QCT method has been used to compute molecular beam sticking probabilities using velocity averaging and Boltzmann averaging for each set of molecular beam parameters. We have shown the comparison of our theoretical results for the four sets of parameters with each other. The agreement between the results obtained with all sets of parameters is quite good for average collision energies up to 0.32 eV.

We have discussed the discrepancy between the theoretical results for translationally narrow and broad beams at the higher collision energies. Comparison between the theoretical results obtained with four sets of parameters and the three sets of experimental data has also been made. MAD values for three different experimental results and four different sets of theoretical results were reported and the success or failure of achieving a chemically accurate description of these three sets of molecular beam experiments was discussed separately. The most important result is that all three sets of experiments can be described with chemical accuracy using molecular beam parameters describing seeded molecular beams that are broad in energy. Performing simulations with different sets of molecular beam parameters also provides insight into under which conditions the experiments should agree with one another. This allows one to arrive at conclusion regarding problems that might affect the experiments. For instance, the simulations suggested that the sticking probabilities measured by Hodgson and co-workers were too low by about 13%, although we cannot rule out

completely that part of this difference might have been due to the use of a lower  $T_s$ .

To address the second problem of the SRP–DFT approach, we performed diffractive scattering calculations comparing with experiments, using the SRP–DF. To compute diffraction probabilities for  $H_2$  scattering from Pt(111) the TDWP method was used and probabilities were obtained for scattering of cold n- $H_2$  (20%  $j = 0$ , 75%  $j = 1$ , 5%  $j = 2$ ) scattering from Pt(111) with an initial translational energy parallel to the surface of 55 meV. The theoretical results have been shown and compared with experimental results for off-normal incidence for two incidence directions. The agreement for diffraction compared to experiments was rather poor in contrast with the agreement obtained for the sticking probabilities. The results show both quantitative and qualitative discrepancies between theory and experiments. The previous theoretical results by Nieto *et al.* [21], which were based on the use of a GGA functional, demonstrated better agreement with the experiments. Our study suggests that the SRP–DF for  $H_2 + Pt(111)$  may not yet be accurate enough to describe the diffraction in this system. Also with the use of a PES exhibiting a van der Waals well, part of the scattering should be indirect. However, the DW theory used to obtain 0 K experimental diffraction probabilities, assumes direct scattering. The previous study has shown that the agreement between experiment and theory with inclusion of a van der Waals well in the PES was improved by assuming a static surface disorder of metal surface for  $H_2$  scattering from Ru(0001) [31]. However, as discussed making this assumption will not improve the agreement between theory and experiment in the case of  $H_2$  scattering from Pt(111).

## 6.A Appendix

This appendix contains comparison of sticking probabilities for two sets of parameters Figure 6.A.1; comparison of the experimental data from Luntz *et al.*, Hodgson and co-workers, and Cao *et al.* with theoretical results (Figure 6.A.2, Figure 6.A.3 and Figure 6.A.1).

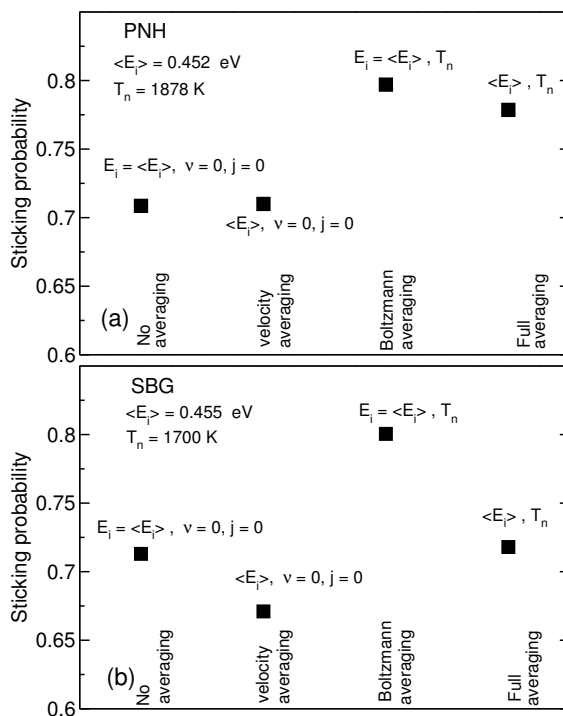


Figure 6.A.1: Comparison of sticking probabilities for two sets of parameters: (a) PNH with narrower energy distributions and (b) SBG with wider energy distributions. Shown are the reaction probability of ( $\nu = 0, j = 0$ )  $D_2$  without velocity averaging, the reaction probability of ( $\nu = 0, j = 0$ )  $D_2$  with velocity averaging, the reaction probability with Boltzmann averaging over rovibrational states only, and the sticking probability computed with full averaging.

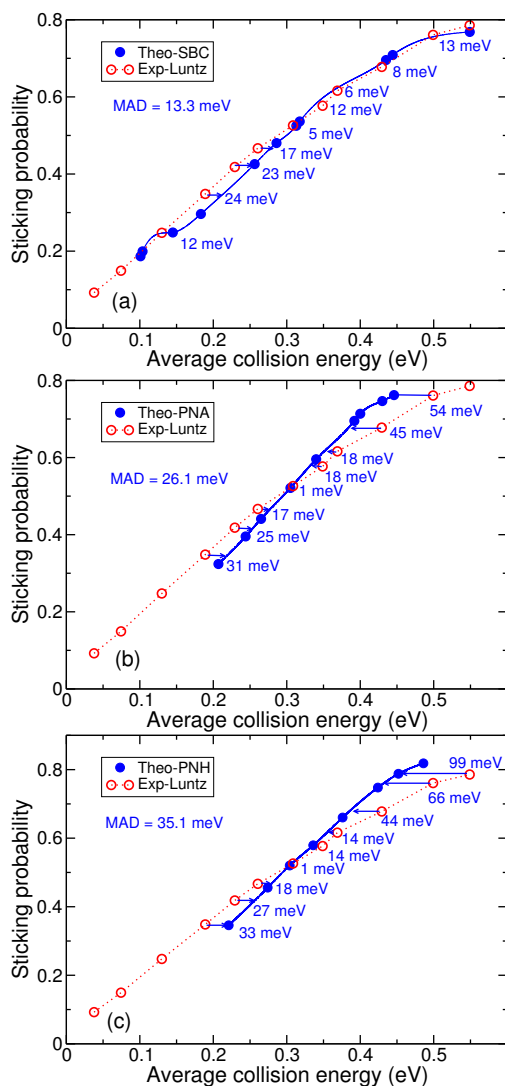


Figure 6.A.2: Comparison of the experimental data from Luntz *et al.* [15], with the theoretical results (a) obtained with the SBC parameters of Cao *et al.* [17], (b) with the PNA [44], and (c) with the PNH parameters of Hodgson and co-workers [36]. In all cases the horizontal arrows and the numbers indicate the energy spacings between the interpolated values of the theoretical results and the actual experimental values. The blue lines show the interpolated curves of the computed data.

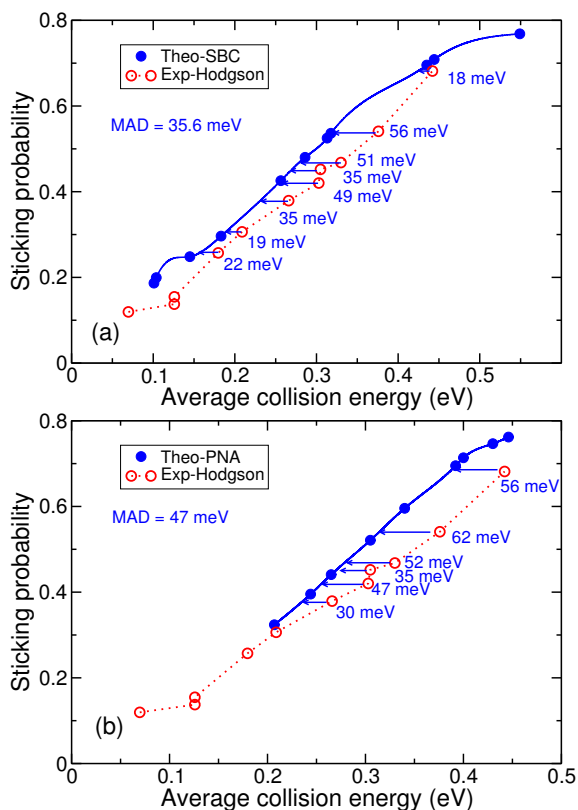


Figure 6.A.3: Comparison of the experimental data from Hodgson *et al.* [16], with the theoretical results (a) obtained with the SBC parameters of Cao *et al.* [17], (b) and with the PNA parameters [44]. In all cases the horizontal arrows and the numbers indicate the energy spacings between the interpolated values of the theoretical results and the actual experimental values. The blue lines show the interpolated curves of the computed data.

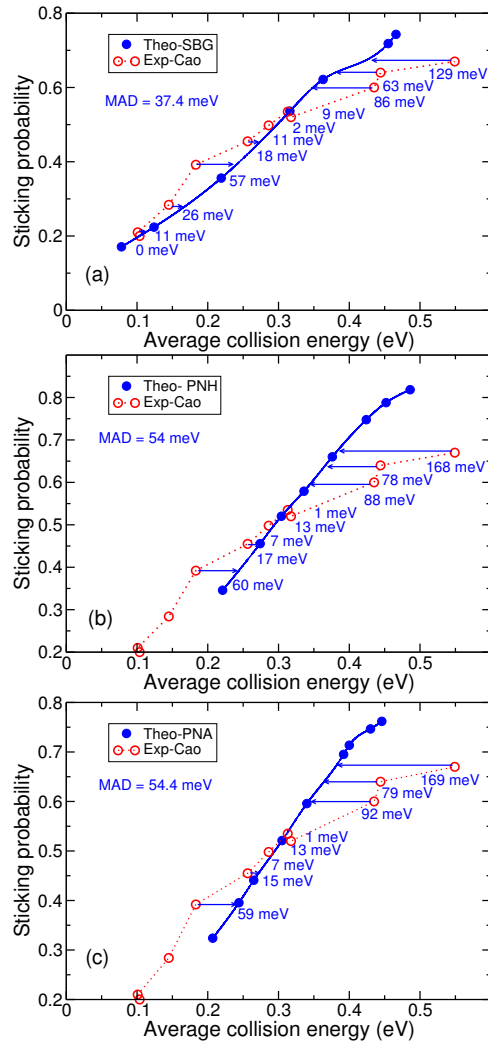


Figure 6.A.4: Comparison of the experimental data from Cao *et al.* [17], with the theoretical results (a) obtained with the SBG parameters of Groot *et al.* [37], (b) with the PNH parameters of Hodgson and co-workers [36], and (c) with the PNA parameters [44]. In all cases the horizontal arrows and the numbers indicate the energy spacings between the interpolated values of the theoretical results and the actual experimental values. The blue lines show the interpolated curves of the computed data.

## References

1. Wolcott, C. A., Medford, A. J., Studt, F. & Campbell, C. T. Degree of Rate Control Approach to Computational Catalyst Screening. *Journal of Catalysis* **330**, 197–207 (2015).
2. Sabbe, M. K., Reyniers, M.-F. & Reuter, K. First-Principles Kinetic Modeling in Heterogeneous Catalysis: An Industrial Perspective on Best-Practice, Gaps and Needs. *Catalysis Science & Technology* **2**, 2010–2024 (2012).
3. Noyori, R. Synthesizing Our Future. *Nature Chemistry*, 5–6 (2009).
4. Ertl, G. Primary Steps in Catalytic Synthesis of Ammonia. *Journal of Vacuum Science & Technology A* **1**, 1247–1253 (1983).
5. Chorkendorff I. Niemantsverdriet, J. W. *Concepts of Modern Catalysis and Kinetics*. 452 (Student Edition ed.; Wiley-VCH Verlag GmbH & Co.: Weinheim, Introduction to surface chemistry and catalysis, 2003).
6. Stegelmann, C., Andreasen, A. & Campbell, C. T. Degree of Rate Control: How Much the Energies of Intermediates and Transition States Control Rates. *Journal of the American Chemical Society* **131**, 8077–8082 (2009).
7. Díaz, C. *et al.* Chemically Accurate Simulation of a Prototypical Surface Reaction: H<sub>2</sub> Dissociation on Cu(111). *Science* **326**, 832–834 (2009).
8. Sementa, L. *et al.* Reactive Scattering of H<sub>2</sub> from Cu(100): Comparison of Dynamics Calculations Based on the Specific Reaction Parameter Approach to Density Functional Theory with Experiment. *Journal of Chemical Physics* **138** (2013).
9. Ghassemi, E. N., Wijzenbroek, M., Somers, M. F. & Kroes, G. J. Chemically Accurate Simulation of Dissociative Chemisorption of D<sub>2</sub> on Pt(111). *Chemical Physics Letters* **683**. Ahmed Zewail (1946-2016) Commemoration Issue of Chemical Physics Letters, 329–335 (2017).
10. Nattino, F. *et al.* Chemically Accurate Simulation of a Polyatomic Molecule-Metal Surface Reaction. *Journal of Physical Chemistry Letters* **7**, 2402–2406 (2016).
11. Migliorini, D. *et al.* Surface Reaction Barriometry: Methane Dissociation on Flat and Stepped Transition-Metal Surfaces. *Journal of Physical Chemistry Letters* **8**, 4177–4182 (2017).



12. Boereboom, J. M., Wijzenbroek, M., Somers, M. F. & Kroes, G. J. Towards a Specific Reaction Parameter Density Functional for Reactive Scattering of H<sub>2</sub> from Pd(111). *Journal of Chemical Physics* **139** (2013).
13. Wijzenbroek, M. & Kroes, G. J. The Effect of the Exchange-Correlation Functional on H<sub>2</sub> Dissociation on Ru(0001). *Journal of Chemical Physics* **140** (2014).
14. D. Navalikhina, M. & V. Krylov, O. Heterogeneous Catalysts of Hydrogenation. *Russian Chemical Review* **67**, 587–616 (1998).
15. Luntz, A. C., Brown, J. K. & Williams, M. D. Molecular Beam Studies of H<sub>2</sub> and D<sub>2</sub> Dissociative Chemisorption on Pt(111). *Journal of Chemical Physics* **93**, 5240–5246 (1990).
16. Samson, P., Nesbitt, A., Koel, B. E. & Hodgson, A. Deuterium Dissociation on Ordered Sn/Pt(111) Surface Alloys. *Journal of Chemical Physics* **109**, 3255–3264 (1998).
17. Cao, K., van Lent, R., Kleyn, A. & Juurlink, L. A Molecular Beam Study of D<sub>2</sub> Dissociation on Pt(111): Testing SRP-DFT Calculations. *Chemical Physics Letters* **706**, 680–683 (2018).
18. Cowin, J. P., Yu, C., Sibener, S. J. & Hurst, J. E. Bound Level Resonances in Rotationally Inelastic HD/Pt (111) Surface Scattering. *Journal of Chemical Physics* **75**, 1033–1034 (1981).
19. Cowin, J. P., Yu, C., Sibener, S. J. & Wharton, L. HD Scattering from Pt(111): Rotational Excitation Probabilities. *Journal of Chemical Physics* **79**, 3537–3549 (1983).
20. Cowin, J. P., Yu, C.-F. & Wharton, L. HD Scattering from Pt(111): Rotationally Mediated Selective Adsorption. *Surface Science* **161**, 221–233 (1985).
21. Nieto, P. *et al.* Reactive and Nonreactive Scattering of H<sub>2</sub> from a Metal Surface Is Electronically Adiabatic. *Science* **312**, 86–89 (2006).
22. Halstead, D. & Holloway, S. Quantum-Mechanical Scattering of H<sub>2</sub> from Metal Surfaces: Diffraction and Dissociative Adsorption. *Journal of Chemical Physics* **88**, 7197–7208 (1988).
23. Darling, G. R. & Holloway, S. The Role of Parallel Momentum in the Dissociative Adsorption of H<sub>2</sub> at Highly Corrugated Surfaces. *Surface Science* **304**, L461–L467 (1994).

24. Pijper, E. *et al.* Six-Dimensional Quantum Dynamics of Scattering of ( $v=0, j=0$ ) H<sub>2</sub> from Pt(1 1 1): Comparison to Experiment and to Classical Dynamics Results. *Chemical Physics Letters* **347**, 277–284 (2001).
25. Pijper, E., Kroes, G. J., Olsen, R. A. & Baerends, E. J. Reactive and Diffractive Scattering of H<sub>2</sub> from Pt(111) Studied Using a Six-Dimensional Wave Packet Method. *Journal of Chemical Physics* **117**, 5885–5898 (2002).
26. Kingma, S. M. *et al.* Diffractive and reactive scattering of ( $v=0, j=0$ ) HD from Pt(111): Six-dimensional quantum dynamics compared with experiment. *Journal of Chemical Physics* **118**, 4190–4197 (2003).
27. Vincent, J., Olsen, R., Kroes, G. J. & Baerends, E. Dissociative Chemisorption of H<sub>2</sub> on Pt(1 1 1): Isotope Effect and Effects of the Rotational Distribution and Energy Dispersion. *Surface Science* **573**, 433–445 (2004).
28. Ludwig, J. & Vlachos, D. G. *Ab Initio* Molecular Dynamics of Hydrogen Dissociation on Metal Surfaces Using Neural Networks and Novelty Sampling. *Journal of Chemical Physics* **127** (2007).
29. Becke, A. D. Density-Functional Exchange-Energy Approximation with Correct Asymptotic Behavior. *Physical Review A* **38**, 3098–3100 (1988).
30. Perdew, J. P. Density-Functional Approximation for the Correlation Energy of the Inhomogeneous Electron Gas. *Physical Review B* **33**, 8822–8824 (1986).
31. Kroes, G. J., Wijzenbroek, M. & Manson, J. R. Possible Effect of Static Surface Disorder on Diffractive Scattering of H<sub>2</sub> from Ru(0001): Comparison Between Theory and Experiment. *Journal of Chemical Physics* **147**, 244705 (2017).
32. Kosloff, R. Time-Dependent Quantum-Mechanical Methods for Molecular Dynamics. *Journal of Physical Chemistry* **92**, 2087–2100 (1988).
33. King, D. A. & Wells, M. G. Reaction Mechanism in Chemisorption Kinetics: Nitrogen on the 100 Plane of Tungsten. *Proceedings of the Royal Society of London A: Mathematical, Physical and Engineering Sciences* **339**, 245–269 (1974).
34. Luntz, A. C. *Personal communication.*

35. Hodgson, A. *Personal communication*.
36. Cottrell, C., Carter, R. N., Nesbitt, A., Samson, P. & Hodgson, A. Vibrational State Dependence of D<sub>2</sub> Dissociation on Ag(111). *Journal of Chemical Physics* **106**, 4714–4722 (1997).
37. Groot, I. M. N., Ueta, H., van der Niet, M. J. T. C., Kleyn, A. W. & Juurlink, L. B. F. Supersonic Molecular Beam Studies of Dissociative Adsorption of H<sub>2</sub> on Ru(0001). *Journal of Chemical Physics* **127**, 244701 (2007).
38. Groot, I. M. N. *Personal communication*.
39. Rettner, C. T., Michelsen, H. A. & Auerbach, D. J. Quantum-State-Specific Dynamics of the Dissociative Adsorption and Associative Desorption of H<sub>2</sub> at a Cu(111) Surface. *Journal of Chemical Physics* **102**, 4625–4641 (1995).
40. Rendulic, K., Anger, G. & Winkler, A. Wide Range Nozzle Beam Adsorption Data for the Systems H<sub>2</sub>/Nickel and H<sub>2</sub>/Pd(100). *Surface Science* **208**, 404–424 (1989).
41. Gallagher, R. J. & Fenn, J. B. Rotational Relaxation of Molecular Hydrogen. *Journal of Chemical Physics* **60**, 3492–3499 (1974).
42. Nour Ghassemi, E., Somers, M. & Kroes, G. J. Test of the Transferability of the Specific Reaction Parameter Functional for H<sub>2</sub> + Cu(111) to D<sub>2</sub> + Ag(111). *Journal of Physical Chemistry C* **122**, 22939–22952 (2018).
43. Michelsen, H. A. & Auerbach, D. J. A Critical Examination of Data on the Dissociative Adsorption and Associative Desorption of Hydrogen at Copper Surfaces. *Journal of Chemical Physics* **94**, 7502–7520 (1991).
44. Auerbach, D. J. *Personal communication*.
45. Michelsen, H. A., Rettner, C. T., Auerbach, D. J. & Zare, R. N. Effect of Rotation on the Translational and Vibrational Energy Dependence of the Dissociative Adsorption of D<sub>2</sub> on Cu(111). *Journal of Chemical Physics* **98**, 8294–8307 (1993).
46. Juurlink, L. B. F. *Personal communication*.
47. Madsen, G. K. H. Functional Form of the Generalized Gradient Approximation for Exchange: The PBE $\alpha$  Functional. *Physical Review B* **75**, 195108 (2007).

48. Lee, K., Murray, É. D., Kong, L., Lundqvist, B. I. & Langreth, D. C. Higher-Accuracy van der Waals Density Functional. *Physical Review B* **82**, 081101 (2010).
49. Busnengo, H. F., Salin, A. & Dong, W. Representation of the 6D Potential Energy Surface for a Diatomic Molecule Near a Solid Surface. *Journal of Chemical Physics* **112**, 7641–7651 (2000).
50. Karplus, M., Porter, R. N. & Sharma, R. D. Exchange Reactions with Activation Energy. I. Simple Barrier Potential for (H, H<sub>2</sub>). *Journal of Chemical Physics* **43**, 3259–3287 (1965).
51. Wijzenbroek, M., Helstone, D., Meyer, J. & Kroes, G. J. Dynamics of H<sub>2</sub> Dissociation on the Close-Packed (111) Surface of the Noblest Metal: H<sub>2</sub> + Au(111). *Journal of Chemical Physics* **145**, 144701 (2016).
52. Sarma, G., Yang, C.-H., Saha, A. K., Parker, D. H. & Wiesenfeld, L. Rotational excitation of HDO and D<sub>2</sub>O by H<sub>2</sub>: Experimental and theoretical differential cross-sections. *Journal of Chemical Physics* **138** (2013).
53. Kresse, G. & Hafner, J. *Ab Initio* Molecular Dynamics for Liquid Metals. *Physical Review B* **47**, 558–561 (1993).
54. Kresse, G. & Hafner, J. *Ab Initio* Molecular-Dynamics Simulation of the Liquid-Metal-Amorphous-Semiconductor Transition in Germanium. *Physical Review B* **49**, 14251–14269 (1994).
55. Kresse, G. & Furthmüller, J. Efficiency of *Ab-Initio* Total Energy Calculations for Metals and Semiconductors Using a Plane-Wave Basis Set. *Computational Materials Science* **6**, 15–50 (1996).
56. Kresse, G. & Furthmüller, J. Efficient Iterative Schemes for *Ab Initio* Total-Energy Calculations Using a Plane-Wave Basis Set. *Physical Review B* **54**, 11169–11186 (1996).
57. Blöchl, P. E. Projector Augmented-Wave Method. *Physical Review B* **50**, 17953–17979 (1994).
58. Román-Pérez, G. & Soler, J. M. Efficient Implementation of a van der Waals Density Functional: Application to Double-Wall Carbon Nanotubes. *Physical Review Letters* **103**, 096102 (2009).
59. Ghassemi, E. N. *et al.* Transferability of the Specific Reaction Parameter Density Functional for H<sub>2</sub> + Pt(111) to H<sub>2</sub> + Pt(211). *Journal of Physical Chemistry C* **123**, 2973–2986 (2019).

60. Pijper, E., Kroes, G. J., Olsen, R. A. & Baerends, E. J. Dissociative and Diffractive Scattering of H<sub>2</sub> from Pt(111): A Four-Dimensional Quantum Dynamics Study. *Journal of Chemical Physics* **116**, 9435–9448 (2002).
61. Díaz, C., Olsen, R. A., Busnengo, H. F. & Kroes, G. J. Dynamics on Six-Dimensional Potential Energy Surfaces for H<sub>2</sub>/Cu(111): Corrugation Reducing Procedure versus Modified Shepard Interpolation Method and PW91 versus RPBE. *Journal of Physical Chemistry C* **114**, 11192–11201 (2010).
62. Kroes, G. J. & Díaz, C. Quantum and Classical Dynamics of Reactive Scattering of H<sub>2</sub> from Metal Surfaces. *Chemical Society Reviews* **45**, 3658–3700 (2016).
63. Chow, H. & Thompson, E. The Optical Potential in the Scattering of Hydrogen and Deuterium Atoms from LiF and NaF(001)\*. *Surface Science* **82**, 1–21 (1979).



# Summary

Many chemical and physical processes, for example in industry and also everyday life, happen on surfaces. One of the most important is reaction of a molecule on a surface in heterogeneous catalysis. Catalysis creates an alternative energy path to increase the speed and outcome of a reaction. There are many complexities to understand catalytic reactions. It is known that in the reaction mechanism for ammonia synthesis, the dissociation of nitrogen on the catalyst surface is the rate limiting step. The availability of accurate barriers for reactions of molecules on metal surfaces is of central importance to understanding and accurately calculating the rate of heterogeneously catalyzed processes.

Implementations of first principle methods provide availability of the chemically accurate calculation of barriers for gas phase reactions. However, for reactions of molecules on metal surfaces there is plenty of room for improvement. Density functional theory (DFT) using functionals at the generalized gradient approximation (GGA) or meta-GGA level, which can be used to map out potential energy surfaces (PESs) for molecule interacting with metal surfaces, is not yet capable of predicting reaction barriers for gas-phase reaction with chemical accuracy. Most recently, an implementation of the specific reaction parameter approach to DFT (SRP-DFT), adopted to molecule surface interactions, was proposed in which usually a single adjustable parameter in the density functional is fitted to reproduce an experiment that is particularly sensitive to the reaction barrier height for the specific system considered. The quality of the SRP density functional (SRP-DF) is tested by checking that the candidate SRP-DF for a system can also reproduce other experiments on the system, which differ from the experiment the functional was fitted to. This approach has provided accurate values of barrier heights for the dissociative chemisorption of  $\text{H}_2$  on Cu(111), Cu(100), and also of  $\text{CH}_4$  on Ni(111), Pt(111) and Pt(211) so

far. However, being semi-empirical and in need of validation, the SRP–DFT approach is not without problems.

In this thesis, the main aim is to provide an improved description of  $\text{H}_2$  dissociative chemisorption on metal surfaces based on the semi-empirical SRP method in which the accuracy of exchange-correlation (XC) functionals is systematically improved in a semi-empirical and system specific way, by comparing the experimental data with theoretical results. The goal is to construct a database of reaction barriers with chemical accuracy for  $\text{H}_2$  interacting with metal surfaces.

In Chapter 3, the aim is to extend the development of SRP density functionals, and the database, with a result for a weakly activated dissociative chemisorption reaction of  $\text{H}_2$  with a transition metal surface. For this aim, a SRP–DF is developed, in which the SRP functional incorporates in the correlation part the revised version of the vdW-DF called vdW-DF2, for the dissociation of dihydrogen on Pt(111). The study has been performed using semi-empirical density functional theory and the quasi-classical trajectory (QCT) method. The validity of the QCT method is investigated by showing that QCT calculations on reaction of  $\text{D}_2$  with Pt(111) closely reproduce quantum dynamics (QD) results for reaction of  $\text{D}_2$  in its rovibrational ground state. The goal is to achieve a chemically accurate description of  $\text{D}_2$  dissociation on Pt(111) with molecular beam simulations, while reproducing the experimental results at normal and off-normal incidence. In this chapter, an SRP-DF for  $\text{H}_2$  on Pt(111) was obtained by adjusting the  $\alpha$  parameter in the  $\text{PBE}\alpha$ -vdW-DF2 functional until reaction probabilities computed with the QCT method reproduced sticking probabilities measured for normally incident  $\text{D}_2$  with chemical accuracy. Reproducing the experimental data by using the SRP–DF functional and QCT calculations for off-normal incidence for  $\theta_i = 30$  and  $45^\circ$ , for which computed reaction probabilities show no dependence on the plane of incidence, confirms the quality of the SRP functional. We report that the minimum barrier height obtained for the reaction is  $-8$  meV, in agreement with the experimental observation of no, or only a small energetic threshold to reaction. This value can be entered into a small, but growing database with barriers of reactions of molecules with metal surfaces, for which chemical accuracy is claimed.

In Chapter 4, the main focus is on the transferability of an SRP functional among chemically related systems. The SRP functional originally developed to describe chemisorption of dihydrogen on Cu(111) (called SRP48 functional) is tested here on dissociation of the same molecule on Ag(111),



with Cu and Ag belonging to the same group of the periodic table. In this chapter, we use the QCT method to compute molecular beam sticking probabilities and initial-state resolved reaction probabilities. To establish the appropriateness of the QCT method, we performed QD calculations for several rovibrational states, and compared with the QCT results. It is found that the QCT method reproduces the QD results very well. It is also found that the barrier heights in the SRP48 PES are higher than obtained with the PBE functional. Furthermore, we computed molecular beam sticking probabilities and compared with the available experimental results. The energy differences between the computed data and the spline interpolated experimental curve were in the range 2-2.3 kcal/mol. Thus, no chemical accuracy was achieved in our theoretical results. Our results show that the SRP48 functional is not transferable to H<sub>2</sub> dissociating on Ag(111) system, although Cu and Ag belong to the same group.

In Chapter 5, the main goal is to address the question whether the SRP-DF functional derived for dissociative chemisorption of H<sub>2</sub> on Pt(111) is transferable to H<sub>2</sub> reacting on Pt(211), which is relevant to heterogeneous catalysis. We use the SRP-DF functional, which was originally derived for the H<sub>2</sub> + Pt(111) system and is able to reproduce experiments on this system with chemical accuracy to model the reaction of H<sub>2</sub> on the stepped Pt(211) surface. We have performed molecular beam simulations with the QCT method using the BOSS model. The accuracy of the QCT method was assessed by comparison with QD results for reaction of the ro-vibrational ground state of H<sub>2</sub>. The study shows that the theoretical results for sticking of H<sub>2</sub> and D<sub>2</sub> on Pt(211) are in quite good agreement with experiment, but uncertainties remain due to a lack of accuracy of the QCT simulations at low incidence energies, and possible inaccuracies in the reported experimental incidence energies at high energies. We also investigate the non-adiabatic effect of electron-hole pair excitation on the reactivity using the molecular dynamics with electron friction (MDEF) method, employing the local density friction approximation (LDFA). Only small effects of electron-hole pair excitation on sticking are found.

In Chapter 6, the focus is on two basic problems of the SRP-DFT methodology. The first problem is that sticking probabilities (to which SRP-DFs functionals are usually fitted) might show differences across experiments, of which the origins are not always clear. The second problem is that it has proven hard to use experiments on diffractive scattering of H<sub>2</sub> from metals for validation purposes, as dynamics calculations using a SRP-DF

may yield a rather poor description of the measured data, especially if the potential used contains a van der Waals well.

To address the first problem of the SRP–DFT approach, we have simulated three sets of measurements of sticking probabilities available for  $D_2 + Pt(111)$ , using four different sets of molecular beam parameters. We compared these experiments on a one-to-one basis. We report that substantial differences exist between the three sticking probability curves measured for  $D_2 + Pt(111)$ . We discuss the origin of the discrepancies between different experimental data and report the mean absolute deviations between the data of the experiments. We also discuss the question of which set of beam parameters can best be used to simulate a particular set of molecular beam experiments. We obtained that all three sets of experiments can be described with chemical accuracy using molecular beam parameters describing seeded molecular beams that are broad in energy. Performing simulations with different sets of molecular beam parameters also provides insight into under which conditions the experiments should agree with one another.

To address the second problem of the SRP–DFT approach, we performed diffractive scattering calculations comparing with experiments, using the SRP–DF. The theoretical results are shown and compared with experimental results for off-normal incidence for two incidence directions. Our results show that there are both quantitative and qualitative discrepancies between theory and experiments. Our study suggests that the SRP–DF for  $H_2 + Pt(111)$  may not yet be accurate enough to describe the diffraction in this system. The van der Waals well plays a role in the description of scattering of  $H_2$  from  $Pt(111)$  and with the use of a PES exhibiting a van der Waals well, part of the scattering should be indirect. A similar study on  $H_2$  scattering from  $Ru(0001)$  has shown that the agreement between experiment and theory with inclusion of a van der Waals well in the PES was improved by assuming a static surface disorder of metal surface. However, our results established that making this assumption will not improve the agreement between theory and experiment in the case of  $H_2$  scattering from  $Pt(111)$ .

# Samenvatting

Vele chemische en fysische processen, bijvoorbeeld in de industrie maar ook in het dagelijks leven, vinden plaats aan oppervlakken. In een van de meest belangrijke in de heterogene katalyse reagent een molecuul aan een oppervlak processen. Katalyse creëert een alternatief reactiepad dat de snelheid en opbrengst van een reactie vergroot. Katalytische reacties zijn zeer complex om te doorgronden. Het is bekend dat in het reactie mechanisme voor de synthese van ammoniak de snelheidsbepalende stap de dissociatie van stikstof op het katalytische oppervlak de snelheidsbepalende stap is. De beschikbaarheid van accurate barrières voor reacties van moleculen aan metaaloppervlakken is van vitaal belang voor het doorgronden en nauwkeurig berekenen van reactiesnelheden van heterogeen gekatalyseerde reacties.

Implementaties van ab initio methoden maken het mogelijk om chemisch nauwkeurige barrières te berekenen voor gasfase reacties. Dit in tegenstelling tot de beschrijving van reacties van moleculen aan metaaloppervlakken, daar is nog zeer veel ruimte voor verbetering. Dichtheidsfunctionaaltheorie (DFT) waarin functionalen gebruikt worden op het niveau van de gegeneraliseerde gradiënt benadering (GGB) of meta-GGB, welke gebruikt kan worden om potentiële energie oppervlakken (PEO'en) voor de interactie van moleculen met metaaloppervlakken uit te rekenen, is nog niet in staat om reactiebarrières van gasfase reacties te voorspellen met chemische nauwkeurigheid. Recent is de specifieke reactieparameter aanpak voor DFT (SRP–DFT) toegepast voor de beschrijving van de interactie tussen moleculen en oppervlakken. In de SRP–DFT aanpak is het gebruikelijk dat een enkele parameter in de dichtheidsfunctionaal op een empirische wijze wordt aangepast opdat een experiment gereproduceerd kan worden, waarbij dat experiment zeer gevoelig is voor de hoogte van de reactiebarrière van het specifieke systeem dat beschouwd wordt. De kwaliteit van de

SRP-dichtheidsfunctionaal (SRP-DF) wordt geverifieerd door te toetsen of de kandidaat SRP-DF voor een systeem ook andere experimenten aan hetzelfde systeem kan reproduceren dan slechts het experiment waaraan de SRP-DF was ontworpen. Deze aanpak heeft vooralsnog nauwkeurige barrièrehogtes opgeleverd voor de dissociatieve chemisorptie van  $H_2$  op Cu(111) en Cu(100), alsook voor de dissociatieve chemisorptie van  $CH_4$  op Ni(111), Pt(111) en Pt(211). Hoewel de SRP-DFT aanpak semi-empirisch en in afwachting van validatie is, is zij niet zonder haar problemen.

Het hoofdoel van dit proefschrift is een verbeterde beschrijving van dissociatieve chemisorptie van  $H_2$  op metaaloppervlakken, gebaseerd op de SRP methode waarbij de nauwkeurigheid van de omwisselings-correlatie functionaal (OC) op semi-empirische en systeem specifieke wijze systematisch wordt verbeterd door vergelijking van experimentele data met theoretische uitkomsten. Hierbij is het doel om een database aan te leggen met chemisch nauwkeurige reactiebarrières voor de reactie van  $H_2$  aan metaal oppervlakken.

Het doel van hoofdstuk 3 is om de ontwikkeling van SRP dichtheidsfunctionalen een stap verder te brengen, alsmede de database, met resultaten voor zwak geactiveerde, dissociatieve chemisorptie reacties van  $H_2$  aan overgangsmetaaloppervlakken. Voor dit doel is er een SRP-DF ontwikkeld, waarin voor het gedeelte dat de correlatie beschrijft de gereviseerde vdW-DF genaamd vdW-DF2 is toegepast, voor de dissociatie van  $H_2$  op Pt(111). Dit onderzoek is uitgevoerd met behulp van semi-empirische DFT en de quasi-klassieke baan (QKB) methode. De validiteit van de QKB methode wordt onderzocht door te laten zien dat QKB berekeningen aan de reactie van  $D_2$  met Pt(111) sterk overeen komen met kwantumdynamica (KD) resultaten voor de reactie van  $D_2$  in zijn rovibrationele grondtoestand. Het doel is tot een chemisch nauwkeurige beschrijving te komen van de dissociatie van  $D_2$  op Pt(111) met moleculaire bundel simulaties, en tegelijkertijd experimentele resultaten voor loodrechte en niet-loodrechte invallen te reproduceren. In dit hoofdstuk is een SRP-DF verkregen voor  $H_2$  reagerend op Pt(111) door de parameter in de PBE $\alpha$ -vdW2-DF2 dichtheidsfunctionaal aan te passen totdat de reactiewaarschijnlijkheden berekend met de QKB methode experimentele reactiewaarschijnlijkheden voor loodrecht inkomend  $D_2$  reproduceerden met chemische nauwkeurigheid. Het reproduceren van experimentele data met behulp van de SRP-DF samen met QKB berekeningen voor niet loodrechte inval voor  $\theta_i = 30$  and  $45^\circ$ , waarvoor de berekende reactiewaarschijnlijkheden geen afhankelijkheid vertonen met het vlak

van inval, bevestigt de kwaliteit van de SRP dichtheidsfunctionaal. We rapporteren dat de minimumhoogte van de verkregen barrière voor de reactie -8 meV is, overeenkomende met de experimentele observatie van geen of slechts een kleine energetische drempel voor reactie. Deze waarde kan worden toegevoegd aan een kleine, maar groeiende, database van barrières van reacties van moleculen aan metaaloppervlakken voor welke chemische nauwkeurigheid wordt geclaimd.

In hoofdstuk 4 ligt de focus op de overdraagbaarheid van een SRP dichtheidsfunctionaal naar andere gerelateerde chemische systemen. De SRP dichtheidsfunctionaal die oorspronkelijk is ontwikkeld om chemisorptie van  $H_2$  op Cu(111) te beschrijven (namelijk de SRP48 dichtheidsfunctionaal) wordt hier getest voor dissociatie van hetzelfde molecuul op Ag(111), waarbij Cu en Ag tot dezelfde groep van het periodiek systeem behoren. In dit hoofdstuk gebruiken we de QKB methode om moleculaire bundel reactiewaarschijnlijkheden uit te rekenen en initiële-toestand-specifieke reactiewaarschijnlijkheden. Om de toepasbaarheid van de QKB methode vast te stellen hebben we KD berekeningen uitgevoerd voor verschillende ro vibrationele toestanden en die vergeleken met QKB resultaten. We tonen aan dat de QKB methode de KD resultaten zeer goed kan reproduceren. Verder laten we zien dat de barrièrehoogtes van het SRP48 PEO hoger zijn dan die verkregen met de PBE dichtheidsfunctionaal. Tevens rekenen we moleculaire bundel reactiewaarschijnlijkheden uit en vergelijken die met experimentele resultaten. De energie verschillen tussen de berekende data en de spline geïnterpoleerde curve lagen in het interval 2–2.3 kcal/mol. Dientengevolge hebben we geen chemische nauwkeurigheid bereikt in onze theoretische resultaten. Onze resultaten laten zien dat de SRP48 dichtheidsfunctionaal niet overdraagbaar is naar de dissociatie van  $H_2$  op het Ag(111) systeem, hoewel Cu en Ag tot dezelfde hoofdgroep behoren.

In hoofdstuk 5 wordt de vraag gesteld of de SRP–DF ontworpen voor dissociatieve chemisorptie van  $H_2$  op Pt(111) overdraagbaar is naar  $H_2$  reagerend op Pt(211), wat relevant is voor heterogene katalyse. We gebruiken de SRP–DF die oorspronkelijk is ontworpen voor het  $H_2 + Pt(111)$  systeem en dit systeem met chemische nauwkeurigheid kan beschrijven voor het modelleren van de reactie van  $H_2$  op het gestapte Pt(211) oppervlak. We hebben moleculaire bundel simulaties uitgevoerd met de QKB methode gebruikmakend van het BOSS model. De nauwkeurigheid van de QKB methode is vastgesteld door te vergelijken met KD resultaten voor de ro vibrationele grondtoestand van  $H_2$ . Dit onderzoek laat zien dat de theoret-

ische resultaten voor de reactie van  $H_2$  en  $D_2$  op Pt(211) goed overeenkomen met experimentele data, hoewel onzekerheden blijven bestaan door een gebrek aan nauwkeurigheid van de QKB berekeningen bij lage translatie energieën en mogelijke onnauwkeurigheden in de gerapporteerde experimentele invalenergiën voor hoge energien. We onderzoeken ook het niet-adiabatische effect van elektron-gat-paar excitaties op de reactiviteit door gebruik te maken van de moleculaire dynamica met elektronische frictie (MDEF) methode, die gebruik maakt van de lokale dichtheid frictiebenaadering (LDFB). Slechts kleine effecten van elektron-gat parenexcitatie op de reactiewaarschijnlijkheid zijn waargenomen.

In hoofdstuk 6 ligt de focus op twee problemen aan de basis van de SRP–DFT methodologie. Het eerste probleem is dat reactiewaarschijnelijkheden (waaraan de SRP–DF' en gewoonlijk aan geparametriseerd worden) verschillen kunnen vertonen tussen experimenten, waarvan de oorzaak niet altijd duidelijk is. Het tweede probleem is dat het moeilijk is gebleken experimenten aan verstrooiing van  $H_2$  aan metaaloppervlakken te gebruiken als validatie omdat dynamica berekeningen die een SRP–DF gebruiken mogelijk een slechte beschrijving opleveren van de gemeten data, zeker wanneer de gebruikte potentiaal een Van der Waals put bevat.

Om het eerste probleem binnen de SRP–DFT methodologie aan te pakken simuleren we drie groepen van metingen aan de reactiewaarschijnelijkheden die beschikbaar zijn voor de reactie van  $D_2$  aan Pt(111), hierbij gebruikmakend van vier verschillende groepen van moleculaire bundel parameters. We hebben deze experimenten op een één-op-één basis vergeleken. We rapporteren dat er substantiële verschillen bestaan tussen de drie reactiewaarschijnlijkheidscurves gemeten voor  $D_2$  reagerend aan Pt(111). We bespreken de oorzaak van deze discrepanties tussen verschillende groepen experimentele data en rapporteren de gemiddelde absolute afwijkingen tussen de verschillende groepen experimentele data. We bespreken ook de vraag welke groep van bundel parameters het beste gebruikt kan worden om om een specifieke set van moleculaire bundel experimenten te simuleren. We beschrijven dat alle drie de groepen van experimenten met chemische nauwkeurigheid beschreven kunnen worden wanneer moleculaire bundel parameters worden gebruikt die verrijkte bundels die breed in energie zijn beschrijven. Het uitvoeren van simulaties met verschillende groepen van moleculaire bundel parameters biedt ook inzicht in onder welke omstandigheden de experimenten met elkaar overeen zouden moeten komen.

Om het tweede probleem van de SRP–DFT methodologie aan te pakken

hebben we verstrooiingsberekeningen uitgevoerd en die vergeleken met experimenten, gebruik makend van de SRP–DF. De theoretische resultaten worden getoond en vergeleken met experimentele resultaten voor niet-lood rechte inval voor twee invalhoeken. Onze resultaten tonen aan dat er zowel kwalitatieve als kwantitatieve discrepanties bestaan tussen het experiment en de theorie. Ons onderzoek suggereert dat de SRP–DF voor  $H_2$  reagerend op Pt(111) misschien nog niet nauwkeurig genoeg is om verstrooiing in dit systeem te beschrijven. De Van der Waals put speelt een rol in de beschrijving van verstrooiing van  $H_2$  van Pt(111), en met het gebruik van een PEO dat een Van der Waals put bezit zou een deel van de verstrooiing indirect moeten zijn. Een vergelijkbaar onderzoek naar  $H_2$  verstrooiing van Ru(0001) heeft uitgewezen dat de overeenkomst tussen experiment en theorie, met inbegrip van de Van der Waals put in het PEO, verbeterd werd door uit te gaan van een statische oppervlakteverstoring. Daar staat tegenover dat onze resultaten vaststellen dat het maken van deze aanname de overeenkomsten tussen theorie en experiment niet verbeteren in het geval van  $H_2$  verstrooiing aan Pt(111).





# Curriculum Vitae

Elham Nour Ghassemi was born on March, 21 1980 in Tabriz (Iran). In 1999, she was graduated in Mathematics and Physics from Tohid high school, Tabriz, Iran. She received her BSc degree in Solid State Physics from Azerbaijan University, Tabriz, Iran. After receiving her bachelor's degree in 2003, she studied Solid State Physics and Electronics at the University of Tabriz from 2003 to 2005, obtaining her master degree. She started working at the lab located in Isfahan University of Technology, as a teacher and research assistance for three years. On September 2008, she moved to Stockholm, Sweden, where she got admitted to work as a research assistance at Stockholm University under supervision of Prof. dr. Åsa Larson and Dr. Jonas Larson in the faculty of science in theoretical physics and the molecular physics department. She received a second master degree in 2011 and continued her collaboration with Stockholm University until 2012. On January 2014, she joined the group of Prof. dr. Geert-Jan Kroes at the Leiden Institute of Chemistry of Leiden University, The Netherlands as a PhD candidate. Her research was funded by an ERC Advanced grant. Her research led to a number of publications and this thesis.



# List of Publications

1. J. Larson, E. Nour Ghassemi and Å. Larson "Anomalous Molecular Dynamics in the Vicinity of a Conical Intersection" *EPL (Europhysics Letters)* 101, 43001 (2013).
2. E. Nour Ghassemi, J. Larson, Å. Larson, "A Diabatic Representation of the Two Lowest Electronic States of  $\text{Li}_3$ " *The Journal of Chemical Physics* 140, 154304 (2014).
3. E. Nour Ghassemi, M. Wijzenbroek, M. F. Somers, and G. J. Kroes, "Chemically Accurate Simulation of Dissociative Chemisorption of  $\text{D}_2$  on Pt(111)" *Chemical Physics Letters*, 683, 329-335 (2017).
4. E. Nour Ghassemi, M. F. Somers and G. J. Kroes, "Test of the Transferability of the Specific Reaction Parameter Functional for  $\text{H}_2 + \text{Cu}(111)$  to  $\text{D}_2 + \text{Ag}(111)$ " *The Journal of Physical Chemistry C*, 122, 22939-22952 (2018).
5. E. Nour Ghassemi, E. W. F. Smeets, M. F. Somers, G. J. Kroes, I. M. N. Groot, L. B. F. Juurlink, G. Füchsel, "Transferability of the Specific Reaction Parameter Density Functional for  $\text{H}_2 + \text{Pt}(111)$  to  $\text{H}_2 + \text{Pt}(211)$ " *The Journal of Physical Chemistry C* 123(5), 2973-2986 (2019).
6. E. Nour Ghassemi, M. F. Somers, and G. J. Kroes, "Assessment of Two Problems of Specific Reaction Parameter Density Functional Theory: Sticking and Diffraction of  $\text{H}_2$  on Pt(111)" *The Journal of Physical Chemistry C* 123(16), 10406-10418 (2019).



# Afterword

On January 2014, when I started my journey as a “ *PhD candidate* ”, to me, it seemed like a magic to finish it. Now the journey is about to finish and the magic is going to happen. I owe this to my kind and supportive supervisors, colleagues, friends and family members. This work would not have been possible without the valuable assistance of them. Here, I would like to devote this space to thanking those who have walked alongside me during this journey and made the magic happen.

To *Geert-Jan Kroes* : thanks for providing me this wonderful opportunity of being a member of the LIC family. I learned, grew and enjoyed every moment of working there.

It is my greatest duty to express my deep regards and gratitude to *Mark Somers*, for under whose guidance and supervision I was able to undertake this project.

I am also grateful to the European Research Council (ERC), who funded this work.

To my committee members, *Prof. dr. H. S. Overkleeft*, *Prof. dr. M. T. M. Koper*, *Prof. dr. H. J. M. de Groot*, *Prof. dr. A. Groß*, *Prof. dr. G. C. Groenenboom*, *Dr. C. Díaz*, and *Dr. I. M. N. Groot*: I am appreciative of you for evaluating my thesis and be a member of my graduation committee.

To my project teammates, *Gernot Fuchs*, *Irene Groot*, *Ludo Juurlink*, *Egidius Smeets* and *Mark Wijzenbroek*: I am so grateful for the support and assistance provided by you. Thank you for all the generous advises. Discussing with you about the challenges has been always constructive and valuable to me. This thesis truly is the result of all those daily discussions.

To my creative and smart colleagues, *Davide Migliorini*, *Khosroe Shakori*, *Francesco Nattino*, *Katharina Doblhoff-Dier*, *Paul Spiering*, *Nick Gerrits*, *Jörg Meyer*, *Sayan Seal*, *Soroush Rasti*, *Theophile Tchakoua*, *Andrew Powell*, *Francesca Costanzo* and *Marc van Hemert* : I am indebted to you all. I

enjoyed every moment that we spent together. I will never forget all those small chats, coffee breaks, Friday talks.

To *Michelle van der Haar*: I am truly appreciated by the assistance provided by you. You have been always there to help me with all the steps that could accelerate required official procedures.

To my master supervisors in Stockholm University, *Asa Larson* and *Jonas Larson*, I would like to thank you for your kind supports and encouragements.

To my truly friends, *Soodeh*, and *Leila*, you have been always like a sister to me. You and your lovely families have been always there to lend me and my family a hand without hesitate. Me and my family will never forget your assistance and support.

To my kind friends, *Faezeh*, *Fatemeh*, *Afsaneh*, *Gerrie*, *Hanieh*, *Sara*, and other my *Gezellig* friends, thank you for all the warm and friendly gatherings.

To my dance teacher, *Sofya*, I released all my tiredness after hard working in your excellent Salsation classes and boosted my energy to do the best for the next day.

To my piano teacher, *Maria*, thank you for your encouraging word during the period that I had been writing my thesis and for our great chats.

To my kind in-laws, *Simin*, *Reza*, *Noushin* and *Farrin*: I owe a deep gratitude and thanks for your positive attitude and encouragement in all the steps.

To my incredible parents, *Farahnaz* and *Jalil*: I cannot express anything that can show my gratefulness for your love and encouragement. You are always ready to provide me hope and motivation for my next step. I would never have enjoyed so many wonderful opportunities without your endless sacrifice.

To my brother, *Behnam*: I am more than grateful to you. You were always kindly supporting my decisions. I hope I can spend more time later with you and your beloved families: *Loyan*, and *Sara*.

I save the last for the best. To my **lifelong friend**, *Afshin*: this would not be achieved without your support and patience. During this journey you have been always passionate, empathetic, persistent and considerate.

Finally I take pride in dedicating the current PhD thesis work to my **beloved son**, *Radin*. I love you for everything, for being so understanding through the toughest moments of my life. I hope be a good mom and spend more time with you.